Studies of the Higgs boson properties and search for new physics beyond the standard model in the top sector with the ATLAS detector

Grigore Tarna

AIX-MARSEILLE UNIVERSITÉ
BUCHAREST UNIVERSITÉ
Ecole Doctorale 352 : Physique et Sciences de la Matière

PARTENAIRES DE RECHERCHE

CPPM/IFIN-HH

Thèse présentée pour obtenir le grade universitaire de docteur

Discipline : Physique et Sciences de la Matière
Spécialité : Physiques des Particules et Astroparticules

Grigore TARNA

Studies of the Higgs boson properties and search for new physics beyond the standard model in the top sector with the ATLAS detector

Soutenue le 18/10/2019 devant le jury composé de :

Anne-Catherine LE BIHAN	IPHC, Strasbourg, France	Rapporteur
Virgil BARAN	University of Bucharest	Rapporteur
Cristinel DIACONU	CPPM, Marseille, France	Examinateur
Jean Baptiste DE VIVIE DE REGIE	LAL, Paris-Orsay, France	Examinateur
Pascal PRALAVORIO	CPPM, Marseille, France	Directeur de thèse
Calin ALEXA	IFIN-HH, Bucarest, Roumanie	Directeur de thèse

Numéro national de thèse/suffixe local : 2019AIXM0321/052ED352

Synthèse en français

Mots clés : LHC, ATLAS, Higgs, top, électrons, FCNC, Yukawa coupling

La physique des particules, ou physique des hautes énergies, étudie la matière à l'échelle subatomique. La théorie actuelle de la physique des particules, appelée modèle standard (MS), fusionne la relativité restreinte avec la mécanique quantique pour obtenir une théorie relativiste des champs quantiques qui décrivent les particules élémentaires et leurs interactions. Cette théorie est valide jusqu'à environ 10^{-18} m, ce qui correspond à une énergie de l'ordre de 100 GeV, appelée échelle électrofaible. Cette valeur est (en principe) un endroit privilégié pour observer de la nouvelle physique.

Le but de cette thèse est de tester la validité du MS à cette frontière en énergie en étudiant le couplage entre les deux particules les plus massives du MS, le quark top et le boson de Higgs. La thèse porte sur l'analyse des collisions proton-proton recueillies auprès du grand collisionneur de hadrons (LHC) situé au CERN (Organisation européenne pour la recherche nucléaire) près de Genève, seule machine aujourd'hui capable d'atteindre cette frontière en énergie dans le monde. La première prise de données (Run1) du LHC a permis la découverte du boson de Higgs en juillet 2012 et a confirmé les prédictions du Modèle Standard. Le LHC a ensuite redémarré au printemps 2015 avec une nouvelle énergie dans le centre de masse de 13 TeV (Run2), significativement plus élevée que celles du Run1 (7 et 8 TeV). Cette période de prise de données s'est arrêtée à la fin 2018. Les données utilisées dans cette thèse sont centrées uniquement sur les trois premières années d'exploitation (2015-2017). ATLAS (A Toroidal LHC ApparatuS), l'une des deux expériences généralistes du LHC, est l'outil idéal pour tirer profit de cette augmentation d'énergie et poursuivre les recherches des théories au-delà du Modèle Standard. Le détecteur ATLAS est situé à 100 mètres sous terre et mesure 44 mètres de long, 25 mètres de diamètre et pèse environ 7 000 tonnes. ATLAS a pour but d'identifier les particules secondaires produites lors des collisions proton-proton et de mesurer leurs positions dans l'espace, leurs charges, leurs vitesses, leurs masses et leurs énergies. Cela permet de reconstruire complètement les évènements engendrés par les collisions proton-proton. Pour ce faire, le détecteur comporte plusieurs sous-détecteurs ayant une excellente herméticité, une granularité très fine et une électronique résistante aux radiations.

La première partie de cette thèse porte sur la mesure de l'efficacité de reconstruction des électrons venant du vertex primaire (électrons "prompts") ainsi que

de deux algorithmes (PLI et PLV) rejettant les électrons provenant d'un jet de quark b (électrons "non-prompts").

La première mesure est notamment cruciale pour comprendre en détails tous les processus électrofaibles comme la mesure des sections efficaces de production des bosons W, Z et H où l'incertitude associée à la reconstruction des électrons est une source importante de l'erreur systématique finale. Les efficacités de reconstruction des électrons, ainsi que les incertitudes associées, sont mesurées dans 200 intervalles de pseudo-rapidité et d'impulsion transverse (E_T) à partir des premières données du Run2 (36 fb^{-1}) en utilisant un échantillon pur d'électrons ($Z \to ee$) par la méthode *tag & probe* (T&P). Ces efficacités sont obtenues pour plusieurs points de fonctionnement pour l'identification, l'isolation et le déclenchement des électrons, étudiés pour répondre aux exigences de toutes les analyses de physique d'ATLAS. Pour l'obtention des résultats de physique, des échantillons correspondant aux sélections effectuées sur les données sont simulés pour reproduire autant que possible l'efficacité mesurée dans les données. Dans l'ensemble, l'efficacité de la reconstruction varie de 97% à 99% avec des erreurs typiques mesurées inférieures à 0.1% pour $E_T > 25$ GeV et pouvant aller jusqu'à 2 % pour des impulsions transverses entre 15 et 25 GeV. Les facteurs de correction qui sont appliqués sur les lots de simulation sont très proches de l'unité avec une erreur, complètement dominée par les systématiques, de 2 % pour $15 < E_T < 25$ GeV et plus petite que 1% pour $E_T > 25$ GeV. Ceci donne confiance dans la description de la réponse du détecteur aux électrons pour $E_T > 15$ GeV. Cela montre aussi l'excellente capacité du détecteur ATLAS pour reconstruire les électrons dans l'environnement hadronique du LHC d'une part et la bonne compréhension des performances des électrons d'autre part.

La deuxième mesure a été développée dans le cadre des analyses mesurant le couplage direct du quark top au boson de Higgs (couplage de Yukawa du top) et recherchant la désintégration rare du quark top en Higgs + quark (top FCNC), expliquées plus loin. Dans les deux cas, les électrons non-prompts sont un des principaux bruit de fond, dont la réduction puis l'estimation est un des principaux défis de l'analyse. L'impact des deux algorithmes PLI et PLV sur l'efficacité des électrons prompts est également estimé à l'aide de méthodes T&P basées sur des échantillons purs d'électrons venant des lots $Z \to ee$. L'efficacité des électrons prompts de passer la coupure sur PLI est mesurée entre 60 et 96% (Figure 3.1) avec 36 fb^{-1} de données. Les facteurs de corrections appliqués sur la simulation sont proches de 1 et sont mesurés avec une erreur variant de 0.5 à 2%. Cette mesure a été une des pièces qui a permis la mise en évidence du couplage de Yukawa du quark top en 2017, puis sa découverte en 2018 – un des objectifs majeurs de l'expérience ATLAS pour le Run2. Cette mesure a ensuite été refaite avec 80 fb^{-1} et l'algorithme PLV.

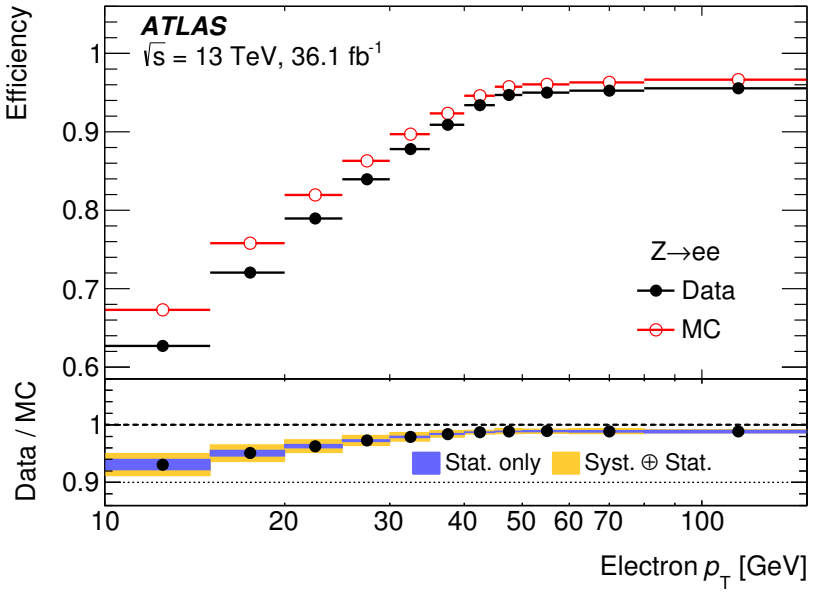

Figure 0.1 – Mesures de l'efficacité des électrons passant la coupure sur l'algorithme PLI dans les événements $Z \to ee$ en fonction de l'énergie transverse E_T pour l'ensemble de données 2015-2016 (points pleins) et pour MC (points vides). Le rapport entre l'efficacité des données et celle de la simulation est affiché sous la figure. Les barres d'erreur incluent des incertitudes statistiques et systématiques.

La deuxième partie de la thèse est tout d'abord consacrée à la recherche du canal $t \to Hq$ avec q=u, c et ensuite à la mesure du couplage de Yukawa du top dans la production du boson de Higgs en association avec une paire de quarks top (ttH). Dans les deux cas, l'analyse s'effectue dans le canal avec deux leptons de même signe ($2lSS$) et/ou trois leptons ($3l$). Elle utilise 36 fb^{-1} et 80 fb^{-1} de données respectivement.

Les désintégrations $t \to Hq$ font appel à des courants neutres qui changent de saveur (FCNC) et sont fortement supprimés dans le Modèle Standard par le mécanisme de GIM. Les rapports d'embranchements prédits sont autour de 10^{-15}. Cependant, plusieurs modèles prédisent une valeur plus grande pour ce rapport d'embranchement. C'est le cas notamment du modèle avec deux doublets de Higgs (2HDM), qui ajoute un champ de Higgs supplémentaire au Modèle Standard, et prédit des rapports d'embranchement pouvant aller jusqu'à 10^{-4}. L'étude se fait dans les canaux $t\bar{t}$ où l'un des deux quark top décroît en $t \to Hq$. Dans cette thèse, les canaux étudiés correspondent aux désintégrations du Higgs en une paire de bosons W ou de bosons Z, qui eux même se désintègrent en paire de leptons. Les états finals avec deux leptons de même charge et trois leptons sont considérés. Une analyse multivariée (MVA) est mise en oeuvre pour distinguer le signal FCNC des deux bruits de fond principaux du Modèle Standard : d'un côté

la production associée de paires de quark top avec un boson W ou un boson Z et de l'autre des leptons venant de jets de b. Ma contribution a consisté à comparer plusieurs lots de variables discriminantes pour trouver celles qui convenait le mieux aux canaux $2lSS$ et $3l$. Le nombre minimum de variables pour avoir une analyse robuste a été retenu. Les deux MVA sont ensuite combinés en un seul, et optimisé pour assurer la meilleure sensibilité sur les rapports d'embranchement $B(t \to Hu)$ et $B(t \to Hc)$. Un ajustement des données est enfin effectué sur ce MVA final à l'aide d'un maximum de vraisemblance pour déterminer la sensibilité finale. Les valeurs obtenues pour $B(t \to Hu)$ et $B(t \to Hc)$ sont compatibles avec 0 et deux limites à 95% de niveau de confiance sont obtenues : BR($t \to Hu$) $<$ **0.19 %** et BR($t \to Hc$) $<$ **0.16 %**, completement dominés par l'erreur statistique. La Figure 4.22 illustre ce résultat, qui place la meilleure limite mondiale sur ces rapports d'embranchement.

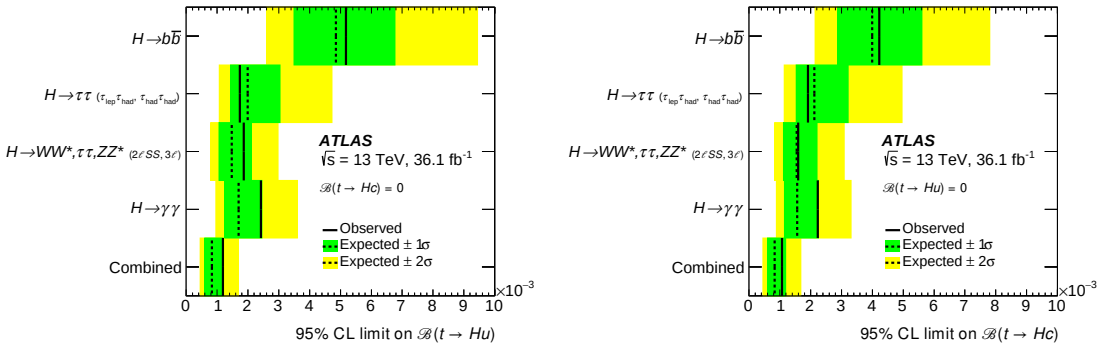

Figure 0.2 – Limite supérieure sur le rapport d'embranchement BR($t \to Hc$) individuel et combiné pour l'observation et la prédiction à 95% de niveau de confiance (gauche). Même résultat pour BR($t \to Hu$) (droite). Dans les deux cas, les autres modes FCNC sont supposés nuls.

Le canal où la production du boson de Higgs se fait en association avec une paire de quarks top (ttH) est la seule façon d'obtenir une mesure directe du couplage de Yukawa du top. Les couplages du Higgs aux fermions étant proportionnels aux masses des fermions, le couplage Higgs-top est le plus grand avec une valeur proche de 1 dans le MS. La mesure du couplage entre les deux plus lourdes particules du MS est aussi particulièrement sensible à la présence de Nouvelle Physique. Le travail s'est concentré sur le canal $2lSS$. Il a permis la mise à jour de l'analyse publiée avec les données 2015+2016 (36 fb^{-1} de données) en rajoutant les données enregistrées en 2017 (44 fb^{-1} de données). La stratégie d'analyse a été la même que celle employée pour l'analyse des données 2015+2016 (et est très proche de celle utilisée pour l'analyse FCNC décrite ci-dessus). Le principal changement vient de la sélection des leptons, avec une coupure plus dure sur l'algorithme PLI, qui permet de diminuer la contribution venant des leptons non-prompt. Ce changement qui a nécessité une réoptimisa-

tion complète de l'analyse et apporte une amélioration de 16% sur la précision avec laquelle la force du signal ttH est mesurée. Cependant il est apparu alors que le bruit de fond venant de la conversion des photons en deux électrons n'était plus correctement estimé par la méthode développée pour l'analyse précedente. Ceci a eu pour conséquence une réorientation de la stratégie d'analyse auquel il ne m'a pas été possible de contribuer – cet effort est toujours en cours.

Contents

Introduction

So far, the known Universe is described by four fundamental forces. These are the gravitational force, the electromagnetic force, the weak force and the strong force. The Standard Model (SM) of particle physics is a theoretical framework that encompasses three of the four forces (the gravitational force is not included in SM). It describes the properties of the elementary particles and their interactions and its predictions have been extensively verified. The last missing piece, the Higgs boson, was discovered in 2012 by the ATLAS and CMS experiments. This very important discovery allowed to confirm the mechanism through which all the fundamental particles acquire mass.

Despite its success, the SM still has some unsolved problems (gravitation, mater-antimatter asymmetry, neutrinos masses, etc.) that could be solved in Beyond SM (BSM) scenarios. New energy frontiers have to be explored and the Large Hadron Collider (LHC), the largest particle accelerator in the world, together with its associated detectors provide best available tools today. The purpose of this thesis is to search for new physics and to further investigate the properties of the Higgs boson, particularly in the top sector, with the help of the ATLAS detector.

The material in this thesis is organized as follows. Chapter 1 gives a brief overview on the theoretical aspects of the SM. Chapter 2 describes the experimental setup, giving a short description of the LHC accelerator, the ATLAS detector and the reconstruction procedure of the objects.

Chapters 3 to 5 summarize the work performed during the thesis and the main obtained results, with chapter 3 being focused on the electron performance aspects of the ATLAS detector and chapters 4 and 5 on the physics analyses. The first part of Chapter 3 describes the measurement of the electron reconstruction efficiency. The second part of chapter 3 describes an algorithm to identify and select non-prompt electrons (originating from heavy flavor decays) and details the efficiency measurement for this selection. These measurements were performed using a Tag-and-Probe method using up to 80 fb^{-1} of data collected in 2015-2017 and are an important component for analyses involving electrons and in particular for the the analyses presented in this thesis.

Chapter 4 details the search for flavor-changing neutral currents (FCNC) in top quark decays to a Higgs boson and using 36 fb^{-1} of proton-proton collision data collected in 2015-2016 by he ATLAS detector. These processes are forbidden at tree level in the SM and any deviations would be immediate proof of New Physics. Advanced multivariate analyses are performed in two channels with

two same-sign leptons (2ℓSS) and three leptons (3ℓ) to separate the signal from the background. Finally, chapter 5 gives an insight in the analysis of Higgs boson production in association with a top-antitop quarks (ttH) with multilepton final states which gives direct access to the top Yukawa coupling.

1 Elementary Particle Physics

Summary

Since the discovery of the first elementary particle in 1897, the electron, a general theory was needed to explain the world of particles and their interactions. So far, the Standard Model (SM) has proven to be a quite extensive, accurate and predictive theoretical framework which is the best available today. This chapters aims at giving a brief overview on the Standard Model and its limitations. Section 1.1 gives a summary of the SM particles and their most important properties. Section 1.2 describes the fundamental interactions. Some of the limitations and possible extensions of the SM are discussed in section 1.3. Finally, section 1.4 gives some Higgs boson phenomenology, subject that is relevant for the scope of this thesis.

1.1 Standard Model of Particle Physics

The SM was established in the 1960s from the work of Glashow [1], Salam [2] and Weinberg [3]. It comprises a total of 17 elementary particles, the Higgs boson being the last one experimentally discovered in 2012 by the ATLAS and CMS experiments at LHC [4, 5]. Figure 1.1 gives a summary of the particle content of the SM together where they are grouped by their properties (mass, spin and electrical charge). The particles are split in two categories based on

their spin. The particles with spin 1/2 are fermions and they satisfy the Fermi-Dirac statistics. They are also referred as "matter" particles since they obey the Pauli exclusion principle (no two identical particles can have the same quantum state). The particles with integer spin are the bosons, with the Higgs boson being a scalar (spin 0) and the vector bosons (spin 1) being the force carriers.

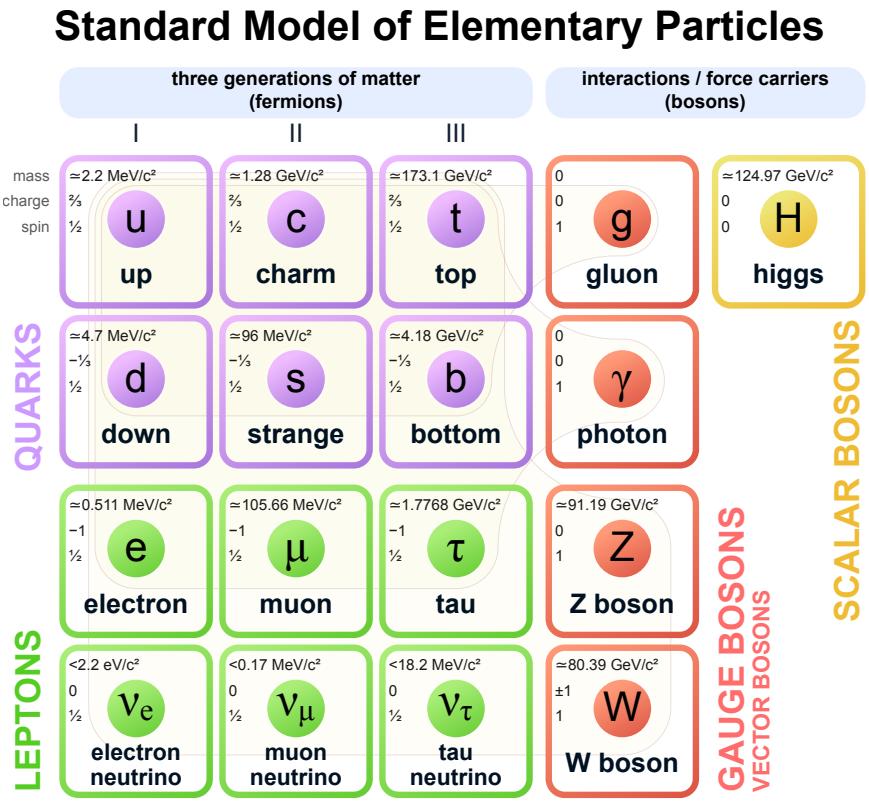

Figure 1.1 – Elementary particles in the Standard Model.

The fermions are split in three generations (flavors). The second and the third generation are basically heavier version of the first generation (the same properties except for the mass), with the third generation being the heaviest one. Based on the type of interactions the fermions are split into six leptons and six quarks (two per generation).

The leptons are the electron e, the muon μ and the tau τ which are massive ($m_e < m_\mu < m_\tau$) and have a electrical charge of -1. For each flavor there is a corresponding neutrino ν_e, ν_μ and ν_τ. One particularity for the neutrinos is that only left-handed helicity neutrinos have been observed in nature. The neutrinos are electrically neutral and are considered massless in SM [1]. The charged leptons

1. Neutrino oscillation experiments have shown that the flavor oscillation are possible for massive neutrinos only [6]. This represents a tension in the SM and requires modifications.

interact electromagnetically and weakly while the neutrinos interact only weakly.

The quarks can interact through all forces. They have a fractional electrical charge, 2/3 for up-type quarks (u, c and t) and -1/3 for the down-type quark (d, s and b) allowing them to interact electromagnetically . A color charge is assigned to every quark allowing them to interact strongly. The color charge was introduced to more intuitively understand the ternary concept of this charge, which by definition can be red, blue and green. One characteristics of the quarks is that they are not observed individually but form hadrons which have an integer electric charge and are color neutral ("white"), a phenomenon known as *confinement*.

1.2 Fundamental forces

The interactions between the elementary particles in SM are described by quantum field theories. The vector bosons (spin 1) are the force carriers that mediate the interactions. The photon mediates the electromagnetic interactions and the gluons mediate the strong interactions. The massive gauge bosons, $W^{\pm}$ si Z, mediate the weak force.

1.2.1 Electromagnetic interaction

The electromagnetic interaction is described by the quantum electrodynamics (QED). The Lagrangian for a free fermion is

$$\mathcal{L}_o = \bar{\psi}(i\gamma^\mu - m)\psi \tag{1.1}$$

where γ^μ are the Dirac matrices, ψ is the particle's wave function expressed as a Dirac spinor and m is the mass of the particle [2]. The Lagrangian is invariant under a global gauge transformation but it is not invariant under a local $U(1)$ symmetry group transformation $\psi \to e^{i\alpha(x)}\psi$,

$$\partial_\mu\psi \to e^{i\alpha(x)}\partial_\mu\psi + e^{i\alpha(x)}\partial_\mu\alpha \tag{1.2}$$

Introducing a covariant derivative $D_\mu = \partial_\mu - ieA_\mu$ and a vectorial field A_μ that transforms as $A_\mu \to A_\mu + \frac{1}{e}\partial_\mu\alpha$ restores the invariance under local gauge transformation.

Finally, the QED Lagrangian is

$$\mathcal{L}_{QED} = \bar{\psi}(i\gamma^\mu - m)\psi + e\bar{\psi}\gamma^\mu\psi A_\mu - \frac{1}{4}F^{\mu\nu}F_{\mu\nu} \tag{1.3}$$

2. Natural units $c = \hbar = 1$ are assumed everywhere in the document unless otherwise specified.

where the $\frac{1}{4}F^{\mu\nu}F_{\mu\nu}$ term corresponds to the kinetic term for the field A_μ, and

$$F_{\mu\nu} = \partial_\mu A_\nu - \partial_\nu A_\mu. \tag{1.4}$$

The photon is massless because no mass term is allowed for the field A_μ since it would break the gauge invariance.

1.2.2 Strong interaction

The theory describing the strong interaction is referred to as quantum chromodynamics (QCD). The Lagrangian for a free fermion as in the case of the electromagnetic interactions is

$$\mathcal{L}_o = \bar{q_j}(i\gamma^\mu - m)q_j \tag{1.5}$$

where q_j is the Dirac spinor for a quark of color j (j=1,2,3). In QCD the symmetry group is the $SU(3)$ and a local gauge transformation can be written as [3]

$$q(x) \to Uq(x) = e^{i\alpha_a(x)T_a}q(x), \tag{1.6}$$

where U is a 3×3 unitary matrix and T_a (a=1,...,8) are the SU(3) group generators (represented by Gell-Mann matrices).

Following a similar procedure as in the case of the electromagnetic interactions, in order to preserve the invariance 8 new fields G^a_μ are introduced and a covariant derivative

$$G^a_\mu \to G^a_\mu - \frac{1}{g_s}\partial_\mu \alpha \tag{1.7}$$

$$D_\mu = \partial_\mu + ig_s T_a G^a_\mu. \tag{1.8}$$

To take into account the non-abelian nature of the SU(3) an additional term is introduced

$$G^a_\mu \to G^a_\mu - \frac{1}{g}\partial_\mu \alpha - f_{abc}\alpha_b G^c_\mu \tag{1.9}$$

where f_{abc} are the symmetry group structure constants $[T_a, T_b] = if_{abc}T_c$.

Finally, the QCD Lagrangian can be written as

$$\mathcal{L}_{QCD} = \bar{q}(i\gamma^\mu D_\mu - m_f)q - \frac{1}{4}G^{\mu\nu}_a G^a_{\mu\nu} \tag{1.10}$$

where $-\frac{1}{4}G^{\mu\nu}_a G^a_{\mu\nu}$ is the kinetic term of the gluon filed G^a_μ and where the field strength tensor is expressed as

$$G^{\mu\nu}_a = \partial_\mu G^\nu_a - \partial_\nu G^\mu_a - g f_{abc} G^\mu_b G^\nu_c. \tag{1.11}$$

3. Only one color is $q_i \to q$ is considered from now on.

Unlike the case for the photons, the kinetic term includes also self-interaction terms for the gluons (3 and 4 gluon interactions). No mass terms are present in the QCD Lagrangian for the gluon fields G^a_μ as this would break the gauge invariance, therefore the gluons are massless.

1.2.3 Electroweak interaction

The weak interaction appeared as a necessity for explaining the β decays. Glashow [1], Salam [2] and Weinberg [3] unified the description of the weak force with the electromagnetic force to get the electroweak (EW) force.

To preserve the invariance under $SU(2)\times U(1)_Y$, massless gauge fields $W^a_\mu (a = 1,2,3)$ and B_μ are introduced, as well as the covariant derivatives that act on left-handed doublets ψ_L and right-handed singlets ψ_R

$$D_\mu \psi_L = (\partial_\mu + ig\frac{\tau_a}{2}W^a_\mu + ig'\frac{Y}{2}B^a_\mu)\psi_L \tag{1.12}$$

$$D_\mu \psi_R = (\partial_\mu + ig'\frac{Y}{2}B^a_\mu)\psi_R \tag{1.13}$$

where τ_a are the Pauli matrices (generators of $SU(2)_L$), g and g' are the $SU(2)_L$ and $U(1)_Y$ coupling constants and $Y_L(R)$ is the weak hypercharge for left-(right-)handed particles. The EW Lagrangian can be written as

$$\mathcal{L}_{EW} = \sum_\psi \bar{\psi}\gamma^\mu(i\partial_\mu - g\frac{\tau_a}{2}W^a_\mu - g'\frac{Y}{2}B^a_\mu)\psi - \frac{1}{4}W^{\mu\nu}_a W^a_{\mu\nu} - \frac{1}{4}B^{\mu\nu}B_{\mu\nu}. \tag{1.14}$$

The field strength tensors are

$$B_{\mu\nu} = \partial_\mu B_\nu - \partial_\nu B_\mu \tag{1.15}$$

$$W^a_{\mu\nu} = \partial_\mu W^a_\nu - \partial_\nu W^a_\mu - g\epsilon^a_{bc}W^b_\mu W^c_\nu \tag{1.16}$$

where ϵ_{abc} is the Levi-Civita symbol. The charged W bosons are linear combinations of the W^1_μ and W^2_μ components

$$W^\pm = \frac{W^1_\mu \mp iW^2_\mu}{\sqrt{2}}, \tag{1.17}$$

while the weak neutral field and and the electromagnetic component are obtained by rotation

$$\begin{pmatrix} Z^0_\mu \\ A_\mu \end{pmatrix} = \frac{1}{\sqrt{2}}\begin{pmatrix} \cos\theta & -\sin\theta \\ \sin\theta & \cos\theta \end{pmatrix}\begin{pmatrix} W^3_\mu \\ B_\mu \end{pmatrix} \tag{1.18}$$

where θ is the Weinberg angle which is defined as $g\sin\theta = g'\cos\theta = e$ (e is the

electromagnetic coupling).

Important consequences derive from the interactions with the quarks. In the weak charged current (W emission) the quarks changes from up-type (down-type) to down-type (up-type). Quark generation can also change because of the flavor mixing

$$\begin{pmatrix} d' \\ s' \\ b' \end{pmatrix} = \mathcal{V} \begin{pmatrix} d \\ s \\ b \end{pmatrix} \tag{1.19}$$

where $\mathcal{V}$ is the Cabibo-Kobayashi-Maskawa (CKM) matrix. For the neutral currents, weak or electromagnetic, no change in flavor or generation is allowed.

1.2.4 Spontaneous symmetry breaking and Higgs mechanisms

The EW Lagrangian in eq. (1.14) introduce no mass term for the gauge boson fields as this would break the gauge symmetry. At the same time, an explicit term for the fermion masses would break the chiral symmetry. This problem is solved by the Higgs mechanism [7, 8, 9, 10], where the $Z, W^{\pm}$ and γ bosons are produced through the spontaneous symmetry breaking of the $SU(2) \times U(1)_Y$ electroweak symmetry group. Additionally, the fermion masses are obtained from the interaction with the Higgs field through Yukawa couplings.

A scalar field, referred to as the Higgs field is defined as

$$\phi = \begin{pmatrix} \phi^+ \\ \phi^0 \end{pmatrix} = \frac{1}{\sqrt{2}} \begin{pmatrix} \phi_3 + i\phi_4 \\ \phi_1 + i\phi_2 \end{pmatrix}. \tag{1.20}$$

The Lagrangian corresponding to this field is

$$\mathcal{L}_{Higgs} = (D_\mu \phi)^\dagger D^\mu \phi - V(\phi) = \left| \left(i\partial_\mu + i \left(g \frac{\tau_a}{2} W_\mu^a + g' \frac{Y}{2} B_\mu^a \right) \right) \phi \right|^2 - V(\phi) \tag{1.21}$$

where the first term corresponds to the kinetic energy and the second term is the Higgs potential

$$V(\phi) = \mu^2 \phi^\dagger \phi + \lambda \left(\phi^\dagger \phi \right)^2. \tag{1.22}$$

This potential requires $\lambda > 0$ for a stable global minimum. For $\mu^2 \geq 0$ the potential presents a single point minimum for $\phi_1 = \phi_2 = 0$. For $\mu^2 < 0$ on the other side, there are an infinite number of minimum points distributed around the origin of the complex plane $(\phi_1, i\phi_2)$ as shown in figure 1.2.

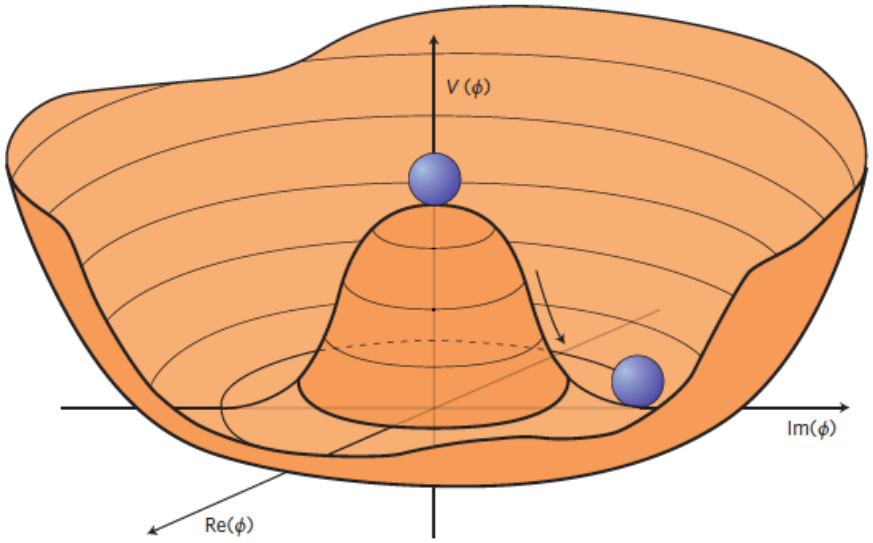

Figure 1.2 – The Higgs potential as a function of the real and imaginary parts of the ϕ_0 component. [11].

The potential minimum is at

$$|\phi^0| = \sqrt{\frac{\phi_1^2 + \phi_2^2}{2}} = \sqrt{\frac{-\mu^2}{\lambda}} = \frac{v}{\sqrt{2}} \tag{1.23}$$

where v is defined as the vacuum expectation value (VEV) and was measured to have a value of $v = 246$ GeV. Choosing a state at the minimum potential like $\phi_1 = \sqrt{2}v$ and $\phi_2 = 0$ breaks the invariance under $SU(2) \times U(1)_Y$.

Treating perturbatively the ground state $\phi_1 = \sqrt{2}v$ and $\phi_2 = 0$ with small perturbations η_j gives

$$\phi = \frac{1}{\sqrt{2}} \begin{pmatrix} \eta_3 + i\eta_4 \\ v + \eta_1 + i\eta_2 \end{pmatrix}. \tag{1.24}$$

The corresponding Lagrangian is

$$\mathcal{L}_{Higgs} = \frac{1}{2} \sum_{j=1}^{4} D_\mu \eta_j D^\mu \eta_j + \mu^2 (\eta_j)^2 + \frac{\lambda v^4}{4} + \mathcal{O}(\eta_1, \eta_2, \eta_3, \eta_4)^3 \tag{1.25}$$

where the second term represents a mass term for η_1 which can be interpreted as a physical field $H = \eta_1$ with a mass $m_H = \sqrt{-2\mu^2} = \lambda v$. The other perturbations are associated to Goldstone bosons which through proper gauge selection are absorbed to generate the massive W and Z bosons.

The fermion masses are generated through Yukawa couplings of the fermions to the Higgs field. For the charged leptons this can be reduced, for the electron

only case here, to

$$\mathcal{L}_{Yukawa,e} = -\frac{\lambda_e v}{\sqrt{2}}\bar{e}e - \frac{\lambda_e}{\sqrt{2}}\bar{e}He \tag{1.26}$$

where the first term correspond to the electron mass $m_e = \frac{\lambda_e v}{\sqrt{2}}$ and the second term represents the Higgs boson interaction with the fermion having the Yukawa coupling λ_e.

Similarly for the the quark masses (up-type quarks U in this example) the Lagrangian can be reduced to

$$\mathcal{L}_{Yukawa,U} = -m_u\bar{u}u - m_c\bar{c}c - m_t\bar{t}t - \frac{\lambda_u}{\sqrt{2}}\bar{u}Hu - \frac{\lambda_c}{\sqrt{2}}\bar{c}Hc - \frac{\lambda_t}{\sqrt{2}}\bar{t}Ht \tag{1.27}$$

where the quark Yukawa couplings are $\lambda_q = \frac{\sqrt{2}m_q}{v}$. Since the top quark has the largest mass among the all fermions (m_t ~173 GeV), the coupling between the Higgs and the top quark is the largest

$$\lambda_t = \sqrt{2}\frac{m_t}{v} \sim 1. \tag{1.28}$$

The Lagrangian (1.27) displays only interactions between same-flavour quarks and the Higgs boson, therefore no flavor-changing neutral currents are possible at tree level in the scalar sector.

1.3 Standard Model limitations and BSM theories

Despite being a very successful and precise theory, the SM suffers from some fundamental limitations. A few of these aspects are described below.

— Dark matter is estimated from cosmological observations to account for about 27% of the total mass-energy of the universe (baryonic mass-energy accounts only for about 5%). It appeared as a required ingredient to explain the evolution of galaxies. It does not interact electromagnetically and despite the large energy density fraction no associated particle has been identified so far.

— Neutrino oscillation experiments have proven that neutrino masses should be different than zero (Nobel Prise 2015). For the moment in SM neutrino masses are considered to be zero.This is a clear limitation of the SM.

— Matter-antimatter asymmetry in the universe is another issue that is not explained by the SM. Despite the fact that CP-violation is allowed by the quark mixing (CKM matrix) it is not enough to explain the existing domination of mater over antimatter.

— Gravity is the fourth fundamental force, it has infinite interaction range (like electromagnetic interactions) and it manifests itself between any objects (mass and energy). The problem is that this force is much weaker

compared to the other three and the SM does not include it. The goal would be to have a single theory ("theory of everything") that would unify the gravitation and the other three forces in a unitary theory that would explain consistently all known phenomena in the universe.

Various models try to extend the SM or completely new theories are proposed like trying at least to explain partially some of these open problems. Some of the most known proposals are Supersymmetry (SUSY) [12, 13, 14], Composite Higgs [15], extra-dimensions [16, 17]. New particles or modifications to the interactions type and strength could emerge and experimental efforts are made to check for these effects. For example, flavor-changing neutral currents are forbidden at tree level and strongly suppressed at higher order in the SM, however other beyond SM scenarios allows for large enhancements for these processes. Chapter 4 gives details about models that predict these type of enhancements and also presents a search for flavor-changing neutral currents in top quark decays to a Higgs boson and an up-type quark.

1.4 Higgs boson phenomenology

1.4.1 Production at LHC

The Higgs boson is produced at the LHC through four main processes:
— gluon-gluon fusion (ggF)
— vector boson fusion (VBF)
— associated production with a vector boson (WH or ZH), (Higgs-Strahlung)
— associated production with a pair of top quarks (ttH)
The Feynman diagrams for these production processes are shown in figure 1.3 (a).

The ggF is the main production process and accounts for about 90% of the Higgs boson production rate at the LHC. Since the gluons are massless and do not couple to the Higgs boson at tree level, the Higgs is produced via a loop (first order). Only quarks couple to gluons so the presence of vector bosons in the loop is excluded. Knowing that the coupling is proportional to the mass the contribution to the loop comes mainly from the heaviest quark, the top quark. For a Higgs boson of mass m_H=125 GeV the cross-section for the ggF process in proton-proton collisions at $\sqrt{s}$ =13 TeV is 48.5 pb [18].

The vector boson fusion (VBF) has the second rate of Higgs boson production at LHC. In this process, the Higgs boson is the results of the fusion of the vector bosons (W or Z) that are radiated by the quarks in a $qq \to q(+V)q(+V) \to qqH$ process. For a Higgs boson of mass m_H=125 GeV the cross-section for the VBF process in proton-proton collisions at $\sqrt{s}$ =13 TeV is 3.78 pb [18]. This process allows to have direct access to the coupling between the Higgs boson and the vector bosons. Since a large fraction of the momenta the incoming quarks is

given to the radiated vector bosons, the outgoing quarks give a characteristic signature in the detector as two jets back-to-back (plus the decay products of the Higgs boson).

The associated production with a vector boson (WH or ZH) is referred to also as Higgs-Strahlung since the produced Higgs boson is radiated from a vector boson. The cross-section of 1.37 (0.88) pb for WH (ZH) makes this process to be the third largest contributor to the Higgs boson production at LHC.

The associated production with a pair of top quarks (ttH) has a much smaller cross-section, $\sigma_{ttH} = 0.507$ pb, compared to the main production mode ggF (two order of magnitude). In this process, as a result of the collision, two gluons generate each a pair of top-antitop quarks, followed by the fusion of a top and a antitop quark (from different pairs) to a Higgs boson. The particularity of this process is that it gives direct access to the top Yukawa coupling, having $\sigma_{ttH} \sim y_t^2$. Chapter 5 is dedicated to the measurement of this process.

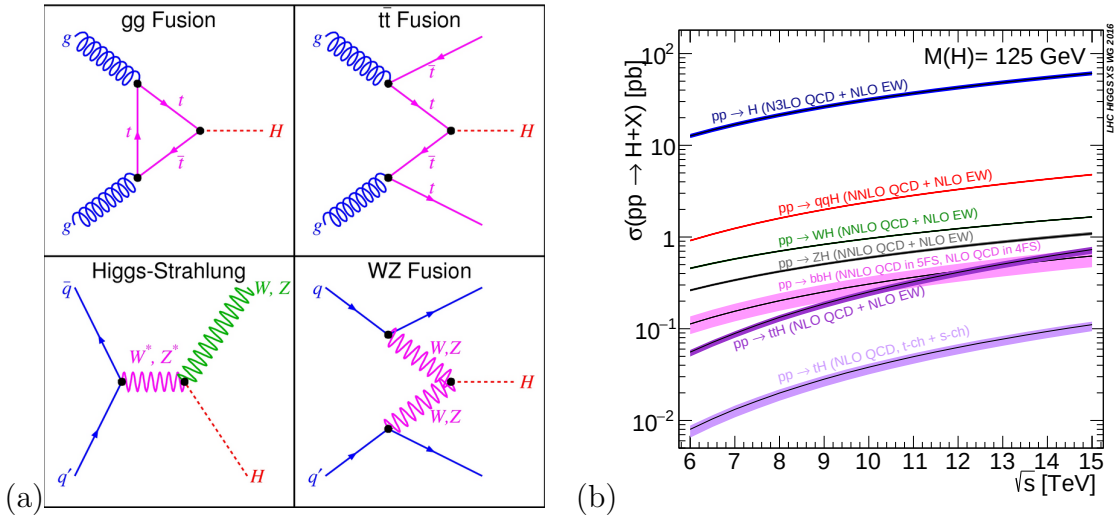

Figure 1.3 – (a) Higgs boson productions modes at LHC: (top left) Gluon-gluon fusion (ggF), (top-right) associated production with a pair of top quarks (ttH), (left-bottom) associated production with a vector boson (WH or ZH) and (right-bottom) vector boson fusion (VBF). (b) Higgs boson production modes cross-sections at LHC in $pp \to H + X$ processes as a function of $\sqrt{s}$ for a Higgs boson mass m_H =125 GeV [19].

The production cross-section as a function of the center-of-mass energy $\sqrt{s}$ in proton-proton collisions is given in figure 1.3 (b).

1.4.2 Decay modes

The Higgs boson is not a stable particle and it decays. It has a very short lifetime ($\tau \sim 10^{-22}$ s). Despite having the largest coupling to the top quark, the Higgs boson can not decay to a pair of top quarks because of kinematic limitation

(the mass of the top quark is larger than the Higgs boson mass). The main decay channels for the Higgs boson are $H \rightarrow b\bar{b}$ (observed experimentally by ATLAS and CMS [20, 21]) with a branching ratio of 58 % and $H \rightarrow WW$ with 21.5 %. Furthermore, it can also decay to a pair of gluons through a quark loop with a branching ratio of 8.6 %. The branching ratio as a function of the Higgs boson mass for different decay modes is given in figure 1.4.

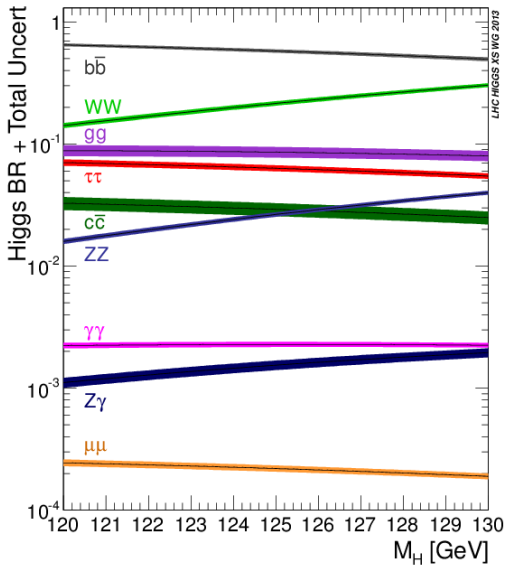

Figure 1.4 – Higgs boson decay branching ratio as a function of Higgs boson mass for different decay modes.

The branching ratio for decays to other lighter fermions are much smaller because of the linear dependence on mass of the Yukawa coupling.

1.4.3 Discovery at LHC

On 4th of July, 2012, ATLAS and CMS collaborations announced the discovery of a new particle with a mass of around 125 GeV [4, 5]. In the analysis performed by the ATLAS experiment several channels were combined using the data from 2011 (4.8 fb^{-1} at $\sqrt{s} = 7$ TeV) and 2012 (5.8 fb^{-1} at $\sqrt{s} = 8$ TeV). Figure 1.5 (left) shows the m_{4l} distribution from $H \rightarrow ZZ \rightarrow 4l$ analysis, where the Higgs boson decays to a pair of Z boson which decay leptonically ($l = e, \mu$). An excess of events around $m_{4l} = 125$ GeV is observed which corresponds to the signal. Similarly, figure 1.5 (right) shows the $m_{\gamma\gamma}$ distribution for the $H \rightarrow \gamma\gamma$ analysis where a bump over the continuous background is observed around $m_{\gamma\gamma} = 125$ GeV. The combined observed significance corresponds to a 5.9σ (background fluctuation probability $\sim 1.7 \times 10^{-9}$).

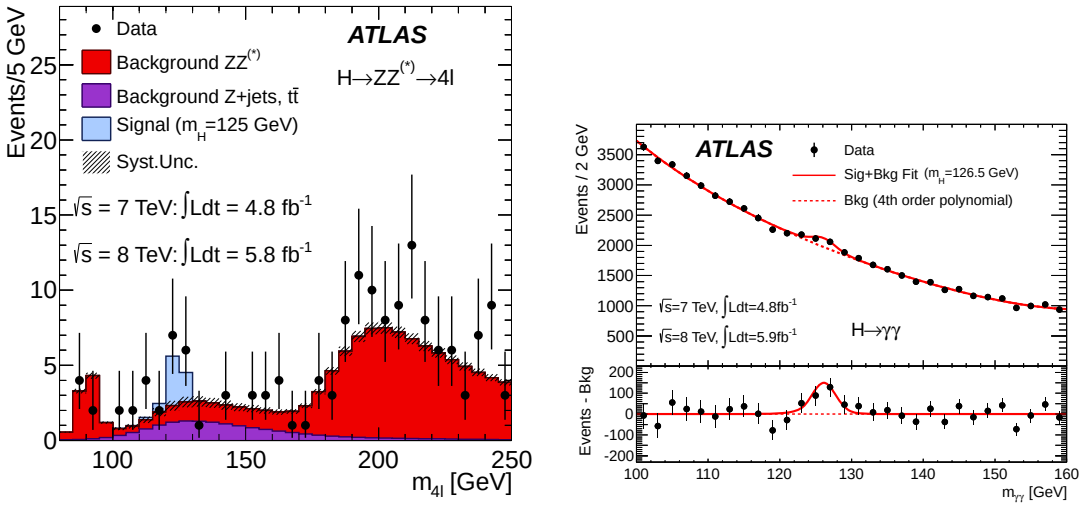

Figure 1.5 – Higgs boson productions in $H \to ZZ^* \to 4l$ channel (left) and in $H \to \gamma\gamma$ (right) [4].

1.4.4 Properties measured at LHC

To confirm the nature of the newly discovered particle requires measurements of its properties.

The mass of the Higgs boson is a free parameter in the SM and can be obtained only from measurements. Figure 1.6 shows a summary of the Higgs mass measurements performed in the $H \to ZZ \to 4l$ and $H \to \gamma\gamma$ channels by ATLAS [22].

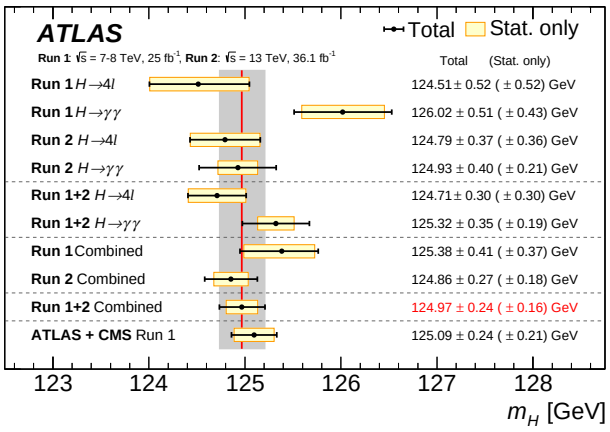

Figure 1.6 – Higgs boson mass measurement Run 1, Run 2 and combined (Run1 +Run 2). Results from ATLAS, CMS and combined. [22].

The results are given for Run 1, Run 2 (36 fb^{-1}) data and combined. The

best-fit value for the Higgs mass combing the result from ATLAS and CMS using the Run 1 data is $m_H = 125.09 \pm 0.21(\text{stat}) \pm 0.11(\text{syst})$, result dominated by the statistical uncertainty.

Other important property measured is the spin (J) and parity (P) quantum numbers. The SM Higgs boson is expected to have $J^+ = 0^+$. The measurement performed by the ATLAS and CMS collaborations using the kinematic properties of the $H \to \gamma\gamma$,$H \to ZZ \to 4l$ and $H \to WW \to l\nu l\nu$ confirmed that the Higgs boson is compatible with SM [23, 24].

Other important properties confirming the SM nature of the discovered particle are the production and decay modes. Using Run 1 data, ATLAS and CMS collaborations have observed (significance > 5σ) the gluon-gluon fusion (ggF) and the vector boson fusion (VBF)(combining ATLAS and CMS) production modes. Also, the decay to ZZ, WW, and $\gamma\gamma$ have been observed and $\tau\tau$ combining ATLAS and CMS. The measurement of the associated production with a pair of top-antitop quarks (ttH) was not sensitive enough to claim discovery using Run 1. Detailed description of the ttH measurement in Run 2 is given in chapter 5.

1.4.5 Yukawa couplings

The Higgs boson couples to the leptons (no neutrino), quarks, vector bosons and to itself. The coupling is proportional to the mass for the fermions and is proportional to the mass squared for the vector bosons.

In the κ framework [25] it is possible to introduce coupling scale factors (κ_i) to account for deviations in the SM such that the cross-section σ_{ii} or the partial decay width Γ_{ii} for the particle i scale with the κ_i^2. Typically, $\kappa_i = \frac{\sigma_i}{\sigma_i^{SM}}$ (ex. for ttH, $\kappa_t = \frac{\sigma_{ttH}}{\sigma_{ttH}^{SM}}$) and the assumed SM predictions are obtained when all $\kappa_i = 1$. For a simplified model all vector boson κ_i are assumed to be equal ($\kappa_Z = \kappa_W = \kappa_V$) and similarly all coupling scale factors are assumed to be the same for the fermions κ_F.

Figure 1.7 (left) shows a contour plot at 68% and 95% confidence level in the (κ_F, κ_V) plan for individual channels and combined. No contributions from physics beyond SM are assumed. The best-fit values are

$$\kappa_V = 1.06^{+0.04}_{-0.04}$$
$$\kappa_F = 1.05^{+0.09}_{-0.09}$$

Figure 1.7 (right) shows the values for the reduced coupling modifiers $\kappa_F \frac{m_F}{v}$ for fermions and $\sqrt{\kappa_V}\frac{m_V}{v}$ for the vector bosons (V=W,Z) as a function of their mass. The vacuum expectation value of the Higgs field is considered $v = 246$ GeV. The compatibility with the SM prediction is p_{SM}=78%, where p is the p-value probability.

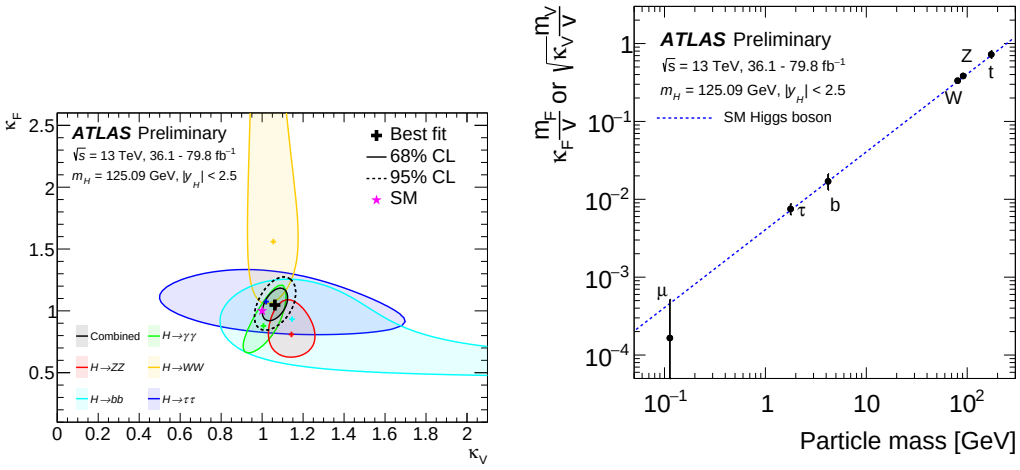

Figure 1.7 – (left) Contour plot at 68% and 95% confidence level in the (κ_F, κ_V) plan for a individual channels and combined. (Right) Values for the reduced coupling modifiers $\kappa_F \frac{m_F}{v}$ for fermions and $\sqrt{\kappa_V}\frac{m_V}{v}$ for the vector bosons (V=W,Z) as a function of their mass. The vacuum expectation value of the Higgs field is considered $v = 246$ GeV. The blue dotted line corresponds to the SM predictions. [26].

All the above mentioned measurements indicate that the newly discovered particle is the predicted SM Higgs boson.

2 The LHC and the ATLAS detector

Summary

The level of accuracy at which the SM predictions have been verified as well as new searches for physics beyond SM would not be possible without state of the art experiments and world-class technologies. The *European Organization for Nuclear Research* (CERN), located near Geneva at the French-Swiss border, has hosted a series of experimental facilities which have led to breakthrough

discoveries (ex. discovery of the W and Z bosons in the UA1 and UA2 experiments). One of the latest large scale project developed at CERN is the *Large Hadron Collider* (LHC) [27]. The LHC is the largest and most powerful particle accelerator in the world in terms of collision center of mass energy ($\sqrt{s}$) . It was built with the goal to cover a broad physics program using four main detectors (ATLAS, CMS, LHCb and ALICE). The most important achievement so far is the discovery of the Higgs boson in 2012 [4, 5] by the ATLAS and CMS experiments. In the following, Section 2.1 gives a general overview of the LHC and its operational status while section 2.2 describes the ATLAS detector with its subdetectors. Section 2.3 describes the object reconstruction in the ATLAS detector.

2.1 The LHC

With a total length of 26.7 km, the LHC was built in the tunnel of the decommissioned *Large Electron Positron* collider (LEP) [28] located at an average depth of around 100 m under the French-Swiss border at CERN. It is a circular hadron accelerator and collider capable of reaching a designed center of mass energy of $\sqrt{s} = 14$ TeV in proton-proton collisions.

The LHC does not function independently but it is instead a part of a larger accelerators complex which uses CERN's already existing infrastructure (LHC injection chain) to allow for beam preparation and pre-acceleration. Figure 2.1 shows a sketch of the full CERN's accelerator complex.

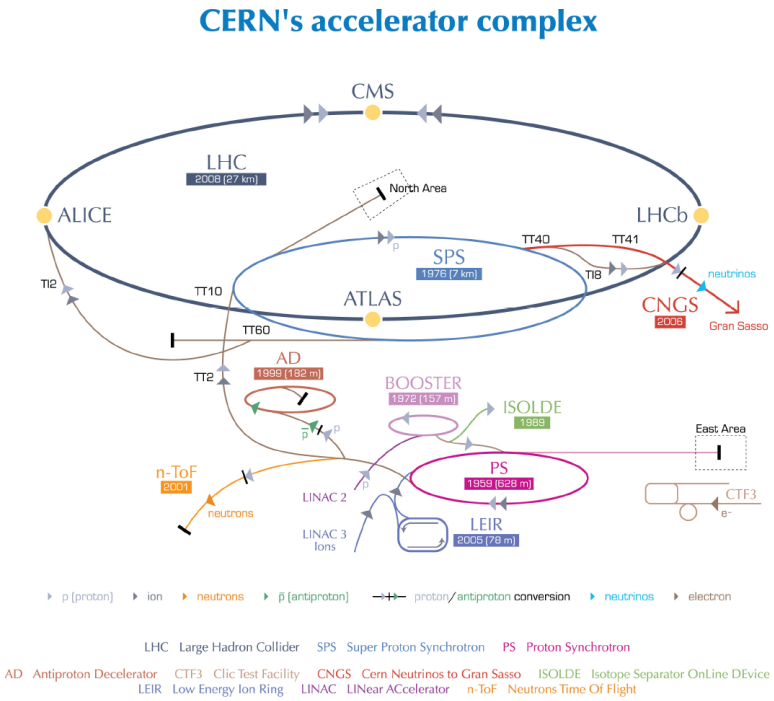

Figure 2.1 – The CERN accelerator complex [29].

The process starts with ionizing the hydrogen gas and separating the protons from the electrons using intensive electric fields. The protons enter the first accelerating stage, LINAC2 (linear accelerator), where they are accelerated up to 50 MeV. Further on, the protons are injected in the Proton synchrotron booster (BOOSTER) and next in the Proton Synchrotron (PS) where they are accelerated up to 1.4 GeV and 25 GeV subsequently. Finally, the last step of the preacceleration is the Super Proton Synchrotron (SPS) where the protons reach 450 GeV and are injected in the LHC. The acceleration is achieved using superconducting radio frequency (RF) cavities operating at voltage of 2 MV at 400 MHz. The LHC is composed of a system on 1232 superconducting *two-in-one* dipole magnets [1], 15 m in length, developing high magnetic fields up to 8.3 T needed to curve the beam (70% of total LHC length). The cross section of such a dipole magnet is shown in figure 2.2. Additionally, a system of 392 superconducting *two-in-one* quadrupole magnets, 5-7 m in length, assures the focusing and stability of the beam.

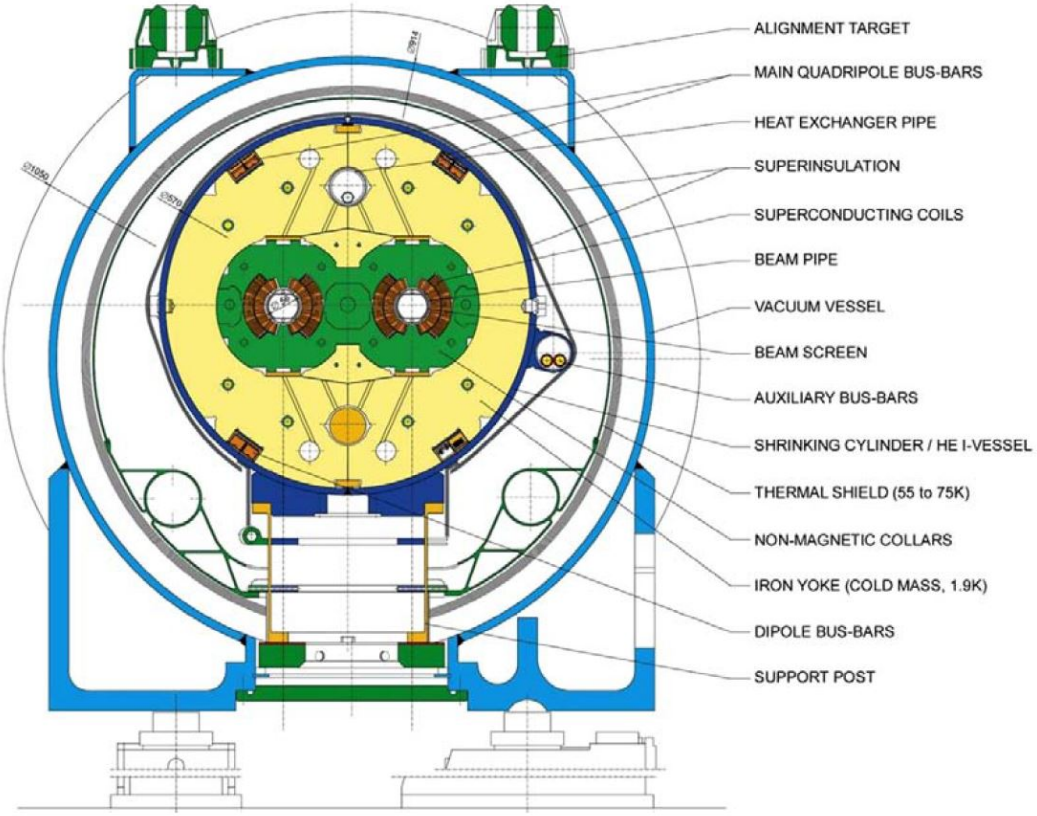

Figure 2.2 – Cross section of a LHC dipole magnet element [27].

The beam is not a continuous distribution of protons but it is split in *bunches*

1. The challenge of the LHC was to host two dipoles with very high magnetic fields but opposite directions in the same cryostat since the proton beams circulate in opposite directions.

with a separation of 25 ns. A bunch contains around 10^{11} protons. A maximum of 2808 bunches can be contained in the beam. Table 2.1 summarizes the main LHC operational parameters for Run 1 and Run 2.

Parameter	design	Run 1		Run 2			
		2010/11	2012/13	2015	2016	2017	2018
center of mass energy $\sqrt{s}$ [TeV]	14	7	8	13	13	13	13
bunch spacing [ns]	25	50	50	25	25	25	25
maximum number of bunches	2808	1380	1380	2224	2200	2556	..
protons per bunch [$\times 10^{11}$]	1	1.3	1.5	1.15	1.15	1.15	..
peak luminosity [$\times 10^{33}$cm^{-2}s^{-1}]	10	3.5	7.7	5.1	14	21	..
integrated luminosity [fb^{-1}]	-	5.5	22.8	4.2	38.5	50.2	63.3
mean pile-up*	-	9.1	21	13.4	25.1	37.8	36.1

Table 2.1 – Operational parameters for the proton-proton collisions at LHC for Run 1 and Run 2.* as recorded by the ATLAS detector.

The rate at which the collisions take place is given by the instantaneous luminosity

$$\mathcal{L} = \frac{n_1 n_2 n_b f_{rev} F}{4\pi\sigma_x\sigma_y} \tag{2.1}$$

where n_1 and n_2 are the number of protons per bunch, n_b is the number of bunches, f_{rev} is the beam revolution frequency, F is a geometrical factor (close to 1) related to the beam crossing angle, σ_x and σ_y are the transverse sizes of the beam (assuming a Gaussian profile) at the interaction point (IP). The number of collisions of a specific process ($pp \to X$) is given by

$$N_{ev}(pp \to X) = L \cdot \sigma_{pp\to X} \tag{2.2}$$

where $L = \int \mathcal{L}\mathrm{d}t$ is the integrated luminosity. The measurement unit of L is the inverse of a cross-section.

The LHC has operated in 2010-2013 and 2015-2018, periods that are commonly referred to as Run 1 and Run 2. At the end of Run 1 it has delivered 5.46 fb^{-1} at $\sqrt{s} = 7$ TeV and 22.8 fb^{-1} at $\sqrt{s} = 8$ TeV. In Run 2, the proton-proton collision energy was increased to $\sqrt{s} = 13$ TeV and 156 fb^{-1} were delivered (figure 2.3 left), 6 fb^{-1} above the 150 fb^{-1} expected value. Figure 2.3 (left) shows the delivered integrated luminosity with respect to time for Run 2.

When two bunches cross more than one proton-proton collision is possible. This quantity is described by the pileup (in-time).

$$\mu = \frac{\mathcal{L}\sigma_{inel}}{f_{rev}} \tag{2.3}$$

Figure 2.3 (right) shows the average pileup $<\mu>$ distribution (right) by year for Run 2.

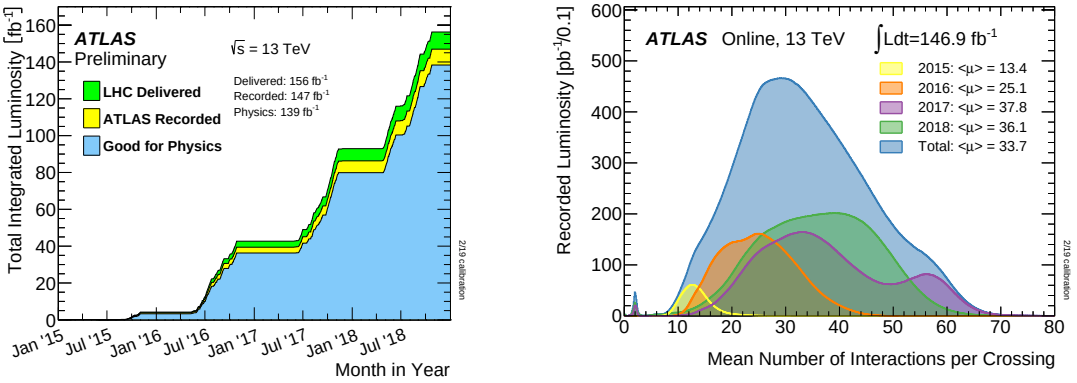

Figure 2.3 – Delivered integrated luminosity (left) and average pileup $< \mu >$ (right) in Run 2 [30].

The LHC has a rich physics program carried out by 4 main experiments. ATLAS and CMS are general purpose detectors and cover a wide range of topics: SM precision measurements (especially top and Higgs particles), direct searches for physics beyond SM, etc. LHCb is a forward, low luminosity experiment dedicated to flavor physics performing indirect (in higher order loops) searches in b meson decays. The LHC has also a heavy ion collision program (Pb-Pb and Xe-Xe) designed to study quark-gluon plasma using the dedicated ALICE detector.

2.2 ATLAS

The *ATLAS* detector (*A Toroidal LHC ApparatuS*) [31] is a general purpose detector with a cylindrical symmetry that covers almost the entire solid angle. The collaboration has formed in 1992 and gathers today more than 3000 physicists from 174 institutes in 38 countries. The structure of such a detector is designed to identify the SM particles with a non negligible life time and to fully reconstruct the event in an unambiguous way. Figure 2.4 illustrates the effect of different particles in different layers of the ATLAS detector. From the center of the detector, the particles emitted at the interaction point are crossing the inner detector (section 2.2.1) where the charged particles leave tracks that are bent by the solenoid magnet. Further on, the energy of the particles is measured from the energy deposits in the calorimeter system (section 2.2.2), which is composed from the electromagnetic and the hadronic calorimeters. The electrons and the photons deposit all their energy in the electromagnetic calorimeter. The hadrons deposit the rest of all their energy in the hadronic calorimeter (the charged hadrons leave some energy in the electromagnetic calorimeter). The muons cross the entire detector unstopped [2] and leave tracks in the outermost layer of the ATLAS

2. The neutrinos also cross the entire detector but without any interaction, therefore they are not detected directly.

detector, the muon spectrometer (section 2.2.3). The structure of the detector system is depicted in Figure 2.5.

The position and momentum/energy of the particles are measured in a right-handed coordinates system with the origin at the center of the detector. The z-axis points along the beam axis while the x-axis points to the center of the LHC ring (therefore y-axis points upward). In the transversal plane (x-y) cylindrical coordinates are used (r, ϕ), with r being the distance from the beam axis and ϕ the azimuth angle around the beam axis. The polar angle θ gives the angle between the particle and the positive z-axis. In practice, the relativistic invariant quantity pseudorapidity η is used

$$\eta = -\ln \tan \frac{\theta}{2}. \tag{2.4}$$

Angular distances between objects are expressed as distances in the η-ϕ plane

$$\Delta R = \sqrt{(\Delta\eta)^2 + (\Delta\phi)^2} \tag{2.5}$$

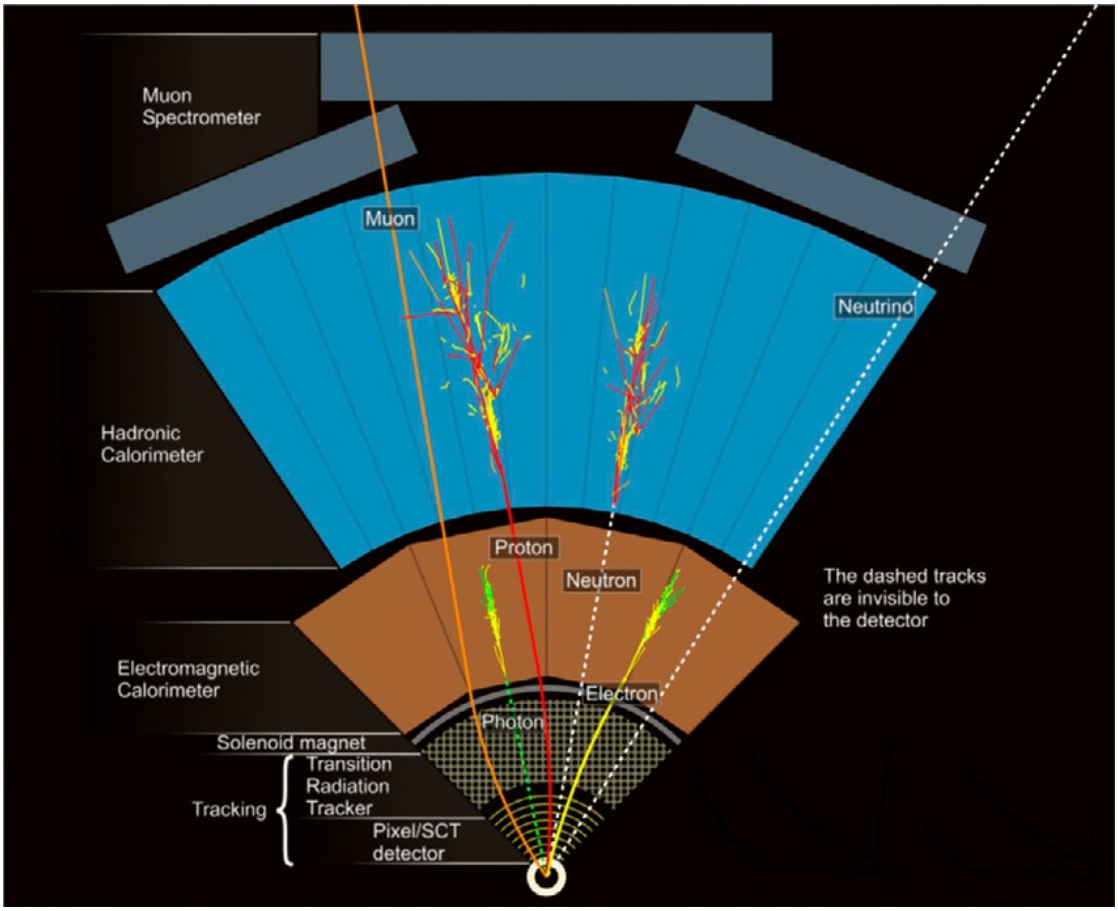

Figure 2.4 – ATLAS detector layers and particle interactions.

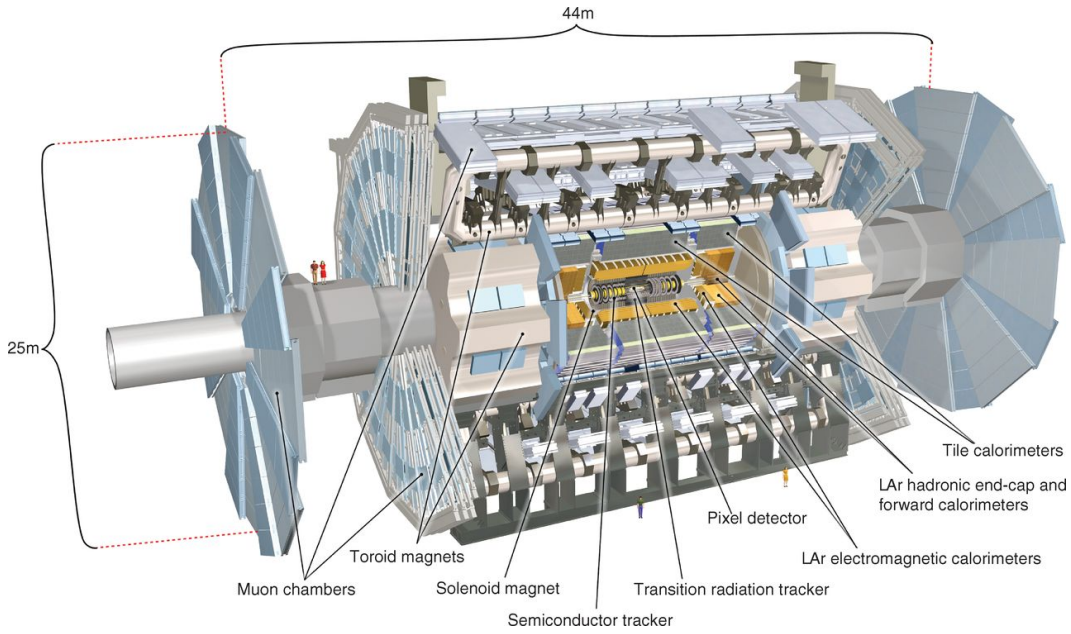

Figure 2.5 – ATLAS detector schematic view [31].

2.2.1 The inner detector

The inner detector (ID) is responsible for measuring the tracks of the charged particles. A solenoid magnet system covers the ID and assures a 2 T magnetic field. From the curvature of the tracks the charge and the transverse momenta p_T is determined in a range covering $|\eta| < 2.5$. Structurally, the ID is composed from three sub-detectors: the pixel detector, the semiconductor tracker and the transition radiation tracker. Figure 2.6 (left) shows a sketch of the ID structure.

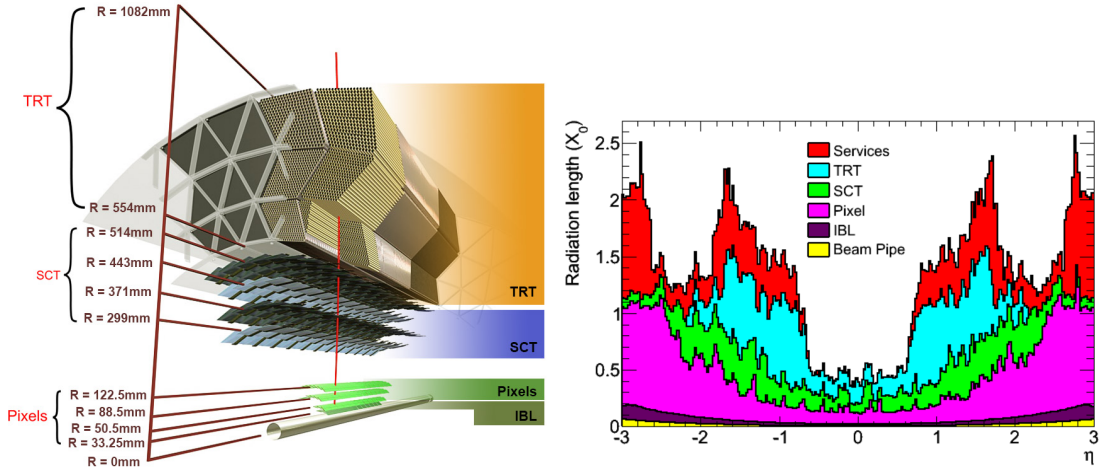

Figure 2.6 – ATLAS inner detector schematic view in the barrel (left) [32] and material budget in terms of radiation length (right) [33].

The material budget in terms of radiation lengths is shown by component in figure 2.6 (right). This information is particularly important for electrons and photons which can interact with the material and loose energy through *bremsstrahlung* photons and $e^{-}e^{+}$ pair creation respectively. A detailed layout of the ID is given in figure 2.7.

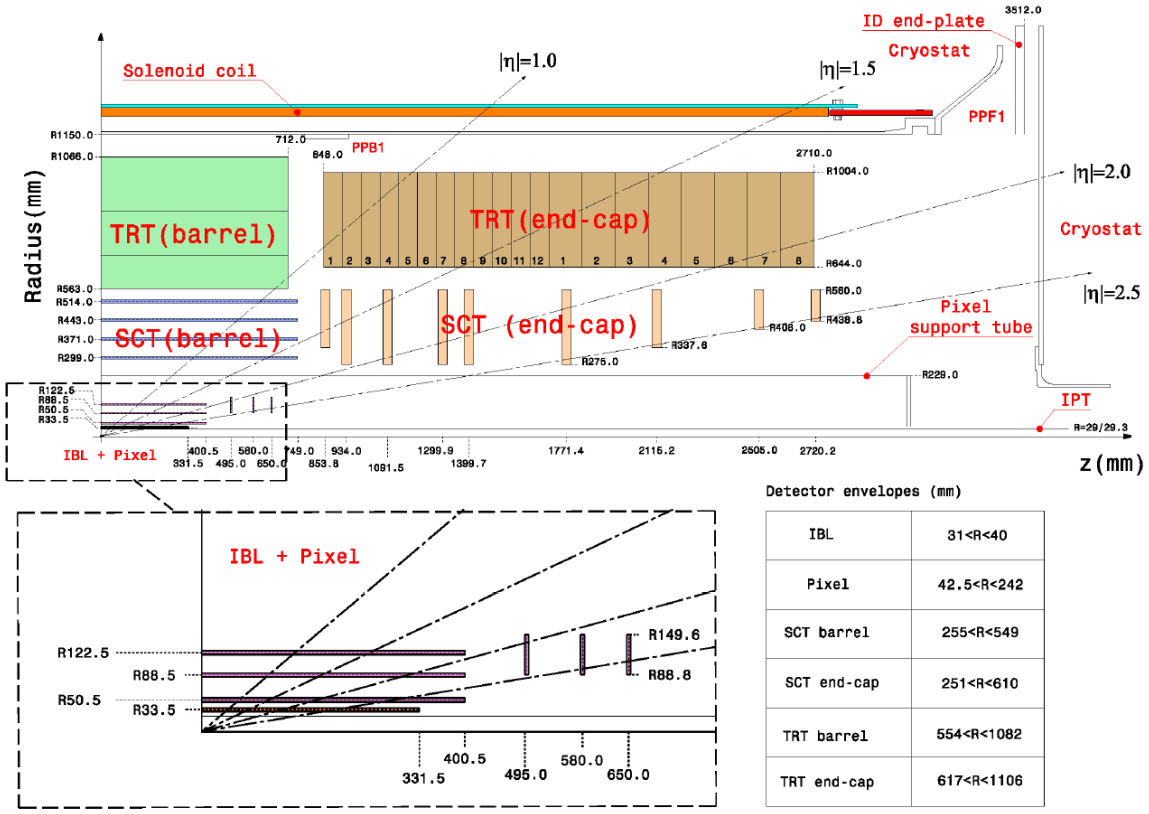

Figure 2.7 – ATLAS Inner detector schematic layout used during Run 2 [34].

2.2.1.1 Pixel detector

The pixel detector is composed of three cylindrical layers (B-layer, Layer 1 and Layer 3) located at a distance R 50.5, 88.5 and 122.5 mm from the center of the beam pipe and three disks that are in the transversal plan (end-caps). The size and positioning of the components can be seen in figure 2.7. Overall, the system is composed of total number of 1744 modules having about 80 millions pixels. The nominal pixel size is 50 $\times$ 400 μm^2 giving an accuracy of 14 $\times$ 115 μm^2 per reconstructed point in x-y directions. During the period between Run1 and Run2, an additional layer was added to the pixel detector, the *Insertable B-Layer* (IBL), to provide better precision for the secondary vertices reconstruction which is crucial for the identification of b-jets. The IBL is the closest layer to the beam pipe (R=33.2 mm) and it has 224 modules (6 millions pixels) with

smaller pixel size (50 $\times$ 250 μm^2) compared to the other pixel layers, providing an improved accuracy of 8 $\times$ 40 μm^2 per reconstructed point in x-y directions.

2.2.1.2 Semiconductor tracker

The semiconductor tracker (SCT) is composed of 4 layers (2112 modules) in the barrel and 2 layers in the end-caps of 9 disks each (1976 modules). Detailed view of the SCT structure with sizes and positioning is given in figure 2.7. Each layer has up to 4 sensors separated by an angle of 40 μrad angle to obtain a three dimensional information (in z for the barrel and radial position for the endcap). The achieved resolution in the SCT is 17 μm in the transversal direction and 580 μm in the longitudinal direction.

2.2.1.3 Transition radiation tracker

The transition radiation tracker (TRT) is the outermost layer of the ID and is composed of 350848 polyimide drift tubes (straws) of 4 mm diameter with a gold-plated tungsten wire (anode) in the center of the tubes (cathode). The detector functions based on the transition radiation emitted when a charged particle passes through an inhomogeneous media (ex. boundary of two different media). The straws are filled with a mixture of gas based mainly on xenon (Xe 76%, CO_2 27% and O_2 3%) which is ionized by the transition radiation photons. The positioning and the overall size of the TRT is shown in figure 2.7. The overall spatial resolution in the TRT is around 130 μm (in $r\phi$ direction) mainly thanks to the high number of points per track.

2.2.2 The calorimeter system

ATLAS's calorimeter system is composed of the electromagnetic (EM) calorimeter and the hadronic calorimeter. Figure 2.8 show a schematic view of the ATLAS calorimeter system. The calorimeters allow to measure the energy of the electrons, photons and hadrons. The EM calorimeter is designed to measure the energy of the particles that interact primarily electromagnetically, the electrons and the photons, which develop showers that are fully contained. The hadronic calorimeter relies on the strong nuclear force as the interaction mechanism between the detector and the particles and as the name suggests it targets the hadrons.

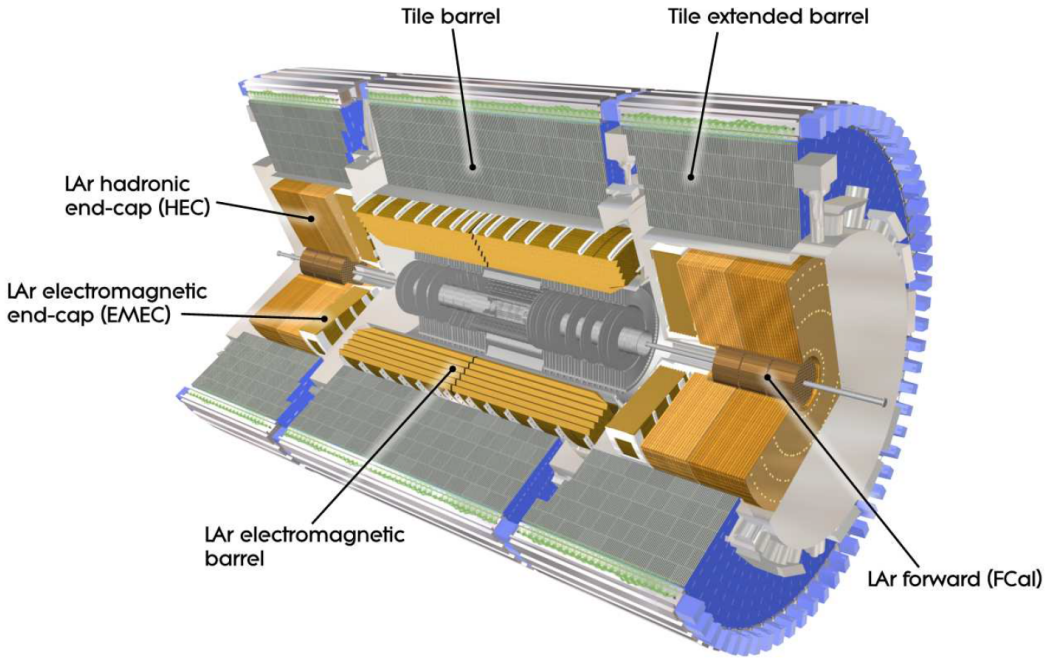

Figure 2.8 – ATLAS detector schematic view: calorimeter system [31].

2.2.2.1 Electromagnetic calorimeters

The electromagnetic calorimeter is a Liquid Argon (LAr) sampling calorimeter with the liquid argon as the active medium and lead (Pb) is used as absorber.

The EM calorimeter is composed of three main parts:

— LAr electromagnetic barrel (EMB), covering $|\eta|<1.475$. The EMB is formed from 2 half-barrel ($-1.475 < \eta < 0$ and $0 < \eta < 1.475$) each containing 16 modules (one module covers $\Delta\phi = 22.5^o$) and presents no discontinuities in azimuth angle.

— LAr electromagnetic end-caps (EMEC), two on each side of the EMB covering $1.375<|\eta|<3.2$.

— LAr forward calorimeter, covering the $3.1<|\eta|<4.9$ region

The central part of the detector ($|\eta|<2.5$) allows for precision measurements of electron and photon energies and position using more than 170000 cells. It is composed of three layers with different granularities with an additional layer, the pre-sampler ($|\eta|<1.8$), used to recover for energy loss in front of the calorimeter. Figure 2.9 shows a section of the EMB at $\eta=0$ specifying the granularity of each layer. Full details on the granularity of the barrel and end-caps are given in table 2.2. Layer 1 features cells with a fine granularity $\Delta\eta \times \Delta\phi = 0.025/8 \times 0.1$ in η to allow to distinguish isolated single photons from collimated two close-by photons from π^0 meson decays. This factor is crucial for analyses involving photons in the final state like $H \to \gamma\gamma$. The second layer is the largest one and encompasses most of the energy of the electromagnetic shower. A coarse

granularity of $\Delta\eta \times \Delta\phi = 0.1 \times 0.1$ (4x4 cells in layer 2) is used for the trigger system for fast decision making on storing or not the event at the first level trigger.

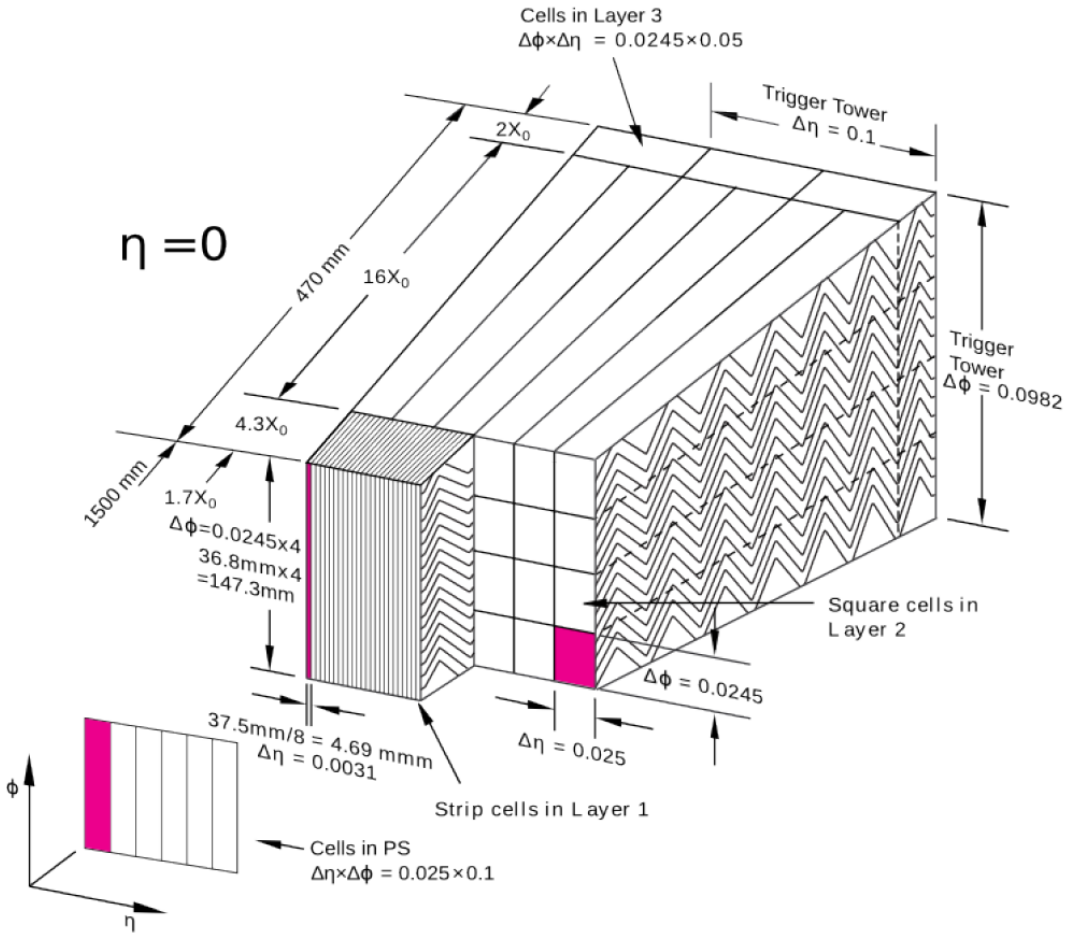

Figure 2.9 – ATLAS detector schematic view: calorimeter system [31].

The relative resolution with respect to the measured energy can be parametrized as

$$\frac{\sigma_E}{E} = \frac{a}{\sqrt{E}} \oplus \frac{b}{E} \oplus c \tag{2.6}$$

where a is the sampling term, b is the noise term and c is the constant term. Typical value for a is 10% GeV$^{1/2}$ in the barrel (a is increasing because of the material in front of the endcap calorimeter). b is approximated by $350 \times \cosh(\eta)$ [MeV] [35] and is dominated by pileup noise at high $|\eta|$. c corresponds to the resolution and is estimated from data to be around 1% [35]. At high energy ($E > 100$ GeV), the relative resolution is dominated by the constant term c.

During 2017 and 2018 data taking period I participated in the daily data quality monitoring for the LAr calorimeter. My task consisted in checking the level of

Layer	Barrel		End-cap	
	Granularity $\Delta\eta \times \Delta\phi$	Coverage $\|\eta\|$	Granularity $\Delta\eta \times \Delta\phi$	Coverage $\|\eta\|$
Pre-sampler	0.025×0.1	<1.52	0.025×0.1	$1.5<\|\eta\|<1.8$
1	$0.025/8 \times 0.1$	<1.40	0.050×0.1	$1.375<\|\eta\|<1.425$
	0.025×0.025	$1.40<\|\eta\|<1.475$	0.025×0.1	$1.425<\|\eta\|<1.5$
			$0.025/8 \times 0.1$	$1.5<\|\eta\|<1.8$
			$0.025/6 \times 0.1$	$1.8<\|\eta\|<2.0$
			$0.025/4 \times 0.1$	$2.0<\|\eta\|<2.4$
			0.025×0.1	$2.4<\|\eta\|<2.5$
			0.1×0.1	$2.5<\|\eta\|<3.2$
2	0.025×0.025	<1.40	0.050×0.025	$1.375<\|\eta\|<1.425$
			0.025×0.025	$1.425<\|\eta\|<2.5$
			0.1×0.1	$2.5<\|\eta\|<3.2$
3	0.050×0.025	$\|\eta\|<1.35$	0.050×0.025	$1.5<\|\eta\|<2.5$
	Number of readout channels			
Presampler	7808		1536	
Calorimeter	101760		62208	

Table 2.2 – Granularity of the EM calorimeter in terms of the $|\eta|$ coverage.

noise with special focus on the tagged noisy cells, particularity by verifying the level of activity in the detector between bunch crossings [36]. The noisy cells are flagged and excluded from energy computation. In severe cases, entire blocks of collected data (lumi block $\sim$1 min) can be flagged as not *Good for Physics*. Figure 2.10 shows the loss of luminosity due to various defects set during LAr data quality monitoring and which cover a part of the difference between *ATLAS Recorded* versus *Good for Physics* in figure 2.3 (left).

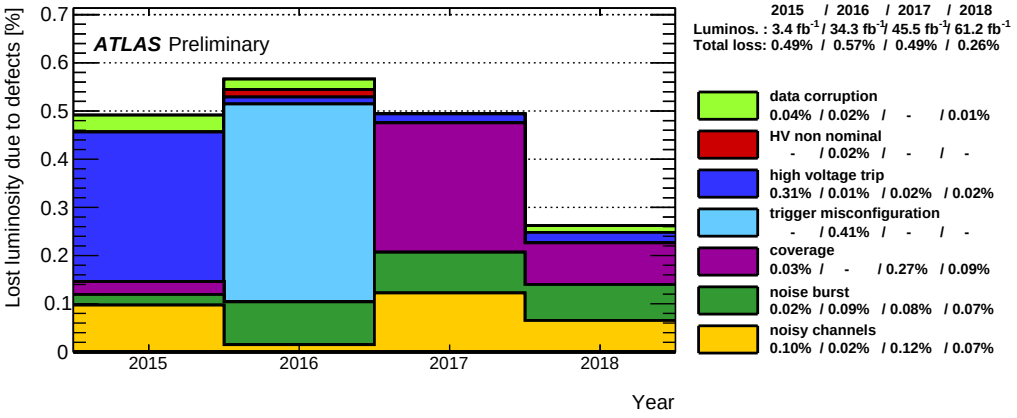

Figure 2.10 – Luminosity loss in the LAr calorimeter due to defects in Run 2 [37].

2.2.2.2 Hadronic calorimeters

The hadronic calorimeter is a sampling calorimeter designed to measure the position and energy of the jets and to stop them in this detector. Hadrons are

stopped by successive interactions in the absorber and generate hadronic showers. The components that form the hadronic calorimeter are:

— the tile calorimeter, covering the $|\eta|<1.7$ region
— two hadronic end-caps (HEC) covering the $1.5<|\eta|<3.2$ region
— the forward calorimeter (FCal), covering the $3.1<|\eta|<4.9$ range

Table 2.3 summarizes the granularity of the hadronic calorimeter.

The tile calorimeter is formed from the tile barrel ($|\eta|<1.0$) and two tile extended barrels ($0.8<|\eta|<1.7$). It uses plastic scintillator as active medium and steel as absorber. Each barrel has 64 modules ($\Delta\phi \sim 0.1$), made of scintillating tiles and steel plates with a periodic structure having a volume ratio of about 1:4.7. Figure 2.11 shows the geometrical structure of a module.

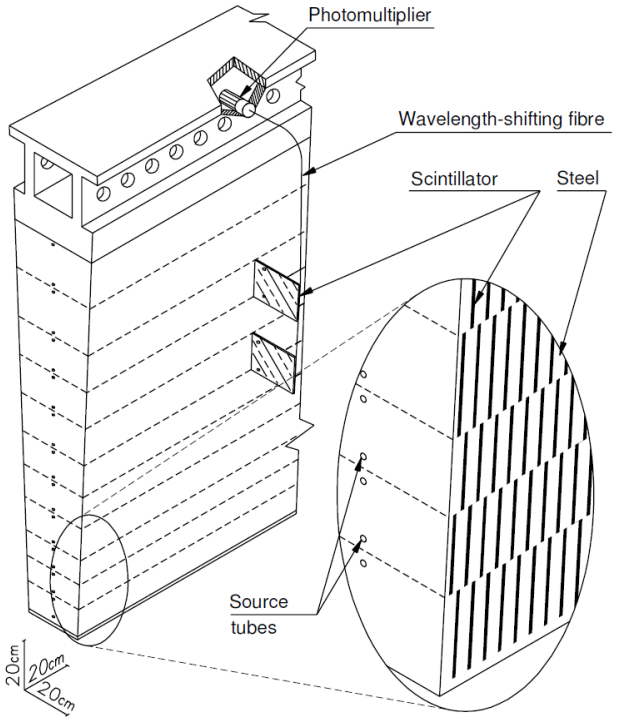

Figure 2.11 – Tile module in the barrel part of the hadronic calorimeter [31].

The HEC is a sampling calorimeter and uses liquid argon as the active medium and copper as absorber.

The forward calorimeter, FCal, is composed of 2 end-caps each containing 3 modules (FCal1,FCal2 and FCal3). The active medium is liquid argon for all the modules however different absorbers are used in different modules. Copper is used for the first module which is an electromagnetic module, while tungsten is used in FCal2 and FCal3 which are designed as hadronic modules.

The behavior of the energy resolution is similar to the equation (2.6). The sampling term, a, is of order of 50% GeV$^{1/2}$ in the barrel and 100% GeV$^{1/2}$ in

the endcaps. The constant term c is of the order of 3 % (10 %) in the barrel (endcaps).

		End-cap	
Hadronic calorimeter end-cap			
Coverage			$1.5<\|\eta\|<3.2$
Number of layers			4
Granularity $\Delta\eta \times \Delta\phi$		0.1×0.1	$1.5<\|\eta\|<2.5$
		0.2×0.2	$5.5<\|\eta\|<3.2$
Readout channels		5632	
Forward calorimeter			
Coverage		$3.1<\|\eta\|<4.9$	
Number of layers		3	
Granularity $\Delta\eta \times \Delta\phi$ (cm)		FCal1: 3.0×2.6	$3.15<\|\eta\|<4.30$
		FCal1: $\sim$x4.0 finer	$3.10<\|\eta\|<3.15$
			$4.30<\|\eta\|<4.83$
		FCal2: 3.3×4.2	$3.24<\|\eta\|<4.50$
		FCal2: $\sim$x4.0 finer	$3.20<\|\eta\|<3.24$
			$4.50<\|\eta\|<4.81$
		FCal3: 5.4×4.7	$3.32<\|\eta\|<4.60$
		FCal3: $\sim$x4.0 finer	$3.29<\|\eta\|<3.32$
			$4.60<\|\eta\|<4.75$

	Barrel	Extended Barrel	
Tile calorimeter			
Coverage	$\|\eta\|<1.0$		$0.8<\|\eta\|<1.7$
Number of layers	3		3
Granularity $\Delta\eta \times \Delta\phi$	0.1×0.1		0.1×0.1
Last layer	0.2×0.1		0.2×0.1
Readout channels	5760	4092	

Table 2.3 – Granularity of the hadronic calorimeter in terms of the $|\eta|$ coverage.

2.2.3 The muon system

The muons pass through the entire ATLAS detector. Their momenta and position are measured in the outer-most layer of the ATLAS detector, the Muon Spectrometer (MS). The MS is composed of a system of several components (figure 2.12), split into a precision component and and a fast triggering one.

The Monitored Drift Tubes (MDTs) cover the central region $|\eta|<2.7$ and provide precise measurements for the muon momentum and charge from the track curvature. The Cathode Strip Chambers (CSC) form the innermost layer in the endcap ($2.0<|\eta|<2.7$).

To allow for fast triggering, coarser resolution subdetectors are used that cover up to $|\eta|<2.4$. The Resistive Plate Chambers (RPCs) are used in the barrel region ($|\eta|<1.05$). The Thin-Gap Chambers (TGCs) cover the region $1.05<|\eta|<2.7$.

	coverage	resolution in			number of	
	in $\|\eta\|$	η-dir.	ϕ-dir.	t	chambers	channels
MDT	< 2.7	35 µm	–	–	1150	354,000
CSC	$[2.0, 2.7]$	40 µm	5 mm	7 ns	32	31,000
RPC	< 1.05	10 mm	10 mm	1.5 ns	606	373,000
TGC	$[1.05, 2.7]$	2–6 mm	3–7 mm	4 ns	3588	318,000

Table 2.4 – ATLAS Muon Spectrometer main parameters during Run 2.

A summary of the MS characteristics is given in table 2.4.

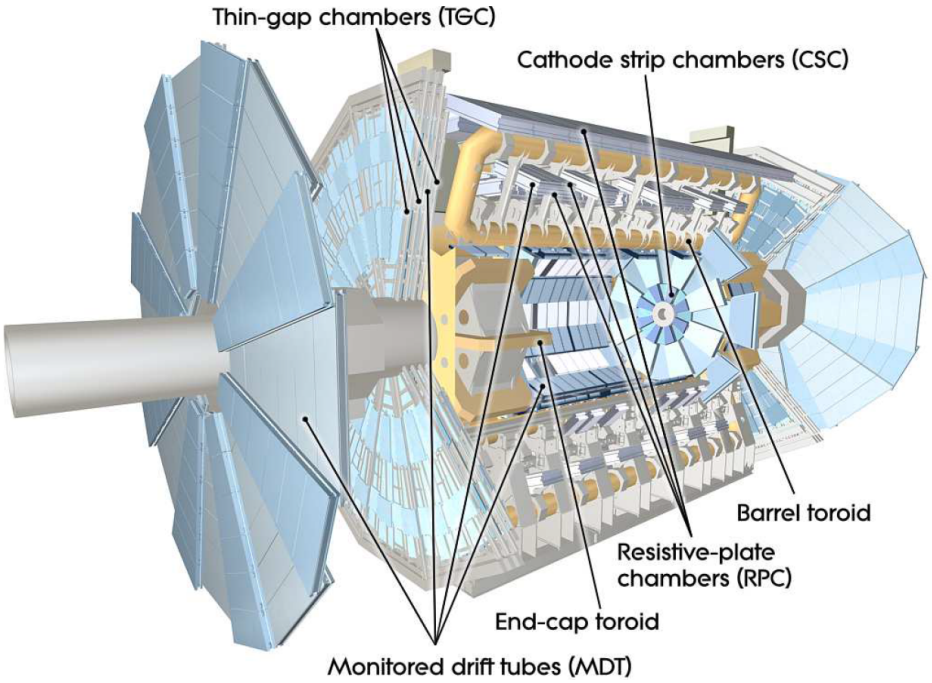

Figure 2.12 – ATLAS detector schematic view: the muon system.

2.2.4 The magnets system

Four magnet systems (1 solenoid, 1 toroid and 2 end-cap toroids) are used to curve the trajectories of the charged particles. The magnet system can be observed in figure 2.5 and detailed characteristics are given in table 2.5.

A system of 8 superconducting air-core barrel toroid magnets are used to bend the muon trajectory in the central region. End-cap toroid magnets provide magnetic field at higher values of $|\eta|$.

Property	Feature	Unit	Solenoid	Barrel toroid	End-cap toroids
Size	Inner diameter	m	2.46	9.4	1.65
	Outer diameter	m	2.56	20.1	10.7
	Axial length	m	5.8	25.3	5.0
	Number of coils		1	8	2×8
Mass	Conductor	t	3.8	118	2×20.5
	Cold mass	t	5.4	370	2×140
	Total assembly	t	5.7	830	2 x 239
Coils	Turns per coil		1154	120	116
	Nominal current	kA	7.73	20.5	20.5
	Magnet stored energy	GJ	0.04	1.08	2 x 0.25
	Peak field in the windings	T	2.6	3.9	4.1
	Field range in the bore	T	0.9–2.0	0.2–2.5	0.2–3.5
Conductor	Overall size	mm^2	30 x 4.25	57 x 12	41 x 12
	Ratio Al:Cu:NbTi		15.6:0.9:1	28:1.3:1	19:1.3:1
	Number of strands (NbTi)		12	38–40	40
	Strand diameter (NbTi)	mm	1.22	1.3	1.3
	Critical current (at 5 T and 4.2 K)	kA	20.4	58	60
	Operating/critical-current ratio at 4.5 K	%	20	30	30
	Residual resistivity ratio (RRR) for Al		> 500	> 800	> 800
	Temperature margin	K	2.7	1.9	1.9
	Number of units $\times$ length	m	4×2290	$8 \times 4 \times 1730$	$2 \times 8 \times 2 \times 800$
	Total length (produced)	km	10	56	2 x 13
Heat load	At 4.5 K	W	130	990	330
	At 60–80 K	kW	0.5	7.4	1.7
	Liquid helium mass flow	g/s	7	410	280

Table 2.5 – ATLAS magnet system details [31].

2.2.5 The trigger system

Taking into account that the rate of proton-proton collisions is 40 MHz and that it takes $\sim$ 1 MB to store one single event (total rate $\sim$ 40 TB/s) it is technically impossible for the moment to store and process this amount of data. However, most of the collisions are soft QCD processes and do not represent new interest compared to previous colliders. Instead, high energy signatures and/or leptons are a good marker of an event of interest. Therefore, a fast two-level decision making mechanism (in real time, "online") was put in place to decide whether an event should be stored or not and subsequently to trigger the recording of the selected events. The first level trigger is referred to as Level1 (L1) and the second level is the High Level Trigger (HLT).

The L1 trigger scans for high energy signatures using custom made hardware to identify Regions of Interest (RoI) in the detector in a fast manner. For electrons, photons, tau-leptons jets and missing transversal energy (E_T^{miss}) the full calorimeter system is used, albeit a coarser granularity is used (0.1x0.1) to speed up the processing. For muons, information from the Muon spectrometers is used (RPC and TGC only). The L1 trigger system has a decision time of 2.5 ms and

selects and outputs events at a rate of around 100 kHz (2 orders of magnitude reduction).

The HLT runs over the evens pre-selected by the L1 triggers. Information from the full detector is used with full granularity and the event is reconstructed with algorithms close to the off-line reconstruction algorithms. The output of the HLT is of the order of 1 kHz.

2.3 Object reconstruction

This section describes the methods and algorithms to reconstruct and identify physical objects by combining various information from all the sub-detectors described in the previous sections. Section 2.3.1 describes track and vertex reconstruction. Section 2.3.2 describe algorithms used to reconstruct and identify electrons and photons. The muon and tau leptons reconstruction is detailed in sections 2.3.3 and 2.3.4. Jet reconstruction, calibration and flavor tagging is described in section 2.3.5. Finally, the missing transverse energy estimation method is described in section 2.3.6.

2.3.1 Track and vertex reconstruction

The charged-particle trajectories ($tracks$) are bent by the magnetic field in the ID and get an helical geometry. The tracks are reconstructed using the spatial information from the ID. In figure 2.13 is shown the parametrization of the tracks based on the cylindrical geometry of the detector and the particle's properties. The tracks are defined by 5 parameters. The distance of the closest point of the track to the beam axis, d_0, is referred to as the transverse impact parameter. The longitudinal impact parameter, z_0, defines the distance from the transverse plane (x-y plane) containing the closest point of the track to the beam axis to the primary vertex or origin of the coordinate system (in case no primary vertex is defined yet). The orientation of the track is given by the azimuth angle ϕ and the polar angle θ. These angles are defined based on the momentum vector at the closest point. The curvature of the track is parametrized by the ratio of the charge and transverse momentum Q/p_T.

The track reconstruction, i.e. the determination of the 5 track parameters, is based on a staged pattern-recognition approach [39]. The reconstruction starts with an iterative track-finding algorithm based on track seeds that requires a set of three space-points from the pixel detector and first layer of SCT. Selected track candidates are extended to the full SCT and a special procedure is put in place to solve ambiguities by using track scores (based on track quality) and neural networks [40]. Global χ^2 fit [41] information, Kalman filter classification [42] and minimum requirements like $p_T >$ 400 MeV, $|\eta| < 2.5$ and other selections based on the number of pixels and SCT clusters are used to reduce fake tracks. Further

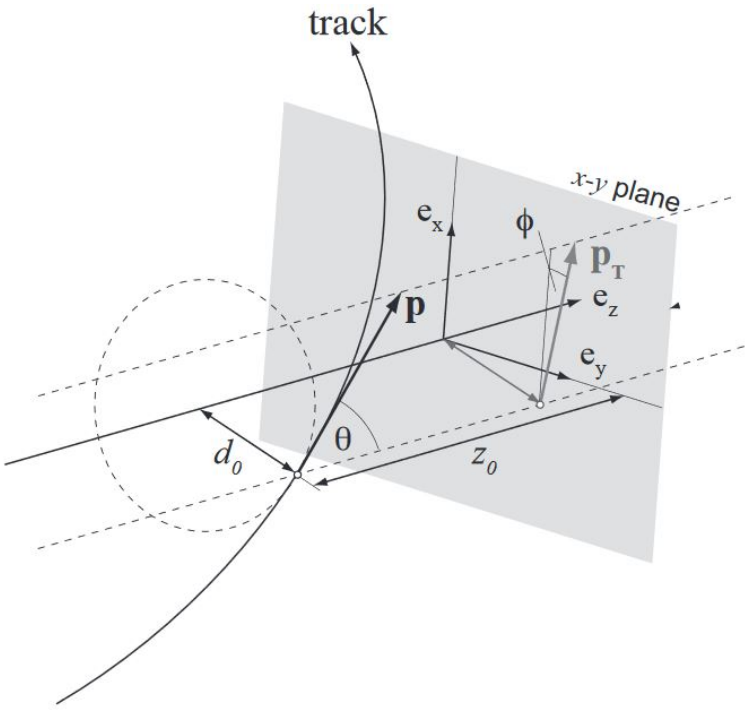

Figure 2.13 – A illustration of track parameters [38].

on, the tracks are extended to the TRT and a high-resolution fit is performed using full information from the ID to complete the track reconstruction.

Once the tracks are reconstructed, primary vertices are obtained by extrapolation of the tracks to the same point on the beam axis. Multiple primary vertices can be reconstructed. The actual primary vertex in an event is considered the one with the highest $\sum_i p_{T,i}^2$, with $p_{T,i} > 400$ MeV, while the others are considered pileup vertices. Secondary vertices are displaced from the beam axis and arise from heavy flavor decays (jets from b quarks have a displaced vertex with respect to the primary vertex), photon conversion or interaction with the material of the detector.

2.3.2 Electrons and photons

The electron and photon deposit their energy and are stopped in the EM calorimeter. Unlike the photons, the electrons have an associated track in the ID. Therefore, a reconstructed electron candidate is an energy cluster in the EM calorimeter matched with a track in the ID. Figure 2.14 shows a sketch of the sub-detectors involved in the electron and photon reconstruction, both sharing a similar procedure.

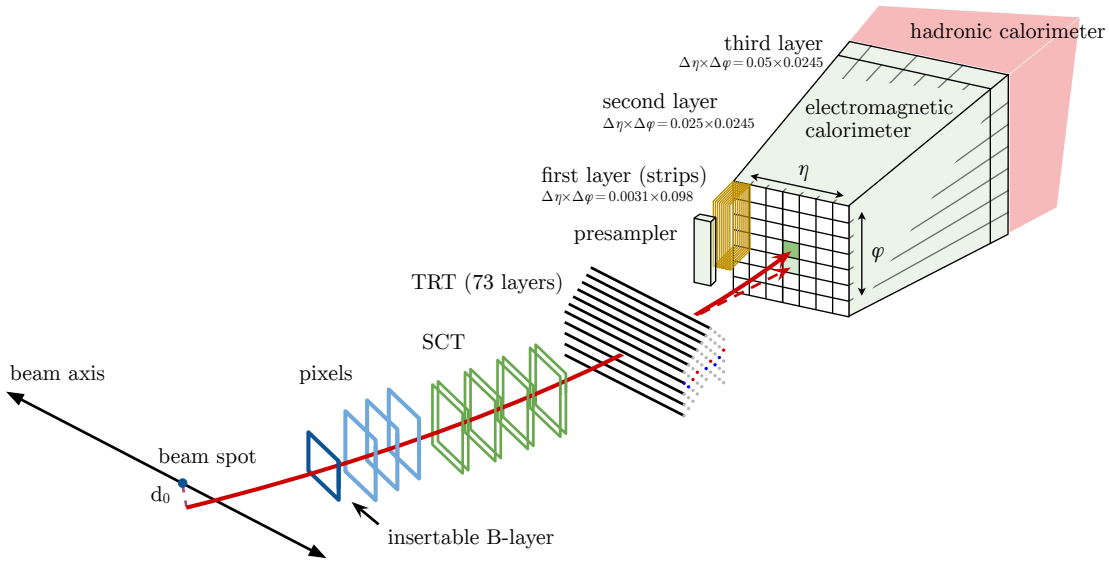

Figure 2.14 – A schematic illustration of the path of an electron through the detector. The red trajectory shows the hypothetical path of an electron, which first traverses the tracking system (pixel detectors, then silicon-strip detectors and lastly the TRT) and then enters the electromagnetic calorimeter. The dashed red trajectory indicates the path of a photon produced by the interaction of the electron with the material in the tracking system [43].

2.3.2.1 Calorimeter Cell Energy Reconstruction

Energy "seeds" are searched in the EM calorimeter in a $\eta \times \phi$ space of 3 x 5 towers using a "sliding window" algorithm [44]. The coverage of one tower is $\Delta\eta \times \Delta\phi$ = 0.025 x 0.0245 and corresponds to the granularity of the second layer of the LAr calorimeter (see figure 2.9). The energy of one tower is obtained by energy summation of all LAr layers for a given tower. A total of 200 x 256 towers cover the $\eta \times \phi$ space. Increments of 1 tower in η or ϕ directions allows to scan the entire $\eta \times \phi$ space and localize energy deposits. A seed cluster is found when its energy reaches at least 2.5 GeV. If two seed clusters overlap within a 5×9 towers region, the highest transverse energy seed cluster is retained. A high efficiency of around 95% is obtained at $E_T = 7$ GeV and at least 99% is reached for $E_T > 15$ GeV.

During Run 2 a new algorithm was implemented for energy cluster reconstruction. Unlike the sliding window algorithm, the new method uses topo-clusters of cells which allow for irregular shapes of the reconstructed energy cluster.

2.3.2.2 Track association

Generally, the tracks are reconstructed following the procedure described in section 2.3.1, which is based on the pion hypothesis in the first instance (neg-

ligible radiative loss in the ID due to relative high mass $m_{\pi^\pm} \approx 273 m_e$). In case this fit fails, the electron hypothesis is considered which allows for up to 30% energy loss at every interaction point. On top of the general procedure, the loosely matched tracks to the energy cluster ($|\eta_{EMcluster} - \eta_{track}| < 0.05$ and $-0.20 < sign(q) \times |\phi_{EMcluster} - \phi_{track}| < 0.05$) that have at least 4 hits (pixel + SCT) are refitted with a Gaussian Sum Filter (GSF) [45] based model which allows for non-linear radiative effects (bremsstrahlung) to be included in the track reconstruction. An EM cluster becomes an electron candidate if two conditions are satisfied:

— 4 points of measurement (or more) in the silicon detectors

— no association to a photon vertex reconstruction

Electron and photon candidates are separated at this step depending if a track is or is not associated to an EM cluster.

2.3.2.3 Calibration

The energy measured in the EM calorimeter does not correspond to the real initial particle energy because of losses due to detector services (cables, cryostat, etc.) and a calibration procedure is necessary. At this stage, the initial seed of 3×5 in $\eta \times \phi$ is extended to 3×7 in the barrel ($|\eta|$<1.37) and 5×5 in the endcaps (1.52$|\eta|$<2.47) to recover any potential energy contribution from radiative losses in the ID. A multivariate technique based on Monte Carlo simulations was developed [46].

A schematic overview of the procedure used to calibrate the energy response of electrons and photons is given in figure 2.15.

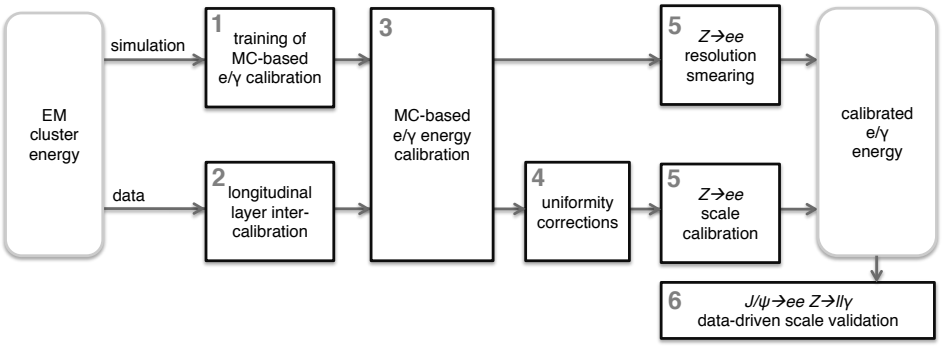

Figure 2.15 – Schematic overview of the procedure used to calibrate the energy response of electrons and photons.

2.3.2.4 Electron reconstruction efficiency

The electron reconstruction efficiency is defined as the ratio of the number of electron candidates that have a good quality track (at least 7 hits in pixel+SCT with at least 1 pixel hit) matched to a reconstructed energy cluster in the EM

calorimeter over the number of all reconstructed energy clusters in the EM calorimeter. The electron reconstruction efficiency is measured with a Tag and Probe method and reaches values of around 96% (around 1% uncertainty) at E_T=15 GeV and increases up to 99% (per-mile level uncertainty) at higher E_T. A detailed discussion of the electron reconstruction efficiency measurement is given in chapter 3.

2.3.2.5 Identification

The electron identification procedure [43] is designed to distinguish between electron candidates and backgrounds that mimic electron signatures like light hadrons loosing all their energy in the EM calorimeter, photon conversions and electrons arising within a jet decay chain (particularly for heavy flavors). This procedure is based on a multivariate likelihood method. An extended set of electron related variables are used. These include information from all the three layers of the EM calorimeter, from hadron leakage, from the track related quantities in the ID and the track-cluster matching. They are summarized and described in table 2.6.

The electron candidate is given a score, or discriminant value d_L, based on the following formula, which combines information from this entire variable set:

$$d_L = \frac{L_S}{L_S + L_B} \tag{2.7}$$

where the likelihood function is built using probability density functions (PDFs) of the identification variables

$$L_{S(B)}(\overrightarrow{\theta}) = \prod_{i=1}^{n} P_{S(B),i}(\theta_i) \tag{2.8}$$

Generally, three operating points are chosen depending on the level of signal efficiency and background rejection that cover most of the needs of the physics analyses. These operating points are commonly labeled as *tight, medium* and *loose* in order of their decreasing background rejection level and correspond increasing thresholds for the discriminant d_L. Additionally, rectangular cuts are used for the number of hits in the pixel and SCT detectors. At least two hits in the pixel detector ($n_{Pixel} \geq 2$) are required with a total of at least seven hits in the pixel and SCT combined ($n_{Si} \geq 7,\ n_{Si} = n_{Pixel} + n_{SCT}$). To reduce photon conversions for the medium and tight working points at least one hit of the minimum two pixel hits is required to be in the innermost pixel layer.

The electron identification efficiency is defined as the ratio of the electron candidates that pass an identification operating point over the total number of electron candidates that pass the good track quality requirements ($n_{Si} \geq 7$ with $n_{pixel} \geq 1$). The Tag and Probe method is used the measure the efficiency in

Type	Description	Name	Rejects			Usage
			LF	γ	HF	
Hadronic leakage	Ratio of E_{T} in the first layer of the hadronic calorimeter to E_{T} of the EM cluster (used over the range $\lvert\eta\rvert < 0.8$ or $\lvert\eta\rvert > 1.37$)	R_{had1}	x	x		LH
	Ratio of E_{T} in the hadronic calorimeter to E_{T} of the EM cluster (used over the range $0.8 < \lvert\eta\rvert < 1.37$)	R_{had}	x	x		LH
Third layer of EM calorimeter	Ratio of the energy in the third layer to the total energy in the EM calorimeter. This variable is only used for $E_{\mathrm{T}} < 80\ GeV$, due to inefficiencies at high E_{T}, and is also removed from the LH for $\lvert\eta\rvert > 2.37$, where it is poorly modelled by the simulation.	f_3	x			LH
Second layer of EM calorimeter	Lateral shower width, $\sqrt{(\Sigma E_i \eta_i^2)/(\Sigma E_i) - ((\Sigma E_i \eta_i)/(\Sigma E_i))^2}$, where E_i is the energy and η_i is the pseudorapidity of cell i and the sum is calculated within a window of 3×5 cells	$w_{\eta 2}$	x	x		LH
	Ratio of the energy in 3×3 cells over the energy in 3×7 cells centred at the electron cluster position	R_{ϕ}	x	x		LH
	Ratio of the energy in 3×7 cells over the energy in 7×7 cells centred at the electron cluster position	R_{η}	x	x	x	LH
First layer of EM calorimeter	Shower width, $\sqrt{(\Sigma E_i (i - i_{\mathrm{max}})^2)/(\Sigma E_i)}$, where i runs over all strips in a window of $\Delta\eta \times \Delta\phi \approx 0.0625 \times 0.2$, corresponding typically to 20 strips in η, and i_{max} is the index of the highest-energy strip, used for $E_{\mathrm{T}} > 150$ GeV only	w_{stot}	x	x	x	C
	Ratio of the energy difference between the maximum energy deposit and the energy deposit in a secondary maximum in the cluster to the sum of these energies	E_{ratio}	x	x		LH
	Ratio of the energy in the first layer to the total energy in the EM calorimeter	f_1	x			LH
Track conditions	Number of hits in the innermost pixel layer	n_{Blayer}		x		C
	Number of hits in the pixel detector	n_{Pixel}		x		C
	Total number of hits in the pixel and SCT detectors	n_{Si}		x		C
	Transverse impact parameter relative to the beam-line	d_0		x	x	LH
	Significance of transverse impact parameter defined as the ratio of d_0 to its uncertainty	$\lvert d_0/\sigma(d_0)\rvert$		x	x	LH
	Momentum lost by the track between the perigee and the last measurement point divided by the momentum at perigee	$\Delta p/p$	x			LH
TRT	Likelihood probability based on transition radiation in the TRT	eProbabilityHT	x			LH
Track–cluster matching	$\Delta\eta$ between the cluster position in the first layer and the extrapolated track	$\Delta\eta_1$	x	x		LH
	$\Delta\phi$ between the cluster position in the second layer of the EM calorimeter and the momentum-rescaled track, extrapolated from the perigee, times the charge q	$\Delta\phi_{\mathrm{res}}$	x	x		LH
	Ratio of the cluster energy to the track momentum, used for $E_{\mathrm{T}} > 150$ GeV only	E/p	x	x		C

Table 2.6 – Variables used for electron identification. The columns labelled "Rejects" indicate whether a quantity has significant discrimination power between prompt electrons and light-flavour (LF) jets, photon conversions (γ), or non-prompt electrons from the semileptonic decay of hadrons containing heavy-flavour (HF) quarks (b- or c-quarks). In the column labelled "Usage," an "LH" indicates that the pdf of this quantity is used in forming L_S and L_B (defined in eq. (2.8)) and a "C" indicates that this quantity is used directly as a selection criterion. In the description of the quantities formed using the second layer of the calorimeter, 3×3, 3×5, 3×7, and 7×7 refer to areas of $\Delta\eta \times \Delta\phi$ space in units of 0.025 × 0.025 [43].

$Z \to ee$ events for $10 < E_T < 150$ GeV and in $J/\psi \to ee$ for $4.5 < E_T < 15$ GeV, combining the results for the overlapping $10 < E_T < 15$ GeV region. Typical values are in the 85-96 % range for the loose operating point and 56-89 % for the tight one considering an energy range from 4.5 GeV to 150 GeV as shown in figure 2.16 (left). The efficiencies are stable with respect to pileup and show only a slight decrease (2-5 %) as shown in figure 2.16 (right).

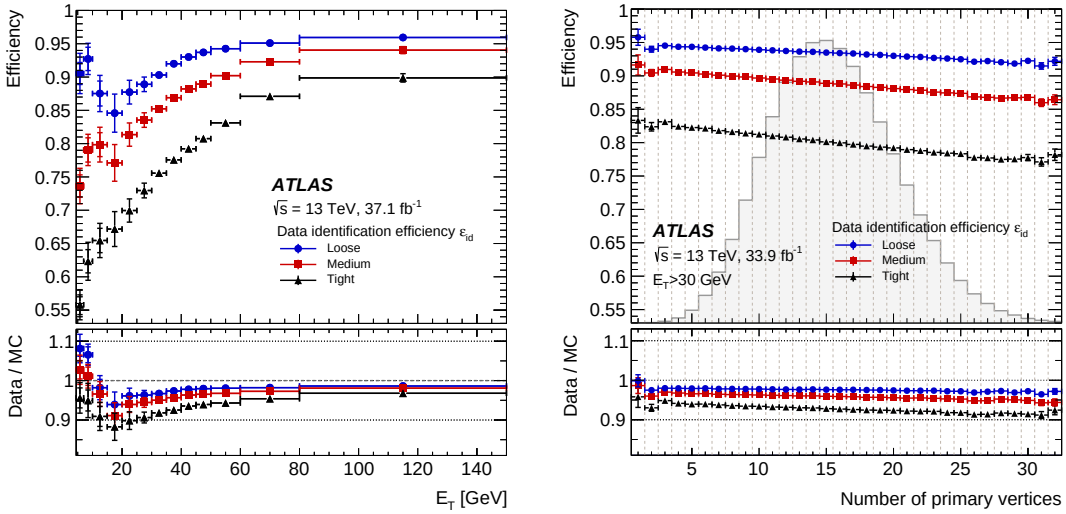

Figure 2.16 – The electron identification efficiency as a function of E_T (left) and number of primary vertices (right) for Loose (blue circle), Medium (red square), and Tight (black triangle) operating points in 2015-2016 data (37.1 fb^{-1}) and 2016 data (33.9 fb^{-1}). The gray distribution (right) shows the normalized number of primary vertices profile. Error bars include statistical and systematic uncertainty [43].

For photons a cut-based identification procedure is used [47]. Two operating points, *tight* and *loose*, are defined based on the desired background rejection levels. The loose operating point uses selections (cuts) on discriminating variables based on the shower shape in the second layer of the EM calorimeter as well as hadronic leakage. For the tight operating point additional information from the finely segmented first EM calorimeter layer (strip layer) is added. An identification efficiency for the tight operating point of 45-60% is obtained at E_T=10 GeV increasing to 95-98 % at E_T>100 GeV.

2.3.2.6 Isolation

A set of variables are introduced to account for the amount of activity in the vicinity of an electron (similar isolation variables are defined for muons, photons) in terms of energy in the calorimeter or momentum of tracks within a specified ΔR cone. Two types of isolation variables are defined.

— calorimeter-based isolation ($E^{isol}_{T,cone}$) accounts for the energy around an electron EM cluster within a cone $\Delta R = 0.2, 03, 0.4$. The isolation $E^{isol}_{T,cone}$ is obtained by subtracting from the total raw energy in a given cone ΔR, $E^{isol}_{T,raw}$, the energy contribution from the electron ($E^{isol}_{T,core}$). Additional corrections are estimated for the leakage from the $E^{isol}_{T,core}$ estimation and pileup contributions.

$$E^{isol}_{T,cone} = E^{isol}_{T,raw} - E^{isol}_{T,core} - E^{isol}_{T,leakeage} - E^{isol}_{T,pileup} \tag{2.9}$$

— track-based isolation ($p_{T,cone}^{isol}$) accounts for the tracks p_T in a given cone around electron's track. Only tracks satisfying basic track quality requirements with a $p_T > 1$ GeV and $|\eta| < 2.5$ are considered. The pileup effects are minimized (z_0 cuts) and the contribution from the electron's own track is subtracted, including tracks from $e \to e\gamma \to eee$ processes by performing an extrapolation up to the second layer in the EM calorimeter. The finer granularity of the tracker allows for a smaller cone size than $\Delta R = 0.2$. A variable-cone-size track isolation can be defined as

$$\Delta R = min\left(\frac{10\text{GeV}}{p_T[\text{GeV}]}, R_{max}\right) \tag{2.10}$$

where R_{max} is the cone size.

Three types of working points are usually defined for the need of physics analyses.

— Loose: a fixed isolation efficiency is targeted uniform in p_T and η
— Gradient: a fixed isolation efficiency is targeted uniform in η but dependent on p_T
— Fix: fixed cut on the isolation variable

A summary of working points definitions for the isolation variables are given in table 2.7.

Operating point	$E_{\text{T,cone}}^{\text{isol}}$ ($\Delta R = 0.2$)	$p_{\text{T,var}}^{\text{isol}}$ ($R_{\text{max}} = 0.2$)	Total ϵ_{iso}
Loose (Track Only)	-	$\epsilon_{\text{iso}} = 99\%$	99%
Loose	$\epsilon_{\text{iso}} = 99\%$	$\epsilon_{\text{iso}} = 99\%$	98%
Gradient	$\epsilon_{\text{iso}} = 0.1143 \times p_{\text{T}} + 92.14\%$	$\epsilon_{\text{iso}} = 0.1143 \times p_{\text{T}} + 92.14\%$	90(99)% at 25(60) GeV
Gradient (Loose)	$\epsilon_{\text{iso}} = 0.057 \times p_{\text{T}} + 95.57\%$	$\epsilon_{\text{iso}} = 0.057 \times p_{\text{T}} + 95.57\%$	95(99)% at 25(60) GeV
Fix (Loose)	$E_{\text{T,cone}}^{\text{isol}}/p_{\text{T}} < 0.20$	$p_{\text{T,var}}^{\text{isol}}/p_{\text{T}} < 0.15$	-
Fix (Tight)	$E_{\text{T,cone}}^{\text{isol}}/p_{\text{T}} < 0.06$	$p_{\text{T,var}}^{\text{isol}}/p_{\text{T}} < 0.06$	-
Fix (Tight, Track Only)	-	$p_{\text{T,var}}^{\text{isol}}/p_{\text{T}} < 0.06$	-
Fix (Calo Only)	$E_{\text{T,cone}}^{\text{isol}} < 3.5$ GeV	-	-
Fix (Track $R_{\text{max}} = 0.4$)	$E_{\text{T,cone}}^{\text{isol}}/p_{\text{T}} < 0.11$	$p_{\text{T,var}}^{\text{isol}}/p_{\text{T}} < 0.06$	-

Table 2.7 – Electron isolation operating points definitions.

2.3.3 Muons

As muons are charged particles, they leave signatures both in the inner detector and in the muon spectrometer. The associated tracks are reconstructed separately and after they are combined for full muon reconstruction. The muon candidates can be split in three categories.

— Combined: The tracks from the ID and MS are reconstructed and fitted in a global manner, allowing for reduced backgrounds. This is the most common category of muons used in the analyses.

— Tagged: Muon candidates reconstructed with hits in only one layer of the MS (MDT or CSC) combining with a track in the ID (muon-tagged) or with energy deposits in the calorimeters (calo-tagged). The muon energy deposits in the calorimeters are used in the reconstruction procedure at $|\eta| < 0.1$ because of the limited coverage of the muons spectrometer in that range, however this method is affected by large backgrounds.

— Standalone: muon candidates with tracks reconstructed only in the MS, extrapolated to the primary vertex with no associated track in the ID, in the $2.5 < |\eta| < 2.7$ region where there is no coverage from the ID ($|\eta| < 2.5$).

Four working point are defined for discriminating against backgrounds: loose (tagged muons), medium (combined or extrapolated muons), tight (medium with additional track requirements) and high p_T. Figure 2.17 shows the muon identification efficiency for the $Medium$ working point in data and in simulations. High efficiency of around 99% is observed over all the p_{T} range with the exception of the low p_{T} region (5-6 GeV). A small mis-modeling is observed below 1% and the uncertainty is below 1% in the whole p_T range.

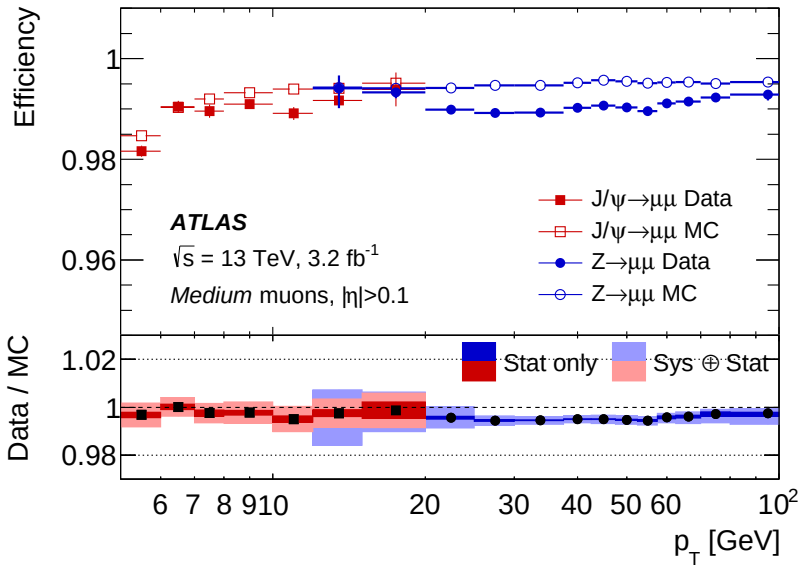

Figure 2.17 – Muon identification efficiency as a function of p_{T} for the $Medium$ working point in the $0.1<|\eta|<2.5$ region measured in $Z \to \mu\mu$ and $J/\psi \to \mu\mu$ events [48].

2.3.4 Taus

The tau leptons are relatively long lived particles ($\tau_0 \sim 10^{-13}$s) and have an observable decay length in the ATLAS detector (order of mm). The tau leptons decay predominantly hadronically to pions and neutrinos (65%) and in proportion of 35% to muons or electrons (with neutrinos) which are reconstructed as light leptons. The hadronically decaying taus, τ_{had}, are developing as jets in the

detector with tracks in the ID and energy deposits in the calorimeters. In 72% (22%) of the times the τ_{had} decay to exactly one (three) charged pions which leave tracks in the ID. A set of variables that characterize the τ_{had} jets are used to perform a multivariate analysis using boosted decision trees (BDT) [49]. Based on the output of the BDT, three identification operating points are defined (loose, medium, tight) that target 60, 55 and 45 % (50,40, and 30 %) for the 1-track (3-track) identification efficiencies [50].

2.3.5 Jets

Due to the color confinement in QCD, the quarks and gluons are not observed in isolation and they hadronise. As a consequence of the hadronisation a shower of particles (pions, kaons, protons, neutrons, light leptons from decays and photons) is observed from the hadron decay chain which is limited to specific solid angle. The manifestation of a quark or gluon in the detector is observed as a jet of particles that leave tracks in the ID and energy in the EM calorimeter and in the hadronic calorimeter where they are eventually stopped.

The jets are reconstructed using the anti-k_T [51] algorithm where the geometrical distance between particles scales with the negative power of the transverse momentum k_T, hence the name anti-k_T. The radius parameter is fixed to $R = 0.4$ and topological clusters [52] in the calorimeters are used as inputs.

2.3.5.1 Jet energy scale

Jets are complex objects and precise measurements of their energy and the systematic uncertainties are very important, particularly in analyses where multiple jets are expected in the final state (high jet multiplicity). The jet energy calibration procedure involves a series of steps that are summarized in a diagram in figure 2.18.

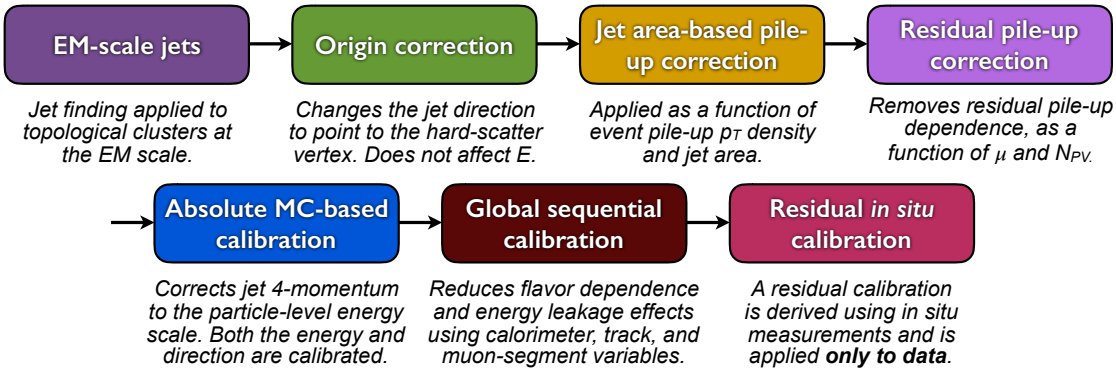

Figure 2.18 – Jet energy calibration stages [53].

In a first step, the tracks of the jet's constituent particles are corrected to point to the primary vertex, without affecting the energy. Further on the 4-vector of the jet suffer step by step corrections. An area based pileup subtraction is performed using a $\eta \times \phi$ mean pileup p_T density map estimated in data event by event. Residual pileup corrections are done using simulations. The absolute jet energy scale (JES) calibration corrects the jet 4-vector to the particle level scale using simulated isolated jets. The response from jets originating from quarks and gluons differ and are corrected using the global sequential calibration, based on energy deposits in the calorimeters, jet width, number of tracks in the jet and jet leakage in the MS. In situ techniques based on reference objects like dijet, γ and Z are then used to reduce the residual calibration bias. The fractional JES response is then computed as

$$\frac{\text{Response}_{\text{data}}}{\text{Response}_{\text{MC}}} = \frac{(p_T^{jet}/p_T^{ref})_{\text{data}}}{(p_T^{jet}/p_T^{ref})_{\text{MC}}} \tag{2.11}$$

Figure 2.19 shows the uncertainty on this fractional JES in 2015 data. It is below 4% at $20 < p_T < 50$ GeV and around 1% in the range 50 GeV up to 1 TeV. As a result it is a leading uncertainty in physics analyses involving top quarks.

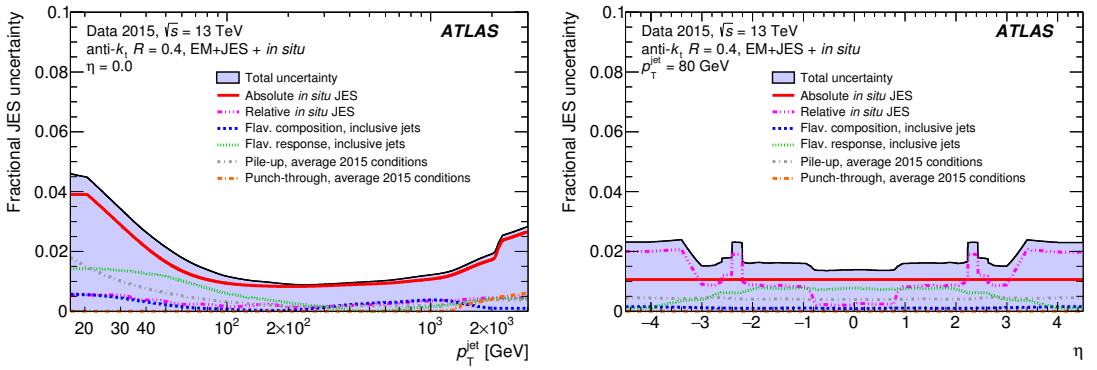

Figure 2.19 – Fractional jet energy scale uncertainty in 2015 data as a function of p_T^{jet} at $\eta = 0.0$ (left) and as a function of η at $p_T^{jet} = 80$ GeV [53].

2.3.5.2 Jet flavor tagging

The jet topology and composition varies depending on the particle that initiates it. The decay length of the b-hadrons (hadrons originating from a b quark) is measurable in the ATLAS detector and is significantly larger compared to the other lighter flavors (order of few mm). The jets coming from a b quark can be discriminated from other jets as they originate from secondary vertex. A BDT is used to exploit this information and assign a score to the jets depending on how likely it is that they originate from b quarks. This procedure is called b-tagging. The MV2c10 algorithm(s) is a top level algorithm as it uses as inputs the output

from other sophisticated algorithms:

1. Impact parameter based algorithms, called IP2D and IP3D, which use longitudinal IP (d_0) only for IP2D or including also transverse IP (d_0 and z_0) for IP3D and their significances.
2. Secondary vertex finding algorithm (SV) is performing a fit of a secondary vertex corresponding to a jet, adjusting accordingly the jet properties like the invariant mass (m_{inv}^{jet}) and vertex displacement from the beam line.
3. JetFitter (JF) algorithm is performing a jet global fit of the full hadron decay chain, being able to reconstruct consecutive vertices in the decay chain.

Using a cut on the MVc10 output allows to discriminate b-jets, c-jets and light jets. Figure 2.20 shows the distribution of the MV2c10 BDT output distribution.

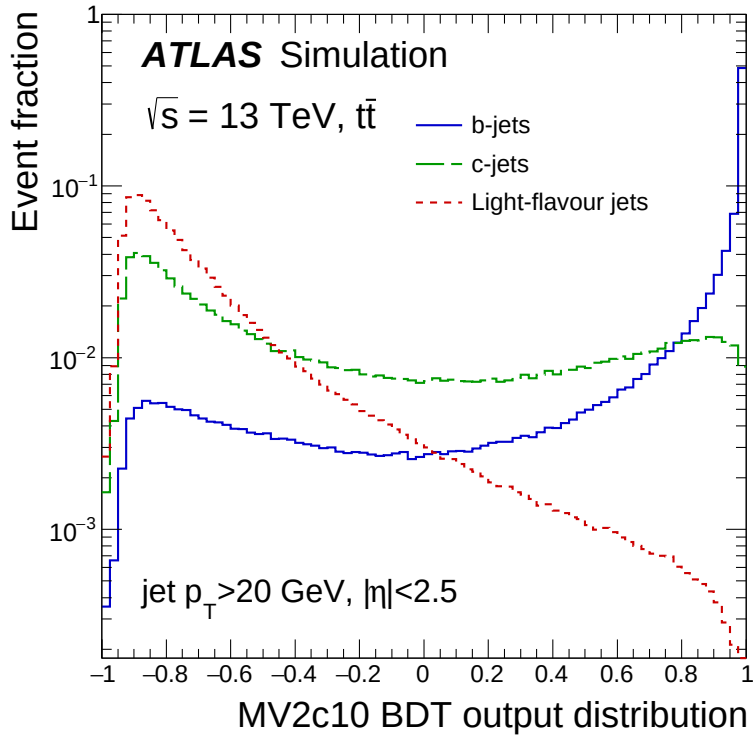

Figure 2.20 – Distribution of the MV2c10 output jet flavor-tagging variable [54].

For example, a b-tagging efficiency of 70% (MV2c10 output> 0.8244) results in light-flavor rejection of 381 and 12 for c-jets. It is interesting to note that the jets originating from the hadronically decaying τ get a rejection factor of 55. Although few variations exist for this algorithm depending on the fraction of c-jets used in training, like MV2c0 (0 % c-jets) and MV2c20 (15% c-jets), and various b-tagging efficiencies (60%, 77%, 85%), the MV2c10 (7% c-jets) at 70% b-tagging efficiency was used in this thesis.

2.3.6 Missing transverse momentum

The total transverse momentum in the proton-proton collision is zero by the virtue of momentum conservation. However, because of the particles that are produced in the collision but which do not interact with the detector (like neutrinos in SM or new, unknown particles), the sum of the transverse momenta of particles reconstructed after the collision could be non-zero. The missing transverse momentum is defined as [55]

$$\overrightarrow{E}_T^{miss} = -1 \times \sum_{i \in objects} \overrightarrow{p}_{T,i} \tag{2.12}$$

where $p_{T,i}$ is the transverse momenta of the object i in the collision event. The objects are actually split in two categories, the *hard* and the *soft* term. The electrons, photons, muons, taus and the jets ($p_T > 20$ GeV) are considered $hard$ objects and the reconstructed and calibrated objects enter in the E_T^{miss} hard term. In the soft term are included tracks from the primary vertex that are not matched to the hard objects. The reconstruction of E_T^{miss} is challenging and the measurement is susceptible to the effects of the pileup, object calibration and detector coverage. Additionally, the E_T^{miss} is an inclusive quantity which summarizes the contributions from all possible $invisible$ particles in the same event, a fact that can lead to ambiguity of interpretations of the individual invisible particles.

3 Electron performance

Summary

3.1 Introduction

The leptons in the proton-proton collisions at LHC represent markers for events of interest as already mentioned in section 2.2.5. The number of events for a given process $pp \to x$, with the cross section σ_x, expected to be found by the

detector for an integrated luminosity $L = \int L(t)\mathrm{dt}$ is given by

$$N_x^{ev} = \sigma_x \cdot L \cdot A \cdot \varepsilon, \tag{3.1}$$

where A and ε are the acceptance and the efficiency of the detector. Therefore, the ability to reconstruct, identify and isolate leptons with high efficiency is very important and challenging. The knowledge of the lepton efficiency is particularly important for analyses involving very rare processes and in searches for new physics. Additionally, high precision measurements require very good control of the efficiency uncertainties since they can be a limiting factor for the measurement precision. For example, the electron efficiencies uncertainties have important contribution to the systematic uncertainty in the Z and $W^{\pm}$ cross section measurement [56], where the uncertainty corresponding to the electron reconstruction efficiency reaches 0.20 % out of the $\delta\sigma_Z$ =0.35 % total experimental uncertainty for σ_Z measurement, as shown in table 3.1. Similar limitations are present in the case of W mass measurement in the electron channels, for which the uncertainty corresponding to the electron reconstruction efficiency is 7.2 MeV for a total systematic uncertainty of δm_W =14.2 MeV [57].

	$\delta\sigma_{W+}$ [%]	$\delta\sigma_{W-}$ [%]	$\delta\sigma_Z$ [%]	$\delta\sigma_{\text{forward}\,Z}$ [%]
Trigger efficiency	0.03	0.03	0.05	0.05
Reconstruction efficiency	0.12	0.12	0.20	0.13
Identification efficiency	0.09	0.09	0.16	0.12
Forward identification efficiency	–	–	–	1.51
Isolation efficiency	0.03	0.03	–	0.04
Data statistical uncertainty	0.04	0.05	0.10	0.18
Total experimental uncertainty	0.94	1.08	0.35	2.29

Table 3.1 – Relative uncertainty ($\delta\sigma$) corresponding to electron efficiencies of measured integrated fiducial cross section (times branching ratio) of $W^{\pm}$ and central and forward Z/γ^* ($66<m_{ee}<116$ MeV) in the electron channels [56].

An important feature of the analyses involving top quarks represents the presence of heavy flavor decays, which in case of multilepton final states can lead to a significant source of non-prompt leptons background. In conjunction with low cross sections of processes involved in analyses like search for flavor-changing neutral currents in $t \to Hq$ decays (top FCNC, see Chapter 4) and ttH production with multilepton final states (ttHML, see Chapter 5) the standard isolation variables (see section 2.3.2.6) are not efficient enough to reject the non-prompt leptons. A new method for better rejection was developed and the electron efficiency measurement in this context is a subject of this chapter.

This chapter describes in details the electron reconstruction and non-prompt electron efficiencies measurement. First, the electron efficiencies generalities are described in section 3.2. Further on, the chapter is split in two large sections. Section 3.3 describes the methodology and the results of the electron reconstruction efficiency measurement while section 3.4 addresses the non-prompt electron efficiency measurement.

3.2 Electron efficiencies generalities

The efficiency ε is defined as the fraction of electron candidates emitted in the active detector volume and satisfying the selection criteria. It is divided into different components which are measured separately. The total efficiency for a single electron can be written by components as:

$$\varepsilon_{\text{total}} = \varepsilon_{\text{reco}} \times \varepsilon_{\text{id}} \times \varepsilon_{\text{iso}} \times \varepsilon_{\text{trig}} = \frac{N_{\text{reco}}}{N_{\text{clusters}}} \times \frac{N_{\text{id}}}{N_{\text{reco}}} \times \frac{N_{\text{iso}}}{N_{\text{id}}} \times \frac{N_{\text{trig}}}{N_{\text{iso}}}. \tag{3.2}$$

Each component is defined as follows:

— $\varepsilon_{\text{reco}}$, the reconstruction efficiency, is defined as the ratio of the number of electron candidates that pass the track quality requirements N_{reco} over the total number of reconstructed clusters in the EM calorimeter N_{clusters} (see section 2.3.2) and accounts for how well tracks are reconstructed and matched to EM clusters. The track quality requirements rely on the number of hits in all silicon detectors (that is Pixel + SCT), n_{Si}, and on the number of hits in the pixel detector n_{Pix}. At least 7 silicon hits are required, $n_{\text{Si}} \geq 7$, with at least one hit in the pixel detector $n_{\text{Pix}} \geq 1$.

— ε_{id}, the identification efficiency is defined as the ratio of number of electron candidates that pass the track quality and a specific identification criteria ($loose,\ medium,\ tight$), N_{id}, depending on the background rejection level of the electron identification (see section 2.3.2) over N_{reco}.

— ε_{iso}, the isolation efficiency is defined as the ratio of the number of electron candidates that pass the track quality, a specific identification criteria and an isolation selection (track based or calorimetric isolation) over N_{id}. The isolation requirement aims at separating electron candidates coming from heavy resonances ($Z \to ee, W \to e\nu$) referred to as $prompt$ electrons from electrons coming from heavy flavor decays (non-prompt electrons).

— $\varepsilon_{\text{trig}}$, the trigger efficiency is defined as the ratio of the number of the electron candidates that pass the track quality requirements, identification, isolation and trigger selections over the numerator defined for ε_{iso}.

The efficiency components are measured in a specific order to preserve consistency. The numerator of one efficiency is the denominator of the previous efficiency in the chain. The selections are more strict moving from left to right in

eq. (3.2), with the electrons passing current efficiency selections being a subset of previous efficiency selections. The level of background decreases, having the highest level of background at the reconstruction efficiency level.

Taking into account that there could be different choices in terms of identification, isolation and trigger selection depending on the needs of the individual physics analyses, a large number of combinations are possible for the total electron efficiency. In particular, throughout the Run 2, measurements were performed for 1 working point for electron reconstruction, 3 for identification, 8 for isolation and 13 for trigger efficiency. This leads to a whooping 312 combinations.

The efficiencies depend on the interactions of the electron with the detector, namely on the amount of detector material and geometry (parametrized by η) and on the electron energy E_{T}. Therefore, the efficiency measurements are performed double differentially in bins of (E_T, η), as specified in Tables 3.2 and 3.3. The justification of the choice of this binning is to capture the detector particularities in terms of material distribution (ex. the transition region $1.37 < |\eta| < 1.52$ with a large dead material amount) and the available data sample size. For residual effects coming from kinematic differences of the physics processes used in the measurements systematic uncertainties are assigned. They are expected to largely cancel out in the data-to-MC efficiency ratios.

Bin boundaries in E_T [GeV]										
15	20	25	30	35	40	45	50	60	80	150	∞

Table 3.2 – Measurement bins in electron transverse energy E_{T}.

Bin boundaries in $\lvert\eta\rvert$										
0	0.1	0.6	0.8	1.15	1.37	1.52	1.81	2.01	2.37	2.47

Table 3.3 – Measurement bins in electron pseudo-rapidity η. The measurements in $Z \to ee$ events are performed in the positive and negative η hemisphere separately.

3.2.1 Tag and Probe method

The Tag and Probe method is used to perform the electron efficiency measurement. This methods exploits the leptonic decays of the resonances like $Z \to ee$, $J/\psi \to ee$ and $W \to e\nu$ which assure a large, clean sample of electrons. The principle of the method is to apply strict requirements on one lepton, called tag [1], to significantly increase the chance that it comes from the resonance

1. In case of the W decays the ν is considered the tag.

decay while applying minimum requirements on the second lepton, called $probe$, provided that their invariant mass is close to the decaying resonance mass (figure 3.1). All electron candidate pairs are checked for tag-probe selections so it is possible to have more than one probe in the same event. Only the probes are used in the efficiency calculation to ensure an unbiased measurement.

The $Z \to ee$ process[2] is used for the measurement of all efficiencies for 10 GeV $< E_{\mathrm{T}} <$ 150 GeV (15 GeV lower limit for reconstruction efficiency) and extrapolating outside this range.

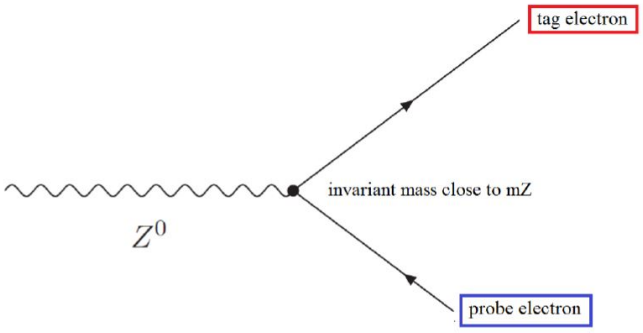

Figure 3.1 – $Z \to ee$ decay.

The measurement is using the tag-probe invariant mass as discriminant variable and is performed in a mass window centered around the Z mass peak ($m_Z = 91.1876 \pm 0.0021$ [58]) which is considered the signal region. Before calculating the efficiencies, any contributions from the backgrounds have to be subtracted. In the Monte Carlo simulation the background is estimated using the $Truth$ information. The background estimation in data is the most complex part of the measurement and different approaches are used for different efficiency components. The backgrounds can be hadrons misidentified as electrons, photon conversions, electrons from heavy flavor decays and they come mainly from W+jets, Z+jets, $b\bar{b}$, $t\bar{t}$ and di-boson processes. $Z \to \tau\tau \to ee$ is also considered as a background as any other pair $e\bar{e}$ not coming from $Z \to ee$.

3.2.2 Event and object selection

The event level selections require to have events with at least one primary vertex including at least 3 tracks. The event should be fired by a single electron trigger and a minimum of two electron candidates are required. Further tight selections are applied individually to the tag electron candidates and loose selection for the probe electron candidates.

The selection for the tag is the following:

2. The $J/\psi \to ee$ decay is used only for low E_{T} ($E_{\mathrm{T}} <$ 15 GeV) identification efficiency measurement

— Transverse energy of E_{T}> 25 GeV
— pass $|\eta|$ <2.47 but excluding the transition region 1.37<$|\eta|$ <1.52
— pass $tight$ identification
— trigger matched

The selection for the probe is the following:

— Transverse energy of E_{T}> 10 GeV (15 GeV for electron reconstruction)
— pass $|\eta|$ <2.47
— electron candidates with a matched track should have no nearby jets (p_T^{jet} >20 GeV) within a solid angle $\Delta R(probe, jet) < 0.4$
— electron candidates with no matched track should have no electron candidate within a solid angle $\Delta R(probe, e) < 0.15$. This selection aims at reducing photon conversions.

Further on, at least one tag-probe pair having opposite signs that passes the above mentioned selections is required the be found in the event. Additionally, an invariant mass 60 GeV<m_{ee}<250 GeV requirement is applied to all selected tag-probe pairs. Only a narrow mass window (10-30 GeV wide) centered on the Z boson mass peak is used as signal region. The complementary regions (low/high invariant mass) are used for background estimation.

For the electron reconstruction there are no opposite-sign requirements for the tag-probe pair because of having no charge defined for the candidates with no matched track.

3.2.3 Data and simulation samples

The measurements presented in this chapter rely on the proton-proton collision data ($\sqrt{s} = 13$ TeV) collected by the ATLAS detector during 2015-2017. Because of the ATLAS software upgrade (release 20.7 to release 21, see section 2.3.2) results are given for 2015-2016 data before the upgrade and also for the reprocessed data. The 2017 data were collected after the upgrade so only one set of results were produced. Around 36 millions $Z \to ee$ events in total are used in the measurement for the full 2015-2017 dataset.

For the Monte Carlo simulations, the $Z \to ee$ events were generated using POWHEG-BOX V2 [59] at NLO using PYTHIA 8 [60] for parton shower modeling.

All events were reweighted to match the <μ> (pile-up) distribution in the data and then passed through a full ATLAS detector simulation using GEANT 4 [61, 62].

3.3 Electron reconstruction efficiency measurement

The electron reconstruction efficiency is based on the ratio between events passing track quality criteria and events with no requirement. It can be written

as:

$$\varepsilon_{\text{reco}} = \frac{N^{\text{sig}}_{\text{pass}}}{N^{\text{sig}}_{\text{pass}} + N^{\text{sig}}_{\text{fail}}} = \frac{N^e_p - B^e_p}{\left(N^e_p - B^e_p\right) + \left(N^e_F - B^e_F\right) + \left(N^\gamma - B^\gamma\right)},$$

where N^e_p and N^e_F are the number of probes passing/failing the track quality requirements (at least 7 precision hits SCT+pixel, with at least 1 pixel hit), B^e_P and B^e_F the associated background terms. N^γ is the number of non-reconstructed probes and B^γ it's associated background. Splitting the denominator into 3 terms allows for an optimized background determination for each case.

Expressed with high mass terms (invariant mass outside Z mass window), it reads:

$$\varepsilon_{\text{reco}} = \frac{P - T\frac{P_H}{T_H}}{P - T\frac{P_H}{T_H} + F - U\frac{F_H}{U_H} + \Gamma} = \frac{U_H\left(ST_H - TS_H\right)}{U_H\left(ST_H - TS_H\right) + T_H\left(RU_H - UR_H\right) + \Gamma T_H U_H}$$

, with P/F the number of candidates passing/failing the track quality requirements, T/U the number of probes in templates passing/failing the same requirements. Γ is the number of non-reconstructed candidates (after background subtraction). The index H stands for the high mass region (outside Z mass peak window). The right hand side, has independent variables, used for the error propagation. S is defined as $P-T$, $S_H = P_H - T_H$, $R = F - U$ and $R_H = F_H - U_H$.

3.3.1 Previous measurements

Electron reconstruction efficiency measurements were performed during Run 1 [63] when the method of measurement itself was established. Figure 3.2 shows the results for reconstruction efficiency for 2011 data (4.7 fb^{-1} at $\sqrt{s} = 7$ TeV) and for 2012 data (20.7 fb^{-1} at $\sqrt{s} = 8$ TeV). For 2011 results the efficiency values range from 90% at high $|\eta|$ (end-cap) and low E_{T} up to 95% at central values of η and high E_{T}. For the 2012 results a significant improvement in the efficiencies was achieved (97-99%) due to improved track reconstruction algorithm which now includes radiative effects (effect more pronounced at high $|\eta|$ due to more material which favors more bremsstrahlung). Additionally, the 2012 results show smaller uncertainties due to a larger dataset used for the measurement and improvements in the background estimates of the efficiency measurements.

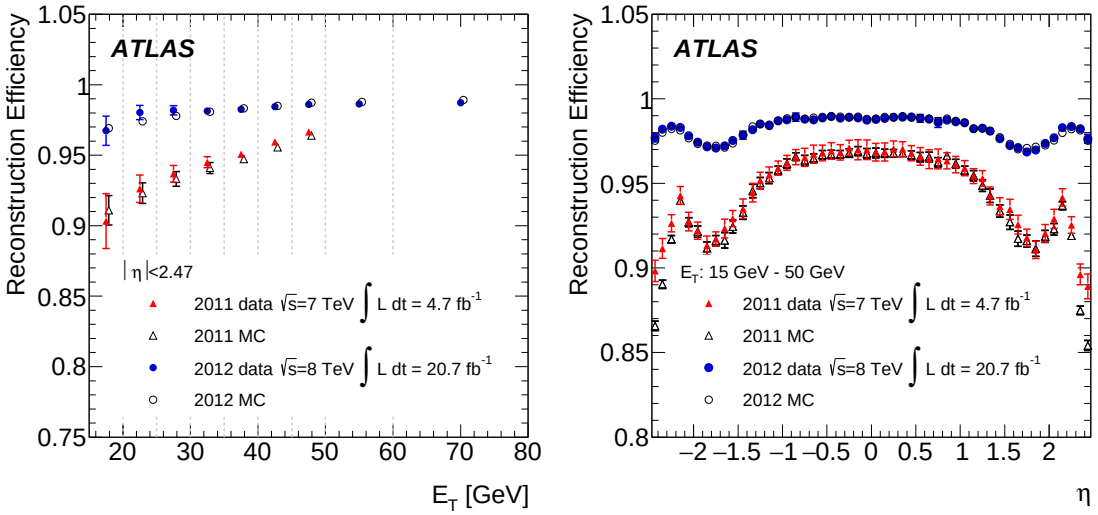

Figure 3.2 – Electron reconstruction efficiency measured as a function of E_T (left) / η (right) with the Run 1 dataset ($\sqrt{s} = 7 - 8$ TeV).

3.3.2 Background estimation

There are two types of background based on the characteristics of the electron candidates.

3.3.2.1 Electron candidates with associated track

The background coming from probes that fail/pass the track quality requirement is estimated using templates. The templates are built by inverting isolation selections and asking for at least 2 failed cuts of the *cut-based Loose* ID working point as detailed in Table 3.4. Following this procedure only the shape of the template is estimated. The normalization is performed in the high/low mass region (tail), outside signal region, which is assumed to be almost signal free. The remaining signal is subtracted using MC simulations. Finally, the estimate for the background coming from probes that fail/pass the track quality requirement in the signal region (Z peak) is given by

$$B^e = N^{\text{template}}_{\text{peak}} \times \frac{N^e_{\text{tail}} - N^{\text{MC}}_{\text{tail}} \times \frac{N^{\text{Data,tight}}_{\text{peak}}}{N^{\text{MC,tight}}_{\text{peak}}}}{N^{\text{template}}_{\text{tail}}},$$

where B^e is the number of background in the signal region, N^e and N^{template} are the total number of probes and the number of probes in the background template in data. Indices N_{peak} and N_{tail} stand for the Z-peak and the high/low mass control region.

Figure 3.3 shows two representative invariant mass distributions for electron candidates passing (top) / failing (bottom) the track quality requirements. The background estimates (red line) for the electron candidates passing the track quality matches well the high and low mass region. The estimates in the signal region (around the Z mass peak) is in good agreement between the total expected (signal MC + background template) and the data. The background estimates (red line) for the electron candidates failing the track quality is less precise because of limited statistics, but in turn does not affect significantly the final results.

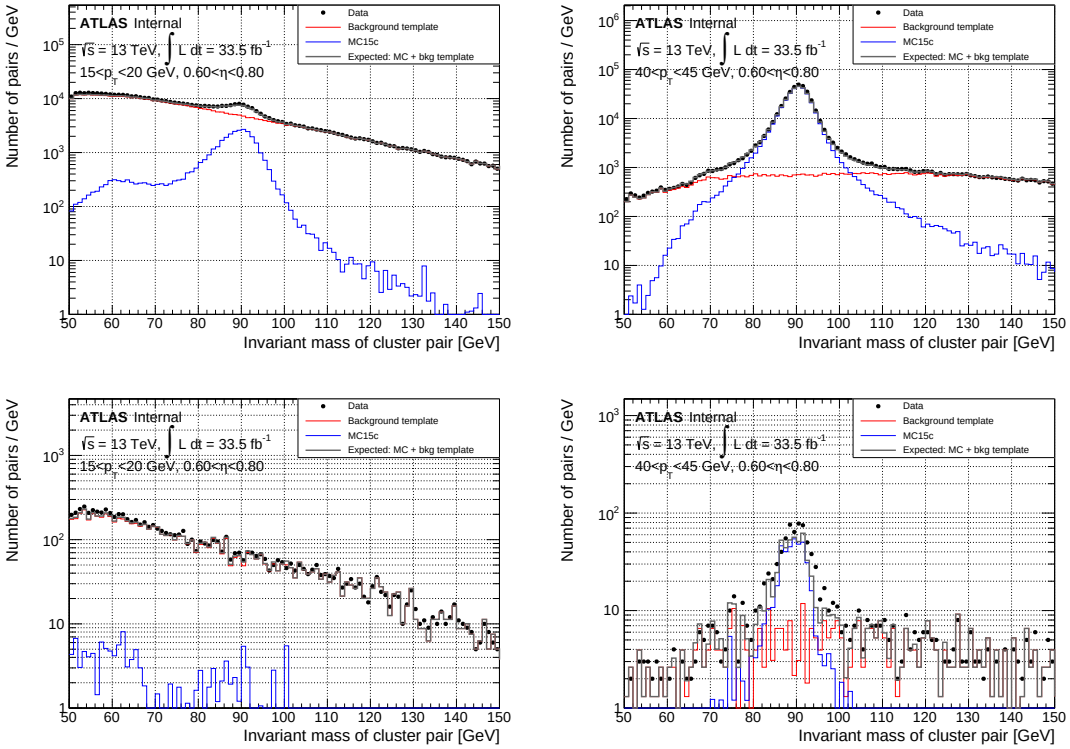

Figure 3.3 – Invariant mass distributions for electron candidates passing (top) / not passing (bottom) the track quality requirement and the corresponding background estimation in representative bins low E_{T}, $15 < E_{\mathrm{T}} < 20$ GeV (left), and high E_{T}, $40 < E_{\mathrm{T}} < 45$ GeV, for $0.6 < \eta < 0.8$.

3.3.2.2 Electron candidates with no associated track

The background associated to the non-reconstructed candidates (EM cluster with no associated track, referred to as "photon") is deduced by fitting the electron-photon invariant mass m distribution using a third order polynomial function. A binned χ^2 fit is performed in the sidebands. The background estimation is then given by taking the integral of the fitted function in the signal region.

Excluding the signal region, the fit is performed on two sidebands (low and high mass), containing a low amount of signal events in order to have a minimal impact on the background estimation. The polynomial function can be written as follows:

$$f(m) = \sum_{i=0}^{3} k_i m^i$$

And the corresponding χ^2 reads:

$$\chi^2 = \sum_{i=1}^{N} \left(n_i - f(m_i)\right)^2,$$

where n_i is the number of events and m_i the invariant mass in the center of the bin i. Bins have $\Delta m = 5\,\text{GeV}$ width. This bin width is chosen to have sufficient statistics to avoid instabilities in the fit. Tests were performed with a smaller width $\Delta m = 1\,\text{GeV}$ once more data was available however no improvement was noticed and $\Delta m = 5\,\text{GeV}$ was maintained. Signal contamination is then subtracted for each bin:

$$n_i = n_i^{\text{data}} - n_i^{\text{MC}}$$

The MC estimation is computed the same way as for data and normalized to the number of *tight-tight* electron-positron pairs. Minimizing χ^2 with respect to its four parameters leads to the following system of linear equations:

$$\sum_{i=1}^{N} \left(n_i - \sum_{j=0}^{3} k_j m_i^j \right) m_i^q = 0$$

Where N is the number of bins. This can be reorganized as:

$$\forall q \in [\![0;3]\!], \quad \sum_{i=1}^{N}\sum_{j=0}^{3} k_j m_i^{j+q} = \sum_{i=1}^{N} m_i^q n_i \iff MA = B \quad \text{with} \quad \begin{cases} M_{qj}A_j = B_q \\ M_{jq} = M_{qj} = \sum_{i=1}^{N} m_i^{q+j} \\ A_j = k_j \\ B_q = \sum_{i=1}^{N} m_i^q n_i \end{cases}$$

And finally reads:

$$\begin{pmatrix} S_{00} & S_{10} & S_{20} & S_{30} \\ S_{10} & S_{20} & S_{30} & S_{40} \\ S_{20} & S_{30} & S_{40} & S_{50} \\ S_{30} & S_{40} & S_{50} & S_{60} \end{pmatrix} \begin{pmatrix} k_0 \\ k_1 \\ k_2 \\ k_3 \end{pmatrix} = \begin{pmatrix} S_{01} \\ S_{11} \\ S_{21} \\ S_{31} \end{pmatrix} \quad \text{with} \quad S_{\alpha\beta} = \sum_{i=1}^{N} m_i^\alpha n_i^\beta$$

Which allows to write:

$$\begin{pmatrix} k_0 \\ k_1 \\ k_2 \\ k_3 \end{pmatrix} = M^{-1} \begin{pmatrix} S_{01} \\ S_{11} \\ S_{21} \\ S_{31} \end{pmatrix}$$

Then the number of background events is obtained by integrating the fitted function in the peak region $[m_{\text{peak low}}, m_{\text{peak up}}]$:

$$B^{\gamma} = k_0\delta^{(1)} + \frac{k_1}{2}\delta^{(2)} + \frac{k_2}{3}\delta^{(3)} + \frac{k_3}{4}\delta^{(4)} \quad \text{with} \quad \delta^{(i)} = m^i_{\text{peak up}} - m^i_{\text{peak low}}$$

Figure 3.4 shows two representative invariant mass plots for low probe E_{T} ($15 < E_{\mathrm{T}} < 20$ GeV) (left) and higher E_{T}($40 < E_{\mathrm{T}} < 45$ GeV). At low E_{T}, the contribution from the electrons with no associated track term to the signal is negligible as the corresponding term (dark blue line) is at the same level as the fit terms (dashed yellow lines). At higher E_{T} the no associated track term peaks around the Z mass above the estimated background from the sidebands fit. The difference corresponds to the signal (real) electron candidates that have no matched track.

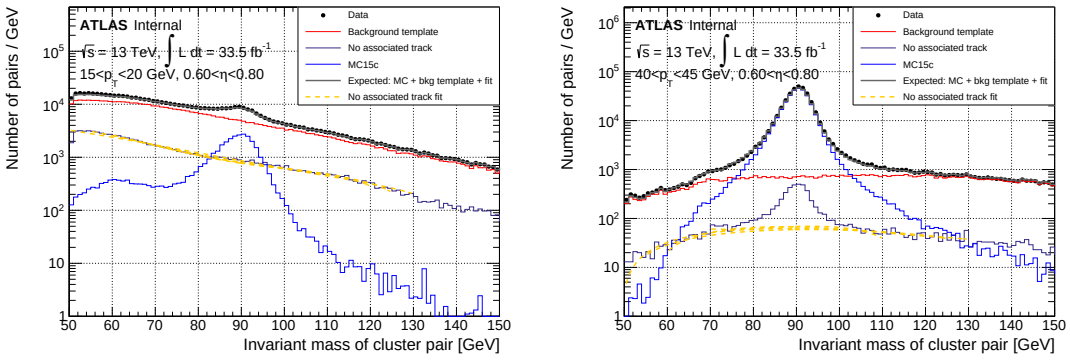

Figure 3.4 – Invariant mass distributions at denominator level for reconstructed and non-reconstructed (no matched track) electron candidates and the corresponding background estimation in representative bins at low E_{T}, $15 < E_{\mathrm{T}} < 20$ GeV (left), and high E_{T}, $40 < E_{\mathrm{T}} < 45$ GeV, for $0.6<\eta<0.8$. Photon background estimations (dashed yellow lines) are shown for the different fit ranges used as systematics.

3.3.2.3 Background level at denominator and numerator

Figure 3.5 displays the estimated fraction of background in the denominator and numerator of 3 different tag variations. The default selection indicates the *tight* tag variation. As expected, the level of background in the loose selection (*medium* and isolated tag variation) is higher than for the tight selection (*tight* and isolated tag variation). The level of background is very high in the low E_{T} re-

gion, approaching even 82% in some η bins in the denominator and 79% in the numerator. It decreases to 4-5% (14%) at medium (high) p_{T} in the denominator and the numerator.

The photon background and the background of the electron probes that fail the track quality (TQ) is estimated in the denominator only. The photon background dominates at low E_{T} and it can even reach 100 % at some η bins as seen in Figure 3.5 (bottom right). The fraction of background can even exceed 100 % in some bins for electron probes that fail the track quality (Figure 3.5 bottom left), effect caused by the overestimation of the background in low mass region (the template is normalized in the high mass region).

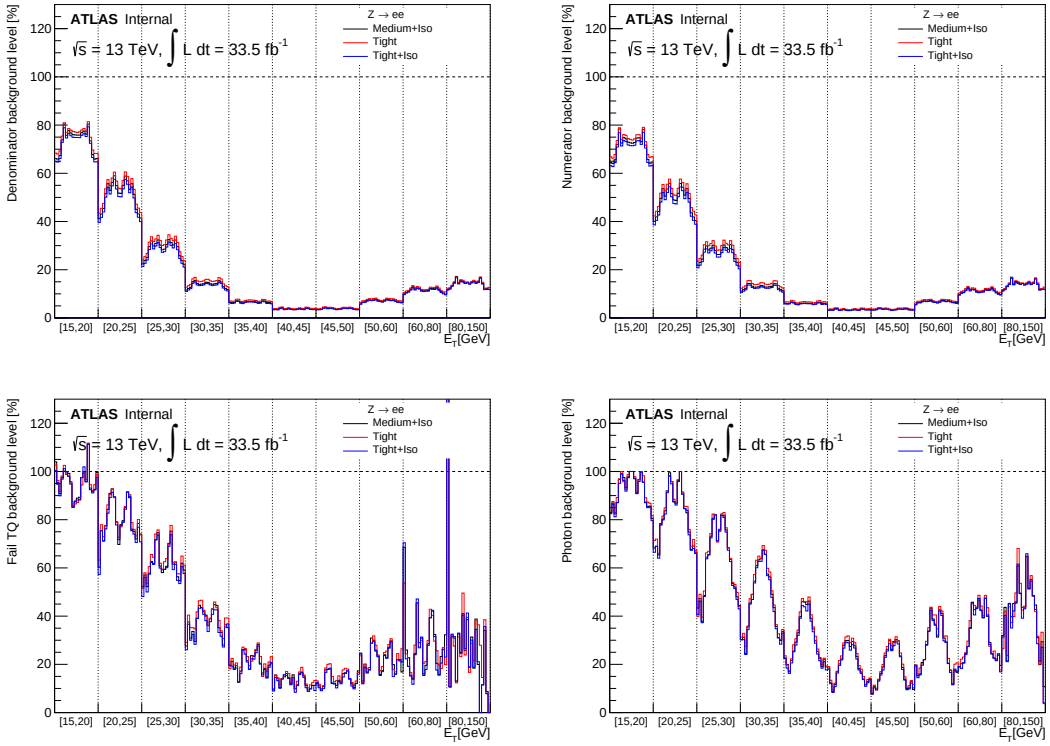

Figure 3.5 – Estimated background fraction (in %) for three tag ID: Medium+Iso, Tight and Tight+Iso in all 200 $E_{\mathrm{T}}\times\eta$ bins at denominator level (top left) and numerator level (top right), for probes that fail TQ (bottom left) and for photons (bottom right). The vertical lines separate the 10 E_{T} bins that include each the 20 η bins.

3.3.3 Uncertainties

Statistical uncertainty The statistical uncertainty is then given by error propagation formula:

$$\begin{aligned}\Delta\varepsilon^2 &= \frac{T_H^2\left(ST_H - TS_H\right)^2}{(\text{denom})^4}\left[U^2R_H^2\Delta U_H^2 + U_H^2\left(U_H^2\Delta R^2 + U_H^2\Delta\Gamma^2 + U^2\Delta R_H^2 + R_H^2\Delta U^2\right)\right] \\ &+\frac{U_H^2\left(RU_H - UR_H + \Gamma U_H\right)^2}{(\text{denom})^4}\left[T^2S_H^2\Delta T_H^2 + T_H^2\left(T_H^2\Delta S^2 + T^2\Delta S_H^2 + S_H^2\Delta T^2\right)\right]\end{aligned}$$

Where "denom" stands for the denominator of the right hand side of $\varepsilon_{\text{reco}}$. $\Delta\bullet$ is the Poisson uncertainty of the related variable $\bullet$. $\Delta\Gamma$ is more complex. Since $\Gamma = N^\gamma - B^\gamma$, $(\Delta\Gamma)^2 = (\Delta N^\gamma)^2 + (\Delta B^\gamma)^2$. ΔN^γ is the Poisson uncertainty on the number of non-reconstructed probes while ΔB^γ is the statistical uncertainty on the associated background estimate from the fit.

ΔB^γ is obtained by error propagation on the number of events in each bin used for the fit. It reads at leading order:

$$(\Delta B^\gamma)^2 = \sum_i \left(\frac{\partial B^\gamma}{\partial n_i}\right)^2 \left(\Delta n_i^{(\text{stat})}\right)^2$$

Where $\Delta n_i^{(\text{stat})}$ is the Poisson uncertainty on the number of events in the i^{th} bin.

Systematics Systematic uncertainties are strongly correlated. They are all estimated at the same time by applying variations on the selection procedure.

— Variations on the tag identification. Three different tag ID are chosen: *Tight*, *Tight* with $E_{\text{T}}^{\text{cone40}} < 5\,\text{GeV}$ and *Medium* with $E_{\text{T}}^{\text{cone40}} < 5\,\text{GeV}$. This allows to modify the amount and composition of background (proportion of events with a real isolated electron from W/Z+jets, and QCD events without any real electron).

— Variations on the Z-mass peak window:]80,100[,]75,105[and]70,110[GeV. Allows the variation of some identification criteria efficiencies depending on the invariant mass (low mass region rich in *bremsstrahlung* electrons)

— Two background template variations, described in Table 3.4, to change contamination signal proportions.

— Four sidebands variations for the fit of the photon background: $[70, 80] \cup [100, 110]$, $[60, 80] \cup [100, 120]$, $[50, 80] \cup [100, 130]$ and $[55, 70] \cup [110, 125]$ GeV to ensure the stability of the analytic form.

Applying all of those variations results in 72 efficiencies and scale factors. The final efficiency and statistical uncertainties are computed as the average of the systematic variations and the corresponding systematic uncertainty is the root mean square (RMS) value of the 72 values for the efficiency.

Template		Variation 1	Variation 2
Inverted cuts		Fails at least 2 *cut-based Loose* cuts	
Isolation requirements	$E_{\mathrm{T}} < 30$ GeV	$\frac{E_{\mathrm{T}}^{\mathrm{cone30}}}{E_{\mathrm{T}}} > 0.02$	$\frac{E_{\mathrm{T}}^{\mathrm{cone30}}}{E_{\mathrm{T}}} > 0.02$
	$E_{\mathrm{T}} \geq 30$ GeV	$\frac{E_{\mathrm{T}}^{\mathrm{cone40}}}{E_{\mathrm{T}}} > 0.05$	$\frac{E_{\mathrm{T}}^{\mathrm{cone40}}}{E_{\mathrm{T}}} > 0.20$
Control region	$E_{\mathrm{T}} < 30$ GeV	$120 < m_{ee} < 250\,\mathrm{GeV}$	$60 < m_{ee} < 70\,\mathrm{GeV}$
	$E_{\mathrm{T}} \geq 30$ GeV	$120 < m_{ee} < 250\,\mathrm{GeV}$	$120 < m_{ee} < 250\,\mathrm{GeV}$

Table 3.4 – Description of the templates used to estimate the background for electrons reconstructed with an associated track.

3.3.4 Efficiency and Scale Factors measurement

Results for the efficiency and scale factor measurements for 2015+2016 data are shown in 4 representative bins in figure 3.6. The efficiencies at low E_{T} vary between 96% to 99% with data efficiency being slightly higher than MC efficiency which leads to scale factor values slightly above 1, up by 2%. The uncertainty is systematics dominated and is at the percent level with some increase up to 2% in some individual $E_{\mathrm{T}} \times \eta$ bins. The main component of the systematic uncertainty is coming from the "photon" sidebands fit variations. At higher E_{T} the efficiencies increase and get flatter with E_{T}, reaching 99% in general. The scale factors are very close to 1, within per-mile level uncertainty.

An alternative way to show all the 200 values for the efficiencies, scale factors and their uncertainties is given in figure 3.7 for 2016 data alone. The SF are in general very close to one. The uncertainties, shared between statistics and systematics, are below 0.3% for electrons probes with E_{T} inside the [30,150] GeV interval. For the lowest E_{T} probes (<30 GeV), the SF uncertainty is higher, 0.3-2.1%. The systematic uncertainty dominates in low E_{T} bins (<30 GeV).

The measured electron reconstruction efficiencies are at the same level as the results from Run 1 (2012 results).

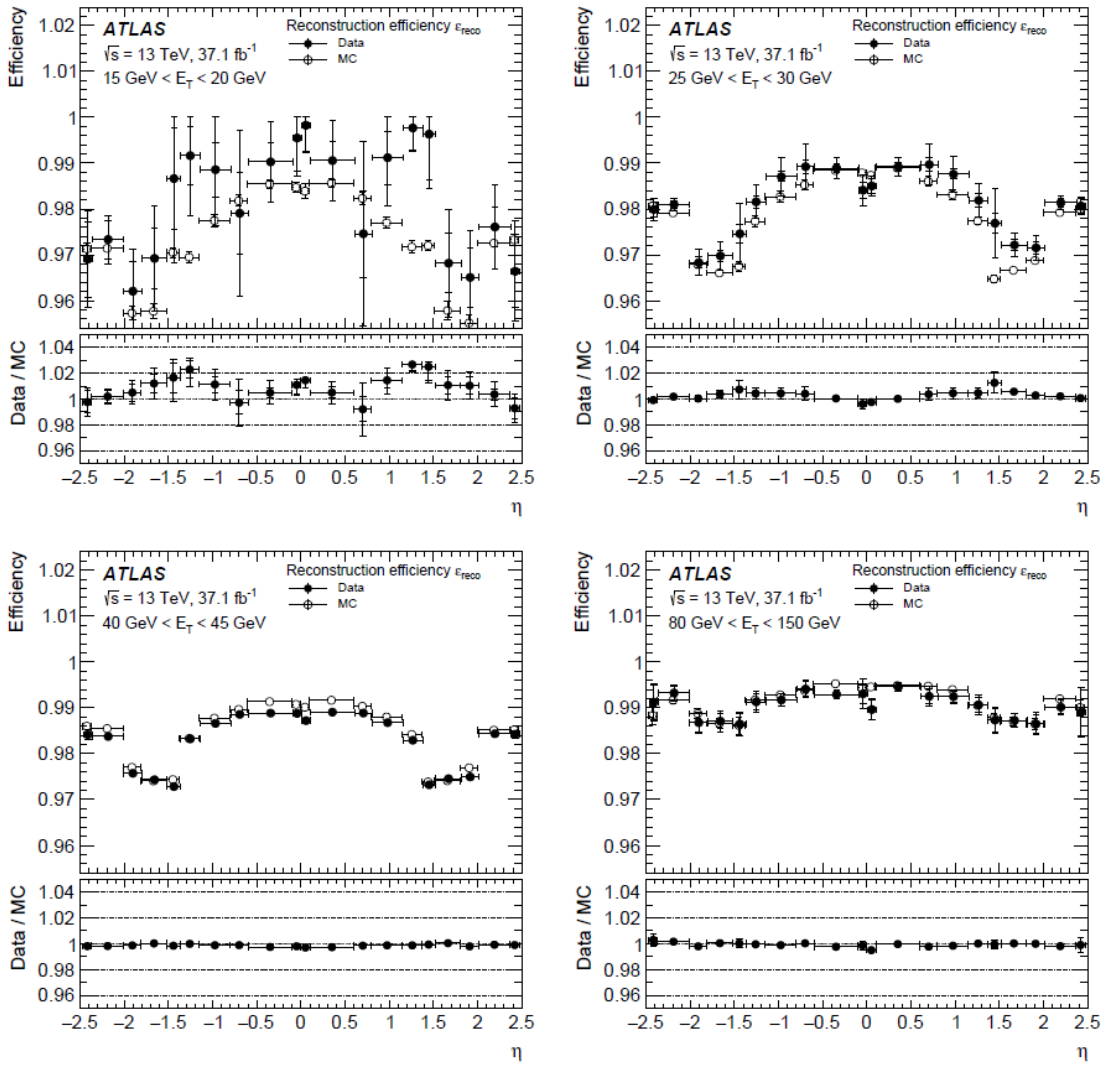

Figure 3.6 – Electron reconstruction efficiency in data (full circle) and for the MC simulations (empty circle) and their ratio for 4 representative E_{T} bins, 15 <η<20 GeV (top left), 25 <η<30 GeV (top right), 40 <η<45 GeV (bottom left), 80 <η<150 GeV (bottom right), for the combined 2015-2016 dataset. The inner error bars represent the statistical uncertainty while the full error bars include the statistical and the systematic uncertainty [43].

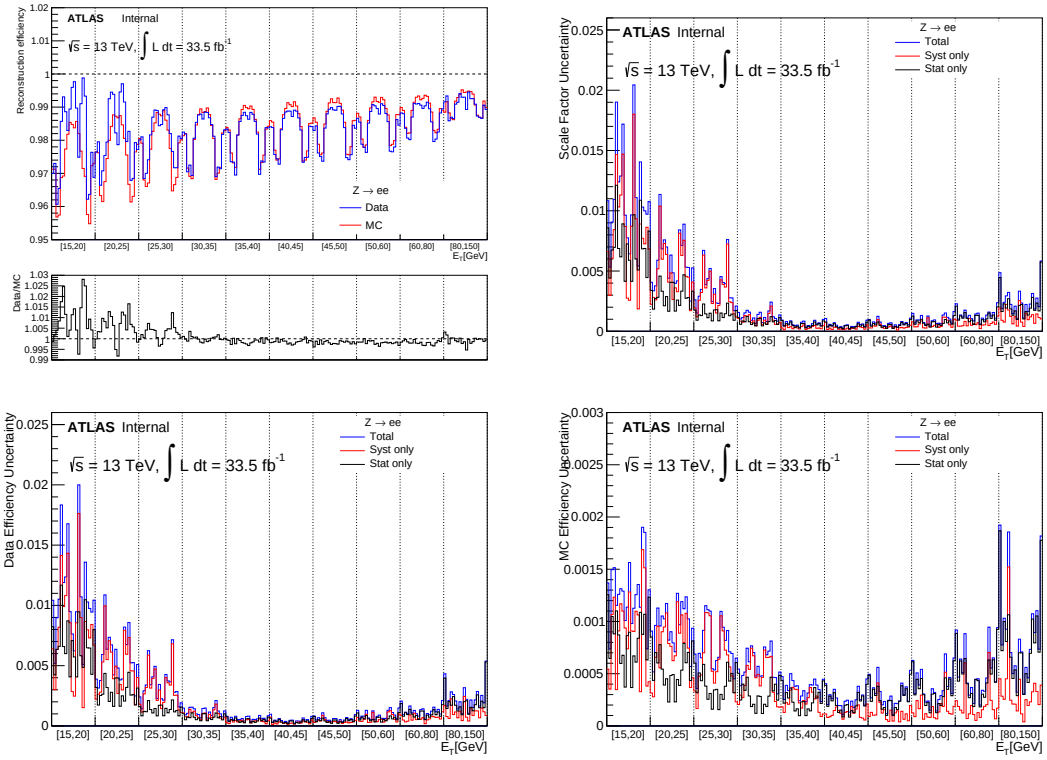

Figure 3.7 – Summary of measured efficiencies and scale factors (top left) for electron reconstruction efficiency as a function of E_{T} and η for $15 < E_{\mathrm{T}} < 150$ GeV for the 2016 datasets. Corresponding summary of uncertainties for data efficiency (bottom left), MC efficiency (bottom right) and scale factors (top right). The vertical lines separate the 10 E_{T} bins which include each the 20 η bins.

3.3.5 Results with new reconstruction and more statistics

For 2017 the main ATLAS software (Athena) was upgraded. A new electron reconstruction was implemented as described in section 2.3.2. The electron reconstruction efficiency was measured for the reprocessed 2015-2016 data as well as for the 2017 data.

A comparison of the efficiencies for 2016 data between different reconstruction software releases is given in figure 3.8. As can be noted, the data and the MC efficiencies experience a slight drop of around 2% in the transition region of the detector ($1.37<|\eta|<1.52$), in particular at low E_{T}, with the new reconstruction algorithm. However slightly better efficiencies are observed at higher E_{T} which cover almost the full η range. The scale factors have the same behavior at low E_{T} and they are slightly closer to 1 for the new release.

The uncertainties for the scale factors are compared in figure 3.9. Except the spikes in the transition region of the detector in the $15 < E_{\mathrm{T}} < 20$ GeV bin, the uncertainties are overall at the same level or marginally better.

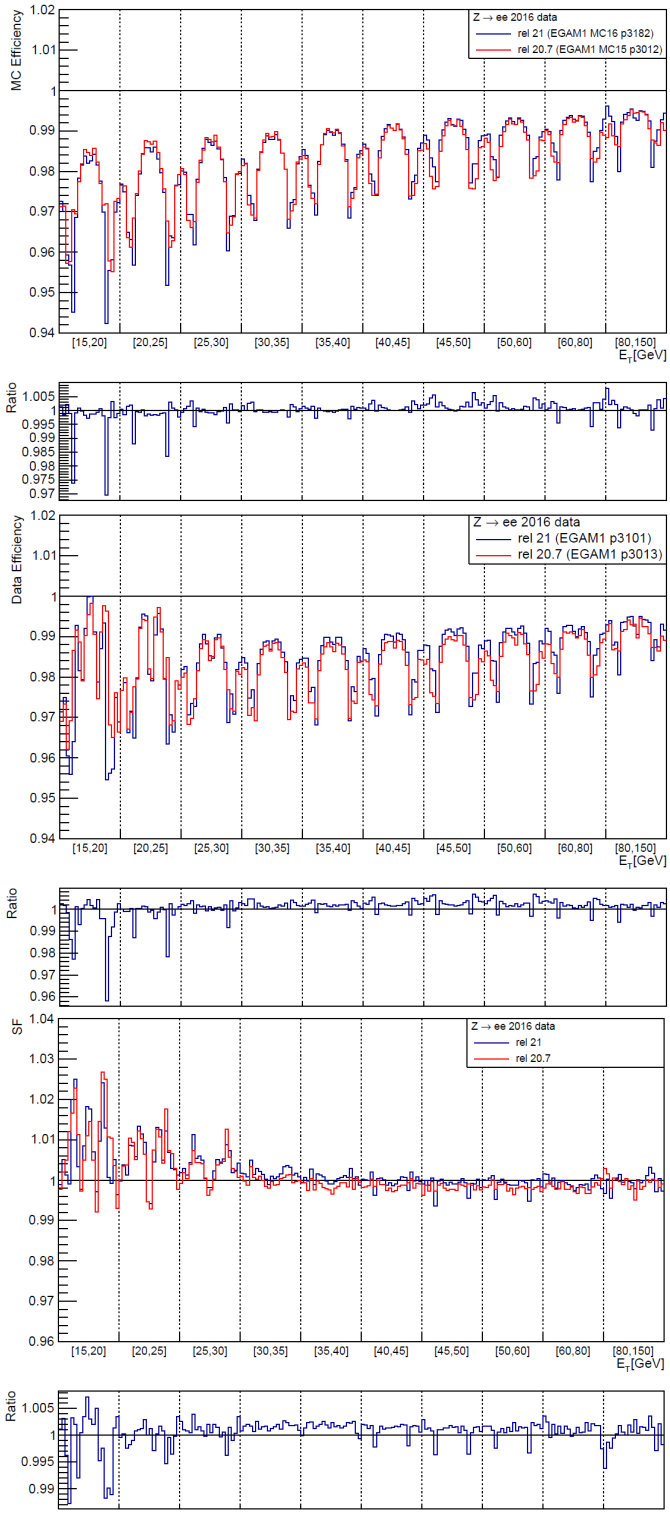

Figure 3.8 – Electron reconstruction data efficiencies (top), MC (middle) and scale factors (bottom) comparison between previous (red) and new reconstruction (blue).

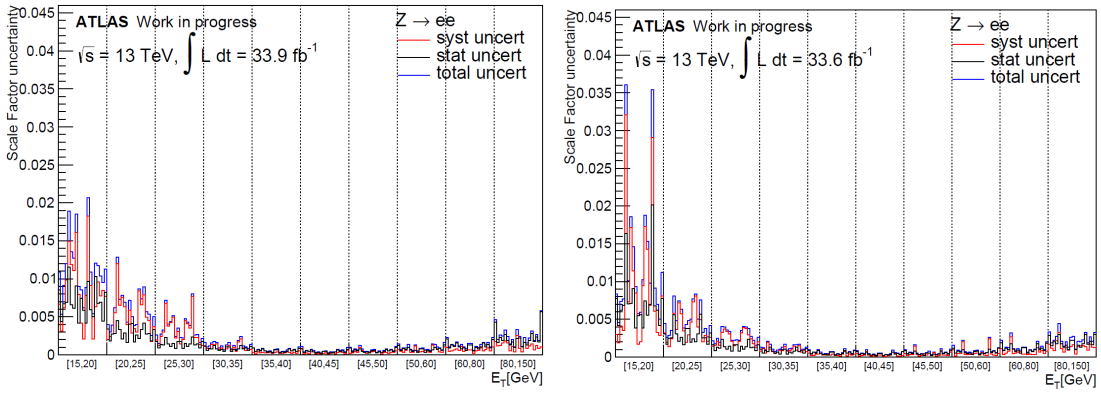

Figure 3.9 – Electron reconstruction scale factors uncertainty for 2016 data in previous (left) and new reconstruction (right).

For completion, results for the efficiency measurements for 2017 (available only in the new software release) are given in figure 3.10. These results are comparable with the 2015-2016 results and similar a conclusion can be drawn.

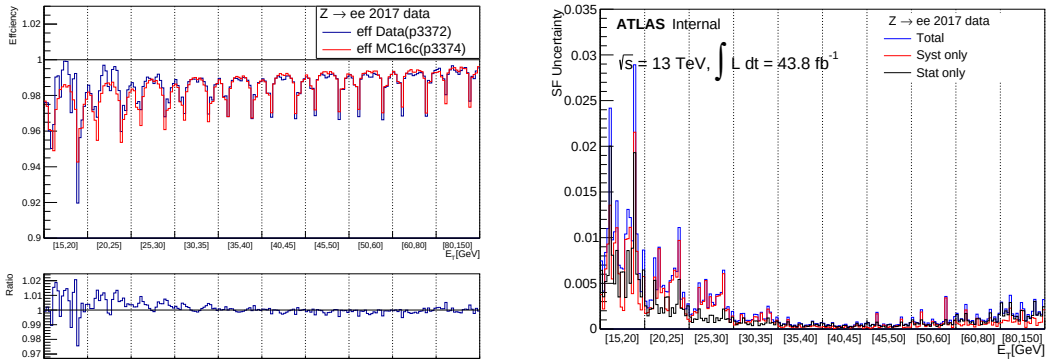

Figure 3.10 – Electron reconstruction efficiency and scale factor (left) and scale factors uncertainty (right) for 2017 data.

A comparison of the efficiencies and scale factors distribution as a function of the number of primary vertices is given in figure 3.11. An increase is observed in the efficiency which corresponds to the fact that at higher Nvtx the chance to have a EM cluster matched randomly by a track is higher. The scale factors are stable and are around 1 within the uncertainties which are well below 1% level. The larger Nvtx range for the 2017 results corresponds to higher pileup in 2017 than 2015 and 2016 (see figure 2.3).

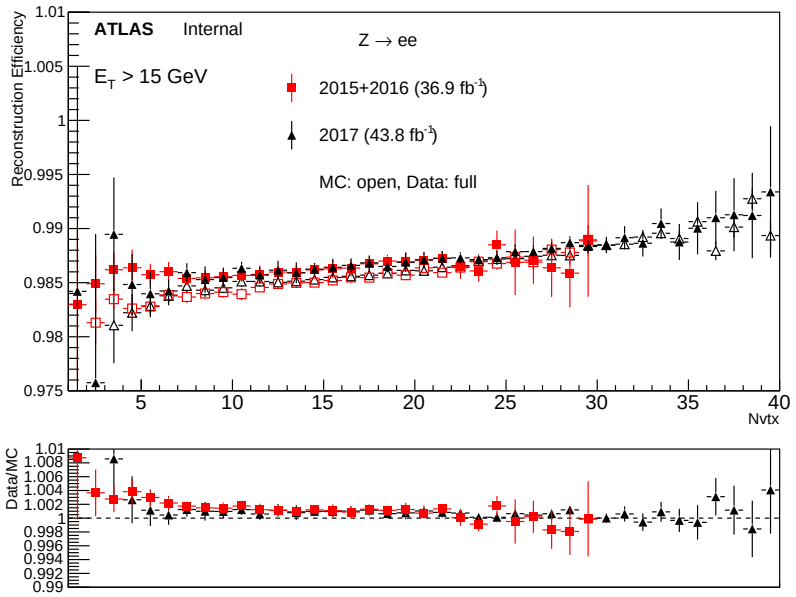

Figure 3.11 – Electron reconstruction efficiency and scale factor dependency on Nvtx.

3.4 Non-prompt electron tagger efficiency

The decays of W and Z bosons are commonly selected by the identification of one or two electrons or muons. The negligible lifetimes of these bosons mean that the leptons produced in the decay originate from the interaction vertex and are thus labeled “prompt". Analyses using these light leptons impose strict reconstruction quality, isolation and impact parameter requirements to remove non-prompt (“fake") leptons. A significant source of the fake light leptons are non-prompt leptons produced in decays of hadrons that contain bottom (b) or charm (c) quarks. Such hadrons typically have microscopically significant decay lengths that can be detected experimentally. A schematic picture defining prompt and non-prompt leptons is presented in Figure 3.12.

A lepton MVA has been developed to better reject non-prompt leptons than standard cut-based selections based on impact parameter, isolation and PID [64]. Such an algorithm represents basically a more sophisticated isolation and a corresponding prompt lepton efficiency measurement is necessary. The next section gives a brief overview of this algorithm, followed by the efficiency method description and the efficiency measurement results for electrons.

3.4.1 `PromptLeptonIso` tagger

The typical isolation cut-based selection may fail to reject the non-prompt leptons mainly because of two reasons. First, the lepton originating from a heavy

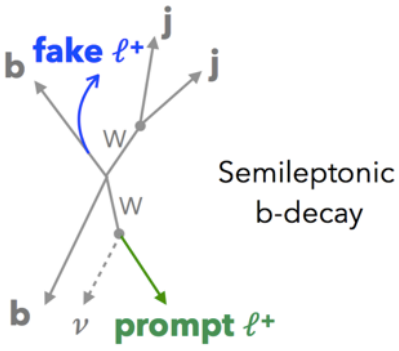

Figure 3.12 – Illustration of prompt and non-prompt (fake) leptons from heavy flavour decays, leading to a final state with two leptons of the same sign (2ℓSS).

flavor decay can have a significant energy fraction of the initial quark energy and in this case the remaining components of the jet would not be energetic enough (the lepton seems isolated because of the reduced activity in the immediate surrounding). Another possibility represents the case when the decay direction of the lepton is further away from the rest of the jet components and it does not fit inside the isolation variable cone. One solution can be to use the nearest track jet (jet reconstructed from tracks) from the selected lepton to test whether they are together compatible with a b or c jet. Additionally, using a track jet increases the probability of associating a lepton (its track) to a jet (99% of the cases) and the larger cone of the track jets than the isolation ones allows to catch potential high p_T tracks at larger angles that would be missed otherwise. This is illustrated in figure 3.13.

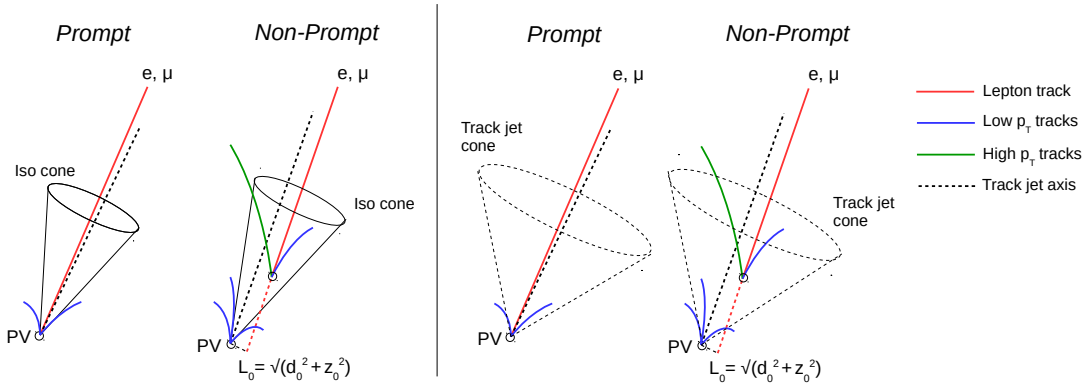

Figure 3.13 – Illustration of prompt and non-prompt leptons in case of isolation selections (left) and in the context of track jets (right). d_0 and z_0 refer to longitudinal and transverse impact parameters with L_0 being the displacement of the secondary vertex.

The main idea of the algorithm is to identify non-prompt light leptons using

lifetime information associated with a track jet that matches the selected light lepton. This lifetime information is computed using tracks contained within the jet. Typically, lepton lifetime is determined using the impact parameter of the track reconstructed by the inner tracking detector which is matched to the reconstructed lepton. Using additional reconstructed charged particle tracks increases the precision of identifying the displaced decay vertex of bottom or charm hadrons that produce a non-prompt light lepton. The MVA also includes information related to the isolation of the lepton to reject non-prompt leptons. Figure 3.14 summarizes the steps of the algorithm in a diagram.

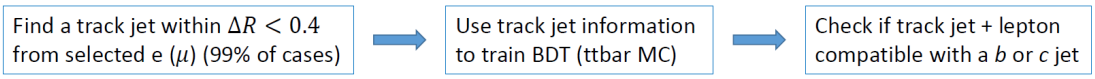

Figure 3.14 – Illustration of the variables used in the `PromptLeptonVeto`.

The algorithm, referred to as `PromptLeptonIso` (PLI), is a gradient Boosted Decision Tree (BDT). The training of the BDT is performed on leptons selected from a POWHEG+PYTHIA6 $t\bar{t}$ sample (excluding fully hadronic final states). Eight variables are used to train the BDT in order to discriminate between prompt and non-prompt leptons. The track jets that are matched to the non-prompt leptons correspond to jets initiated by b or c quarks, and may contain a displaced vertex. Consequently, three of the selected variables are used to identify b-tag jets by ATLAS flavour tagging algorithms (see section 2.3.5.2), namely IP2D $\log(P_b/P_{\text{light}})$, IP3D $\log(P_b/P_{\text{light}})$ and N_{TrkAtVtx} SV + JF. Two variables use the relationship between the track jet and lepton: the ratio of the track lepton p_T with respect to the track jet p_T and ΔR between the lepton and the track jet axis. Finally three additional variables test whether the reconstructed lepton is isolated: the number of tracks collected by the track jet and the lepton track and calorimeter isolation variables. A summary of the variables used in the training are listed in table 3.5. Example of the distribution for prompt and non-prompt electrons in a $t\bar{t}$ sample is shown in figure 3.15 for two of the eight variables.

Variable	Description
IP2 $\log(P_b/P_{\text{light}})$	Log-likelihood ratio between the b and light jet hypotheses with the IP2D algorithm
IP3 $\log(P_b/P_{\text{light}})$	Log-likelihood ratio between the b and light jet hypotheses with the IP3D algorithm
N_{TrkAtVtx} SV + JF	Number of tracks used in the secondary vertex found by the SV1 algorithm
N_{track} in track jet	Number of tracks collected by the track jet
p_T^{rel}	lepton p_T projected on the track jet direction
$\Delta R(\text{lepton}, \text{track jet})$	ΔR between the lepton and the track jet axis
$p_T\text{VarCone30}/p_T$	Lepton track isolation, with track collecting radius of $\Delta R < 0.3$
$E_T\text{TopoCone30}/p_T$	Lepton calorimeter isolation, with topological cluster collecting radius of $\Delta R < 0.3$

Table 3.5 – Table of the variables used in the training of `PromptLeptonIso`.

The information in the prompt and non-prompt distributions from the input variables are combined in a final, single score for each lepton which quantifies

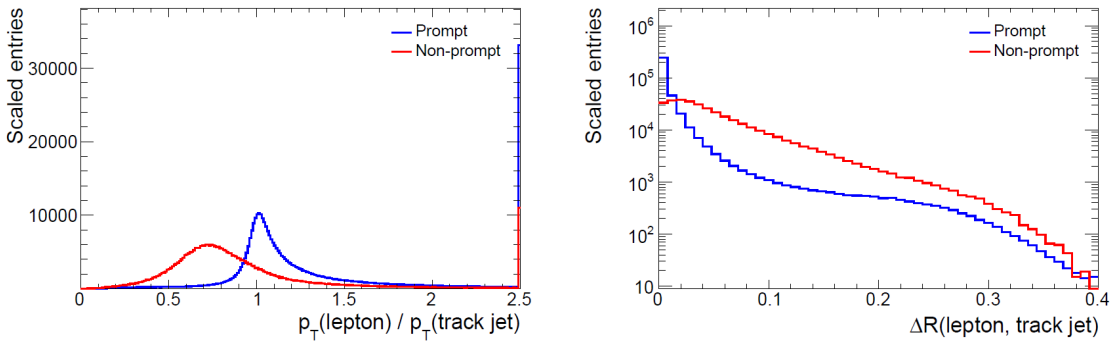

Figure 3.15 – Example of input variables used in the training of PLI for electrons in $t\bar{t}$ events, p_T^{rel} (left) and $\Delta R(\text{lepton}, \text{track jet})$ (right). Prompt electron distribution (blue) is scaled to the non-prompt electron distribution [64].

the likelihood of the lepton to be prompt or non-prompt. By convention, the score varies from -1 to +1, with -1 representing prompt leptons and +1 non-prompt. The distribution for the electrons PLI weight (score) is shown in figure 3.16 (left). The leptons that are not associated to any track jets are considered as prompt.

The PLI performance in terms of non-prompt rejection as a function of prompt efficiency for electrons can be seen in Figure 3.16 (right). It can be seen that the FixedCutTight isolation working point underperforms compared to any working point from the PLI MVA. For a prompt efficiency of 90% the *FixedCutTight* isolation working point has a rejection factor of roughly 3 times smaller than PLI for electrons.

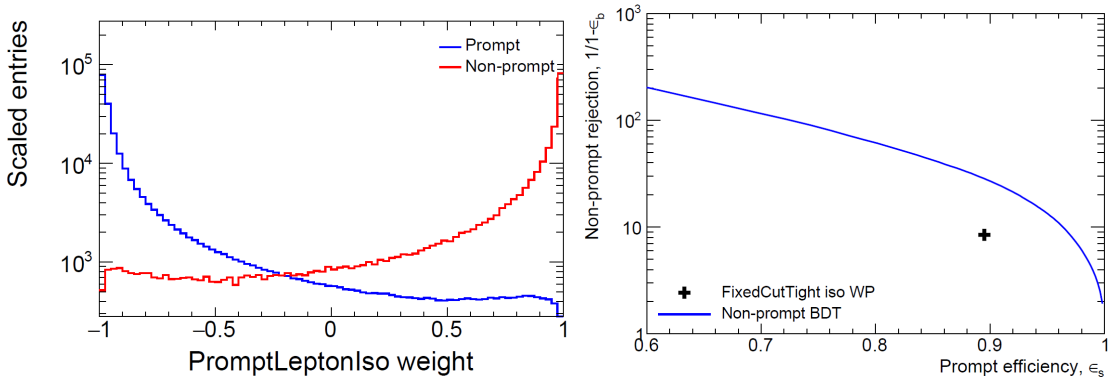

Figure 3.16 – ROC curves `PromptLeptonIso`, as well as the performance of FixedCutTight working point, for electrons in $t\bar{t}$ events [64].

The data modeling for two representative input variables and for the PLI score distribution is shown in the validation plots in figure 3.17. The validation is performed in a $t\bar{t}$ control region (CR) requiring two leptons of the same sign with 2-3 jets with at least one of them being a b-jet. A good overall agreement

between simulations and data is observed within the uncertainties. It is interesting to note that the leading (higher p_T) electrons are mostly prompt while the sub-leading ones are mostly non-prompt.

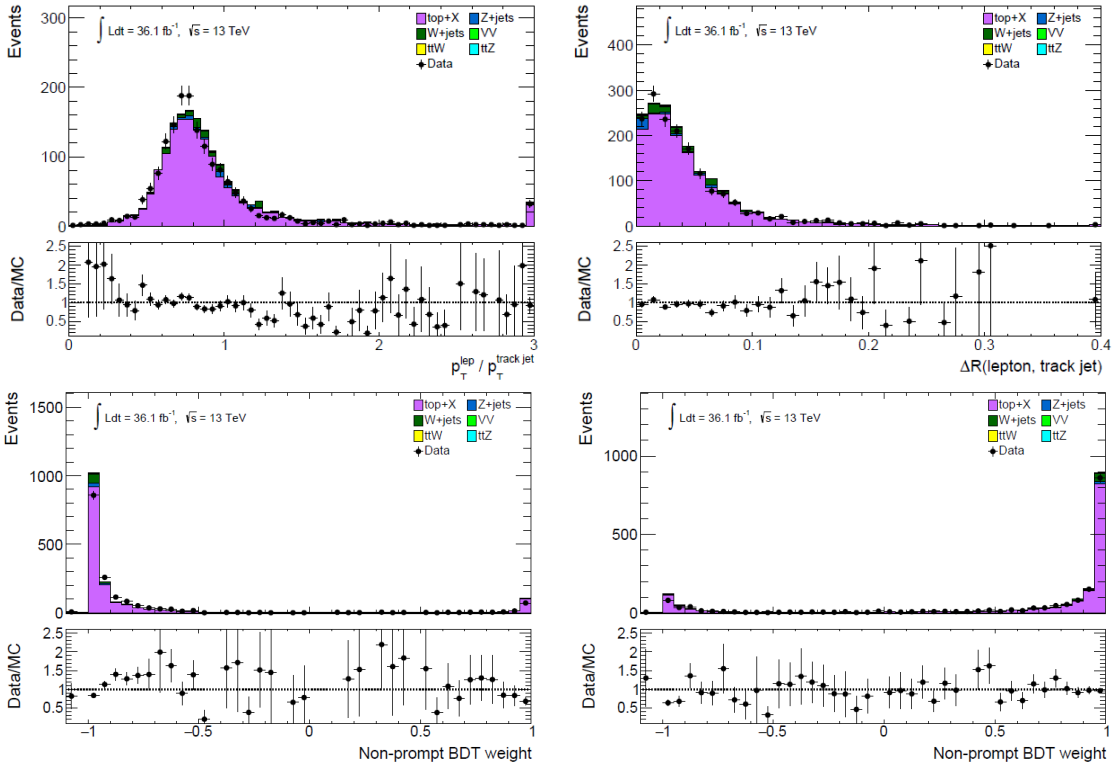

Figure 3.17 – Modeling of two PLI input variables (top) and modeling of the PLI output for leading electron (bottom left) and the subleading electron (bottom right) in 2 same-sign electrons $t\bar{t}$ control region with 36.1 fb^{-1} of $\sqrt{s}$ =13 TeV data [64]. BDT scores smaller than -1 correspond to electrons with no associated track jet.

3.4.2 Charge flip tagger

A relevant background for the dilepton same-sign analyses is the electron charge flips (rates for muon charge flips are negligible). This background results from opposite sign dilepton events when one electron has a wrongly assigned electric charge. This can result either from a mis-measurement of the track curvature (higher p_T or η results in a smaller curvature) or from assigning a wrong track to the electron candidate. The source of most of the wrong track assignment is the trident processes $e^{\pm} \rightarrow e^{\pm}\gamma \rightarrow e \pm ee$ (bremsstrahlung followed by pair production). These processes are more probable at higher η (>1.5) where more material is present (figure 3.18 right).

In order to reduce this type of background a dedicated MVA was developed [43], referred to as the Charge Flip Tagger (CFT). It relies on a BDT using eight

electron variables to distinguish and reduce the numbers of electrons that are reconstructed with a wrong charge. The input variables and their definitions are listed in Table 3.6. They cover the quality of the chosen primary electron track, combined tracking and calorimeter quantities (E/p) and shower shape in the EM calorimeter (a narrower cluster is expected for electrons that do not undergo bremsstrahlung). Figure 3.18 show the distribution for correct/wrong track and charge of the electron for two of the eight input variables, E/p (left) and η (right). This BDT was designed to have a baseline performance of a factor 14 background rejection for a 95% signal efficiency, which corresponds to a charge misID BDT score of 0.0670415 in the latest version using Tight electrons.

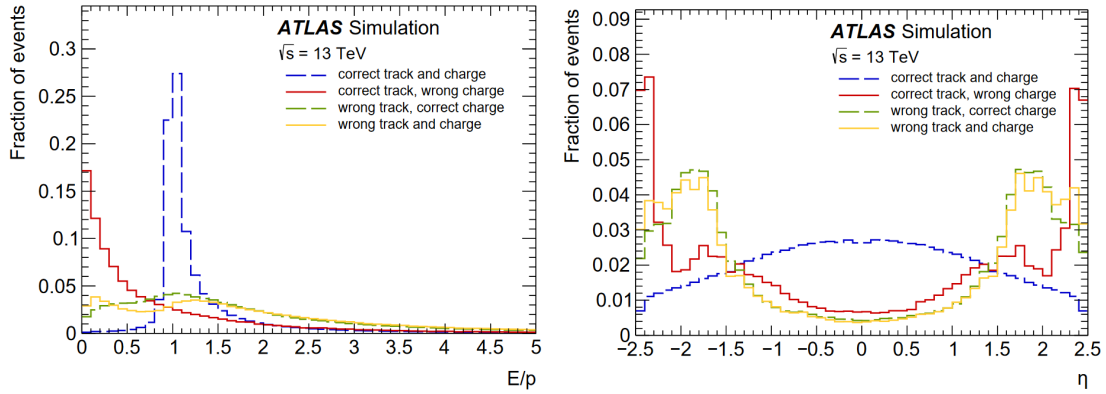

Figure 3.18 – Properties of electrons in a $Z \to ee$ sample used as input variables in the CFT MVA [43].

The selection on this MVA will be used jointly with the non-prompt lepton tagger for the efficiency measurement.

Variable	Description
p_T	Transverse momentum
η	Pseudo-rapidity
charge$\times d_0$	Electric charge times the transverse impact parameter
E/p	Ratio of the cluster energy to the track momentum
R_ϕ	Ratio of the energy in 3×3 cells over the energy in 3×7 cells centred at the electron cluster position
$\Delta\phi_1$	$\Delta\phi$ between the cluster position in the strip layer and the extrapolated track
$\Delta\phi_{rescaled}$	$\Delta\phi$ between the cluster position in the middle layer and the extrapolated track, where the track momentum is rescaled to the cluster energy before extrapolating the track to the middle layer
$\frac{q/p}{\sigma_{q/p}}$	Significance of the curvature of the track defined as the ratio of the reconstructed charge to the track momentum

Table 3.6 – Table of the variables used in the training of the electron charge misID BDT (CFT).

3.4.3 Efficiency definition

The need to measure the efficiency of PLI based working point comes from the analyses that suffer from large non-prompt lepton backgrounds like top FCNC

(see Chapter 4) and ttHML (see Chapter 5). The non-prompt lepton algorithms provide in essence just a more sophisticated isolation with regard to the efficiency definition

$$\varepsilon_{\text{PLI}} = \frac{N_{\text{PLI}}}{N_{\text{id}}} \tag{3.3}$$

The isolation efficiency denominator requires the electron candidates to pass $Tight$ identification. At the numerator level, the requirements for the `PromptLeptonIso` measurements are defined as follows:

— Pass $Tight$ identification (denominator requirement)
— `PromptLeptonIso` weight < -0.5
— `CFT` weight > 0.0670415
— pass $loose$ isolation (to ensure safety net)

The selection on PLI and CFT come from an optimization procedure performed in the ttHML analysis. The requirement on the $loose$ isolation (minimum isolation requirement) serves as a safety net for the unlikely case that non-prompt isolated lepton would pass PLI selection. For convenience, the working point involving all the selections is noted as WP2. The working point with all the selection except the selection on CFT is noted as WP1 and is necessary to understand the impact of the CFT. In virtue of the total efficiency equation (3.2) then, altering the isolation term leads to the necessity of also measuring the trigger efficiency for the newly defined isolation working points

$$\varepsilon_{\text{trig}} = \frac{N_{\text{trig}}}{N_{\text{PLI}}} \tag{3.4}$$

to have full set of efficiencies.

3.4.3.1 Background estimation

Unlike the case of the electron reconstruction, the level of background is much lower for the isolation efficiency. The background is estimated using templates and the same procedure is used to estimate the numerator and denominator. The background templates are built from opposite sign invariant mass and their full definitions are given in table 3.7. The template is normalized to the number of same-sign events passing the ID requirement in the tail. This is because the opposite-sign distribution has much more signal in the tails than the same sign one. Instead of attempting to estimate and subtract the signal in the opposite-sign tails, the same-sign tail is used for normalization, and assumed to have negligible contribution from signal. The background estimate is then:

$$N_{\text{bkg}}^{\text{Num}}|_{\text{peak}} = N^{\text{template}}|_{\text{peak}} \times \left.\frac{N_{\text{SS}}^{\text{Num}}}{N^{\text{template}}}\right|_{\text{tail}}$$

	< 30 GeV	> 30 GeV
Variation 1	os,!2*multilepton*, EtCone30/E_{T}>0.02 Normalize High-m_{ee} (120-250 GeV)	os,!2*loose* cut-based, EtCone40/E_{T}>0.05 Normalize High-m_{ee} (120-250 GeV)
Variation 2	os,!*multilepton*, EtCone30/E_{T}>0.02 Normalize Low-m_{ee} (60-70 GeV)	os,!2*loose* cut-based, EtCone40/E_{T}>0.20 Normalize High-m_{ee} (120-250 GeV)

Table 3.7 – Templates and normalizations used in the different E_{T} ranges. In the region $30 < E_{\mathrm{T}} < 45$ GeV the two-normalization-region and the two-template systematic scheme was found to yield equivalent results in Run 1. Above 45 GeV a lack of statistics was observed for the low m_{ee} tail, so the low m_{ee} normalization is only used in the low E_{T} range. "os" refers to opposite-sign, !2 refers to fail at least 2 cut-based selection for the legacy *multilepton* or *loose* electron ID operating points.

3.4.3.2 Systematic uncertainties

The systematic uncertainties are derived as described in section 3.3.3. The same *tag* ID and Z mass windows variations are used. The only differences are related to the background estimation variations. As in the case of electron reconstruction efficiency background estimations for electron candidates with associated track, two template variations are used however they are defined as shown in table 3.7. Additional, no sideband fit variations are performed as the electron candidates with no associated track are not involved in the non-prompt electron efficiency measurement. In conclusion, there are 18 (3x3x2) systematic variations used to derive the systematic uncertainty.

3.4.4 `PromptLeptonIso` results

Data efficiency and MC simulation efficiencies were performed using 2015-2016 datasets.The data efficiency measurements are then compared to the simulation ones to obtain corrections (scale factors, SF) as a function of E_{T} and η of the electron. These SF 2D maps $\eta \times E_{\mathrm{T}}$ are later used in analyses to correct the simulation efficiency to the data efficiency. In particular, the results for WP2 selections are used in the top FCNC and ttHML analyses.

A total set of 8 $\eta \times E_{\mathrm{T}}$ maps of SF are computed.

— 2 with 2015 and 2016 data for $\mathrm{SF}_{\texttt{PromptLeptonIso}}$;

— 3 with 2015 data (3.2 fb^{-1}) for $\mathrm{SF}_{\mathrm{trigger}}$:

  — logical 'OR' of 3 single lepton triggers (e24_lhmedium_L1EM20VH or e60_lhmedium or e120_lhloose)

  — di-electron trigger (2e12_lhloose_L12EM10VH)

  — multi-lepton trigger e-mu (only electron leg e17_lhloose);

— 3 with 2016 data for $\mathrm{SF}_{\mathrm{trigger}}$:

  — logical 'or' of 3 single lepton triggers (e26_lhtight_nod0_ivarloose or e60_lhmedium_nod0 or e140_lhloose_nod0)

  — di-electron trigger (2e17_lhvloose_nod0)

— multi-lepton trigger e-mu (only electron leg e17_lhloose_nod0);

Figure 3.19 (up) shows the efficiencies and $SF_{\texttt{PromptLeptonIso}}$ values as a function of η in two representative E_T bins.

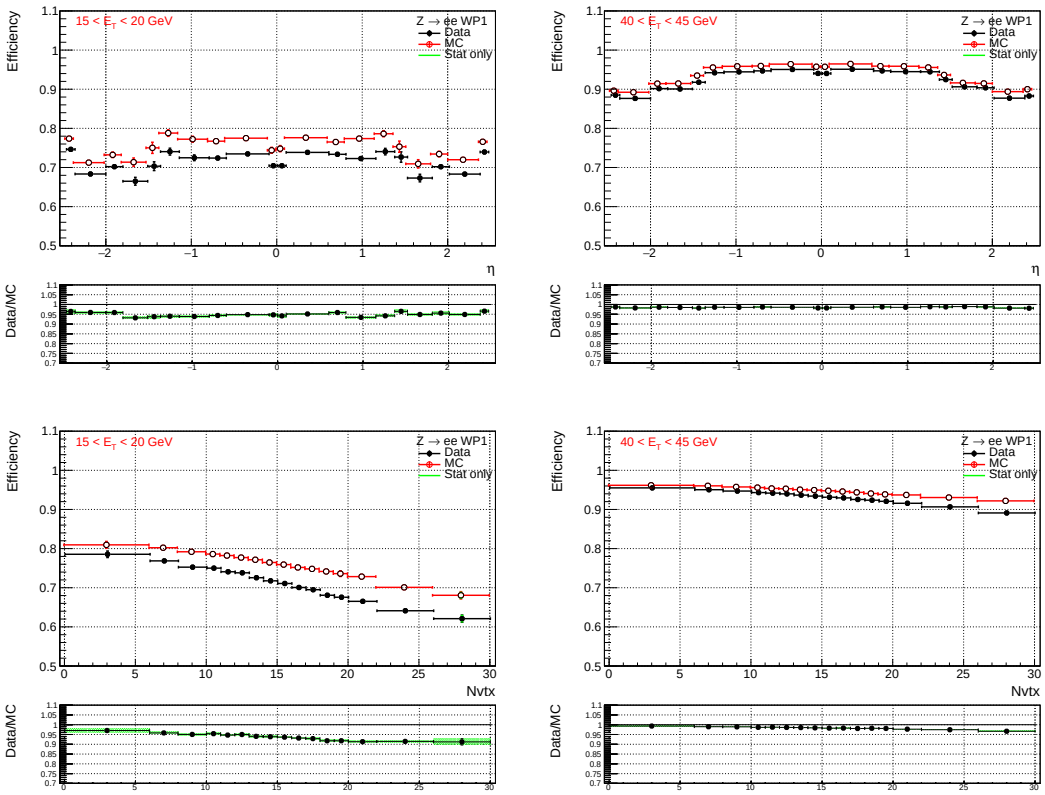

Figure 3.19 – Typical `PromptLeptonIso` efficiency values for two p_T bins : $15 < p_T < 20$ GeV (left) and $40 < p_T < 45$ GeV (right) versus η (top) and versus Number of primary vertices Nvtx (bottom).

Figure 3.20 left shows $SF_{\texttt{PromptLeptonIso}}$ variation as a function of all E_T bins for WP1 (up) and WP2 (down). Inside each E_T bin, 20 bins in η are shown. A smooth variation is observed as a function of E_T from 0.9 to 0.98 for WP1. A similar trend is observed for WP2, with the drop observed at high $|\eta|$ coming from inappropriate modeling of the material in front of the calorimeter that increases the charge flip rates (WP2 = WP1 + CFT cut). Figure 3.20 right shows SF statistical and systematic uncertainties for WP1 (up) and WP2 (down). Uncertainties are dominated by statistical uncertainties and amounts to 2% at low E_T and decrease to 0.8% at high E_T for the central value of η (blue line). The variation of SFs as a function of the number of vertices (Nvtx), number of jets, $\Delta R(\text{probe}, \text{jet})$ and $\Delta R(\text{probe}, \text{b} - \text{jet})$ was studied. The only significant variation is observed as a function of the number of vertices, as shown in Figure 3.19 (down). A specific

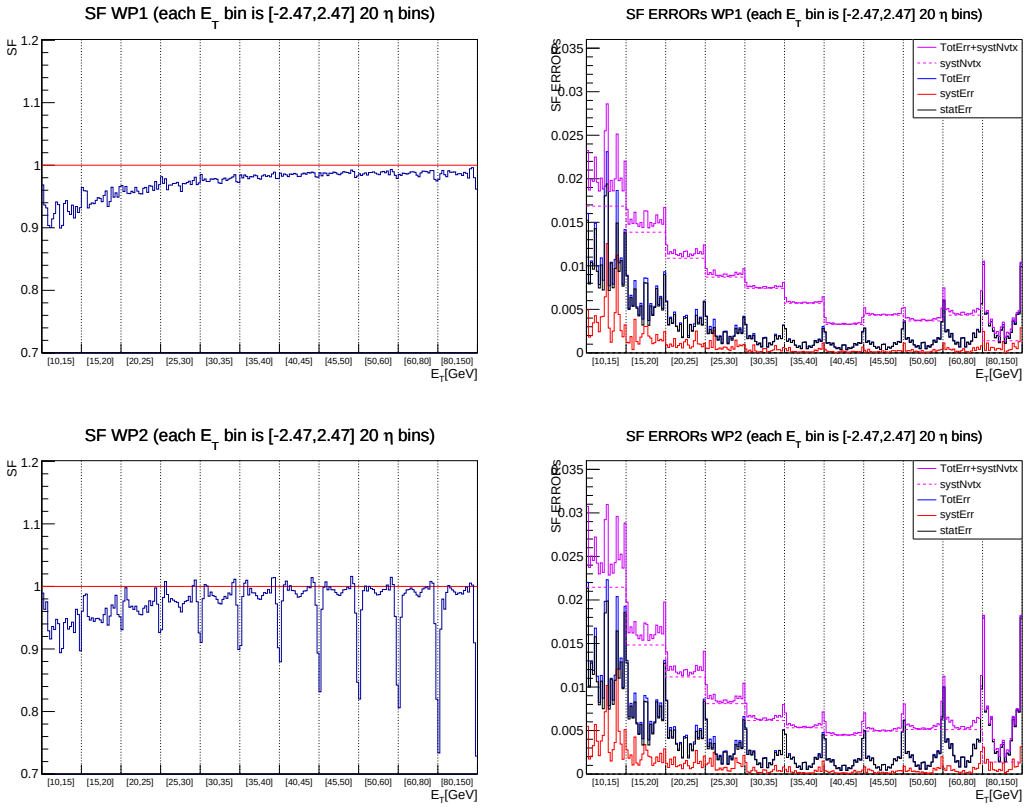

Figure 3.20 – `PromptLeptonIso` scale factor values (left) and associated statistic / systematic uncertainties (right) for WP1 (up) and WP2 (down).

systematics is therefore associated per each E_{T} bin, which amounts to about 2 (0.5)% at low (high) E_{T}. It was derived from the RMS error of the SF distribution for each E_{T} bin. It is added in quadrature with the uncertainties shown in Figure 3.20 right (purple line) to give the total uncertainty.

Figure 3.21 shows a summary plot of the efficiencies and SF for WP2, integrated over η, for the merged 2015-2016 datasets.

Single lepton trigger scale factor values are shown in Figure 3.22 (top left) as well as their associated uncertainties on Figure 3.22 (top right) for WP2. Similarly, Figure 3.22 (bottom) shows the trigger scale factor values (bottom left) and uncertainties (bottom right) for the dilepton trigger. All SF are very close to 1 except for the low E_{T} and high η bin. The uncertainties are generally below 1% and are dominated by statistical component.

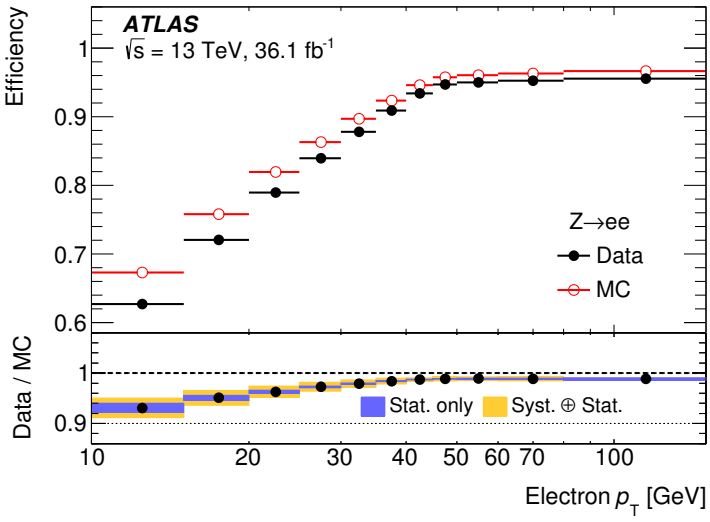

Figure 3.21 – PLI scale factor values statistic / systematic uncertainties (right) WP2 (down) [65].

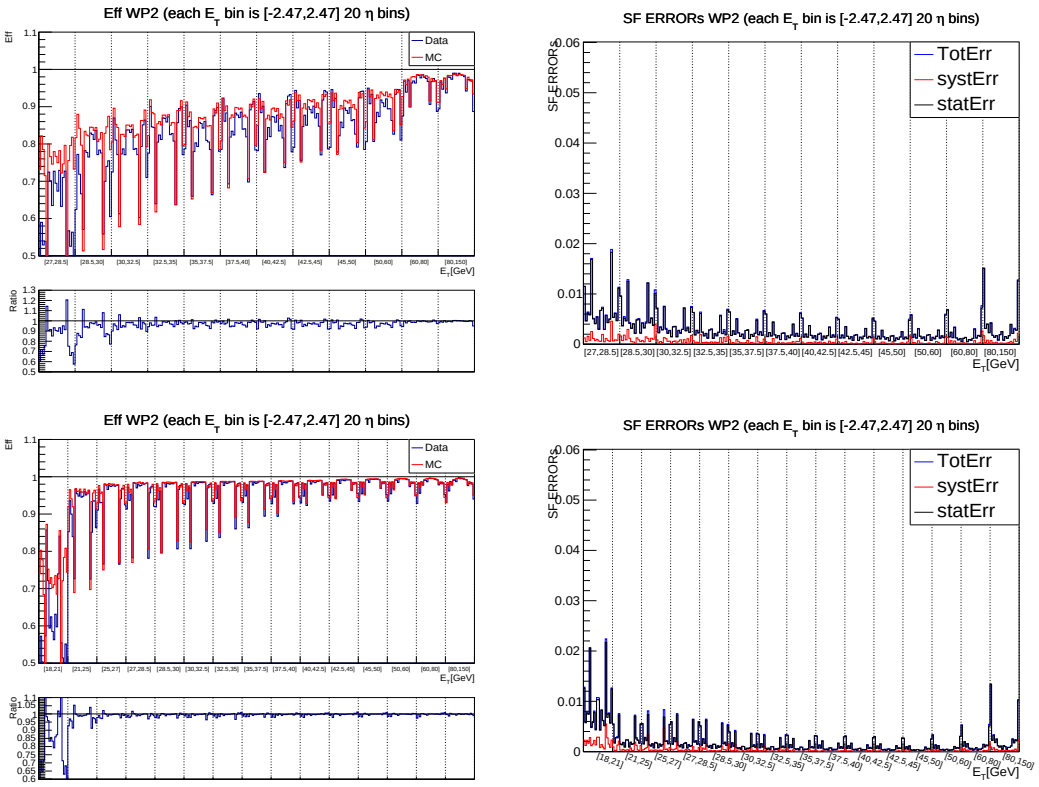

Figure 3.22 – Single lepton (top) and dilepton (bottom) trigger scale factor values (left) and associated statistic / systematic uncertainties (right) WP2 using 2016 dataset.

3.4.5 `PromptLeptonVeto` tagger

The `PromptLeptonVeto` (PLV) represents an updated version of the non-prompt lepton tagger. The main difference consists in the input variables used for PLV. It also uses eight variables, with four variables remaining the same (number of tracks in the track jet, angular distance between the lepton and the jet and the lepton isolation variables). Variables that changed are related to the flavor tagging group, replacing the impact parameter based variables and the secondary vertex fit variable with new, more advanced variables based on recurrent neural networks (rnnip [3]) and deep learning (DL1mu [4]). Table 3.8 shows the change in the list variables.

Variable	PromptLeptonIso	PromptLeptonVeto
N_{track} *in track jet*	✓	✓
sv1_jf_ntrkv	✓	✗
$IP2log(P_b/P_{light})$	✓	✗
$IP3log(P_b/P_{light})$	✓	✗
$p_T(lepton)/p_T(track\ jet)$	✓	✗
$\Delta R(lepton, track\ jet)$	✓	✓
$\Sigma E_T(\Delta R < 0.3)/p_T$	✓	✓
$\Sigma p_T(\Delta R < 0.3)/p_T$	✓	✓
rnnip	✗	✓
DL1mu	✗	✓
p_T^{rel}	✗	✓
Track $p_T(lepton)/p_T(track\ jet)$	✗	✓

Table 3.8 – Comparison of the input variables included in the `PromptLeptonIso` and `PromptLeptonVeto` MVAs. 'x' means the variable is not used.

3.4.5.1 PLV efficiency and associated uncertainties

The PLV was designed after a major ATLAS software upgrade and was trained on new $t\bar{t}$ POWHEG+PYTHIA8 sample. For fair comparison, the PLI was also trained with this new sample. The final BDT discriminants for `PromptLeptonIso` and `PromptLeptonVeto` are presented in Figure 3.23. The fact that the prompt and non-prompt distributions for PLV are better separated (overlap area 0.115 vs 0.137) indicates better performance for PLV. The PLV was the chosen algorithm for the new iteration of the ttHML analysis based on 2015-2017 dataset (80 fb^{-1}) (see Chapter 5). An optimization was performed for the working point which enters at the numerator level in the efficiency definition. The requirements for the `PromptLeptonVeto` based efficiency measurements are defined as follows:

— Pass $Tight$ identification (denominator requirement)

3. Recurrent Neural Network with additional impact parameter information of tracks inside the track-jet

4. DL1 (deep learning tagger) extended with Soft Muon Tagging information

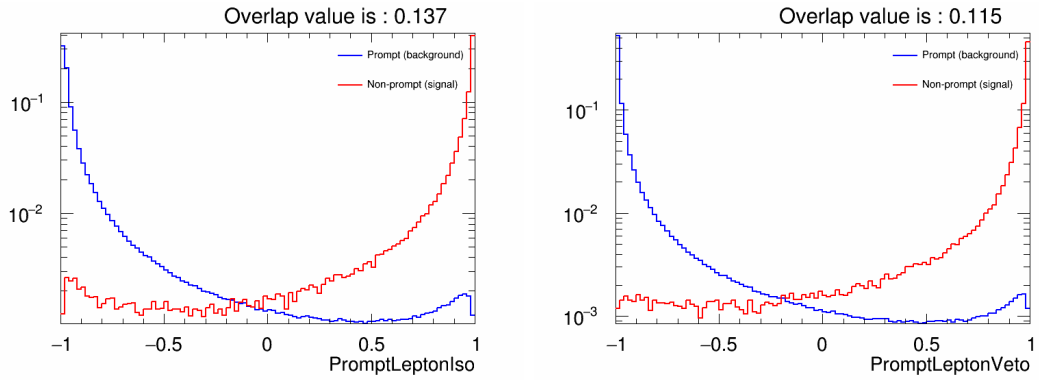

Figure 3.23 – Final BDT discriminant for the `PromptLeptonIso` (left) and `PromptLeptonVeto` (right) for electrons in $t\bar{t}$ events.

— `PromptLeptonVeto` weight < -0.7
— `CFT` weight > 0.7
— pass *loose* isolation (to ensure a safety net for the unlikely case that non-prompt isolated lepton would not pass `PromptLeptonVeto` selection)
— pass ambiguity selection (aimed at reducing photon conversions) [5]

The CFT was kept unchanged, except for a new cut value.

The efficiency and the SFs are computed for the working point specified above and for simplicity this WP is referred to as WP3.

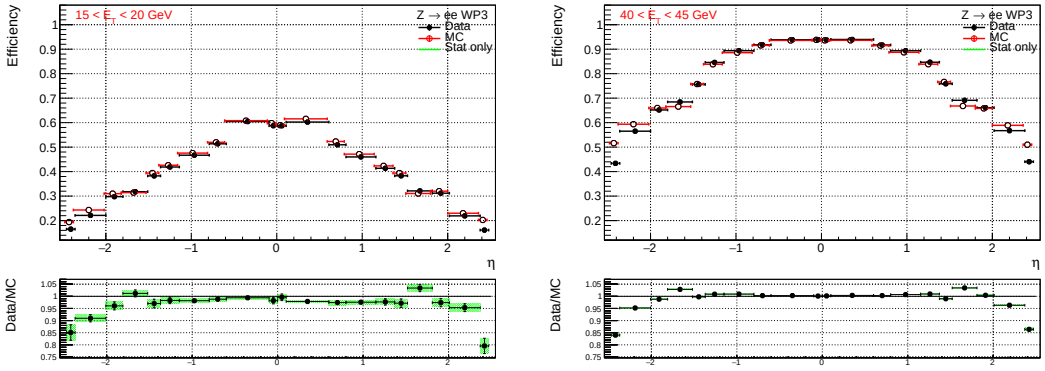

Figure 3.24 – Typical WP3 efficiency values for two bins : $15 < p_{\mathrm{T}} < 20$ GeV (left) and $40 < p_{\mathrm{T}} < 45$ GeV (right) versus η.

Figure 3.24 shows typical efficiency and SF values for WP3 as a function of η in two E_{T} bins. No variation of SF as a function of η is observed in central region ($|\eta|$<2.0), except for the "crack" region (1.37<$|\eta|$<1.52) where a slight jump above 1 is observed. On the contrary, for $|\eta|$>2.0 a 15% drop in SFs is observed.

5. The ambiguity selection refers to the ambiguity in the identification of a object as an electron or a photon candidate.

Similar behavior can be observed across all E_{T} regions as shown in Figure 3.25 (top), where inside each E_{T} bin, the 20 bins in η are shown. The drops in efficiency and SF at high $|\eta|$ are introduced by the CFT selection. Figure 3.25 (bottom) shows the efficiency and SF for a working point similar to WP3 except that the CFT cut is not applied [6]. As can be seen, for this working point the large drops in efficiency and particularly in SFs are not present anymore. Figure 3.26 shows SF statistical and systematic uncertainties from the Tag-and-Probe method for WP3, by year. Uncertainties are dominated by statistical uncertainties and amount to 4% (2%) at low E_{T} and decrease to below 1% (0.5%) at high E_{T} for the central values of η for 2015 (2016 and 2017) dataset.

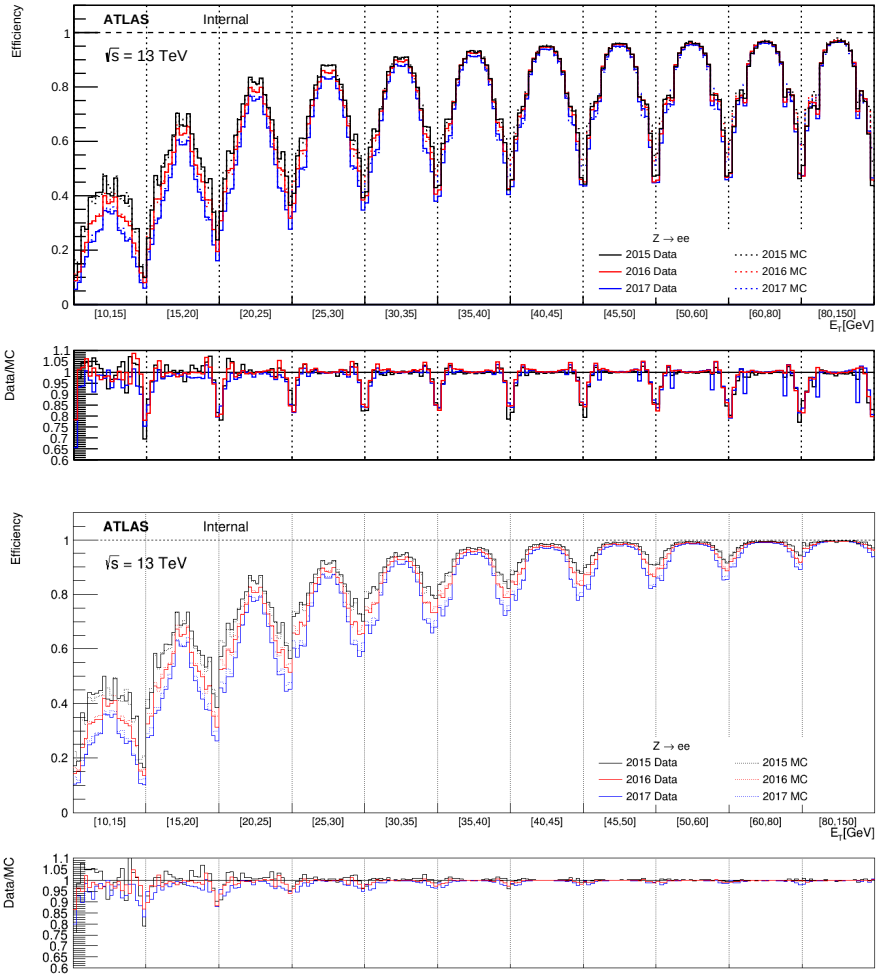

Figure 3.25 – Efficiency and SF for WP3 (top) and WP3 with no CFT selection (bottom) in bins of E_{T} (each E_{T} bin contains 20 η bins).

6. Also the ambiguity selection is not applied, but the impact from this cut has been found to be minimal.

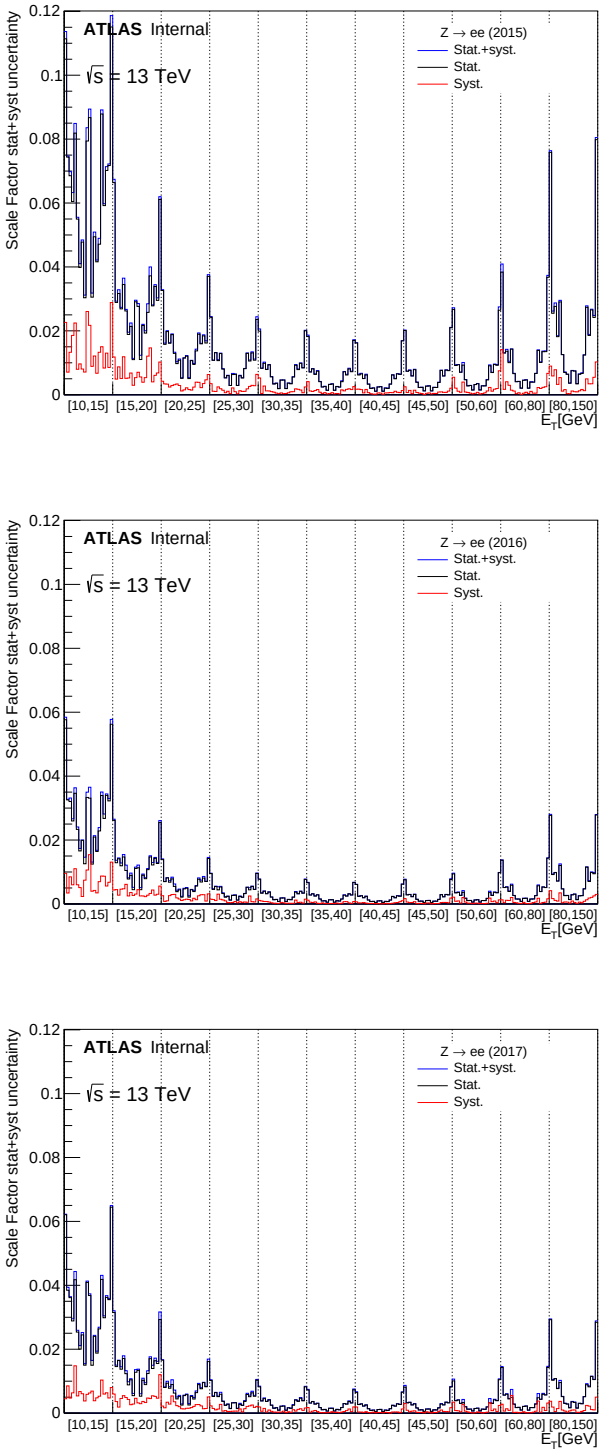

Figure 3.26 – Uncertainties associated to the WP3 SFs for 2015 (top), 2016 (center) and 2017 (bottom).

3.4.5.2 Extra uncertainties on PLV

Three other systematics are considered on top of the Tag-and-Probe ones.

SF dependency on pileup

Since the SFs are parameterized in terms of η and E_{T} any dependency on pileup would need to be taken into account either through some corrections or by including a systematic for this effect. Figure 3.27 shows the efficiency and SF dependency on number of primary vertices (left) and on pileup $<\mu>$ (right). Little to no dependency is observed for the SF in these inclusive distributions.

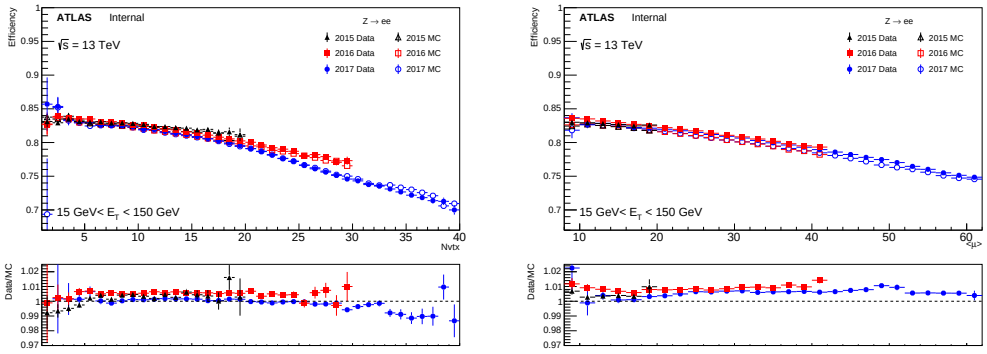

Figure 3.27 – Efficiency and SF dependency on number of primary vertices (left) and on average pileup $<\mu>$ (right) for WP3, for 2015, 2016 and 2017.

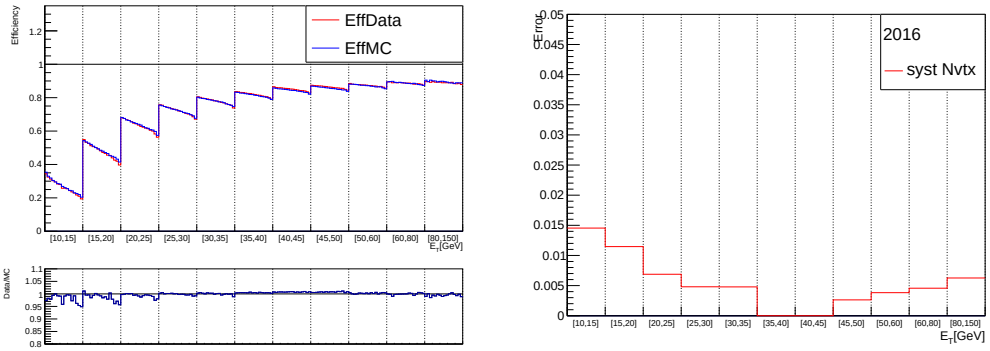

Figure 3.28 – Efficiency and SF dependency on number of primary vertices (Nvtx) in bins of E_{T} (left) and the additional systematic derived from SF dependence on Nvtx (right) for WP3 for 2016 data. Similar results for 2015 and 2017 are shown in appendix A.3.1 (Figure A.7 and A.8).

In figure 3.28 (left) is given the dependency on Nvtx for efficiency and SFs in bins of E_{T}. An important dependency on Nvtx is observed at low E_{T} for the

efficiency and to a lower extent for the SFs. An additional systematic uncertainty parameterized in E_{T} is derived based on the spread of the SFs in each E_{T} bin (RMS of histogram of SFs). This additional systematic uncertainty can be seen in figure 3.28 (right).

Charge asymmetry dependency

Checks were performed on the behavior of SFs when both the denominator and the numerator are split by charge of the probe electron. In figure 3.29 is shown the efficiency and SFs split by charge and nominal. A large asymmetry is observed in the extreme η bins. Efficiency and SFs of "-" distribution have large drops in the extreme bins of $+\eta$, while retaining higher efficiency and SF close to 1 in the extreme bins of $-\eta$. As the situation is the other way around for the "+" distribution the asymmetry effect is canceled/masked in the nominal merged case.

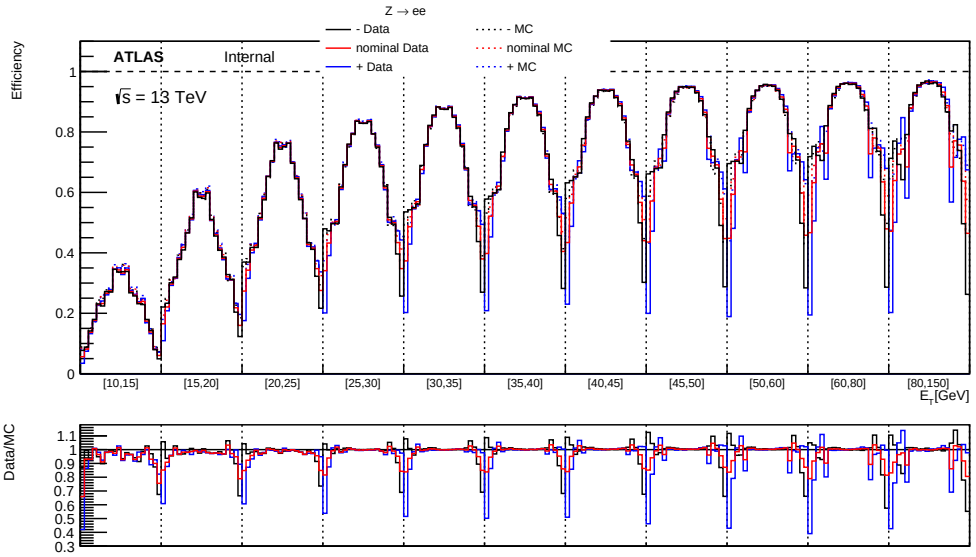

Figure 3.29 – Efficiency and SF for nominal WP3 (red line) and WP3 split by charge in bins of E_{T} (each E_{T} bin contains 20 η bins) for 2017 data. Inclusive distributions in η and E_{T} are given in appendix A.3.2 (figure A.9).

An additional systematic for this effect was derived in bins of E_{T} and η as $syst = |SF(+) - SF(-)|/2$ (using distributions in figure 3.29). This additional systematic uncertainty can be seen in figure 3.30.

The source of the charge asymmetry in the efficiencies and SFs is coming from the `CFT` working point as can be seen in figure 3.31. Splitting by charge the working point with PLV<-0.7 alone does not lead to such dramatic asymmetry like WP3.

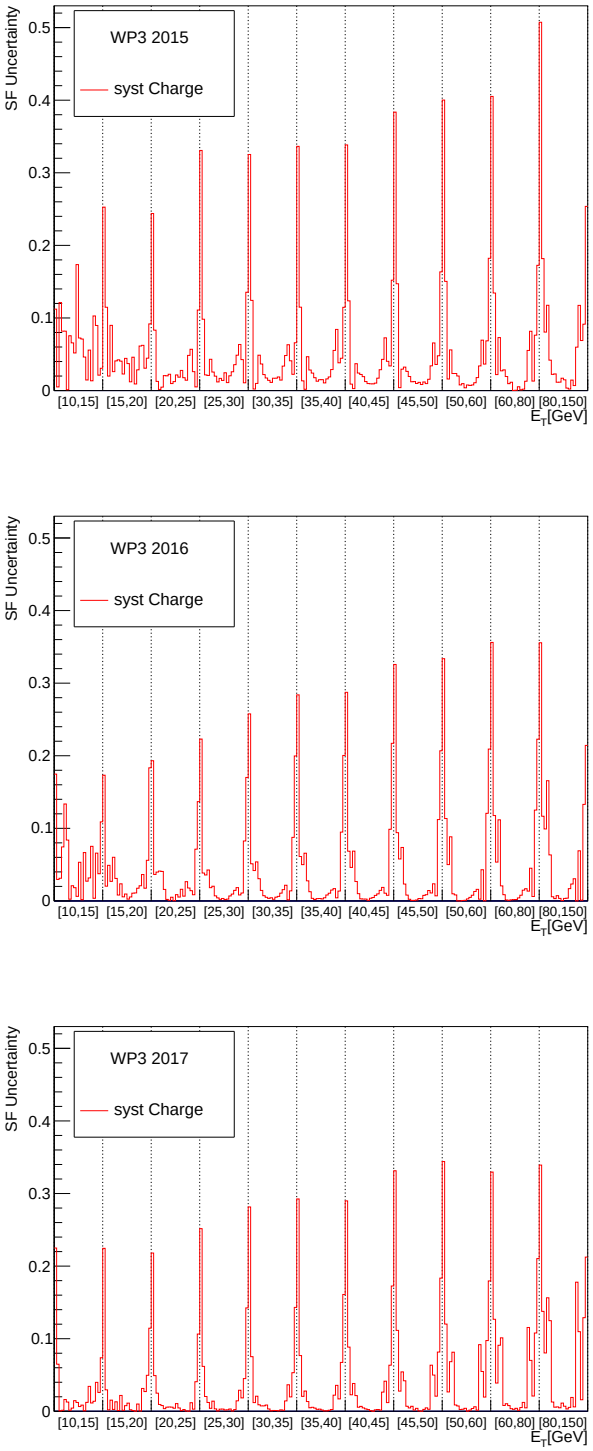

Figure 3.30 – Additional systematic uncertainty derived for WP3 SFs from SFs asymmetry when splitting by charge in bins of E_{T} for 2015 (top), 2016 (center) and 2017 (bottom). Each E_{T} bin contains 20 η bins.

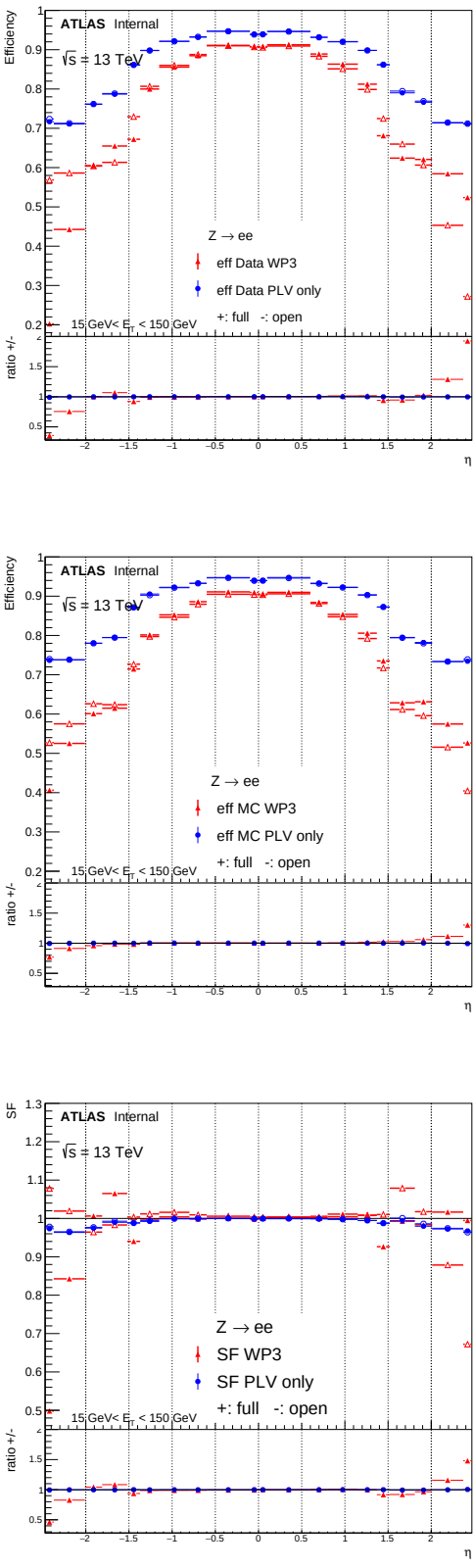

Figure 3.31 – Dependency on η for Data efficiency (top), MC efficiency (center) and SFs (bottom) for WP3 and an working point with PLV<-0.7 only for 2017 data.

Behavior at high E_{T}

A reliable measurement using the Tag-and-Probe method with $Z \to ee$ decays is possible up to 150 GeV. Figure 3.32 shows the η inclusive dependency of the efficiency and SFs for E_{T} up to 500 GeV. Having only a slight drop in efficiency and SF above 150 GeV demonstrates the stability of the SFs and the following extrapolation is used for high E_{T}. For SFs computed for E_{T} above 150 GeV the measured SFs from last E_{T} bin (80-150 GeV) are used with 2% additional uncertainty for $E_{\mathrm{T}} < 250$ GeV and 5% additional uncertainty on SFs for $E_{\mathrm{T}} > 250$ GeV.

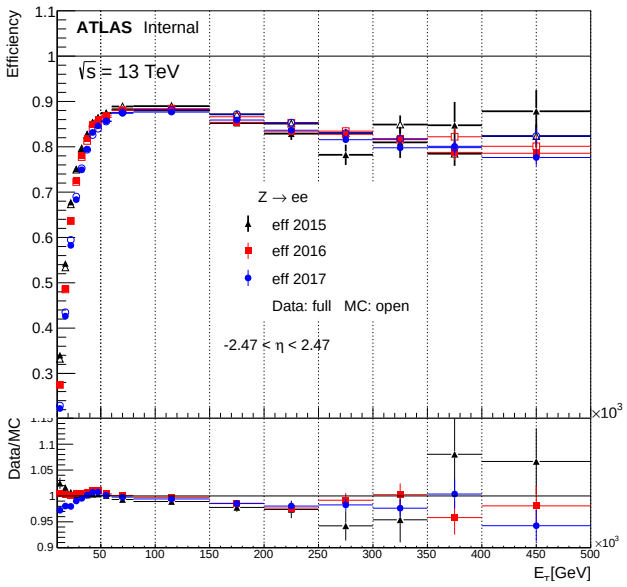

Figure 3.32 – Efficiency and SF dependency in E_{T} (inclusive in η) for WP3 including high E_{T} regions for 2015, 2016 and 2017 data.

Figure 3.33 shows the total final uncertainty on SFs. The additional systematics discussed above are added in quadrature with the statistical and systematical uncertainty from the Tag-and-Probe method. The uncertainty is fully dominated by the uncertainty coming from charge asymmetry at high $|\eta|$ reaching up to $\sim$0.35 ($\sim$50% - at high $|\eta|$ SF has drops). In central η region the total uncertainty is below 0.02 ($\sim$2% - SF close to 1 at central $|\eta|$) except the first E_{T} bin (10-15 GeV) where it goes up 5% in 2017 data.

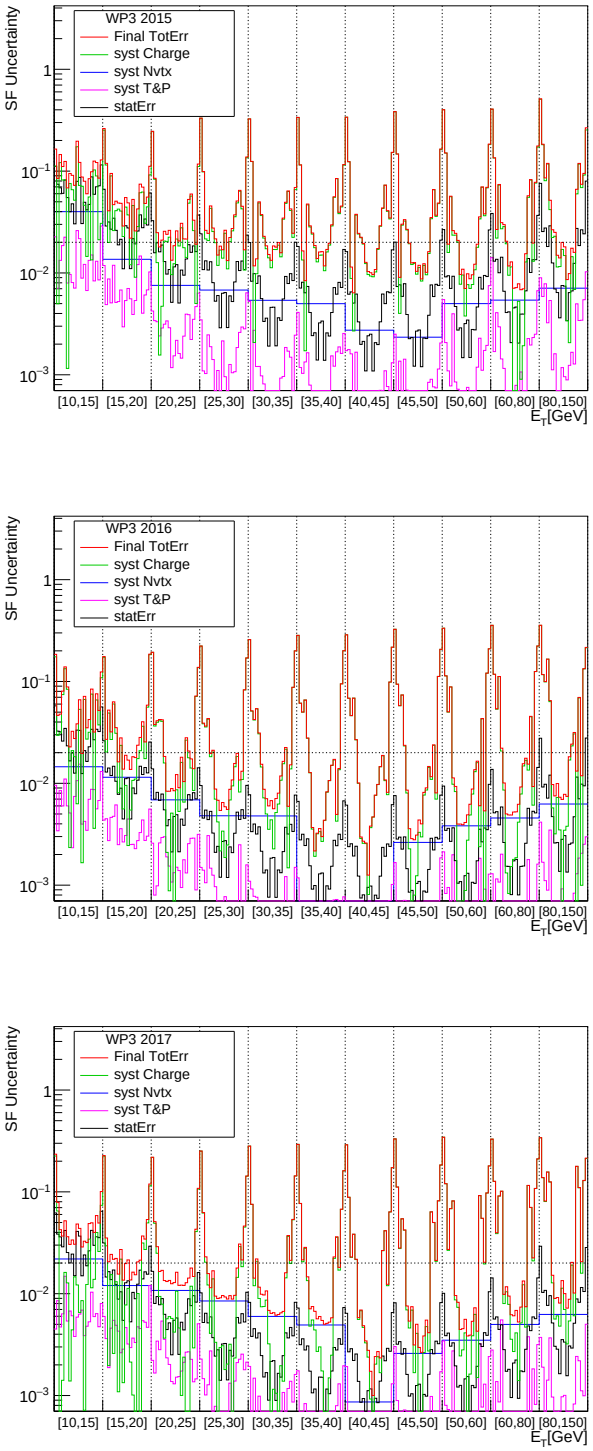

Figure 3.33 – Final total uncertainties associated to the SFs for WP3 in log scale for 2015 (top), 2016 (center) and 2017 (bottom). The dashed horizontal line in the log plots represents the level of an uncertainty of 0.02 (2% for a SF=1).

3.5 Conclusion

Electron efficiencies were measured using 2015-2017 data collected by the ATLAS detector at $\sqrt{s} = 13$ TeV. The electron reconstruction efficiencies have a value of 96-99 % with an uncertainty below 2%. The SFs are between 0.99-1.03 at low E_{T} (15-20 GeV) with an uncertainty around 1%. At higher E_{T} the SF are very close to 1 (within 1 %) with an uncertainty below 1%. The results on electron reconstruction efficiency measurements are generally used by all the physics analyses selecting electrons. Additionally, a dedicated electron performance paper for 2015-2016 dataset was published [43] and another publication is in preparation for the 2015-2017 datasets.

The non-prompt electron tagger SFs are generally between 0.92-0.99 (increasing from low E_{T} to higher E_{T}) and have an uncertainty of around 2% at low E_{T} and going below 1% at higher E_{T}. An additional systematics was added to take into account pileup effects. The results on the non-prompt lepton tagger efficiency measurements were used in a few important analyses. The results based on PLI (36.1 fb^{-1}, 2015-2016 datasets) were used for the top FCNC paper [66] (see Chapter 4), the ttH *evidence* paper [65] and the *observation* paper [67]. The results based on PLV are used in the ttHML analysis (80 fb^{-1}, 2015-2017 datasets) which is ongoing at the moment (see Chapter 5).

4 Search for flavor changing neutral currents in top decays

Summary

4.1 Introduction

Within the Standard Model, processes involving a change in flavor (at tree level) are always mediated by a W boson and described by the CKM matrix.

Thus, processes involving flavor changing neutral currents (FCNC) are forbidden. Instead, FCNC processes are possible at higher order (in loops), however they are strongly suppressed by the Glashow-Iliopoulos-Maiani (GIM) mechanism [68]. A typical example of FCNC processes are the decays of the heaviest quark, the top quark, to a neutral boson (Higgs H, photon γ, gluon g or Z boson) and a up-type quark (u or c). Figure 4.1 shows the Feynman diagram for $t \to Hq$ at tree level (forbidden in SM)(a) and in a one loop process (b). The expected branching ratio in the SM for such decays are compared with theory predictions of several BSM theories in figure 4.2. In the SM, BR($t \to Hu$) $\sim 10^{-16}$ and BR($t \to Hc$)$\sim 10^{-14}$ [69]. These values are beyond the sensitivity of any foreseeable future experiment.

However, as it can be seen in figure 4.2, there are BSM scenarios for which large enhancement in these processes are predicted. The largest enhancement in the branching ratio is predicted in the two-Higgs-doublet model with flavor violation, 2HDM(FV), at the tree level, where BR($t \to Hc$) is predicted to go up to 0.15%. This is possible through the off-diagonal interactions of the light Higgs boson (Cheng-Sher ansatz [70]) which lead to a coupling of type $\lambda_{tHq} \sim \sqrt{2m_t m_q}/v$, where v is the Higgs field vacuum expectation value. The mass dependence of the coupling explains the much lower prediction for BR($t \to Hu$)$\sim 10^{-5}$ in this model as the mass of u quark is much smaller than that of the c quark ($m_u \approxeq$ 2.2 MeV and $m_c \approxeq$ 1.28 GeV). Even with tree level flavor conservation the two Higgs doublet model, 2HDM(FC), brings important contribution to BR($t \to Hq$) via enhanced loop level interactions. Other models with flavor conservation at tree level that bring contributions to the BR($t \to Hq$) are minimal supersymmetric SM (MSSM) and supersymmetry with R-parity violation (RPV) where GIM mechanism suppression can be relaxed with loops with new mediating bosons. Warped extra dimensions models, known as Randall–Sundrum models (RS), also feature a high BR($t \to Hc$) of up to $\sim 10^{-5}$. A summary for these models and their limits on BR($t \to Hq$) can be found in [69].

These large differences between the SM and BSM predictions (which are close to the current experimental limits) give a very strong motivation to perform searches for FCNC as any discoveries of such processes would provide an irrefutable proof of New Physics.

In the analysis described in this chapter, a search for FCNC was performed in $t\bar{t}$ events with one of the top quarks decaying to a Higgs boson and an up-type quark ($t \to Hq$, q = u or c) with multilepton final states. This analysis is based on 36.1 fb^{-1} of data collected in 2015 and 2016 by the ATLAS detector at $\sqrt{s} = 13$ TeV. The structure of the chapter is as follows. Previous results from ATLAS and CMS on $t \to Hq$ are discussed in section 4.2. The analysis strategy is given in section 4.3 and the object definitions and event selection are detailed in section 4.4. Section 4.5 describes the background estimation and section 4.6 gives an insight into a multivariate technique used to improve the signal-background separation. Finally, sections 4.7 and 4.8 give the results and

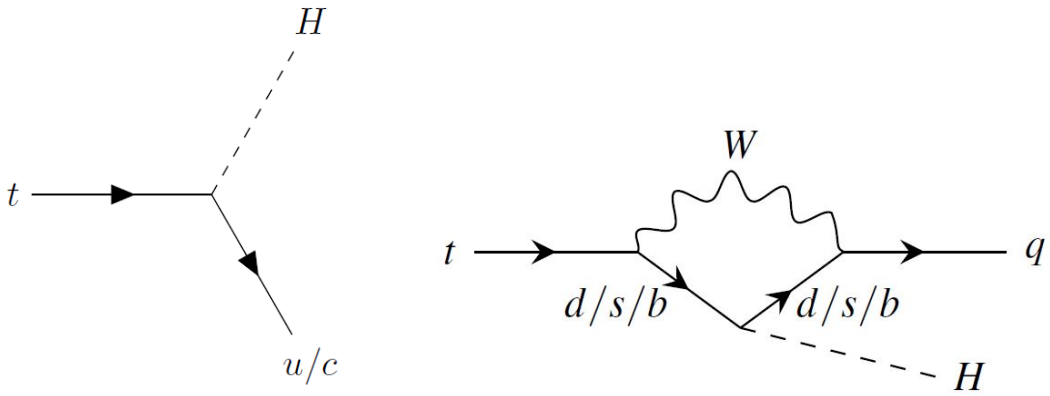

Figure 4.1 – Top quark decay to Higgs boson and an up-type quark ($t \to Hq$) at tree level (left) and in one loop (right). The tree level vertex does not exist in the SM.

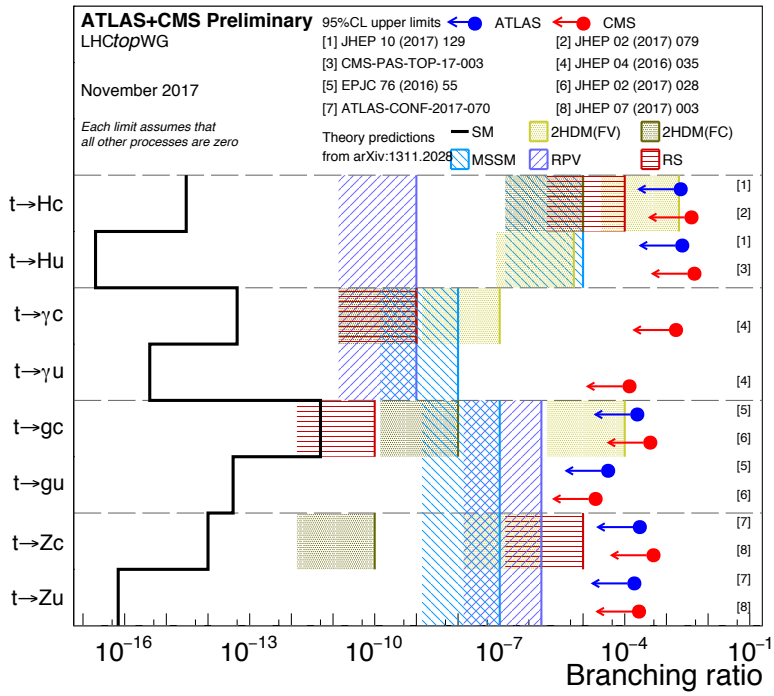

Figure 4.2 – Summary of observed upper limits at 95% confidence level of the branching ratio of top quark decays to a neutral boson (Higgs H, photon γ, gluon g or Z boson) established by ATLAS (blue) and CMS (red). The expected SM values are given by the solid black line. Hashed areas give the interval of prediction for various BSM scenarios.

the conclusions.

4.2 Previous results

Previous searches for top FCNC $t \to Hq$ were performed at LHC, once the Higgs boson was discovered in 2012 and its mass was measured. Both ATLAS and CMS experiments have performed a series of analyses to attempt to observe BR($t \to Hq$). The searches have been performed in $t\bar{t}$ decays where only one of the top quarks decays via FCNC while the other decays via the dominant $t \to Wb$ mode. The measurement of BR($t \to Hu$) assumes BR($t \to Hc$)=0 and vice versa. All the measurements have found values compatible with 0 for the BR($t \to Hq$)(i.e. no $t \to Hq$ FCNC has been discovered so far) and 95% CL upper limits were established. The individual analyses were split and performed by Higgs decay mode:

1. $H \to WW, ZZ, \tau_{\text{lep}}\ \tau_{\text{lep}}$: targets multileptonic final states with exactly two lepton of same sign (2ℓSS) or three leptons (3ℓ)
2. $H \to \gamma\gamma$: features clean final states but suffers from low branching ratio (BR ($H \to \gamma\gamma$)=0.23% [71])
3. $H \to bb$: enjoys the highest branching ratio (BR ($H \to bb$)=57% [71]), however it is limited by complex multijet final states with large backgrounds

The results from these complementary and orthogonal measurements are combined to get the best limit on BR($t \to Hq$).

The results for the 95% CL upper limits on BR($t \to Hq$) using the Run 1 datasets are summarized in table 4.1. The analyses from the ATLAS experiment used $20.3\ fb^{-1}$ of data collected at $\sqrt{s} = 8$ TeV ($H \to \gamma\gamma$ analysis included also $4.5\ fb^{-1}$ at $\sqrt{s} = 7$ TeV [72]) and $19.7\ fb^{-1}$ at $\sqrt{s} = 8$ TeV were used by the CMS analyses. The combined observed limit from the ATLAS (CMS) experiment is 0.45% (0.55%) for BR($t \to Hu$) and 0.46% (0.40%) for BR($t \to Hc$). The results from the ATLAS experiment for the observed limits and expected limits (with $\pm 1\sigma$ and $\pm 2\sigma$) for the individual measurements and combined measurement are also shown in figure 4.3. These limits are not strict enough yet to constrain any BSM scenarios described earlier in section 4.1.

In Run 2, the center of mass energy for the pp collisions increased to $\sqrt{s} = 13$ TeV which led to an increase in the $t\bar{t}$ cross section by a factor of ~3.5 [73]. A summary of results obtained with a partial dataset from Run 2 (2015-2016) of around $36\ fb^{-1}$ is given in table 4.1. At the time of performing the $t \to Hq$ to multileptons analysis with $36\ fb^{-1}$ at $\sqrt{s} = 13$ TeV, which is the subject of the current chapter, only the $t \to Hq$ ($H \to \gamma\gamma$) analysis from the ATLAS experiment [74] and $t \to Hq$ ($H \to bb$) analysis from the CMS experiment [75] had public results. The results from the $H \to \gamma\gamma$ individual measurement already surpass the combined results from Run 1, with an observed 95% CL upper limit for BR($t \to Hu$) (BR($t \to Hc$)) of 0.24% (0.22%).

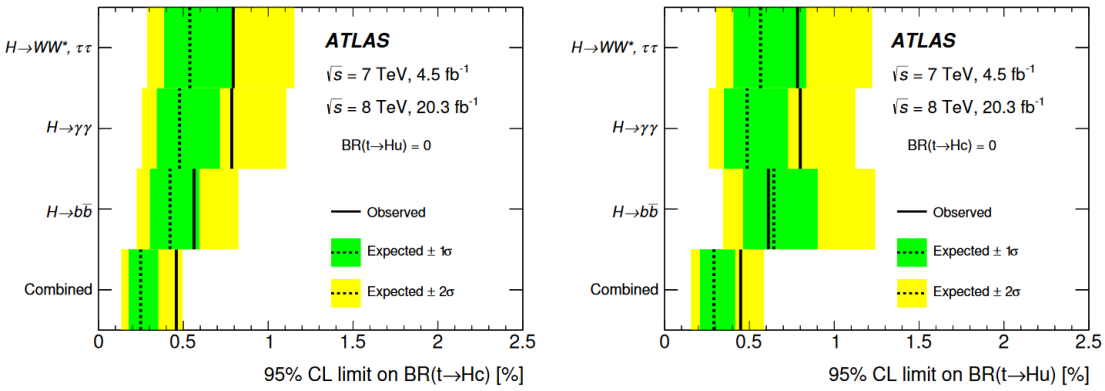

Figure 4.3 – Observed and expected upper limits at the 95% CL on the top FCNC BR($t \to Hc$) (left) and BR($t \to Hu$) (right) in % for ATLAS results for individual measurements and combined using Run 1 data.

Channel	B ($t \to Hu$) Observed	B ($t \to Hu$) Expected	B ($t \to Hc$) Observed	B ($t \to Hc$) Expected
Run 1, 20 fb^{-1}				
$H \to WW, ZZ, \tau_{\text{lep}}\ \tau_{\text{lep}}$ (2ℓSS)	0.86 (0.93)	0.62 (0.85)	0.89 (0.99)	0.61 (0.93)
$H \to WW, ZZ, \tau_{\text{lep}}\ \tau_{\text{lep}}$ (3ℓ)	2.91 (1.34)	1.97 (1.47)	2.34 (1.26)	1.59 (1.33)
$H \to WW, ZZ, \tau_{\text{lep}}\ \tau_{\text{lep}}$ (Comb)	0.78* (0.86)	0.57* (0.82)	0.79* (0.93)	0.54* (0.89)
$H \to \gamma\gamma$	0.79 (0.42)	0.51 (0.60)	0.79 (0.47)	0.51 (0.67)
$H \to bb$	0.61 (1.92)	0.64 (0.84)	0.56 (1.16)	0.42 (0.89)
Full combination	0.45 [76] (0.55 [77])	0.29 [76] (0.40 [77])	0.46 [76] (0.40 [77])	0.25 [76] (0.43 [77])
Run2, 36 fb^{-1}				
$H \to \gamma\gamma$	0.24 [74] (–)	0.17 [74] (–)	0.22 [74] (–)	0.16 [74] (–)
$H \to bb$	– (0.47 [75])	– (0.34 [75])	– (0.47 [75])	– (0.44 [75])

Table 4.1 – Observed and expected upper limits at the 95% CL on the top FCNC branching ratio in % for ATLAS (CMS). * includes also the channel 2ℓSS τ_{had} .

4.3 Analysis strategy

The search for FCNC is performed in $t\bar{t}$ events where the top quark (or the anti-top quark) decays via FCNC (the probability of simultaneous decay of both top and anti-top quarks via FCNC is negligible). The corresponding cross section is given by

$$\sigma_{FCNC} = 2 \times \sigma_{t\bar{t}} \times BR_{FCNC}(1 - BR_{FCNC}) \approxeq 2 \times \sigma_{t\bar{t}} \times BR_{FCNC}, \qquad (4.1)$$

where the factor 2 corresponds to the fact that both the top and the anti-top can decay via FCNC. The FCNC process branching ratio is the parameter of interest (POI) in this analysis.

The analysis is focused on the top quark decay to a Higgs boson and an up-type quark ($t \to Hq$, q = u or c). Due to the similarities of the two processes, the treatment of $t \to Hu$ and $t \to Hc$ follows the same procedure. Two multilepton final states are considered. One final state targets events with exactly

two light leptons (e or μ) of the same electrical charge sign (2ℓSS) and the other one targets events with exactly three light leptons (3ℓ). Additionally, jets and missing transverse energy are required. The same sign requirement for the 2ℓSS is to reduce the overwhelming background from $t\bar{t}$ events with two leptons of opposite sign (2ℓOS). A typical full decay chain, assuming the dominant Higgs decay mode $H \to WW^*$, summarizing the two channels is

$$pp \to t\bar{t} \to Hq + Wb \to 3W + bq \to \begin{cases} 2l + E_T^{miss} + 4jets(1b) \\ 3l + E_T^{miss} + 2jets(1b) \end{cases} . \quad (4.2)$$

Figure 4.4 shows the corresponding Feynman diagram for the full decay chain for 2ℓSS channel. Beside the dominant $H \to WW^*$, important contributions in the two channels are brought by $H \to \tau_{lep}\tau_{lep}$ (leptonically decaying τ) and $H \to ZZ^*$.

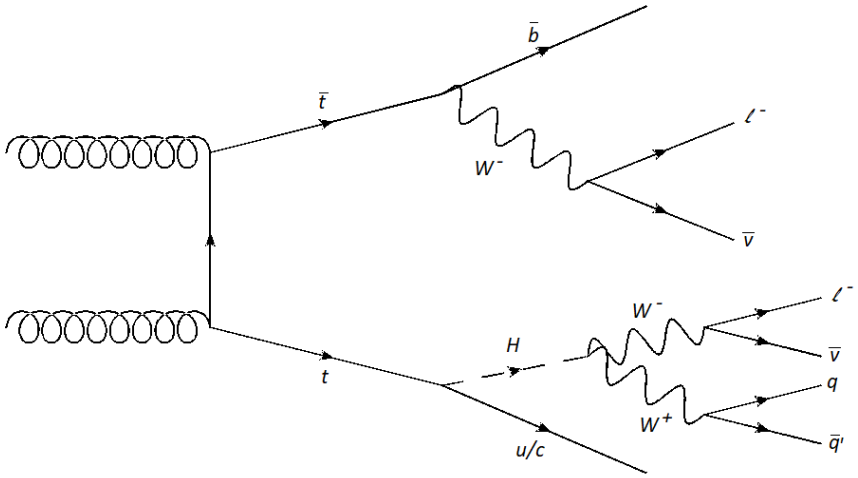

Figure 4.4 – Full decay chain for the $t \to Hq$ in $t\bar{t}$ processes for 2ℓSS channel.

Because of the topology of these events, the invariant mass from the leptons is not peaking above the background and can not be used as a discriminating variable. The strategy of this analysis is therefore to rely on the jet multiplicity information. Figure 4.5 shows a diagram in terms of number of jets (N_{jet}) vs number of b jets (N_{b-jet}), which maps the regions mostly dominated by the signal ($t \to Hq$) and by the main backgrounds. ttV ($V = Z, W$) processes have one more b-jet while ttH has two more jets (including one b-jet). There is a partial overlap between these regions as some jets might not be reconstructed or there could be extra jets from radiations. The low jet number region is reserved for the control region (CR) used to estimate the fake lepton backgrounds, e.g. events with leptons coming from heavy flavor decays and photon conversions originating mainly from $t\bar{t}$.

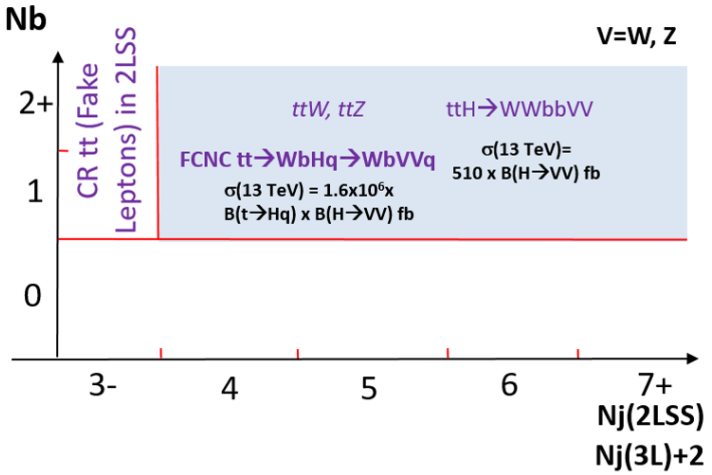

Figure 4.5 – Mapping of the FCNC signal and the main backgrounds (fake leptons, ttV, ttH) in a Njet vs. Nb-jet diagram.

To reduce the backgrounds in the signal regions (SR) a two step approach is implemented.

1. Tight requirements are used to define the signal regions. Additionally, to reduce the events with light leptons coming from the heavy flavor decays (non-prompt leptons) the `PromptLeptonIso` MVA described in section 3.4 was used. The `CFT` MVA, described in section 3.4.2, was used to reduce the charge flip background in the 2ℓSS channel.
2. Various variables in the signal region are used to further separate the signal from the main backgrounds using multivariate techniques, the output being a final discriminant variable.

After these steps a maximum likelihood fit is performed on the event MVA discriminant variable to extract the best-fit value and the upper limit at 95% confidence level for the branching ratio B($t \to Hq$).

This analysis follows closely the search for Higgs boson production in association with $t\bar{t}$ ($t\bar{t}H$) with multilepton final states analysis [65] due to the similarities of the final states (one less b-jet and one less light jet in the case of $t \to Hq$ for the same leptonic channel, without additional radiation). The same data events samples and simulations, object and event selections, non-prompt lepton rejection algorithm and calibration are used. However, particular care is taken in the fakes leptons background estimation because of the FCNC lower jet multiplicity (signal contamination in the control region) and additionally the multivariate analysis is fully dedicated and optimized for the FCNC signal.

4.4 Object and event selections

All the objects are defined as detailed already in section 2.3, with additional baseline requirements for this analysis.

Electron (e) candidates are required to pass the loose or tight likelihood identification criteria and to have a transverse momentum value of $p_T > 10$ GeV. Additionally, the candidates in the regions $|\eta_{cluster}| > 2.47$ and $1.37 < |\eta_{cluster}| < 1.52$ ("crack" region) are excluded. To reduce the background from non-prompt leptons the track compatibility with the primary vertex is validated with selections on the transverse impact parameter significance ($|d_0|/\sigma_{d_0} < 5\sigma$) and on the longitudinal impact parameter ($|z_0 \sin\theta| < 0.5$ mm).

Muon (μ) candidates are required to pass the loose likelihood identification. A transverse momentum of $p_T > 10$ GeV and $|\eta| < 2.5$ are required. As in the case of the electrons, selections on the transversal impact parameter significance ($|d_0|/\sigma_{d_0} < 3\sigma$) and on the longitudinal impact parameter ($|z_0 \sin\theta| < 0.5$ mm) are applied.

Additionally, the light leptons (e and μ) have to pass `PromptLeptonIso` selection. The charge mis-assignment veto is applied only for electron candidates. Isolation requirements based on track and calorimeter variables are applied, with an overall 99% efficiency in $Z \to ll$ events.

A summary of all light lepton definitions used in the analysis is provided in table 4.2.

	e			μ	
	L	L*	T	L	L* T
Isolation	No	Yes		No	Yes
Non-prompt lepton MVA	No	Yes		No	Yes
Identification	Loose		Tight	Loose	
Charge mis-assignment veto	No		Yes	N/A	
Tranverse impact parameter significance $\lvert d_0\rvert/\sigma_{d_0}$	$< 5\sigma$			$< 3\sigma$	
Longitudinal impact parameter $\lvert z_0 \sin\theta\rvert$	< 0.5 mm				

Table 4.2 – Loose (L), Loose, isolated and pass the non prompt BDT (L*), tight (T) light lepton definitions. Selections for the tighter leptons are applied in addition to the looser ones.

Tau leptons that are hadronically decaying (τ_{had}) are reconstructed from clusters in the calorimeters and associated tracks in the inner detector. τ_{had} candidates are required to have $p_T > 25$ GeV and $|\eta| < 2.5$, excluding the "crack" region of the EM calorimeter. The candidates are required to have one or three

matched tracks, with a total charge of ± 1. Multivariate techniques are used to suppress backgrounds from jets.

Jets are reconstructed using a anti-k_t algorithm with a radius parameter $R = 0.4$, following the details given in section 2.3.5. Selected jets have to pass the transverse momentum of $p_T > 25$ GeV and $|\eta| < 2.5$ requirements. A 70% b-tagging efficiency working point is used for b-jet definition.

To avoid double counting of objects an overlap removal procedure is used.

— The **electron** candidate with higher p_T is selected if two electron candidates are closer than $\Delta R < 0.1$. Jets within $\Delta R < 0.3$ and τ candidates within $\Delta R < 0.2$ of an **electron** candidate are removed.

— Electrons within $\Delta R < 0.1$ and τ within $\Delta R < 0.2$ of an **muon** are removed.

— Jets within $\Delta R < 0.3$ of τ lepton candidate are removed

4.4.1 2ℓSS channel selections

Events with exactly two light leptons of the same charge are selected. Both leptons have to pass the tight (T) definition specified in table 4.2. The `PromptLeptonIso` and `CFT` selections are included in the tight definition. A minimum requirement of 20 GeV is applied to both leptons. Events containing τ_{had} (medium ID) are vetoed. At least 4 jets are required with 1 or 2 of them being b-tagged. The leptons are labeled as l_0 and l_1 and they are sorted by p_T with $p_T(l_0) \geq p_T(l_1)$.

4.4.2 3ℓ channel selections

Events with exactly three light leptons with total charge of ± 1 and with no τ_{had} (medium ID) are selected. The leptons are labeled as l_0, l_1 and l_2, with l_0 having opposite charge compared to l_1 and l_2. l_0 is required to pass only loose identification with additional isolation and `PromptLeptonIso` and `CFT` (for electrons) selections. This corresponds to the L* identification defined in table 4.2. $p_T > 10$ GeV is required for l_0 and $p_T > 15$ GeV for the same sign leptons. A minimum of three jets are required with at least one b-jet. Events with the invariant mass of any opposite charge lepton pair less than 12 GeV are removed (to veto events with low mass resonances decays). Additional selections are imposed to the invariant mass of any same flavor opposite charge (SFOC) pair of leptons to be outside the Z boson mass window to reduce contamination from $t\bar{t}Z$. Moreover, the invariant mass of the three leptons must be outside Z boson mass window to reject events with $Z \to ll\gamma^{(*)} \to lll'(l')$ with (l') not being reconstructed because of its low p_T.

Finally, a summary of the selections for the two channels is provided in table 4.3.

	2ℓSS	3ℓ
	Pre-MVA region selection	
Light leptons	$(l_0^{\pm}, l_1^{\pm})$= (T, T)	$(l_0^{\mp}, l_1^{\pm}, l_2^{\pm})$ = (L*, T, T)
	trigger matching (see text)	trigger matching (see text)
Sum of lepton Charge	± 2	± 1
p_{T} lepton cut in GeV	$(l_0^{\pm}, l_1^{\pm}) \geq$ (20, 20)	$(l_0^{\mp}, l_1^{\pm}, l_2^{\pm}) \geq$ (10, 15, 15)
τ_{had}	0 Medium	0 Medium
N_{jets}	≥ 4	≥ 2
$N_{b-\mathrm{jets}}$	$= 1, 2$	≥ 1
Other cuts	None	$m(\ell^+\ell'^-) > 12$ GeV
		$\lvert m(\ell^+\ell^-) - 91.2 \text{ GeV}\rvert > 10$ GeV
		(for all SFOC pairs)
		$\lvert m(3\ell) - 91.2 \text{ GeV}\rvert > 10$ GeV

Table 4.3 – Summary of basic characteristics and strategies of the two analysis channels. The lepton selection is given in Table 4.2. SFOC stands for same-flavour, opposite-charge lepton pairs.

4.5 Signal and Backgrounds

As already mentioned, the data and simulation samples used in this analysis are the same used in the ttH to multileptons search (36 fb^{-1} at $\sqrt{s} = 13$ TeV) [65]. The signal from the ttH to multileptons search, the $t\bar{t}H$ processes, becomes a background process in the current analysis and its cross section is set to the theoretical SM value, $\sigma_{ttH} = 507^{+35}_{-50}$ fb [18], as no significant disagreement with SM was observed [65, 67, 78].

The only samples not present in the $t\bar{t}H$ analysis are the FCNC $t \to Hq$ signal samples. The signal events $t \to Hq$ (from $pp \to tt$) are generated at next-to-leading order using the MADGRAPH5_AMC@NLO generator [79]. MadSpin [80] was used for the top quark decays, while for the parton showering, hadronization, underlying-event generation and Higgs boson decay PYTHIA 8 was used [81]. The $t\bar{t}$ production cross section was estimated at next-to-next-leading order with TOP++2.0 [82] and was found to be $\sigma_{t\bar{t}} = 832^{+40}_{-46}$ fb ($\sqrt{s} = 13$ TeV). A compressive summary of all the processes and their corresponding cross sections, cross section uncertainty and order are given in Table 4.4 [1].

Depending on the type of background, they are split in reducible and irreducible.

1. For even more details on the event generation configurations used for the background estimation Table A.1 can be consulted.

Process	Cross section [pb]	QCD scale [%]	PDF+α_S [%]	Order
$t\bar{t}W$	0.60	$^{+12.9}_{-11.5}$	±3.4	NLO QCD+EWK
$t\bar{t}(Z/\gamma^* \to \ell\ell)$	0.12	$^{+9.6}_{-11.3}$	±4.0	NLO QCD+EWK
$t\bar{t}H$	0.51	$^{+5.8}_{-9.2}$	±3.6	NLO QCD+EWK
$t\bar{t}t\bar{t}$	0.0092	$^{+30.8}_{-25.6}$	$^{+5.5}_{-5.9}$	NLO QCD
$t\bar{t}W^+W^-$	0.0099	$^{+10.9}_{-11.8}$	±2.1	NLO QCD
$tHqb$	0.074	$^{+6.5}_{-14.7}$	±3.7	NLO QCD
tHW	0.015	$^{+4.9}_{-6.7}$	±6.3	NLO QCD
tZ	0.61	±50		LO QCD
tWZ	0.16	±50		NLO QCD
s-, t-channel,	10, 217	±4		NLO QCD
Wt single top	72	±5		NLO QCD + NNLL
$t\bar{t}$*	832	$^{+2.4}_{-3.5}$	±4.2	NNLO QCD + NNLL
$t\bar{t}\gamma$	5.7	±50		NLO QCD
$VV(\to \ell\ell XX)$	37	±50		NLO QCD
$Z \to \ell^+\ell^-$	2070	±5		NNLO QCD

Table 4.4 – The cross sections used for each of the Monte Carlo simulated samples used in the analysis. The size of the QCD and PDF+α_S scale uncertainties are indicated as well as the order of the cross section calculation. The uncertainties for $t\bar{t}\gamma$, tZ, tWZ, and $VV(\to \ell\ell XX)$ include extrapolation uncertainties into the analysis phase space.* In this analysis, PDF++α_S and QCD scale are merged, i.e 6% cross-section uncertainty is considered on $t\bar{t}$.

4.5.1 Irreducible backgrounds

The irreducible backgrounds are SM processes that have similar final states as the signal and they can not be reduced without affecting significantly the signal. The estimation of these backgrounds rely on using Monte Carlo simulations.

The main contributions to this background comes from $t\bar{t}V$, $t\bar{t}H$ and VV processes. A typical decay chain for $t\bar{t}V$ is given in equation (4.3).

$$t\bar{t}V \to 2W2b + V \to \begin{cases} 2l + E_T^{miss} + 4jets(inc.2b) \\ 3l + E_T^{miss} + 2jets(inc.2b) \end{cases} \tag{4.3}$$

The $t\bar{t}V$ has been validated in various regions where an enhanced contribution from these processes was obtained. Figure 4.6 shows a comparison between data and MC estimations for the jet multiplicity variable in the 3ℓ $t\bar{t}W$ validation region (left) and 3ℓ $t\bar{t}Z$ validation region (right). Good agreement can be observed within the uncertainties.

More contributions come from rare processes ($t\bar{t}WW, tHqb$) but they have a rather small contribution to the total background.

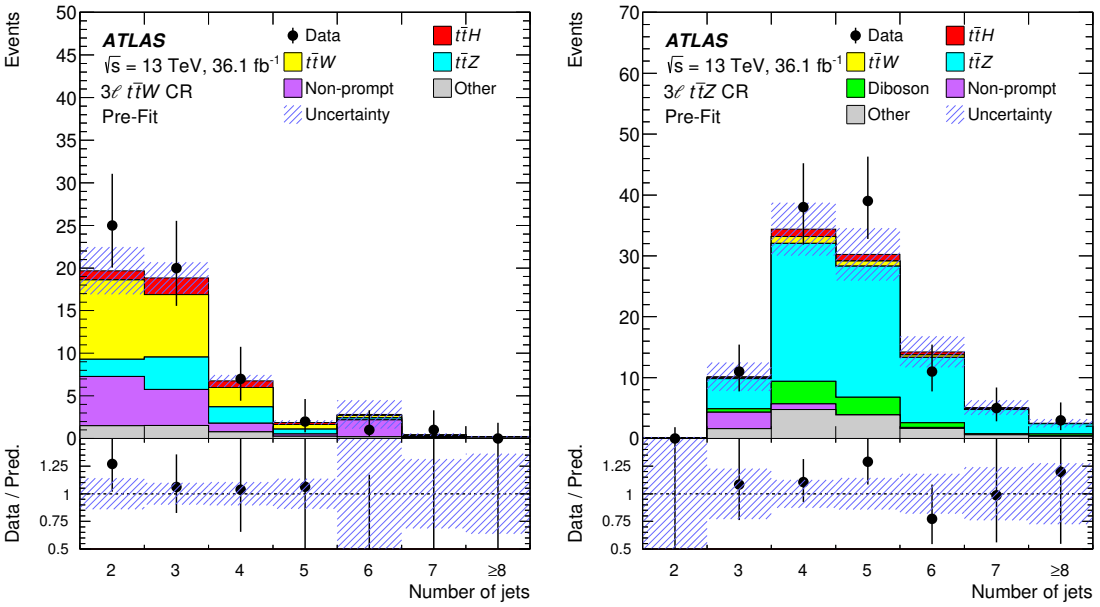

Figure 4.6 – Validation regions for $t\bar{t}W$ (left) and $t\bar{t}Z$ (right) in the 3ℓ category. The last bin in each figure contains the overflow. The bottom panel displays the ratio of data to the total prediction. The hashed area represents the total uncertainty in the sign-plus-background prediction. Errors on prediction include statistic and all systematic uncertainties.

4.5.2 Reducible backgrounds

The reducible backgrounds are processes that have final states different from the signal. However, because of the detection imperfections, reconstructed final states mimic the signal final states.

Two types of reducible backgrounds are affecting this analysis.

1. charge mis-identified background (QmisID) refers to the events that have leptons with the electric charge wrongly identified by the detector
2. Fakes/non-prompt lepton

Both backgrounds are measured using data-driven methods.

4.5.2.1 Charge misidentification

Only the 2ℓSS channel is affected by this background. The main source of this background is the $t\bar{t}$ process that decay to a $2\ell OS$ final state and one of the leptons has the charge mis-identified (charge flip). A typical decay chain of such

a process is given by:

$$t\bar{t} + jets \rightarrow 2W2b + jets$$
$$\rightarrow 2l(OS) + E_T^{miss} + jets(inc.2b) \rightarrow 2l(SS) + E_T^{miss} + jets(inc.2b). \quad (4.4)$$

The reason why the charge is not correctly measured is either because of a trident process ($e^{\pm} \rightarrow e^{\pm}\gamma^* \rightarrow e^{\pm}e^+e^-$) in which the initial electron radiates a hard photon (material interaction) which undergoes an asymmetric conversion and the opposite charge electron is reconstructed or because of wrongly measured track curvature (particularly at high p_T). Because the rate at which this process occurs for muons is small, no measurement is done for muon charge flip.

The rates for electron charge flip are measured in $Z \rightarrow ee$ decays using a likelihood method. The rates are measured in terms of electron p_T and $|\eta|$. Figure 4.7 shows the results of the measurements. The range of the measured rates varies from $5 \cdot 10^{-5}$ at $|\eta| < 0.6$ and low p_T to 10^{-2} at $2 < |\eta| < 2.5$ and high p_T. As expected, the rates increase with p_T because the curvature of the electron track decreases. Similarly, the rates increase with $|\eta|$ because the amount of the material in the inner detector increases with $|\eta|$.

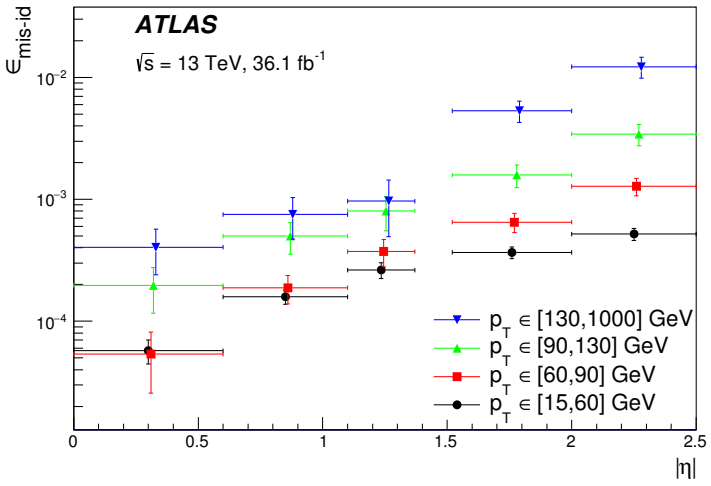

Figure 4.7 – Charge mis-identification rates computed in data with the likelihood method for *tight* electrons in terms of p_T and $|\eta|$.

In terms of systematic uncertainties, the charge flip rates are affected by the $Z \rightarrow ee$ sample size and by the Z peak window size definition. Additionally, a systematic uncertainty was added to cover the difference in the results between running this method on simulated $Z \rightarrow ee$ events and the results from the truth information of the same events. A total systematic uncertainty of around 30% is assigned.

To get an estimate for the number of charge flip events in the 2ℓSS SR an event

weight is computed using the rates, as given by

$$w_{QmisID} = \epsilon_{\text{mis id},1}(1 - \epsilon_{\text{mis id},2}) + \epsilon_{\text{mis id},2}(1 - \epsilon_{\text{mis id},1}). \quad (4.5)$$

The event weights w_{QmisID} are then applied to the events in the 2ℓSS SR except that leptons should be opposite sign instead of same sign. As a reminder, the charge misidentified events are estimated after the dedicated CFT BDT selection is applied (see section 3.4.2) and which is found to give a reduction of the electrons with mis-identified charge by a factor 17 retaining 95% efficiency for the electrons with the correct charge.

4.5.2.2 Fake lepton background estimation in 2ℓSS and 3ℓ channels

The fake lepton background has a few components. The main component comes from the leptons that are produced in the b decay chains in $t\bar{t}$ events. These leptons are referred to as non-prompt leptons due to the relatively long lived b quarks compared to W/Z ($\sim$13 orders of magnitude difference). Other contributions come from photon conversions (photon converts to an electron-positron pair through interactions with the detector material). Smaller contributions come from wrongly reconstructing leptons from jets (energy deposits in the EM calorimeter or leakage from the hadron calorimeter to the muon spectrometers). An example of realization of 2ℓSS and 3ℓ final states with one non-prompt lepton is given by:

$$t\bar{t} + jets \rightarrow 2W2b + jets \rightarrow \begin{cases} l^{prompt} + l^{non-prompt} + E_T^{miss} + jets(inc.1b) \\ 2l^{prompt} + l^{non-prompt} + E_T^{miss} + jets(inc.1b) \end{cases} . \quad (4.6)$$

Because of the complexity of the processes involved and limitations in the MC simulations a data-driven method is used to get reliable estimates for this background. This method is the $Matrix\ Method$ [83].

Description of the Matrix Method

The method is based on the connection between the quality of the leptons (tight/loose identification) and the rates at which a loose (L) prompt lepton (real efficiency ε_r) or loose non-prompt lepton (fake efficiency ε_f) could be also tight (T). The matrix method gives the number of non-prompt leptons in the pre-MVA regions by splitting the events in four orthogonal categories:

— N^{TT} : event with both leptons passing tight selection .
— $N^{T\bar{T}}$: event with leading lepton passing tight selection and subleading lepton failing tight selection, but passing the loose one.
— $N^{\bar{T}T}$: event with leading lepton failing tight selection, but passing the loose one, and subleading lepton passing tight selection.

— $N^{\bar{T}\bar{T}}$: event with both leptons failing tight selection, but passing the loose one.

A 4×4 efficiency matrix can be defined to map the total number of such events into the total number of events in four dileptonic regions characterized by different real and fake lepton composition, namely:

— N^{rr} : event with both leptons being real.

— N^{rf} : event with leading lepton being real and subleading lepton being fake.

— N^{fr} : event with leading lepton being fake and subleading lepton being real.

— N^{ff} : event with both leptons being fake.

In a matrix form this can be written as

$$\begin{pmatrix} N^{TT} \\ N^{T\bar{T}} \\ N^{\bar{T}T} \\ N^{\bar{T}\bar{T}} \end{pmatrix} = \begin{pmatrix} \varepsilon_{r,1}\varepsilon_{r,2} & \varepsilon_{r,1}\varepsilon_{f,2} & \varepsilon_{f,1}\varepsilon_{r,2} & \varepsilon_{f,1}\varepsilon_{f,2} \\ \varepsilon_{r,1}\bar{\varepsilon}_{r,2} & \varepsilon_{r,1}\bar{\varepsilon}_{f,2} & \varepsilon_{f,1}\bar{\varepsilon}_{r,2} & \varepsilon_{f,1}\bar{\varepsilon}_{f,2} \\ \bar{\varepsilon}_{r,1}\varepsilon_{r,2} & \bar{\varepsilon}_{r,1}\varepsilon_{f,2} & \bar{\varepsilon}_{f,1}\varepsilon_{r,2} & \bar{\varepsilon}_{f,1}\varepsilon_{f,2} \\ \bar{\varepsilon}_{r,1}\bar{\varepsilon}_{r,2} & \bar{\varepsilon}_{r,1}\bar{\varepsilon}_{f,2} & \bar{\varepsilon}_{f,1}\bar{\varepsilon}_{r,2} & \bar{\varepsilon}_{f,1}\bar{\varepsilon}_{f,2} \end{pmatrix} \begin{pmatrix} N^{rr} \\ N^{rf} \\ N^{fr} \\ N^{ff} \end{pmatrix}. \tag{4.7}$$

To get the unknown number of events with real and fake leptons the matrix in eq. 4.7 has to be inverted

$$\begin{pmatrix} N^{rr} \\ N^{rf} \\ N^{fr} \\ N^{ff} \end{pmatrix} = \begin{pmatrix} \varepsilon_{r,1}\varepsilon_{r,2} & \varepsilon_{r,1}\varepsilon_{f,2} & \varepsilon_{f,1}\varepsilon_{r,2} & \varepsilon_{f,1}\varepsilon_{f,2} \\ \varepsilon_{r,1}\bar{\varepsilon}_{r,2} & \varepsilon_{r,1}\bar{\varepsilon}_{f,2} & \varepsilon_{f,1}\bar{\varepsilon}_{r,2} & \varepsilon_{f,1}\bar{\varepsilon}_{f,2} \\ \bar{\varepsilon}_{r,1}\varepsilon_{r,2} & \bar{\varepsilon}_{r,1}\varepsilon_{f,2} & \bar{\varepsilon}_{f,1}\varepsilon_{r,2} & \bar{\varepsilon}_{f,1}\varepsilon_{f,2} \\ \bar{\varepsilon}_{r,1}\bar{\varepsilon}_{r,2} & \bar{\varepsilon}_{r,1}\bar{\varepsilon}_{f,2} & \bar{\varepsilon}_{f,1}\bar{\varepsilon}_{r,2} & \bar{\varepsilon}_{f,1}\bar{\varepsilon}_{f,2} \end{pmatrix}^{-1} \begin{pmatrix} N^{TT} \\ N^{T\bar{T}} \\ N^{\bar{T}T} \\ N^{\bar{T}\bar{T}} \end{pmatrix}. \tag{4.8}$$

All the events with tight leptons and at least one fake lepton

$$N^{f}_{TT} = w_{TT}N^{TT} + w_{\bar{T}T}N^{\bar{T}T} + w_{T\bar{T}}N^{T\bar{T}} + w_{\bar{T}\bar{T}}N^{\bar{T}\bar{T}} \tag{4.9}$$

The w weights are functions of the measured prompt and non-prompt lepton efficiencies.

Real and fake efficiency measurement for the Matrix Method

The efficiencies are measured in $t\bar{t}$ events with a tag-and-probe method in the low jet multiplicity ($2 \leq N_{jet} \leq 3$) CRs. The low jet multiplicity assures orthogonality to the high jet multiplicity SR ($N_{jet} \geq 4$). Additionally, at least 1 b-jet is required.

The real efficiency is defined as

$$\varepsilon_r = \frac{N^{T}_{data} - N^{T}_{non-prompt(MC)}}{N^{L}_{data} - N^{L}_{non-prompt(MC)}} \tag{4.10}$$

where $N^{T(L)}_{non-prompt(MC)}$ represents the tight (loose) non-prompt events that are subtracted from data. The real efficiency is measured in opposite charge and opposite flavour events (OCOF) to reduce backgrounds. The Tag lepton is required to be $tight$, while the $probe$ is required to pass $loose$ requirement with a $p_T > 20$ (15) GeV for 2ℓSS (3ℓ) channel. The real efficiency is parametrized in p_{T} (8 bins) and figure 4.8 show the results of the real efficiency measurement for electrons and muons. Electron real efficiency is lower by 10-30% compared to the muon real efficiency.

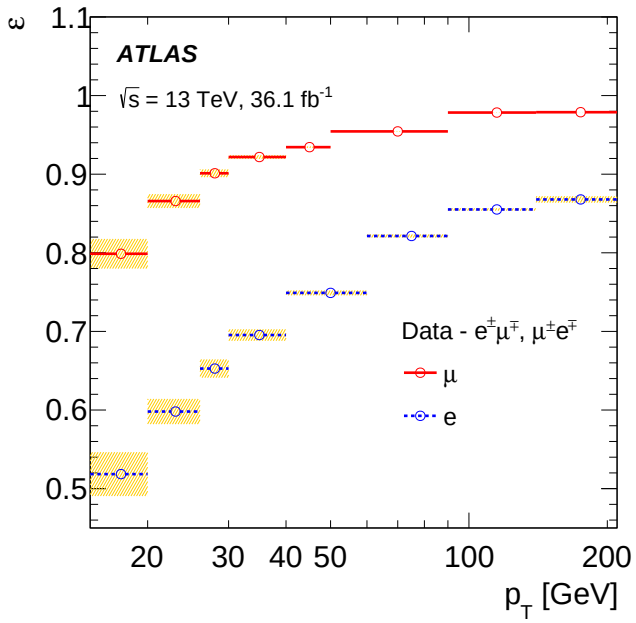

Figure 4.8 – Real efficiency for electrons and muons in terms of p_T. The orange band represents the systematic uncertainty.

The fake efficiency is defined as

$$\varepsilon_f = \frac{N^T_{data} - N^T_{qmis-ID(data)} - N^T_{prompt(MC)}}{N^L_{data} - N^L_{qmis-ID(data)} - N^L_{prompt(MC)}} \tag{4.11}$$

where $N^{T(L)}_{prompt(MC)}$ represents the tight (loose) prompt events that are subtracted from data. The $N^{T(L)}_{qmis-ID(data)}$ represents the prompt contribution from the data-driven the charge misassignment estimate.

Figure 4.9 (left) shows the electron fake efficiency measurement results in terms of p_{T} and N_{b-jet}. The parametrization in N_{b-jet} allows to better take into account the variations in the fake lepton composition. Figure 4.9 (right) shows the muon fake efficiency measurement results in terms of p_{T} and $\Delta R(\mu, jet)$. The effects of the nearby jets are included in the $\Delta R(\mu, jet)$ parametrization. The

Region	Selection criteria
	$2 \leq N_{\text{jets}} \leq 3$ and $N_{b-\text{jets}} \geq 1$
	One tight T, one loose light L lepton with $p_{\text{T}} > 20$ GeV for 2ℓSS channel
	One tight T, one loose light L lepton with $p_{\text{T}} > 15$ GeV for 3ℓ channel
	Zero τ_{had} Medium candidates
ε_{r}	Opposite charge; opposite flavour
Electron ε_{f}	Same charge; Opposite flavour (tag=μ T)
Muon ε_{f}	Same charge; $\mu\mu$ (tag=μ T)

Table 4.5 – Control region definitions used for the non-prompt lepton estimates. Final selection applied to obtain prompt lepton efficiencies (ε_r) and fake lepton rates (ε_f) are given.

binning has been optimized to capture the main features of the fake efficiency variations, without compromising on signal sensitivity.

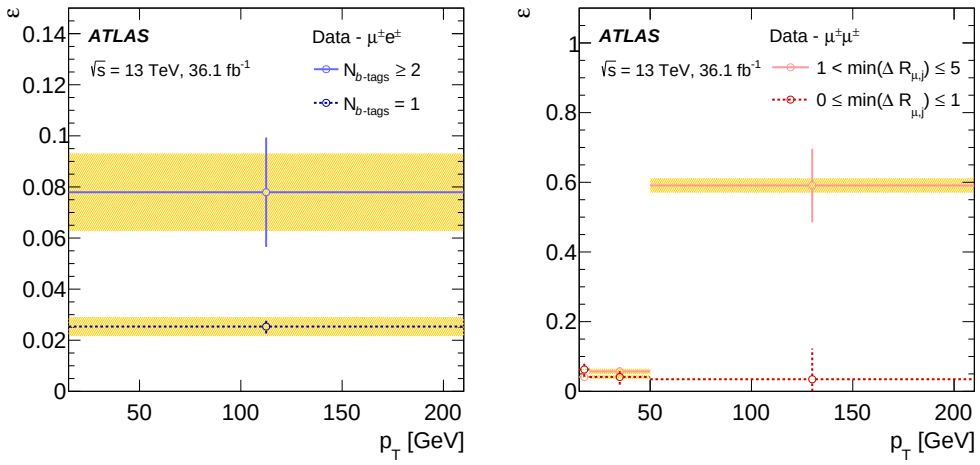

Figure 4.9 – Fake rates for electrons (left) in terms of p_T and N_{b-jets} and for muons (right) in terms of p_T and angular distance to the closest jet $\min\Delta R_{\mu,j}$. The orange bands represent the systematic uncertainty on the fake rate.

A summary of the control region definitions used for non-prompt background estimation using the Matrix Method is given in table 4.5.

4.5.2.3 Treatment of signal contamination in the control regions

In the 2ℓSS channel the signal peaks at $N_{jet} = 4$ as exactly 4 jets are expected in the final state. However, due to efficiency and acceptance effects the signal leaks in the neighboring CRs used for the non-prompt estimates ($2 \leq N_{\text{jets}} \leq 3$). For a BR($t \rightarrow Hq$) =0.2% the signal contamination accounts for 30% of the total prompt backgrounds in the CR used to measure the fake efficiency. If this signal would be real, its prompt contribution would need to be subtracted in the

fake efficiency computation, in order to have proper non-prompt background estimation.

$$\varepsilon_f = \frac{N^T_{data} - N^T_{qmis-ID(data)} - N^T_{prompt(MC)} - N^T_{t\to Hq}}{N^L_{data} - N^L_{qmis-ID(MC)} - N^L_{prompt(MC)} - N^L_{t\to Hq}} \tag{4.12}$$

Performing this test leads to a 40% (30%) decrease in the non-prompt background yields in the 2ℓSS (3ℓ) SR. Since the BR($t \to Hq$) is the parameter of interest and is extracted from the fit, this strong anti-correlation requires the non-prompt background to be dependent on the branching ratio during the fit procedure. A linear parametrization on the branching ratio is therefore introduced.

$$N_{\text{non-prompt}}(\mathfrak{B}) = N^{\text{B=0\%}}_{\text{non-prompt}} - \frac{\mathfrak{B} \times (N^{\text{B=0\%}}_{\text{non-prompt}} - N^{\text{B=0.2\%}}_{\text{non-prompt}})}{0.2\%} \tag{4.13}$$

This dependence was verified by obtaining non-prompt estimates using the Matrix Method for several branching ratio values between 0% and 0.3%. The impact of the signal contamination is not only on the overall value of the non-prompt background but it also affects the shape. To take into account this effect a shape only systematics is added, which is below statistical uncertainty for BR($t \to Hq$)<0.2 %.

In conclusion, after reviewing the most important backgrounds, the pre-fit yields for each background is given in table 4.6 for 2ℓSS and 3ℓ SRs. A visual representation of the background composition is given in figure 4.10 (right). The non-prompt background is the main background with a contribution of around 50% (45%) in the 2ℓSS (3ℓ) channel. The $t \to Hq$ signal composition by Higgs decay mode in the 2ℓSS and 3ℓ channel is given in figure 4.10 (left). Clear dominance of the $H \to WW^*$ decay mode can be observed.

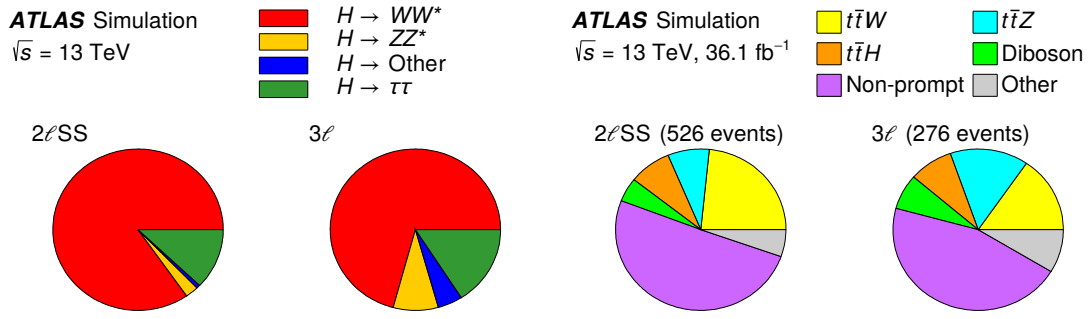

Figure 4.10 – Signal contributions by H decay (left). Background composition in 2ℓSS and 3ℓ channels (right).

Pre-MVA Region	Non-prompt lep.	$t\bar{t}W$	$t\bar{t}Z$	$t\bar{t}H$	Diboson	Other	Total Bkg
			Pre-fit yields				
2ℓSS	266 $\pm$ 40	123 $\pm$ 18	41.4 $\pm$ 5.7	42.6 $\pm$ 4.3	25 $\pm$ 15	28.4 $\pm$ 5.9	526 $\pm$ 39
3ℓ	126 $\pm$ 31	42.5 $\pm$ 6.5	41.1 $\pm$ 5.1	23.1 $\pm$ 2.7	19.6 $\pm$ 11.0	23.9 $\pm$ 5.0	276 $\pm$ 33

Table 4.6 – Pre-fit expected yields in the pre-MVA regions of 2ℓSS and 3ℓ with 36.1 of data at $\sqrt{s} = 13$ TeV. Uncertainties in the background expectations due to systematic effects and MC statistics are shown. "Non-prompt" refers to the data-driven background estimates and includes the "q-mis-id" contribution (32.6 ± 11.4) for 2ℓSS. Others refers to rare processes (tZ, tW, tWZ, $t\bar{t}WW$, triboson production, $t\bar{t}t$, $t\bar{t}t\bar{t}$, tH). Extra shape uncertainty coming from top FCNC subtraction in the control region is not included in the uncertainty given for fake lepton.

4.6 Event MVA

In order to have a better signal-to-background separation and thus an enhanced sensitivity, a multivariate analysis (MVA) technique is introduced. *Boosted Decision Trees* (BDTs) are trained using TMVA [84] for discriminating the signal against the two main types of backgrounds, ttV and $non-prompt$ leptons (coming mainly from $t\bar{t}$). Given the similarities between the $t \to Hu$ and $t \to Hc$ signal processes in the 2ℓSS category, the signal used for trainings in this category was the combination of the two ($t \to Hu$ + $t \to Hc$). It is not the case for the 3ℓ category and separate trainings are performed to achieve better separation. The summary of the BDTs used in the analysis is given in table 4.7.

For each BDT a number of input variables (pre-MVA selections) like kinematic properties, lepton flavor, jet properties and angular distances between objects are fed in. Individual input variables have limited signal-to-background discrimination, however they grasp a relatively complementary level of information about the difference between the signal and the background.

For each variable, the separation power S for a variable distribution plotted in an histogram with N_{bin} is computed as:

$$S = \frac{1}{2} \sum_{i=1}^{N_{\text{bin}}} \frac{(N_i^S - N_i^B)^2}{N_i^S + N_i^B} \tag{4.14}$$

channel / measurement	BR($t \to Hu$)	BR($t \to Hc$)
2ℓSS	($t \to Hu$+ $t \to Hc$) *vs.* $t\bar{t}V$ ($t \to Hu$+ $t \to Hc$) *vs.* non-prompt	
3ℓ	$t \to Hu$ *vs.* $t\bar{t}V$ $t \to Hu$ *vs.* non-prompt	$t \to Hc$ *vs.* $t\bar{t}V$ $t \to Hc$ *vs.* non-prompt

Table 4.7 – Summary of the BDT trainings performed per category.

where N_i^S and N_i^B are the entries in each bin i of the normalized signal and background distributions, respectively. It is illustrated in Figure 4.11 for the most discriminant variable in the 2ℓSS (left) and 3ℓ (right) channels.

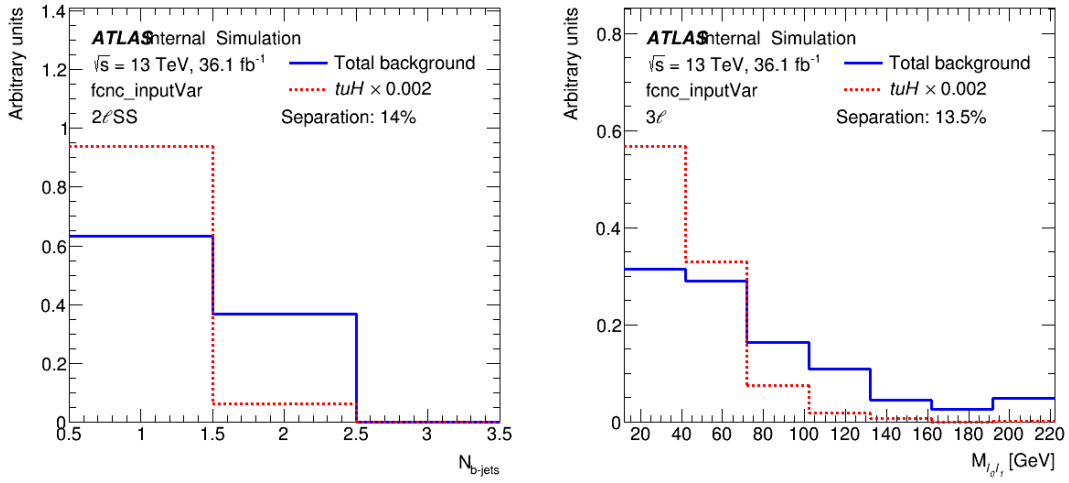

Figure 4.11 – Normalized distribution of the most discriminant variable for $t \to Hu$ signal and all background : Number of b-jet in 2ℓSS pre-MVA region (left) and ℓ_0-ℓ_1 invariant mass (right). The first and last bins include the underflows and overflows.

The choice of the variables rely on a few factors.

— The variables are defined to have a physical meaning so that they could be easily understood and interpreted
— The separation power
— Highly correlated variables are not desired as no new information is added
— For reliable results good data modeling is required

Taking into account all the above mentioned criteria allowed us to develop a robust and optimal setup.

Overall, the $t \to Hq$ signal events are softer events compared to the two main backgrounds having a lower effective mass, m_{eff} [2], and have one true b-jet in final state (eq. 4.2 vs. eq. 4.3 and 4.6). The BDT is able to exploit this fact and to encapsulate all these informations into a single number. The output of the BDT is a score that accounts for the likelihood of an event being background or signal (usually from -1 to 1). The input variables for 2ℓSS (3ℓ) category are discussed in section 4.6.1 (4.6.2). For simplicity the same set of input variables were used for both $t\bar{t}V$ and non-prompt discrimination in the same category.

Finally, the BDT scores for the two backgrounds are combined (linear combination parametrized by the weight a) into a final BDT discriminant that is subject

2. The effective mass is defined as $m_{eff} = E_T^{miss} + H_T$, where H_T is the scalar sum of the jets and leptons p_T in the event.

of fit procedure after an optimization is performed.

$$BDT = \frac{BDT(t\bar{t}V) + a \times BDT(\textit{non-prompt})}{1 + a} \tag{4.15}$$

4.6.1 2ℓSS category

For the 2ℓSS channel a total of 11 input variables were used for the BDTs training. These variables are enumerated in table 4.8, sorted by their separation power. The most discriminating variable (for both $t\bar{t}V$ and non-prompt) is the number of b-jets. This is explained by the fact that for the signal processes only one b-jet is expected in the final state, while for the backgrounds two b-jets are expected. Important discrimination for the non-prompt is brought by lower p_T of the sub-leading lepton of the non-prompt leptons.

Compared to the $t\bar{t}V$ system, the $t\bar{t}$ ($t \to Hq$) system is less energetic in terms of m_{eff} and has lower $p_T(l_0)$ (non-boosted production). Figure 4.12 shows the plots for all the input variables. Good agreement between data and the prediction is observed for all variables within the uncertainty. The overall impact of using the BDT is an increase in the separation by ≈ 1.4 for $t \to Hu$ and ≈ 1.75 for $t \to Hc$ comparing the final BDT discriminant and the most powerful input variable (table 4.8).

Signal	$t \to Hu$			$t \to Hc$		
Background	All	Fake lepton	$t\bar{t}V$	All	Fake lepton	$t\bar{t}V$
Number of b-tagged jets	14.0	10.8	20	6.1	3.8	10.6
m_{eff} =E_T^{miss} +H_T	7.3	2.0	14.0	8.0	2.7	14.6
ΔR l_1–closest jet	3.2	5.2	2.7	3.6	5.8	3.0
Missing transverse energy E_T^{miss}	2.8	0.4	6.7	2.5	0.3	6.2
Leading lepton p_T	2.8	2.7	7.8	2.2	3.2	6.2
ΔR l_0–closest jet	2.1	4.0	1.6	1.9	3.8	1.4
Lepton flavour	2.0	4.2	0.1	1.9	4.0	0.2
Second leading lepton p_T	1.4	7.3	3.7	1.2	6.5	4.2
Maximum $\|\eta\|$ between two leptons	1.0	1.7	0.6	1.5	2.0	1.3
Number of jets	1.0	0.2	1.5	2.0	0.7	2.7
Dilepton invariant mass M(l_0,l_1)	1.0	4.3	2.5	0.4	4.1	1.9
BDT_ttbar(2l), 8bins	16.4	25.6	–	11.9	18.6	–
BDT_ttV(2l), 8bins	18.6	–	36.2	13.2	–	31
(BDT_ttbar(2l)+BDT_ttV(2l))/2, 8bins	19.6	–	–	14	–	–

Table 4.8 – Separation power between different type of background and $t \to Hu$ or $t \to Hc$ signal in % for the variables used in the multivariate analysis of the 2ℓSS channel. l_0 and l_1 are the leading and subleading leptons, respectively.

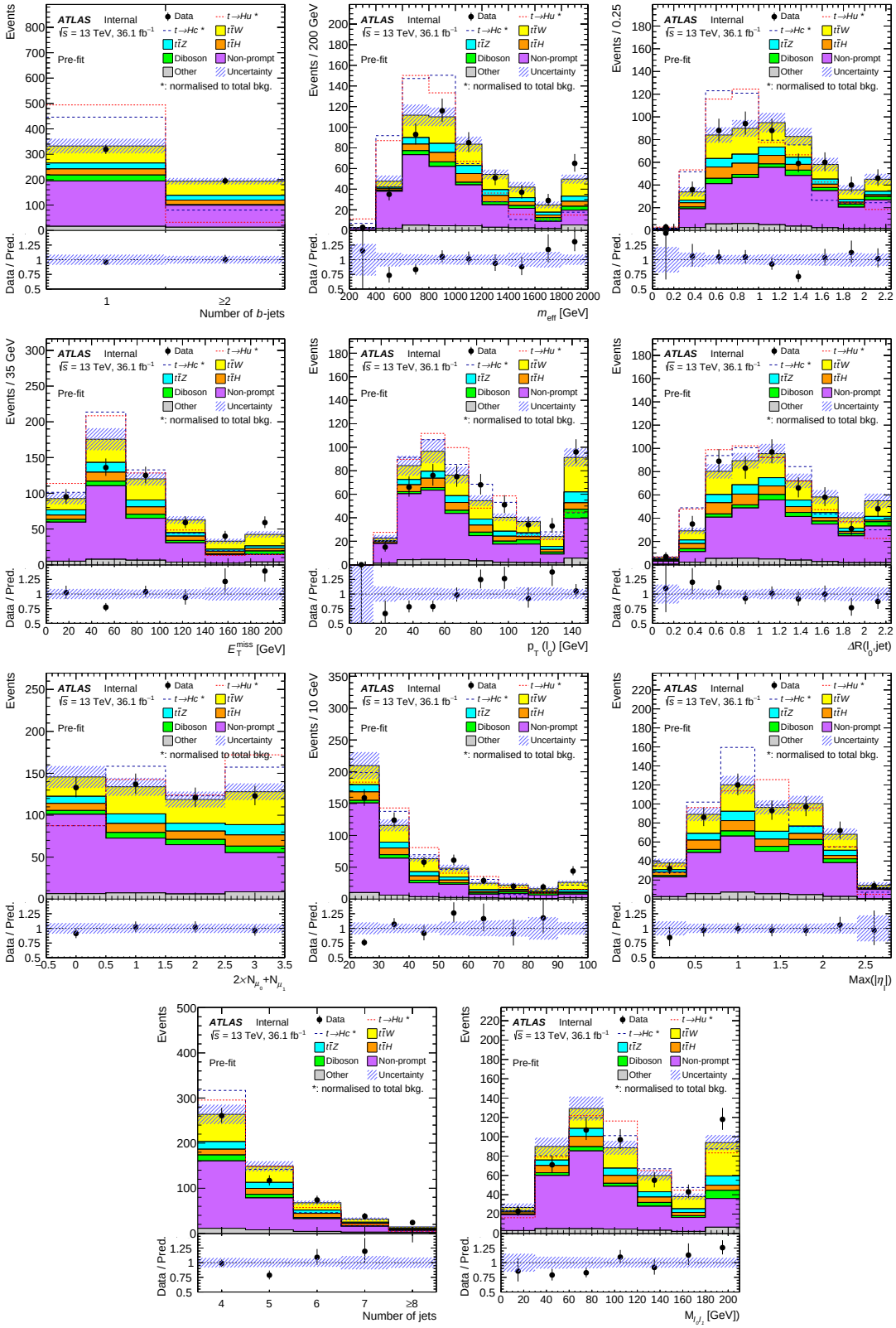

Figure 4.12 – Input variables for 2ℓSS category sorted by separation power. The red dotted (blue dashed) line shows the $t \to Hu$ ($t \to Hc$) shape normalized to the background. The errors for the prediction correspond to statistical and systematic uncertainties. The errors assigned to data are Poissonian.

Figure 4.13 (left) shows the non-prompt BDT distributions where non-prompt background is collected on the lower BDT part while the signal peaks clearly in the high BDT region. A similar picture can be seen in the case of the $t\bar{t}V$ BDT in figure 4.13 (middle). Finally, figure 4.13 (right) shows the combination of the two BDTs.

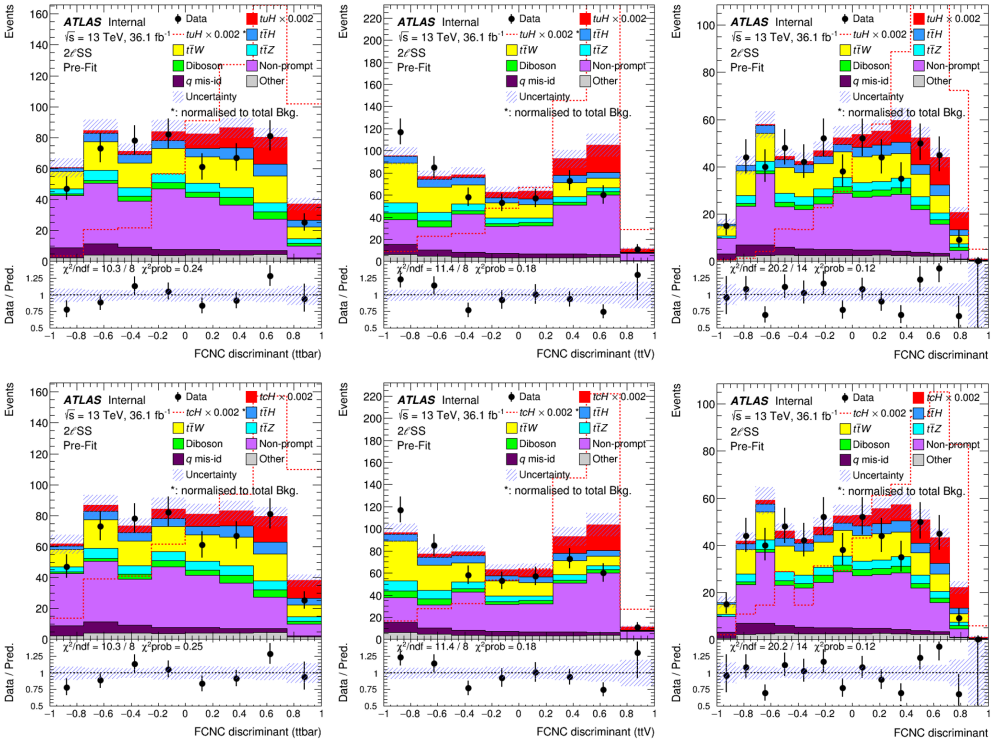

Figure 4.13 – Pre-fit distributions of the output MVA variable distributions in the 2ℓSS pre-MVA region for data and signal $t \to Hu$ ($t \to Hc$) + background prediction in the upper (lower) plot(up). From left to right $BDTG\_ttbar(2l)$, $BDTG\_ttV(2l)$ and the average sum of both. The signal is not included in the prediction of the ratio plot. Events with fake/non-prompt leptons and charge-flip electrons are estimated using data-driven methods and the irreducible background using MC samples. Errors on prediction include statistic and all systematic uncertainties described in Table 4.13 and are Poissonian for data.

4.6.2 3ℓ category

Because there is one more lepton in the 3ℓ category compared to 2ℓSS, there are more options in terms of input variables, particularly because of relative quantities involving combinations of objects (like the invariant mass of a pair of leptons or angular distances between leptons and/or jets). From an initial pool

of 25 variables, a total of 18 variables were selected based on the separation power. Configurations using either all the initial variables or a shorter list (best 10 variables) are tested and the chosen option is found to be the optimal one. The 18 selected variables are listed in table 4.9, sorted by their separation power.

Signal	$t \to Hu$			$t \to Hc$		
Background	All	Fake lepton	$t\bar{t}V$	All	Fake lepton	$t\bar{t}V$
Dilepton invariant mass M(l_0,l_1)	13.5	8.4	23.0	12.2	7.4	21.2
m_{eff} =E_T^{miss} +H_T	11.0	3.1	23.0	5.2	0.8	14.9
Number of b-tagged jets	10.4	4.7	20.1	4.4	0.9	12.1
Leading lepton p_{T}	8.6	9.8	9.8	9.7	10.8	11.2
Dilepton invariant mass M(l_0,l_2)	7,3	6.9	11.9	7.4	6.8	12.1
ΔR l_0–l_1	6.9	10.4	7.4	4.9	7.9	6.2
Best Z-candidate dilepton invariant mass	6.7	8.9	8.6	10.2	12.8	11.7
Three-lepton invariant mass	6.3	5.6	12.6	7.3	6.2	13.5
Number of jets	4.9	3.3	9.2	2.6	2.6	6.1
Smallest ΔR l_0–b-tagged jet	4.5	3.6	9.2	1.0	0.8	3.8
Second leading jet p_{T}	4.2	4.2	9.6	2.9	4.1	7.8
Third leading lepton p_{T}	3.7	5.3	6.4	3.2	6.1	4.0
Second leading lepton p_{T}	3.5	3.8	8.2	1.3	6.2	4.0
Leading jet p_{T}	3.3	1.7	6.8	2.0	1.1	4.9
ΔR l_0–l_2	2.0	2.9	2.0	2.8	4.1	3.1
ΔR l_1–closest jet	1.7	4.1	0.8	2.0	4.9	0.3
Dilepton invariant mass M(l_1,l_2)	1.5	1.2	3.9	0.8	1.1	2.8
Leading b-tagged jet p_{T}	1.5	1.6	3.1	2.4	2.0	4.6
BDT_ttbar(3l)*, 8bins	17.9	27.3	–	16.9	26.8	–
BDT_ttV(3l)*, 8bins	26.5	–	50.2	16.5	–	37.0
(BDT_ttbar(3l)+BDT_ttV(3l))/2*, 8bins	28.9	–	–	21.7	–	–

Table 4.9 – Separation power between different type of background and $t \to Hu$ or $t \to Hc$ signal in % for the variables used in the multivariate analysis of the 3ℓ channel. For 3ℓ, l_0 is the lepton of opposite charge to the same-charge pair, while the same-charge leptons are labeled with increasing index (l_1 and l_2) as p_{T} decreases. The best Z-candidate dilepton invariant mass is the mass of the dilepton pair closest to the Z boson mass. *BDTs for $t \to Hu$ and $t \to Hc$ are different.

Like in the case of the 2ℓSS category, m_{eff}, the number of b-jets and the leading lepton p_T have large separation power. The dilepton invariant masses M(l_0,l_1) and M(l_0,l_2), and the angular distance $\Delta R(l_0, l_1)$ have large separation power and this is related to the spin correlation in the dominant $H \to WW^*$ decay mode. Figure 4.14 shows the first half of the variables while figure 4.15 show the second half. Good data to prediction agreement is observed for all variables, within the uncertainties.

Figure 4.16 (left) shows the non-prompt BDT distributions where non-prompt background is collected on the lower BDT part while the signal peaks clearly in the high BDT region. A similar picture can be seen in the case of the $t\bar{t}V$ BDT in figure 4.16 (middle). Finally, figure 4.16 (right) shows the combination of the two BDTs.

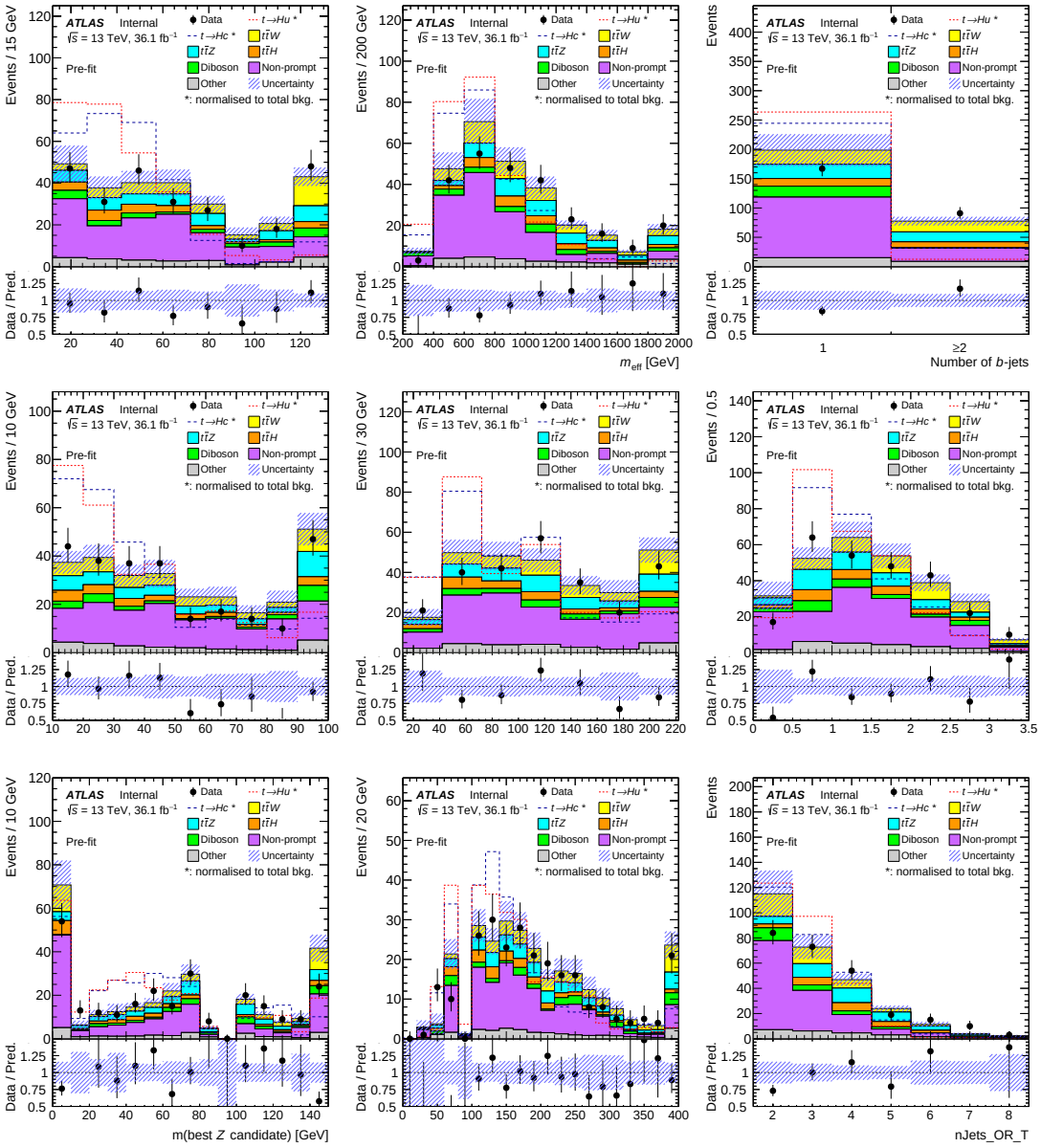

Figure 4.14 – First 9 input variables for 3ℓ category sorted by separation power. The red dotted (blue dashed) line shows the $t \to Hu(t \to Hc)$ shape normalized to the background.The errors for the prediction correspond to statistical and systematic uncertainties. The errors assigned to data are Poissonian.

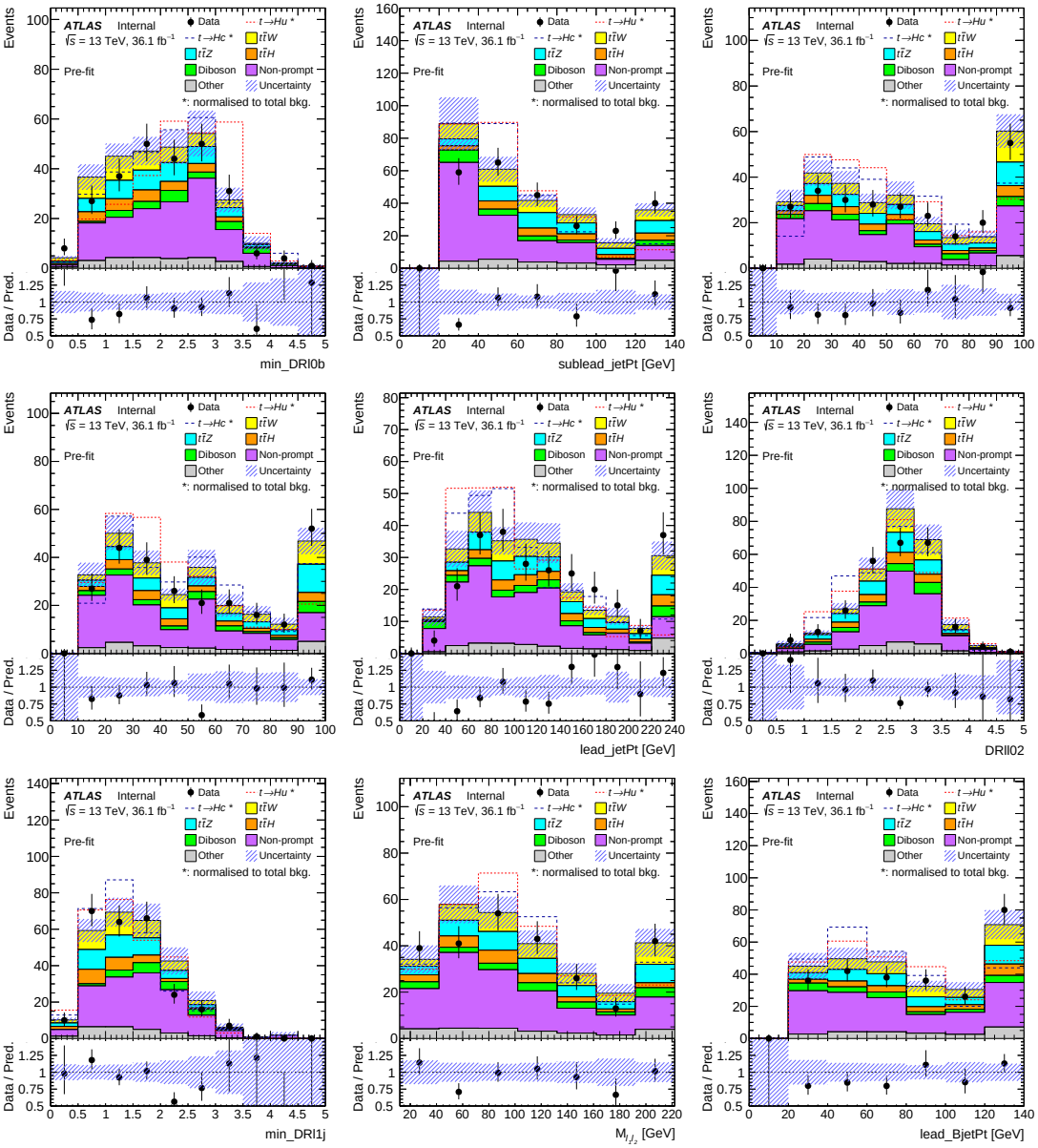

Figure 4.15 – Last 9 input variables for 3ℓ category sorted by separation power. The red dotted (blue dashed) line shows the $t \to Hu$ $(t \to Hc)$ shape normalized to the background. The errors for the prediction correspond to statistical and systematic uncertainties. The errors assigned to data are Poissonian.

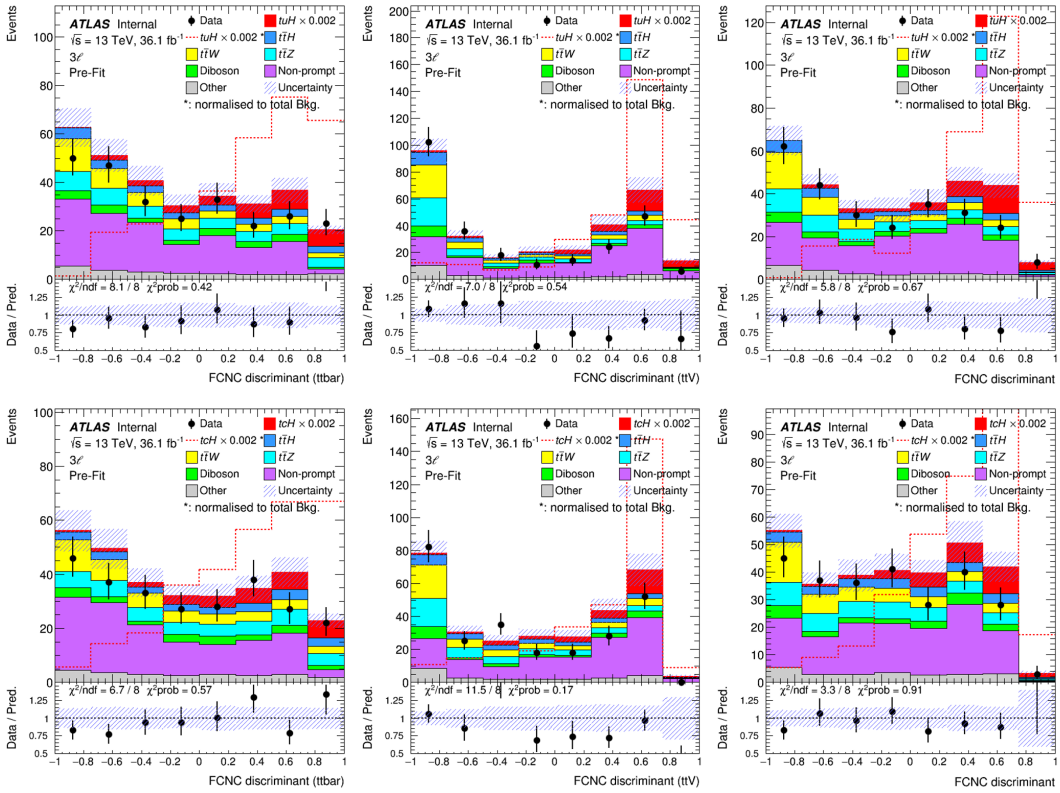

Figure 4.16 – Pre-fit distributions of the output MVA variable distributions in the 3ℓ pre-MVA region for data and signal $t \to Hu$ ($t \to Hc$) + background prediction in the upper (lower) plot. From left to right $BDTG\_ttbar(3l)$, $BDTG\_ttV(3l)$ and the average sum of both. The signal is not included in the prediction of the ratio plot. Events with fake/non-prompt leptons and charge-flip electrons are estimated using data-driven methods and the irreducible background using MC samples. Errors on prediction include statistic and all systematic uncertainties described in Table 4.13 and are Poissonian for data. T

4.6.3 Optimization

Further improvement in sensitivity is achieved with three parameters:

1. a, weight in the weighted average of the final discriminant (eq. (4.15))
2. $N(bin)$, number of bins in the final discriminant
3. width of bins in the final discriminant

The width of the bins is determined using an iterative algorithm, with the purpose to avoid large statistical uncertainties in particular bins and to improve signal and background separation. Initially, the BDT distribution is split into a large number of bins (10^5 for this analysis). Starting from the upper limit, the BDT distribution is scanned and the fine bins are merged. When a specific amount of signal and background events is reached, the final bin boundary is defined. The condition for defining the bin boundary is $Z \geq 1$ with

$$Z = z_b \frac{n_b}{N_b} + z_s \frac{n_s}{N_s}, \tag{4.16}$$

where N_b and N_s are the total number of background and signal events, n_b and n_s are the amount of background and signal events in the merged bin, and z_b and z_s are tunable parameters satisfying

$$N(bin) = z_b + z_s. \tag{4.17}$$

This binning transformation is refereed to as `TransfoD(`z_b`,`z_s`)`. For the extreme case $z_s = N(bin)$ ($z_b = N(bin)$), a flat distribution in signal (background) is obtained, which corresponds to equal amount of signal (background) in every bin.

The optimization of the final discriminant is performed for top FCNC $t \to Hu$ and $t \to Hc$ signal. The 95% CL upper limit on B($t \to Hu$) and B($t \to Hc$) is the quantity that is optimized for and it is obtained using a close-to-final fit set-up (detector systematics not included). This allowed to speed up the optimization as a large number of fits are required and it explains the slight difference compared to the final results presented in Table 4.15 and 4.16.

4.6.3.1 2ℓSS channel

Table 4.10 summarizes the optimization procedure for the final discriminant $BDT(2\ell SS)$ as given by the equation (4.15). The optimization is performed for both the B($t \to Hu$) and B($t \to Hc$) however only one set of parameters is chosen finally for both processes.

The best compromise for the optimized parameters:
— The weight for non-prompt BDT in the linear combination, a=3
— Number of bins for the final discriminant, N(bin) = 6

Test Characteristics	Number of bin scan with $a = 1$				
$z_s + z_b$ =N(bin)=	5	**6**	7	8	9
95% CL Upper limit on B($t \to Hu$)	0.229%	**0.205%**	0.201%	0.198%	0.199%
95% CL Upper limit on B($t \to Hc$)	0.183%	**0.181%**	0.182%	0.180%	0.183%

Test Characteristics	Background weight scan with $a = 1$ and N(bin)=6			
z_b =	**0**	1	2	3
95% CL Upper limit on B($t \to Hu$)	**0.205%**	0.197%	0.193%	0.201%
95% CL Upper limit on B($t \to Hc$)	**0.181%**	0.178%	0.194%	0.206%

Test Characteristics	Slope scan with $z_s = 6$ and $z_b = 0$			
a=	1	2	**3**	4
95% CL Upper limit on B($t \to Hu$)	0.205%	0.205%	**0.203%**	0.207%
95% CL Upper limit on B($t \to Hc$)	0.181%	0.170%	**0.178%**	0.176%

Table 4.10 – Expected 95% CL Upper limit on B($t \to Hu$) and B($t \to Hc$) obtained when scanning the a, z_b and z_s parameters used to build the final discriminant for 2ℓSS category. The signal sensitivity is defined from the Asimov fit. The final choice is indicated in bold.

— Bins width determined by `TransfoD(`z_b`,`z_s`)`, with (z_b,z_s)=(0,6), which corresponds to a flat signal distribution

The final discriminant for the 2ℓSS category is therefore given by

$$BDT(2\ell SS) = \frac{BDT(t\bar{t}V) + 3 \times BDT(\text{non-prompt})}{4}, \text{with } \texttt{TransfoD(0,6)} \tag{4.18}$$

A 2D visualization of this discriminant is proposed in Figure 4.17. The 6 bins of the final discriminant $BDT(2\ell SS)$ in the 2D plan are separated by the black lines which have a slope determined by the relative contribution of each BDT in the final discriminant. In the 2ℓSS category the non-prompt BDT has larger impact due to the weight a=3 in the final discriminant. The events populating the bottom left part mostly have 2 b-jets.

4.6.3.2 3ℓ channel

Table 4.11 summarizes the optimization procedure for the final discriminant $BDT(3\ell)$ as given by the equation (4.15). The optimization is performed for both the B($t \to Hu$) and B($t \to Hc$) however only one set of parameters is chosen finally for both processes.

The best compromise for the optimized parameters:

— The weight for non-prompt BDT in the linear combination, a=1

— Number of bins for the final discriminant, N(bin) = 4

— Bins width determined by `TransfoD(`z_b`,`z_s`)`, with (z_b,z_s)=(0,4) , which corresponds to a flat signal distribution

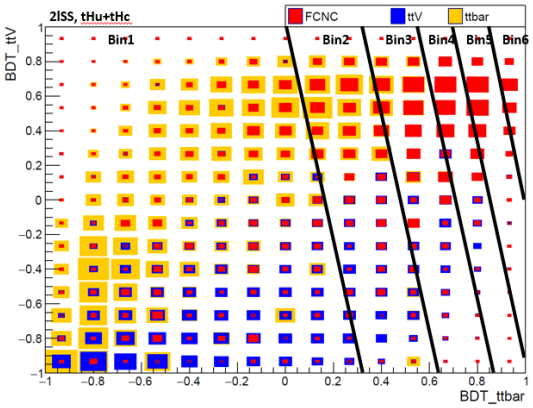

Figure 4.17 – 2D map of the final discriminant for 2ℓSS. The black lines show the bins boundaries after optimization.

The final discriminant for the 3ℓ category is therefore given then by

$$BDT(3\ell) = \frac{BDT(t\bar{t}V) + BDT(\text{non-prompt})}{2}, \text{with } \texttt{TransfoD(0,4)} \qquad (4.19)$$

A 2D visualization of this discriminant is proposed in Figure 4.18 . The 4 bins of the final discriminant $BDT(3\ell)$ in the 2D plan are separated by the black lines which have a slope determined by the relative contribution of each BDT in the final discriminant. Unlike the case of the 2ℓSS category, in the 3ℓ category the non-prompt BDT and the $t\bar{t}V$ BDT have the same weight (a=1) which lead to a final discriminant that is simply the average of the two. Subsequently, the slope of the lines defining the bins in the 2D plan is -1. The events populating the bottom left part mostly have 2 b-jets.

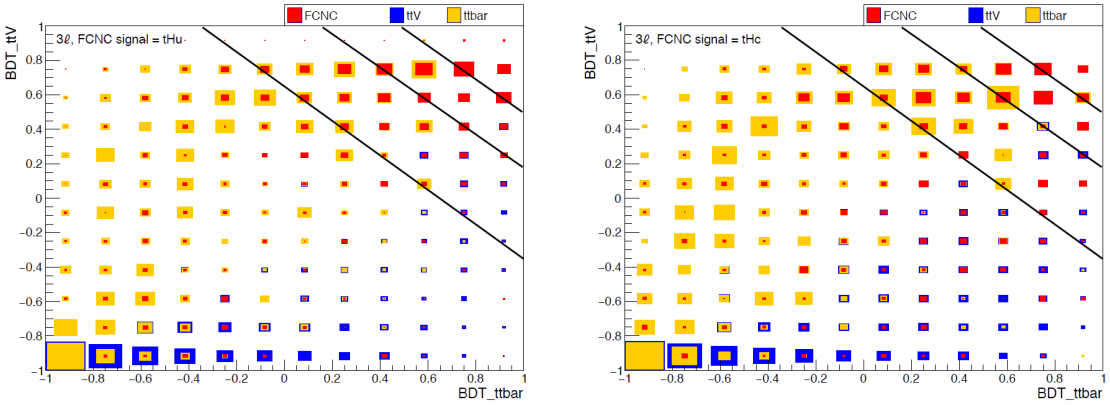

Figure 4.18 – 2D map of the final discriminant for 3ℓ category for $t \to Hu$ (left) and $t \to Hc$ (right). The black lines show the bins boundaries after optimization.

The final discriminants given by the equations (4.18) and (4.19) are used in

Test Characteristics	Number of bin scan with $a = 1$				
$z_s + z_b$ =N(bin)=	3	**4**	5	6	7
95% CL Upper limit on B($t \to Hu$)	0.222%	**0.205%**	0.192%	0.191%	0.200%
95% CL Upper limit on B($t \to Hc$)	0.367%	**0.266%**	0.287%	–	–

Test Characteristics	Background weight scan with $a = 1$ and N(bin)=4	
z_b =	**0**	1
95% CL Upper limit on B($t \to Hu$)	**0.205%**	0.217%
95% CL Upper limit on B($t \to Hc$)	**0.266%**	0.318%

Test Characteristics	Slope scan with $z_s = 4$ and $z_b = 0$		
a=	0.5	1	1.5
95% CL Upper limit on B($t \to Hu$)	0.214%	**0.205%**	0.212%
95% CL Upper limit on B($t \to Hc$)	0.314%	**0.266%**	0.262%

Table 4.11 – Expected 95% CL Upper limit on B($t \to Hu$) and B($t \to Hc$) obtained when scanning the a, z_b and z_s parameters used to build the final discriminant for 3ℓ category. The signal sensitivity is defined from the Asimov fit. The final choice is indicated in bold.

the final fit to extract the best-fit BR($t \to Hq$) and the 95% CL upper limit for the BR($t \to Hq$). These discriminants are the 1D projection of the delimited bins in figure 4.17 and 4.18. The final discriminants are shown in figure 4.19 where a flat signal distribution can be observed.

4.7 Results

4.7.1 Fit model

A maximum-likelihood fit is performed on 2ℓSS and 3ℓ channels simultaneously to extract the branching ratio of the top FCNC $\mathfrak{B}$=B($t \to Hu$) and B($t \to Hc$) as well as its 95% CL upper limit. In the Asimov fit, pseudo-data are taken to be sum of the expected signal, assuming a given B($t \to Hq$), and total background.

The statistical analysis of the data uses a binned likelihood function $\mathcal{L}(\mathfrak{B}, \vec{\theta})$, which is constructed from a product of Poisson probability terms, to estimate B($t \to Hq$) with $q = u, c$. The Higgs boson branching fractions are fixed to their SM values. The fit uses a BDT shape as final discriminant with 10 bins (6 for 2ℓSS and 4 for 3ℓ channel respectively). The impact of systematic uncertainties on the signal and background expectations is described by nuisance parameters (NPs), $\vec{\theta}$, constrained by Gaussian or log-normal probability density functions. The latter are used for normalization factors to ensure that they are always positive. The expected numbers of signal and background events are functions of $\vec{\theta}$. The prior for each NP is added as a penalty term to the likelihood to decrease it

as soon as θ is shifted away from its nominal value. The statistical uncertainties in the simulated background predictions and the control regions used for the non-prompt and fake lepton estimates are included as bin-by-bin NPs using the Beeston–Barlow technique [85].

The test statistic, $q_{\mathfrak{B}}$, is constructed from the profile log-likelihood ratio: $q_{\mathfrak{B}} = -2\ln\Lambda_{\mathfrak{B}} = -2\ln\mathcal{L}(\mathfrak{B},\hat{\hat{\vec{\theta}}})/\mathcal{L}(\hat{\mathfrak{B}},\hat{\vec{\theta}})$, where $\hat{\mathfrak{B}}$ and $\hat{\vec{\theta}}$ are the parameters that maximize the likelihood and $\hat{\hat{\vec{\theta}}}$ are the NPs that maximize the likelihood for a given $\mathfrak{B}$. The test statistic is used to quantify how well the observed data agrees with the background-only hypothesis. The same likelihood is also used to obtain 95% CL upper limit on $\mathfrak{B}$ using the CL_s method [86, 87].

4.7.2 Systematics

A summary of all systematic uncertainties is given in Table 4.13. This list covers experimental systematics for the physics objects, systematics for the data-driven fake leptons and electron charge mis-assignment estimates (Table 4.12) that were discussed in section 4.5 as well as signal and background modeling theoretical uncertainties.

Systematic uncertainty	Type	Components
Control region statistics (fake leptons)	SN	6* (2ℓSS), 4* (3ℓ)
Control region statistics (electron QmisID)	SN	6* (2ℓSS)
Real lepton efficiencies	SN	1
Fake lepton rate	SN	6 (μ), 2 (e), 3 (bkg sub.**)
Top FCNC sub. shape in Fake lepton rate CR	S	1
Fake lepton estimate: non-closure	N	3 (2ℓSS), 1 (3ℓ)
γ-conversion fraction	N	4
Electron charge mis-assignment	SN	1
TOTAL	–	38

Table 4.12 – Sources of systematic uncertainties considered in the 2ℓSS and 3ℓ analyses for data-driven fake leptons and electron charge mis-assignment. "N" means that the uncertainty is taken as normalisation-only for all processes and channels affected, whereas "S" denotes systematics that are considered shape-only in all processes and channels. "SN" means that the uncertainty is taken on both shape and normalisation. * Corresponds to the number of bins of the final discriminant. ** $t\bar{t}W$, dibosons and combined all other prompt lepton.

Systematic uncertainty	Values	Type	Components
Luminosity	2.1%	N	1
Pile-Up reweighting		SN	1
Physics Objects			
Electron		SN	6
Muon		SN	15
Tau		SN	10
Jet energy scale and resolution		SN	26
Jet vertex fraction		SN	1
Jet flavour tagging		SN	126
E_T^{miss}		SN	3
Total (Experimental)		–	189
Data-driven non-prompt/fake leptons and charge misassignment			
Total (Table 4.12 for details)		–	38
Higgs boson branching ratio		N	4
FCNC $t \to Hq$ modelling			
Cross-section	Tab. 4.4	N	1
Renormalisation and factorisation scales		S	3
Parton Shower, Generator and ISR/FSR		SN	3
$t\bar{t}H$ modelling			
Cross section	Tab. 4.4	N	2
Renormalisation and factorisation scales		S	3
Parton shower and hadronisation model		SN	1
Shower tune		SN	1
$t\bar{t}W$ modelling			
Cross section	Tab. 4.4	N	2
Renormalisation and factorisation scales		S	3
Matrix-element MC generator		SN	1
Shower tune		SN	1
$t\bar{t}Z$ modelling			
Cross section	Tab. 4.4	N	2
QCD scale		S	3
Matrix-element MC generator		SN	1
Shower tune		SN	1
Other background modelling			
Cross section	Tab. 4.4	N	15
Shower tune (for diboson only)		SN	1
Total (Signal and background modeling)		–	48
Total (Overall)		–	275

Table 4.13 – Sources of systematic uncertainty considered in the analysis. “N" means that the uncertainty is taken as normalisation-only for all processes and channels affected, whereas “S” denotes systematics that are considered shape-only in all processes and channels. “SN" means that the uncertainty is taken on both shape and normalisation. Some of the systematic uncertainties are split into several components, as indicated by the number in the rightmost column.

4.7.3 Fit results

The extraction of the signal in the fit is performed independently for $t \to Hu$ and $t \to Hc$. The contributions from $t \to Hu$ ($t \to Hc$) is assumed to be zero when measuring $t \to Hc$ ($t \to Hu$).

Individual fits are performed per channel and a combined fit is performed as well. The results of the combined fit of the two are quoted as the final results of the measurements.

The post-fit plots of the final discriminants are given in figure 4.19. The flat signal distribution corresponds the optimized choice of binning described in section 4.6.3. Table 4.14 gives the corresponding post-fit yields together with the pre-fit yields for comparison. No significant change in the backgrounds is observed. The fitted signal has values close to 0 with high relative uncertainty (more than 100%). The fitted signal in the case of the $t \to Hc$ measurement is negative (not plotted in the post-fit plots) as no constraints are put on the measurement. This can be justified by the goal of the current analysis to perform a search for new phenomenon rather than doing a precision measurement.

The best-fit results for BR($t \to Hu$) and BR($t \to Hc$) are given in table 4.15 and 4.16. The observed branching ratios for the combined fit for $t \to Hu$ gives

$$BR(t \to Hu) = 0.04^{+0.06}_{-0.06}(stat.)^{+0.05}_{-0.04}(syst.) = 0.04^{+0.08}_{-0.07}\% \tag{4.20}$$

and

$$BR(t \to Hc) = -0.01^{+0.06}_{-0.06}(stat.)^{+0.05}_{-0.05}(syst.) = -0.01^{+0.08}_{-0.08}\% \tag{4.21}$$

for $t \to Hc$. These values are compatible to 0 as it can be also seen in figure 4.20 (left). No $t \to Hq$ FCNC processes are observed in this analysis with the current sensitivity and datasets.

Upper limits at 95% confidence level are established. These are given table 4.15 and 4.16 for $t \to Hu$ and $t \to Hc$ and are also represented graphically

Category		Non-prompt leptons	$t\bar{t}V$	$t\bar{t}H$	Diboson	Other prompt SM	Total SM	FCNC	Data
				$t \to Hu$					
2ℓSS	Pre-fit	266 ± 40	165 ± 19	43 ± 4	25 ± 15	28 ± 6	526 ± 39	61 ± 13	514
	Post-fit	240 ± 37	167 ± 18	43 ± 4	24 ± 14	28 ± 6	502 ± 33	13 ± 21	
3ℓ	Pre-fit	126 ± 31	84 ± 8	23 ± 3	20 ± 11	24 ± 5	276 ± 33	32 ± 6	258
	Post-fit	104 ± 20	84 ± 8	23 ± 3	19 ± 10	24 ± 5	254 ± 18	7 ± 11	
				$t \to Hc$					
2ℓSS	Pre-fit	266 ± 40	165 ± 19	43 ± 4	25 ± 15	28 ± 6	526 ± 39	62 ± 13	514
	Post-fit	264 ± 41	165 ± 18	42 ± 4	20 ± 11	28 ± 6	520 ± 36	-3 ± 25	
3ℓ	Pre-fit	126 ± 31	84 ± 8	23 ± 3	20 ± 11	24 ± 5	276 ± 33	30 ± 6	258
	Post-fit	116 ± 21	84 ± 8	23 ± 3	15 ± 8	23 ± 5	262 ± 19	-1 ± 12	

Table 4.14 – Pre-fit and post-fit yields for 2ℓSS and 3ℓ channels for $t \to Hu$ and $t \to Hc$. FCNC pre-fit values correspond to a BR($t \to Hq$)=0.2%.

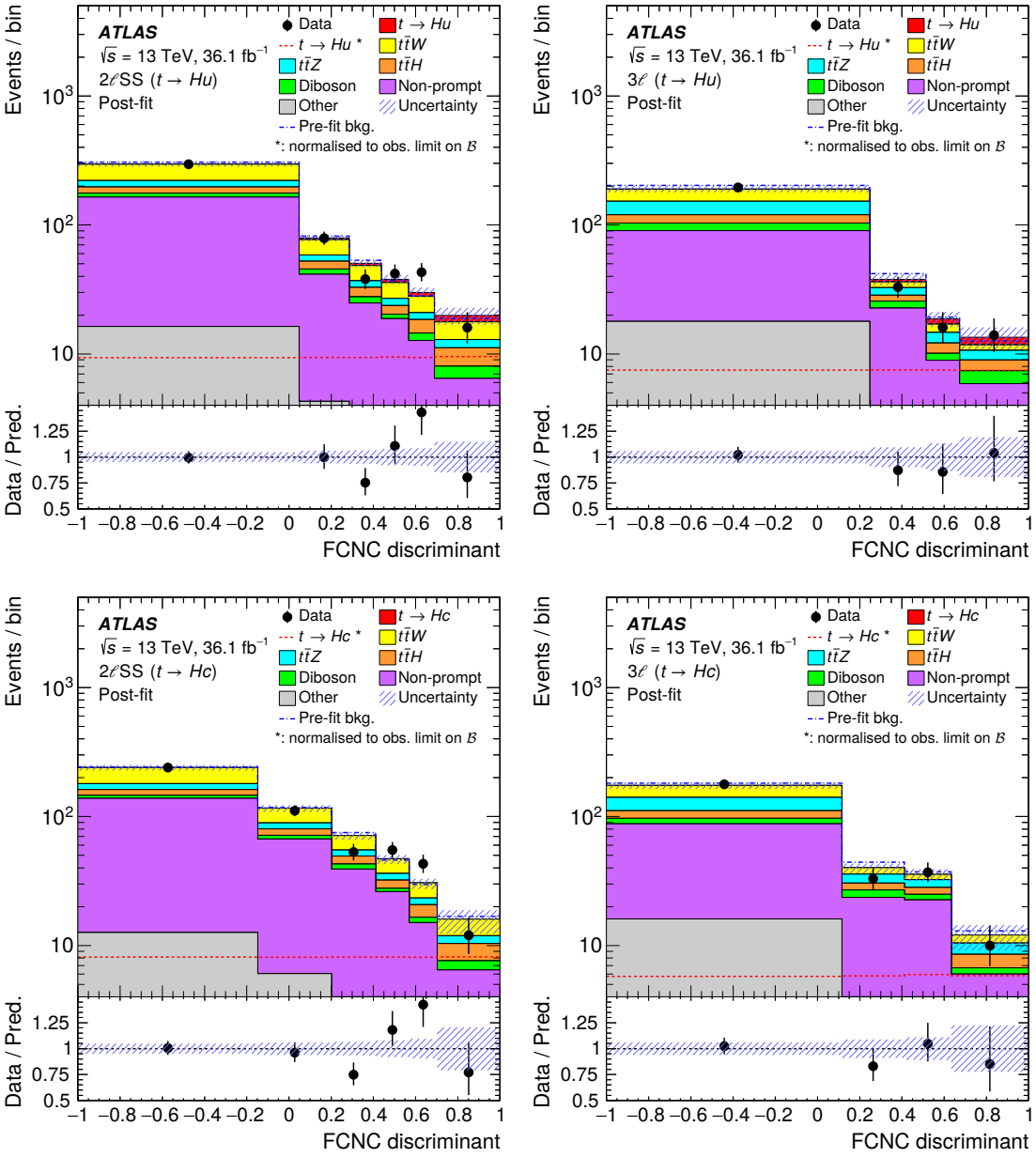

Figure 4.19 – Post-fit distribution of the FCNC discriminant for $t \to Hu$ (top) and $t \to Hc$ (bottom) in the 2ℓSS (left) and 3ℓ (right) channels. The hashed band indicates the total uncertainty in the signal-plus-background prediction, including the statistical uncertainty in the bestfit FCNC signal. The dashed red lines show the expected contribution of the respective FCNC decay with the 95% C.L. upper limit branching fraction (0.19% for $t \to Hu$, 0.16% for $t \to Hc$).

in figure 4.20 (right). The observed (expected) limits on the combined measurement are:

— BR($t \to Hu$) < **0.19 (0.15) %**

	Best-fit $\mathcal{B}(t \to Hu)$ [%]		Observed (Expected) Upper Limit on $\mathcal{B}(t \to Hu)$ [%]	
	stat.	stat. + syst.	stat.	stat. + syst.
2ℓSS	$0.08\ ^{+0.08}_{-0.08}$	$0.08\ ^{+0.11}_{-0.10}$	0.23 (0.15)	0.28 (0.21)
3ℓ	$0.01\ ^{+0.09}_{-0.08}$	$0.01\ ^{+0.10}_{-0.09}$	0.20 (0.18)	0.22 (0.21)
Combined	$0.04\ ^{+0.06}_{-0.06}$	$0.04\ ^{+0.08}_{-0.07}$	0.17 (0.12)	0.19 (0.15)

Table 4.15 – Best-fit values and 95% C.L. upper limits for B($t \to Hu$), assuming B($t \to Hc$)=0.

	Best-fit $\mathcal{B}(t \to Hc)$ [%]		Observed (Expected) Upper Limit on $\mathcal{B}(t \to Hc)$ [%]	
	stat.	stat. + syst.	stat.	stat. + syst.
2ℓSS	$0.05\ ^{+0.08}_{-0.08}$	$0.05\ ^{+0.11}_{-0.10}$	0.22 (0.15)	0.25 (0.20)
3ℓ	$-0.09\ ^{+0.10}_{-0.09}$	$-0.09\ ^{+0.11}_{-0.11}$	0.19 (0.23)	0.20 (0.25)
Combined	$-0.01\ ^{+0.06}_{-0.06}$	$-0.01\ ^{+0.08}_{-0.08}$	0.15 (0.13)	0.16 (0.15)

Table 4.16 – Best-fit values and 95% C.L. upper limits for B($t \to Hc$), assuming B($t \to Hu$)=0.

— BR($t \to Hc$) < **0.16 (0.15) %** .

These limits are the best limits for $t \to Hq$ at the time when this analysis finished and they are still the best limits to date in single measurement at the time of writing this thesis.

The systematic uncertainty is dominated by the non-prompt lepton estimation related nuisance parameters. Large effects come from the limited statistics available in the CR where the matrix method weights are applied and from the non-prompt lepton efficiency estimation. Figure 4.21 shows the first 15 nuisance parameters with the highest impact on the BR($t \to Hu$) (left) and BR($t \to Hc$) (right). As could be noted in equation (4.20) and (4.21), these results are completely dominated by the available statistics of the data set. Taking into account that the full Run 2 collected data is around 150 fb^{-1}, significant improvement is expected. A simple scaling of the integrate luminosity in the current analysis setup to 150 fb^{-1} predict a limit of 0.10 %.

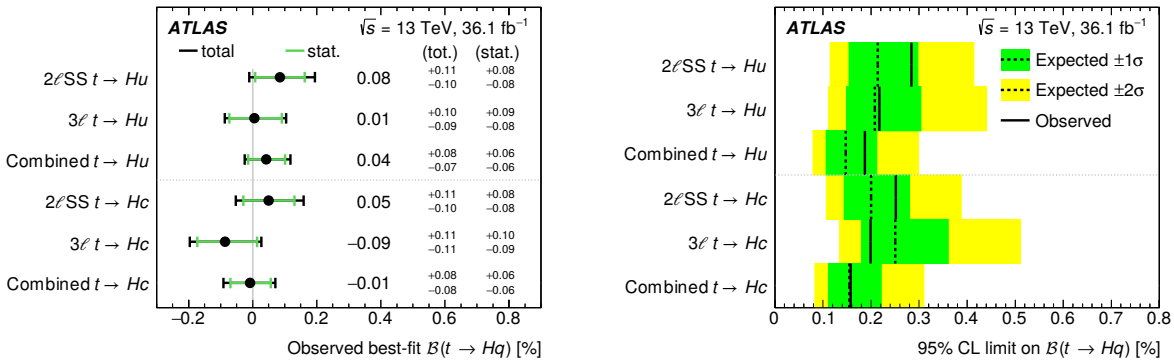

Figure 4.20 – (left) Observed best-fit values for BR($t \to Hq$). (right) Observed and expected 95% C.L. upper limits on BR($t \to Hu$) and BR($t \to Hc$). In each case, the other FCNC decay is assumed to have zero branching fraction.

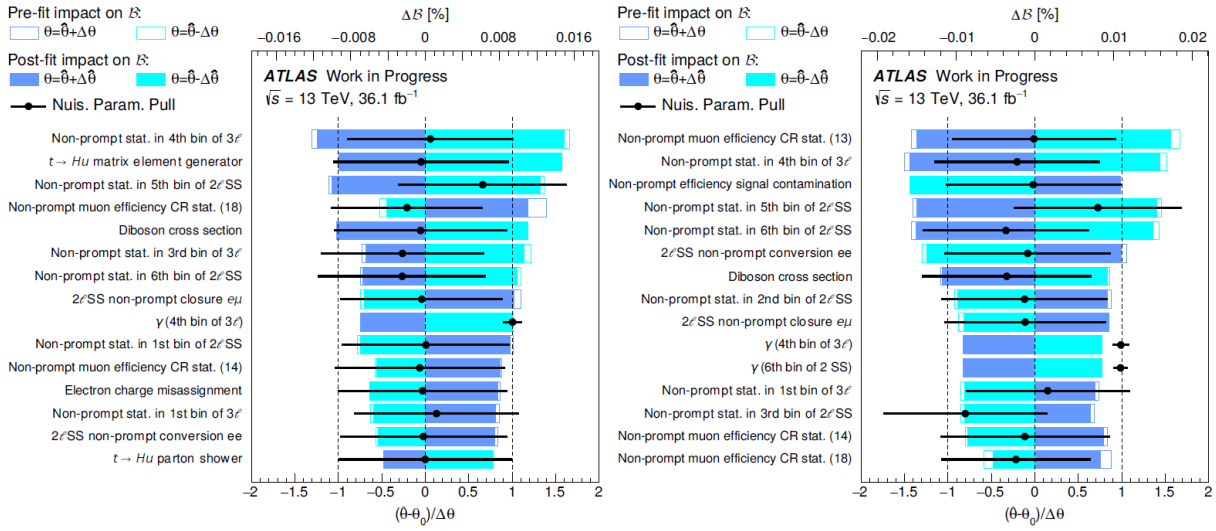

Figure 4.21 – Ranking plots of the first 15 high impact NPs for BR($t \to Hu$) (left) and BR($t \to Hc$) (right).

4.7.4 ATLAS combination

The analysis presented in this chapter is a part of a broader program of $t \to Hq$ FCNC searches at the ATLAS experiment. Orthogonal analysis are targeting other Higgs boson decays modes. A combined fit of $t \to Hq$ ($H \to WW, \tau_{lep}\tau_{lep}, ZZ$) (analysis presented in this chapter) , $t \to Hq$ ($H \to bb$) [88], $t \to Hq$ ($H \to \tau_{had}\tau_{had}, \tau_{lep}\tau_{had}$) [88] and $t \to Hq$ ($H \to \gamma\gamma$) [74] channels is performed and the upper limits at 95% CL are shown in figure 4.22.

The observed (expected) limits on the $t \to Hq$ FCNC ATLAS combined mea-

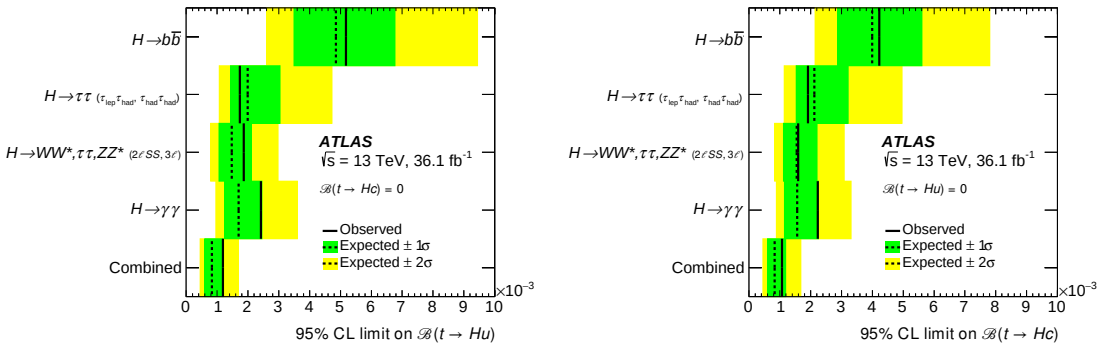

Figure 4.22 – Individual and combined observed and expected 95% C.L. upper limits on BR($t \to Hu$) (left) and BR($t \to Hc$) (right). In each case, the other FCNC decay is assumed to have zero branching fraction.

surement [88] are:

— BR($t \to Hu$) < **0.12 (0.083) %**

— BR($t \to Hc$) < **0.11 (0.083) %** .

No CMS combination results are available at the time of writing this thesis.

Including this new limits in the summary plot presented at the beginning of this chapter shows us that the 2HDM(FV) predictions starts to get constrained as can be seen in figure 4.23.

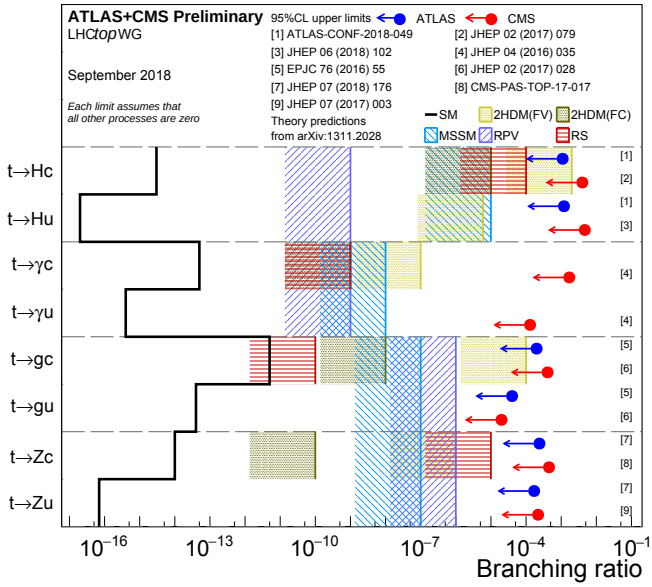

Figure 4.23 – Summary of observed upper limits at 95% confidence level of the branching ratio of top quark decays to a neutral boson (Higgs H, photon γ, gluon g or Z boson) established by ATLAS (blue) and CMS (red). The expected SM values are given by the solid black line. Hashed areas give the interval of prediction for various BSM scenarios.

4.8 Conclusions

This chapter presents a search for FCNC in top decays to a Higgs boson and an up-type quark with multilepton final states using the 36 fb^{-1} of p-p collision data collected in 2015-2016 at $\sqrt{s}$=13 TeV by the ATLAS detector.

This work allowed to set the best limit at 95% C.L. (at the time of publishing) on the top FCNC decay $t \to Hq$ ($q = u, c$) and to be sensitive to BSM theories (2HDM(FV)) for the first time.

My main contributions in this analysis are the efficiency measurement for the electron working point definition that involve the `PromptLeptonIso` and `CFT` BDTs (see section 3.4), the optimization of the MVA used (in terms of the input variables used) and optimization of the final discriminant, and running various fit crosschecks.

This analysis is published in the $Phys.RevD$ journal [66].

5 Search for Higgs boson production in association with a top-antitop quark pair

Summary

Once the Higgs boson was discovered (see section 1.4.3), the measurement of its various properties has become a priority and has led to a rich physics program at LHC to better understand the electroweak symmetry breaking mechanism. One important property of the Higgs boson is the coupling to massive particles. The coupling to fermions, the Yukawa coupling, is predicted in SM to be proportional to the mass of the fermion. In case of the top quark, $y_t = \frac{\sqrt{2}m_t}{\nu}$ (m_t is the top quark mass and ν is the *Vacuum Expectation Value* of the Higgs field), it is expected to be close to unity, $y_t \sim 1$. Any deviations from the SM would be an important hint for physics beyond SM.

The top Yukawa coupling can be measured *indirectly* in processes involving top quark loops coupled to a Higgs boson. A typical example is the most dominant

Higgs boson production process at LHC, the gluon-gluon fusion $gg \to H$, where the massless gluons do not couple directly to the Higgs boson (see figure 1.3) but rather through top and bottom quarks. Since other new particles can contribute to this process and alter the coupling y_t measurement, a comparison with a direct measurement is crucial. Any difference between the direct and indirect measurements would be an important proof of new physics.

The Higgs boson production in association with a pair of $t\bar{t}$ quarks ($t\bar{t}H$) allows *direct* measurement of the top Yukawa coupling [1]. The relatively low cross-section of the $t\bar{t}H$ production ($\sigma^{SM}_{ttH} = 0.51$ pb^{-1} at $\sqrt{s}$ =13 TeV, see figure 1.3) makes this measurement a challenging one. The $t\bar{t}H$ process has a rich and complex variety of possible final states that are usually grouped in the individual physics analyses by the Higgs decay mode. The $t\bar{t}H(H \to b\bar{b})$ analyses present final states with a large number of jets and b-jets with one or two leptons (opposite sign) from the W bosons (from top decay) [2]. Although a large number of events are selected in this analysis, the backgrounds are quite high and difficult to estimate. On the other hand, $t\bar{t}H(H \to \gamma\gamma)$ gives a cleaner final states with small background (higher S/B), however the number of events is much smaller because of the small $H \to \gamma\gamma$ branching ratio. Multilepton final states target the $t\bar{t}H(H \to WW^*, ZZ^*, \tau\tau)$ (figure 5.1) and present relatively clean final states with S/B values in between $t\bar{t}H(H \to b\bar{b})$ and $t\bar{t}H(H \to \gamma\gamma)$.

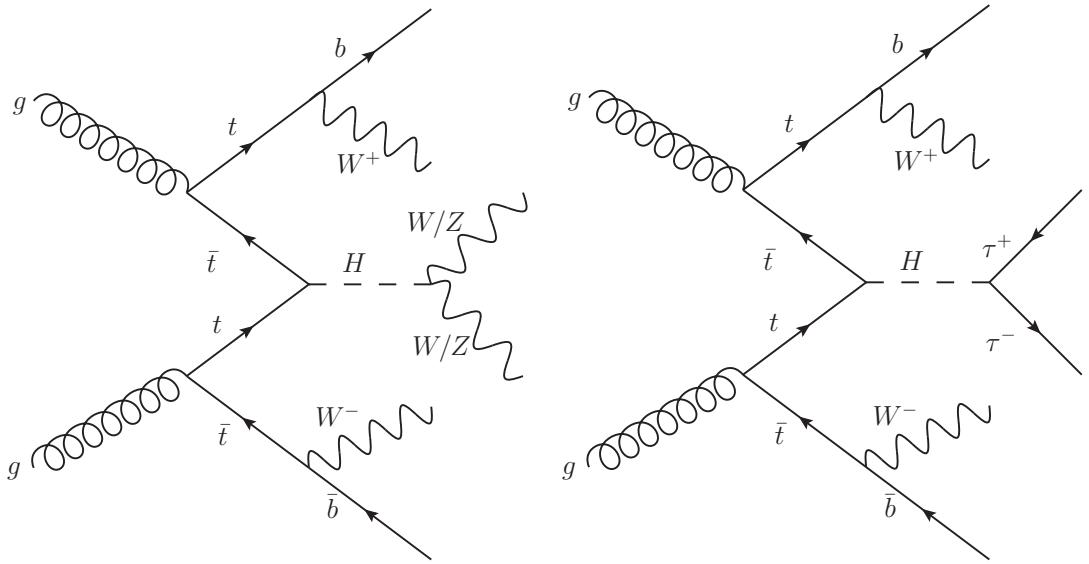

Figure 5.1 – Examples of Feynman diagrams for ttH production with H decaying to ZZ,WW (left) and $\tau\tau$ (right).

1. $t\bar{t}H$ allows for absolute value measurement of the top Yukawa coupling, $|y_t|$. The sign of the coupling can be measured in the tH processes [89] which has a lower cross-section than $t\bar{t}H$.

2. No lepton in the final state is also possible (fully hadronic final states) but they are highly dominated by background

Section 5.1 will briefly describe the above mentioned channels, with a particular focus on $t\bar{t}H(H \to WW^*, ZZ^*, \tau\tau)$ (ttHML), and present the result of their combination allowing the observation of the ttH process. Section 5.2 details then the next analysis of ttH multilepton with two times more statistics ($\sim 80\text{fb}^{-1}$) in the two lepton same-sign channel (2ℓSS) and give its current status as the analysis is still ongoing (section 5.3). A lot of similarities exist with the top FCNC analysis (Chapter 4) which will be used as an reference for the analysis methods.

5.1 Observation of the ttH production mode

5.1.1 ttH Multilepton (36 fb^{-1})

The ttH multilepton analysis strategy relies on the jet/b-jet multiplicity information to distinguish between signal and background (described in Chapter 4) and on the lepton multiplicity. The events are classified in 7 categories (channels) based on the number of light leptons and the number of hadronically decaying τ (τ_{had}), assuring orthogonality across the channels. Figure 5.2 (left) shows the diagram of the 7 channels used in the ttHML analysis (36.1 fb^{-1}).

The channels are:

— 2ℓSS: 2 light lepton of the same electric charge (no τ_{had})
— 3ℓ: 3 light leptons (no τ_{had})
— 4ℓ: 4 light leptons
— 1ℓ+2τ_{had}: 1 light lepton and two opposite-charge τ_{had}
— 2ℓSS+1τ_{had}: 2 same-sign light leptons and 1 τ_{had}
— 2ℓOS+1τ_{had}: 2 opposite-sign light leptons and 1 τ_{had}
— 3ℓ+1τ_{had}: 3 light leptons and 1 τ_{had}

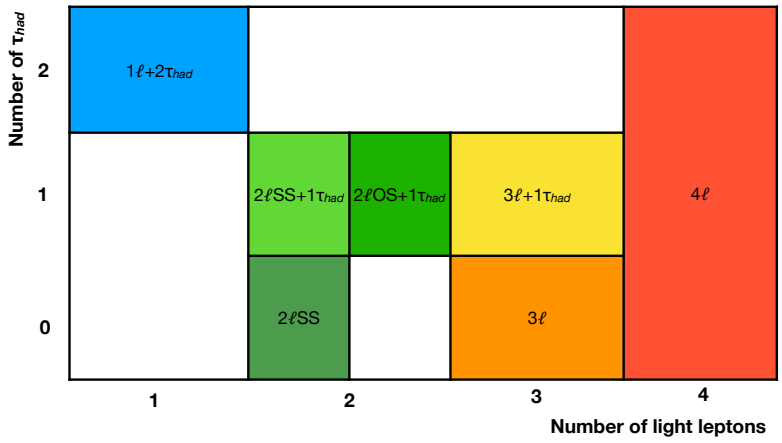

Figure 5.2 – Signal regions considered in the ttHML analysis categorized by the number of τ leptons and the number of light leptons.

Channel	Selection criteria
Common	$N_{\text{jets}} \geq 2$ and $N_{b\text{-jets}} \geq 1$
2ℓSS	Two very tight light leptons with $p_{\text{T}} > 20$ GeV Same-charge light leptons Zero medium τ_{had} candidates $N_{\text{jets}} \geq 4$ and $N_{b\text{-jets}} < 3$
3ℓ	Three light leptons with $p_{\text{T}} > 10$ GeV; sum of light-lepton charges ± 1 Two same-charge leptons must be very tight and have $p_{\text{T}} > 15$ GeV The opposite-charge lepton must be loose, isolated and pass the non-prompt BDT Zero medium τ_{had} candidates $m(\ell^+\ell^-) > 12$ GeV and $\lvert m(\ell^+\ell^-) - 91.2 \text{ GeV}\rvert > 10$ GeV for all SFOC pairs $\lvert m(3\ell) - 91.2 \text{ GeV}\rvert > 10$ GeV
4ℓ	Four light leptons; sum of light-lepton charges 0 Third and fourth leading leptons must be tight $m(\ell^+\ell^-) > 12$ GeV and $\lvert m(\ell^+\ell^-) - 91.2 \text{ GeV}\rvert > 10$ GeV for all SFOC pairs $\lvert m(4\ell) - 125 \text{ GeV}\rvert > 5$ GeV Split 2 categories: Z-depleted (0 SFOC pairs) and Z-enriched (2 or 4 SFOC pairs)
1ℓ+$2\tau_{\text{had}}$	One tight light lepton with $p_{\text{T}} > 27$ GeV Two medium τ_{had} candidates of opposite charge, at least one being tight $N_{\text{jets}} \geq 3$
2ℓSS+$1\tau_{\text{had}}$	Two very tight light leptons with $p_{\text{T}} > 15$ GeV Same-charge light leptons One medium τ_{had} candidate, with charge opposite to that of the light leptons $N_{\text{jets}} \geq 4$ $\lvert m(ee) - 91.2 \text{ GeV}\rvert > 10$ GeV for ee events
2ℓOS+$1\tau_{\text{had}}$	Two loose and isolated light leptons with $p_{\text{T}} > 25, 15$ GeV One medium τ_{had} candidate Opposite-charge light leptons One medium τ_{had} candidate $m(\ell^+\ell^-) > 12$ GeV and $\lvert m(\ell^+\ell^-) - 91.2 \text{ GeV}\rvert > 10$ GeV for the SFOC pair $N_{\text{jets}} \geq 3$
3ℓ+$1\tau_{\text{had}}$	3ℓ selection, except: One medium τ_{had} candidate, with charge opposite to the total charge of the light leptons The two same-charge light leptons must be tight and have $p_{\text{T}} > 10$ GeV The opposite-charge light lepton must be loose and isolated

Table 5.1 – Event selections for the ttHML analysis performed with 36 fb^{-1} of data [65].

The complete event selection for each category is given in table 5.1. The 2ℓSS and 3ℓ channels selections were already discussed in details in Chapter 4 as they are exactly the ones corresponding to the 2ℓSS and 3ℓ channels in the top FCNC analysis[3]. A measurement of the prompt electron efficiency using the PLI tagger was also discussed in the section 3.4.

Overall 8 signal regions are defined, with one signal region per channel except the 4ℓ channel where a Z-depleted and a Z-enriched signal region is defined. Multivariate analysis are performed in the 2ℓSS, 3ℓ, 1ℓ+$2\tau_{\text{had}}$, 2ℓSS+$1\tau_{\text{had}}$ and 3ℓ+$1\tau_{\text{had}}$ channels where sufficient statistics is available. The 3ℓ+$1\tau_{\text{had}}$ channel does not have enough statistics and a simple cut-and-count analysis is performed.

3. The top FCNC analysis is based on the ttHML analysis with 36.1 fb^{-1}, using the same object definitions, PLI algorithm and non-prompt background estimation method.

The 4ℓ channel, which is also limited in statistics, uses a BDT to reduce the ttZ background in the Z-enriched region however the two signal regions have 1 bin each. The MVA analysis in the 2ℓSS channel follows a very similar procedure as described in Chapter 4, however a different approach is used for the 3ℓ channel where a five dimensional BDT is used instead to separate the signal (ttH) against 4 main backgrounds (ttZ,ttW,tt and diboson). Four control regions (1 bin per region) are built for these backgrounds.

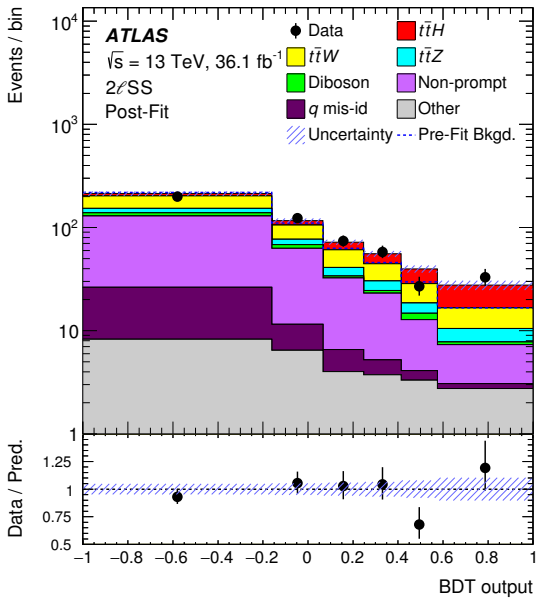

Figure 5.3 – Post-fit distribution of the final BDT in the 2ℓSS region [65].

A combined profile likelihood fit is performed using all the signal regions and the 3ℓ control regions simultaneously to extract the ttH signal strength, $\mu_{ttH} = \sigma^{obs}_{ttH}/\sigma^{SM}_{ttH}$. Table 5.2 summarizes the fit results for the individual channels and the combination. The combined best-fit signal strength is $1.6^{+0.3}_{-0.3}(\text{stat})^{+0.4}_{-0.3}(\text{syst})$, with the 2ℓSS channel being the most sensitive (figure 5.3). A total observed (expected) significance of 4.1(2.8) standard deviations (σ) is achieved over the background-only hypothesis [65]. This results passes the 3σ threshold that is usually used to claim an evidence.

5.1.2 Combination including $t\bar{t}H(H \to \gamma\gamma)$ (79.8 fb^{-1}) and $t\bar{t}H(H \to b\bar{b})$ (36 fb^{-1})

The $t\bar{t}H(H \to \gamma\gamma)$ analysis suffers from low statistics but enjoys low backgrounds and a good resolution of the electromagnetic calorimeter necessary to reconstruct and identify photons. In the analysis based on 79.8 fb^{-1} of data at $\sqrt{s}$ =13 TeV [67] two isolated photons with p_T of at least 35 GeV and 25

Channel	Best-fit μ		Significance	
	Observed	Expected	Observed	Expected
2ℓOS+$1\tau_{\text{had}}$	$1.7\ ^{+1.6}_{-1.5}$ (stat.) $^{+1.4}_{-1.1}$ (syst.)	$1.0\ ^{+1.5}_{-1.4}$ (stat.) $^{+1.2}_{-1.1}$ (syst.)	0.9σ	0.5σ
1ℓ+$2\tau_{\text{had}}$	$-0.6\ ^{+1.1}_{-0.8}$ (stat.) $^{+1.1}_{-1.3}$ (syst.)	$1.0\ ^{+1.1}_{-0.9}$ (stat.) $^{+1.2}_{-1.1}$ (syst.)	–	0.6σ
4ℓ	$-0.5\ ^{+1.3}_{-0.8}$ (stat.) $^{+0.2}_{-0.3}$ (syst.)	$1.0\ ^{+1.7}_{-1.2}$ (stat.) $^{+0.4}_{-0.2}$ (syst.)	–	0.8σ
3ℓ+$1\tau_{\text{had}}$	$1.6\ ^{+1.7}_{-1.3}$ (stat.) $^{+0.6}_{-0.2}$ (syst.)	$1.0\ ^{+1.5}_{-1.1}$ (stat.) $^{+0.4}_{-0.2}$ (syst.)	1.3σ	0.9σ
2ℓSS+$1\tau_{\text{had}}$	$3.5\ ^{+1.5}_{-1.2}$ (stat.) $^{+0.9}_{-0.5}$ (syst.)	$1.0\ ^{+1.1}_{-0.8}$ (stat.) $^{+0.5}_{-0.3}$ (syst.)	3.4σ	1.1σ
3ℓ	$1.8\ ^{+0.6}_{-0.6}$ (stat.) $^{+0.6}_{-0.5}$ (syst.)	$1.0\ ^{+0.6}_{-0.5}$ (stat.) $^{+0.5}_{-0.4}$ (syst.)	2.4σ	1.5σ
2ℓSS	$1.5\ ^{+0.4}_{-0.4}$ (stat.) $^{+0.5}_{-0.4}$ (syst.)	$1.0\ ^{+0.4}_{-0.4}$ (stat.) $^{+0.4}_{-0.4}$ (syst.)	2.7σ	1.9σ
Combined	$1.6\ ^{+0.3}_{-0.3}$ (stat.) $^{+0.4}_{-0.3}$ (syst.)	$1.0\ ^{+0.3}_{-0.3}$ (stat.) $^{+0.3}_{-0.3}$ (syst.)	4.1σ	2.8σ

Table 5.2 – Best fit values and significance for the ttHML channels as well as the combination [65].

GeV, having the invariant mass falling in the range $105 < m_{\gamma\gamma} < 160$ GeV are selected. Two signal regions, Had and Lep, are defined targeting ttH in fully hadronic decays (no isolated leptons) and in semi-leptonic decays (at least one isolated lepton). To further separate signal and background two BDT are used. Only the high BDT score events (more signal-like) are kept and are further split in 4 (3) categories in the Had (Lep) region to optimize the expected signal sensitivity. A combined unbinned maximum-likelihood fit to the $m_{\gamma\gamma}$ distribution is performed to estimate the ttH signal. Figure 5.4 (left) shows the $m_{\gamma\gamma}$ distribution which presents a peak around the Higgs boson mass (m_H=125 GeV) which is fit under the Signal+Background hypothesis. The observed (expected) significance over the background-only hypothesis is 4.1 (3.7) σ.

The $t\bar{t}H(H \to b\bar{b})$ enjoys the highest Higgs boson branching ratio ($\sim$ 58%) and offers access not only to the top Yukawa coupling but also to the b-quark Yukawa coupling. However, there are big experimental challenges like the large $t\bar{t}$+jets background contributions (especially when the associated jets originate from c- or b-quarks) and small combined efficiency to reconstruct and identify the numerous objects in the final states. The $t\bar{t}H(H \to b\bar{b})$ analysis based on 36 fb^{-1} at $\sqrt{s}$ =13 TeV targets single and dilepton final states (e or μ originating from semi-leptonic decays of the top quarks) which benefit from lower background already at the trigger level (compared to the fully hadronic final states which are not considered in this analysis). The events in the single lepton (dilepton) final states are split in 6 (3) signal regions and 6 (4) control regions based on the number of jets and b-jets. BDTs are used in every signal region to improve the separation between signal and backgrounds. Figure 5.4 (right) shows the reconstructed Higgs boson candidate mass (m_{bb}^{Higgs}) in a signal region requiring at least 6 jets and 4 b-jets, one of the purest signal region. The ttH contribution peaks around the Higgs boson mass and its small contribution shows the limitation of this analysis in terms of very high backgrounds. All these event categories

are used in a combined profile likelihood fit to determine the signal and to constrain the important background components. An excess of 1.4σ (1.6σ) over the observed (expected) background-only hypothesis was obtained [90]. The corresponding measured signal strength μ_{ttH} is $0.84^{+0.64}_{-0.61}$, being compatible with the Standard Model expectation.

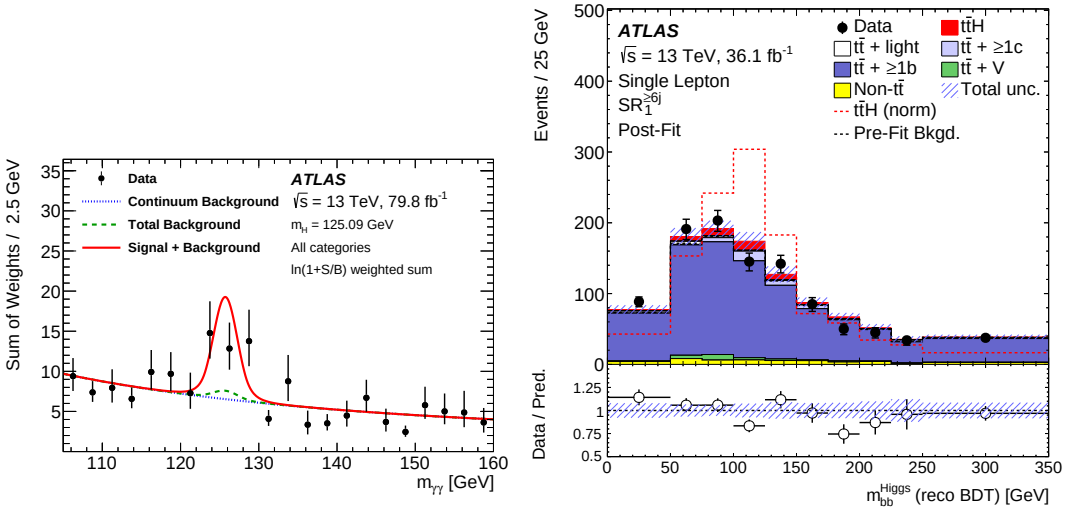

Figure 5.4 – Invariant mass distributions as formed from the Higgs boson candidate decay products in the ttH channel, (left) in the diphoton channel for 79.8 fb^{-1} of data at $\sqrt{s}$ =13 TeV [67] and (right) in the $H \to bb$ channel in one signal region ($N_j \geq 6$, single lepton) for 36.1 fb^{-1} of data at $\sqrt{s}$ =13 TeV [90].

A combined fit was performed using the $t\bar{t}H(H \to WW^*, ZZ^*, \tau\tau)$(multilepton) and $t\bar{t}H(H \to bb)$ analyses with 36.1 fb^{-1} and $t\bar{t}H(H \to \gamma\gamma)$ analysis with 79.8 fb^{-1} at $\sqrt{s}$=13 TeV[4]. Figure 5.5 summarizes the results. The combined signal strength $1.32^{+0.28}_{-0.26}$ which is within the standard Model expectations. A combined observed (expected) significance of 5.8 (4.9) σ is obtained relative to the background-only hypothesis.

4. A dedicated analysis was performed for $t\bar{t}H(H \to ZZ^* \to 4\text{leptons})$ channel [67] with 79.8 fb^{-1} at $\sqrt{s}$=13 TeV which is excluded in the ttH multilepton analysis and is included in the combined fit.

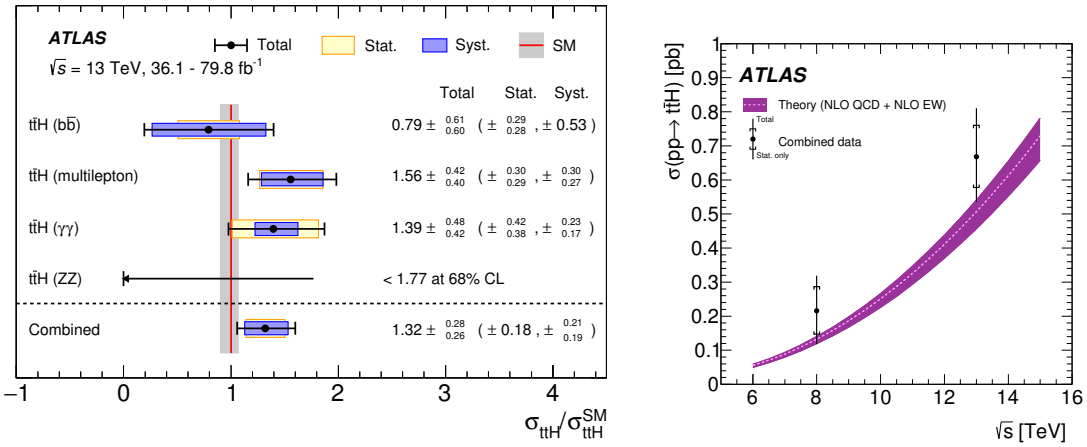

Figure 5.5 – (Left) Overall result for the ttH analysis. (Right) Evolution of the ttH cross section as a function of the center of mass energy and comparison with the SM prediction [67].

Performing a combined fit with the 7, 8, and 13 TeV data results in an observed (expected) significance of 6.3 (5.1) σ [67]. This result represents a direct observation for the $t\bar{t}H$ process. The corresponding $t\bar{t}H$ production cross section measurements give $220 \pm 100(\text{stat}) \pm 70(\text{syst})$ fb for the 8 TeV analysis and $660 \pm 100(\text{stat})^{+110}_{-100}(\text{syst})$ fb for the 13 TeV analysis. These results are compatible with the SM expectations as can seen in figure 5.5 (right).

The $t\bar{t}H$ process was also independently observed by the CMS experiment [78] with an observed (expected) significance of 5.2 (4.2) σ using the combined 7 TeV (5.1 fb^{-1}), 8 TeV (19.7 fb^{-1}), and 13 TeV (35.9 fb^{-1}) datasets.

5.2 Two-lepton same-sign analysis with 80 fb^{-1}

A new iteration of the ttHML analysis is performed following the same procedure as in the ttHML analysis based on the 2015-2016 datasets (36.1 fb^{-1}) but including also the 2017 dataset (43.7 fb^{-1}), giving a total of 79.8 fb^{-1} for the full 2015-2017 dataset. This section addresses only the 2ℓSS channel, which I worked on.

Although the same global strategy is used as in the previous analysis, there are a series of important updates at each step of the strategy.

— The lepton definition is similar to the one in defined in table 4.2 but with a new definition for the non-prompt lepton MVA (`PromptLeptonVeto` instead of `PromptLeptonIso`). For the charge mis-assignment veto the same algorithm is used (`CFT`) but with a different operating point. The selection for the non-prompt leptons and charge mis-assignment MVA was obtained after an optimization procedure in terms of $S/\sqrt{B}$ and were found to be

PLV<-0.7 and CFT >0.7. The details of this working point and the corresponding electron efficiency are discussed in section 3.4.5.

— The event selection for the 2ℓSS channel are the same with the exception of $N_{b\text{-jets}}$ which was $N_{b\text{-jets}} = 1, 2$ and is now $N_{b\text{-jets}} \geq 1$. An investigation performed in data events in $N_{b\text{-jets}} \geq 3$ region is performed section 5.2.1.

— The Fake lepton background estimation is still based on the data-driven Matrix Method but it is updated (section 5.2.2).

— The MVA used for the discriminant used in the final is updated (section 5.2.4)

The new expected sensitivity for this updated 2ℓSS analysis is given in section 5.2.5.

5.2.1 $\mu\mu(N_{b\text{-jets}} \geq 3)$ Region

A study was performed in the 2 muon same-sign channel where the pre-MVA selections are applied, except for the number of b-jets where a minimum of 3 b-jet is required (this region is fully dominated, around 85%, by prompt backgrounds, mainly $t\bar{t}W$ and 4 tops). In the previous analysis a large excess of 2.6 sigma (3.6 sigma stat. only) was observed in this region (figure 5.6 left). This excess was not understood and the full region $N_{b-jet} \geq 3$ was excluded, including the 2 electrons and opposite flavor channels although no excess was observed in these channels. In the period between the end of the previous analysis and the beginning of the new analysis a major ATLAS reconstruction software upgrade was performed and all the data were reprocessed. We distinguish three cases:

1. previous analysis results (pre-upgrade), figure 5.6 left
2. results using the reprocessed data, using the same selections as in the previous analysis, figure 5.6 center
3. results using the reprocessed data, using the new non-prompt lepton tagger PLV (used in the new analysis), figure 5.6 right

In the new analysis this excess is not present anymore as figure 5.6(center) shows for the same working point used in the previous analysis (`PromptLeptonIso` <-0.5 and isolLoose, with PromptLeptonIso re-trained after the ATLAS software upgrade). Figure 5.6 (right) shows the results for the baseline working point used in the new analysis (`PromptLeptonVeto` <-0.7 and isolFixedCutLoose).

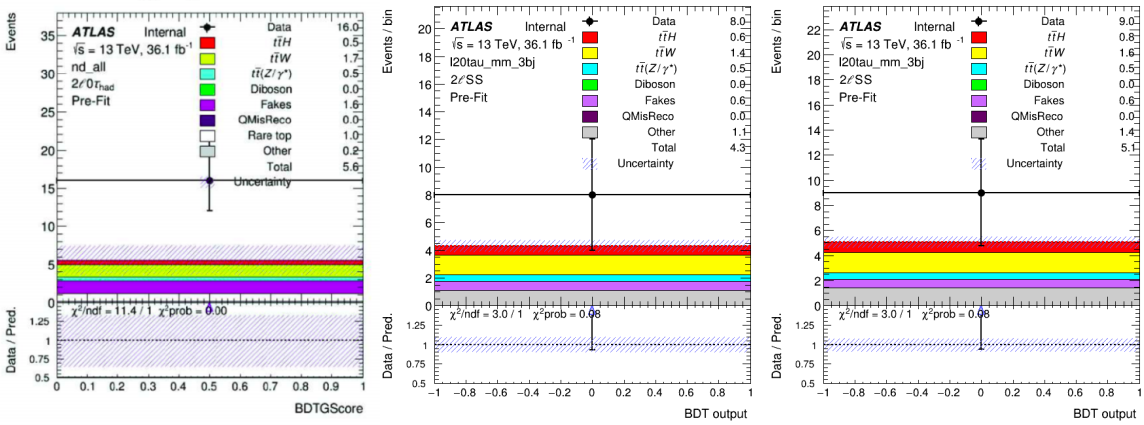

Figure 5.6 – Event yields for 2 muons same-sign with $N_{b-jet} \geq 3$ in previous analysis (left), after ATLAS software upgrade but for WP from previous analysis (centre) and after ATLAS software upgrade for the new analysis WP (right).

A more detailed study was carried out to better understand these changes. The 8 events of the initial 16 (Figure 5.6 left) are selected in the new analysis. The 8 events that were selected in the previous analysis but not selected after the reprocessing are presented in table 5.3.

6 out of the 8 events do not pass requirements for b-jet selection ($N_{b\text{-jets}} \geq 3$) because of lower b-tagging weight and the different b-tagging discriminant after the upgrade compared to before the upgrade [5] in the case of 4 events, or because the p_{T} of the b-jet falls below the jet p_{T} cut (25 GeV) for 2 events. For the 2 events (out of 8) that pass the b-jet requirements in one event the subleading muon does not pass the PLV selection and for the other one the subleading muon is not reconstructed. In conclusion, as the excess is not present anymore and the differences between release were investigated, this $N_{b\text{-jets}} \geq 3$ region is included

5. mv2c10_70 weight threshold is 0.83, but it was before 0.8244273

Event Number	N of b-jets after (before) upgrade	Pass in pre-MVA region with Nb=1,2 after upgrade	Comments
22128429	2(3)	Yes	b-tag weight below threshold(weight change: 0.859→ 0.709)
3393833868	1(3)	Yes	Both missing jets below pT threshold
502118906	2(3)	No	Subleading muon not pass PLI/V selection (+b-jet pT cut)
1762961539	2(3)	Yes	b-tag weight below threshold(weight change: 0.890→ 0.705)
1651615427	2(3)	Yes	b-tag weight below threshold(weight change: 0.983→ 0.173)
2630074250	3(3)	No	Subleading muon not pass PLI/V selection
1716355946	2(3)	Yes	b-tag weight below threshold(weight change: 0.870→ 0.744)
1437019256	5(4)	No	Subleading muon not present after

Table 5.3 – Events that pass selection in before the upgrade but do not pass after.

back in the 2ℓSS pre-MVA region. A small increase around 2% is brought in signal, S/B and significance.

5.2.2 Fake lepton estimation

The fake lepton background is estimated using the Matrix Method. The same low Njet CR region is used for the real and fake efficiency measurement, as defined in table 4.5. However a new parametrization is used for the real and fake efficiencies with the purpose to better capture the particularities of the fakes distribution shape. Figure 5.7 shows the real efficiency for electrons (left) and for muons (right). The novelty with respect to the previous round is that the electron real efficiency is parametrized also with respect to η, beside the electron p_{T}. The electron real efficiency decreases with respect to η down to 0.288±0.008 in the high η bin at low p_{T}, however it is increasing with respect to p_{T}. The muon real efficiency is parametrized in a very similar way as in the previous round and it is showing a slightly higher efficiency.

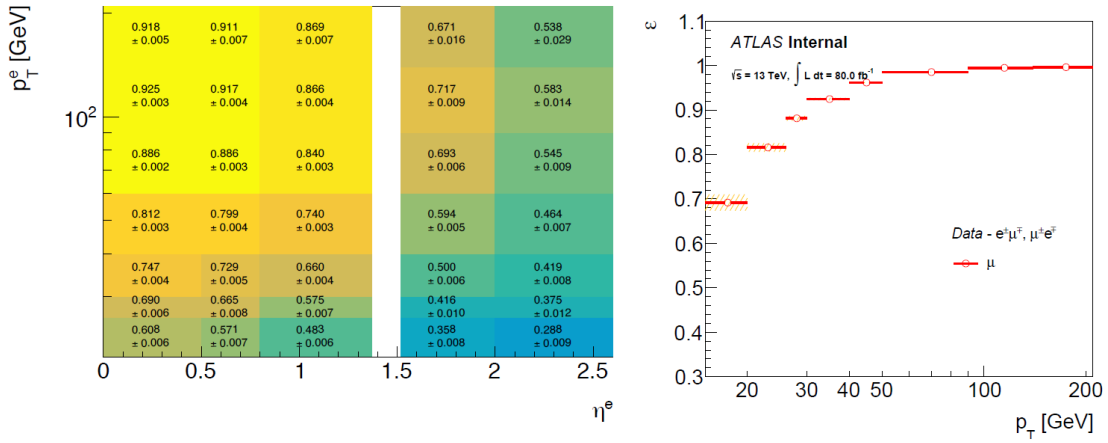

Figure 5.7 – Real efficiency for electrons (left) parametrized in p_{T} and $|\eta|$ and real efficiency for muons (right) for the 2ℓSS analysis with 80 fb^{-1} of data at $\sqrt{s}$ =13 TeV.

Figure 5.8 shows the fake efficiency for electrons (left) and for muons (right). The electron fake efficiency is parametrized with respect to number of b-jets (N_{b-jets}) and p_{T}, like in the previous analysis iteration with 36 fb^{-1}, however the binning in p_{T} is now finner (3 bins instead of 1) for $N_{b-jets} = 1$ to better capture the effects at low p_{T}. In the case of the muon fake efficiency the same parametrization (and binning) in minimum distance between the muon and a jet ($min(\Delta R_{\mu,jet})$) and p_{T} is preserved.

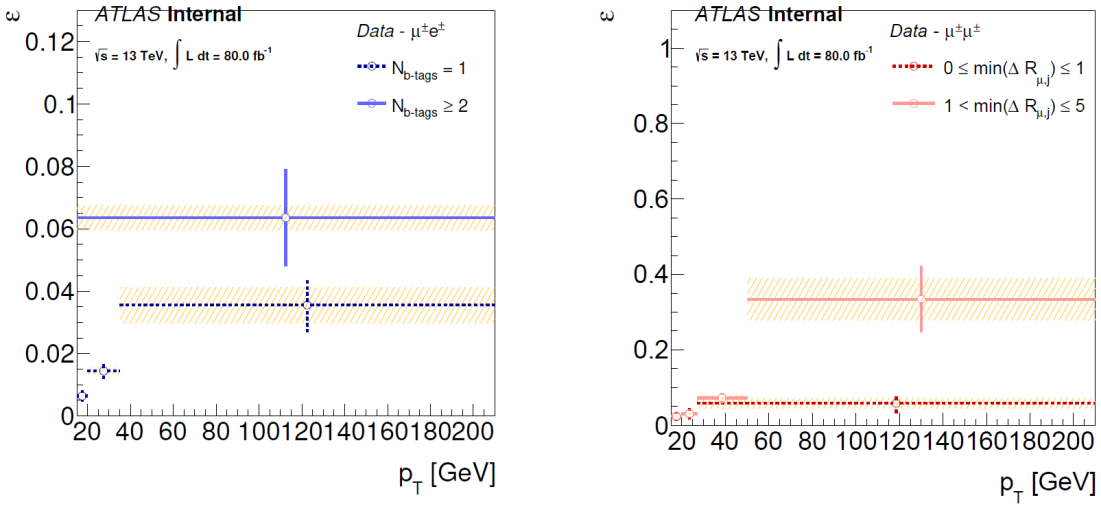

Figure 5.8 – Fake lepton efficiency for electrons (left) and for muons (right) for the 2ℓSS analysis with 80 fb^{-1} of data at $\sqrt{s}$ =13 TeV. The orange band represents the systematics uncertainty on the fake rate.

Figure 5.9 shows the fake leptons background composition in the loose (left) and tight regions (right). A significant change can be noted with reduction in heavy flavor and increase in photon conversions. This increase is due to the tighter cut applied on the PLV that enhance the relative proportion of conversion, a side effect of the reduction of the overall number of fake leptons from b-jets. It is translated in considering a higher number of nuisance parameters (10 instead of 4) to account for the photon conversion background in p_{T} and N_{b-jets}.

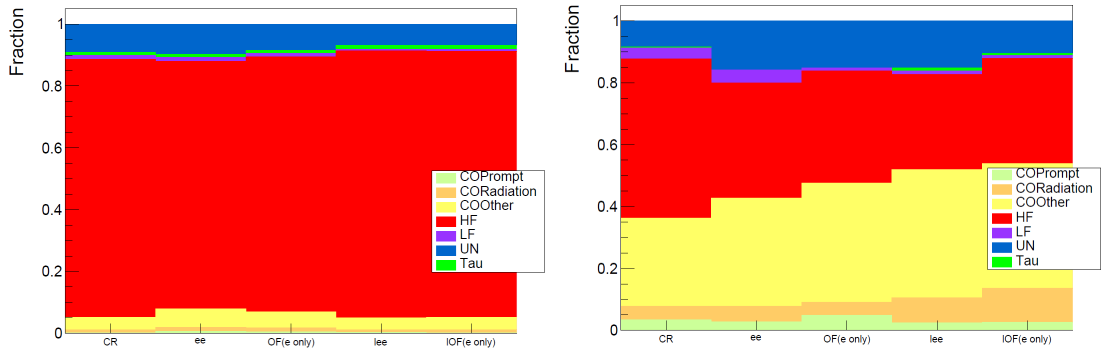

Figure 5.9 – Fake lepton background composition with loose leptons (left) and with tight (right).

5.2.3 Event yields in the pre-MVA region

As in the previous analysis, a "relaxed" region is defined which requires two same-sign signal leptons with $p_{\mathrm{T}}(\ell)$ above 20 GeV, ≥ 4 jets with p_{T} above 25 GeV

Type Type	Signal (S)	Background (B) Irreducible (MC)	Reducible (DD)	Prediction S+B
ee	15.0	68.9	93.6	177.5
$e\mu$	20.8	96.1	121.1	238.0
μe	18.4	83.0	94.5	195.9
$\mu\mu$	29.5	137.4	94.8	261.7
Total	83.7	385.4	404.0	873.1

Type	Signal	Irreducible Background				Reducible Background		S+B
	$t\bar{t}H$	$t\bar{t}W$	$t\bar{t}Z$	VV	Rare	Fake / non-prompt lepton	charge-flip electron	
ee	15.0 ±1.8	37.9 ±9.6	14.9 ±	6.1 ±6.2	10 ±	87.8 ± 34.9	5.8 ±2.9	177.5 ±28.3
$e\mu$	20.8 ±3.2	54.5 ±14.0	19.6 ±	7.6 ±7.6	14.4 ±	117.8 ± 65.8	3.3 ±1.7	238.0 ±50.0
μe	18.4 ±2.5	48.0 ±12.2	16.4 ±	7.1 ±7.1	11.5 ±	93.0 ± 45.9	1.5 ±0.7	195.9 ±41.5
$\mu\mu$	29.5 ±3.9	82.2 ±20.7	24.1 ±	10.7 ±10.7	20.4 ±	94.8 ± 37.7	-	261.7 ±24.8
Total	83.7 ± 5.9	222.5 ±56.3	75.0 ±	31.6 ±31.6	56.4 ±	393.4 ± 114.2	10.6 ± 5.2	873.1 ±97.0

Table 5.4 – Summary of event yields in the pre-MVA region of the 2ℓSS channel with L=79.9 fb^{-1} of data at $\sqrt{s}$ = 13 TeV. The bottom table gives the breakdown of the background contributions when summing ee, $e\mu$, μe and $\mu\mu$ with the total uncertainty including pre-fit statistic and systematic uncertainties. The "Rare" category gathers tZ, $t\bar{t}\,t\bar{t}$, $ttWW$, WtZ, VVV, $tHjb$, WtH, $tt\bar{t}$ and top rare decay (low mass ttll is included in ttZ).

and at least one b-jet (region N_{b-jets}>3 was included back). The MV2c10 algorithm is used with 70% b-tag efficiency. Lowering the number of jets further is not possible since these regions are used as control regions for data driven estimate of reducible background. Similarly, lowering further $p_{\mathrm{T}}(\ell)$ does not bring additional signal sensitivity. This selection is called "pre-MVA" in the following.

Table 5.4 shows the event count in the pre-MVA region with prediction from MC for irreducible backgrounds and data-driven (DD) methods for reducible backgrounds. The signal and the background is roughly multiplied by a factor 2 with respect to the previous analysis. The tighter CFT operating point reduces significantly the charge-flip electron background.

This reduction of charge-flip electron and fake/non-prompt lepton events with dedicated MVA discriminants, mitigates the dependency on the lepton flavor type. This is illustrated in Figure 5.10 (left). S/B values and significance $S/\sqrt{B}$ are given in Figure 5.10 (right). The fake/non-prompt lepton background is

slightly above 50% in the channels involving electrons. In the $\mu\mu$ channel, $t\bar{t}V$ ($t\bar{t}W$ + $t\bar{t}Z$) is the dominant background.

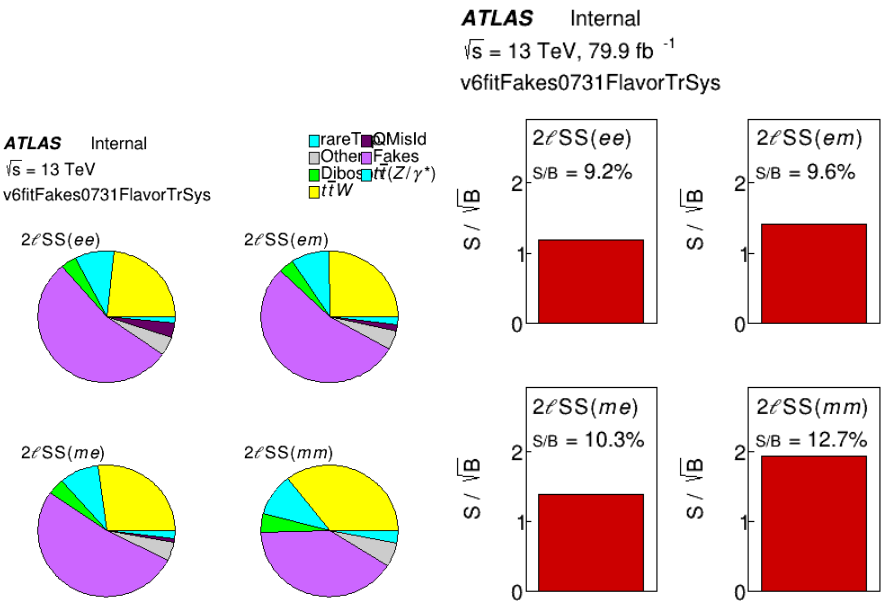

Figure 5.10 – Background composition in pre-MVA region (left) and S/B and $S/\sqrt{B}$ values (right) for individual sub-channels split by lepton flavor.

5.2.4 Event MVA

A MVA based on BDTs is optimized to further reject the "reducible" fake/non-prompt lepton events all predominantly coming from $t\bar{t}$ as well as the irreducible $t\bar{t}W$ and $t\bar{t}Z$ background.

MVA techniques have been developed to reduce the two main remaining backgrounds, fake/non-prompt leptons and $t\bar{t}V$ with V=W or Z. Fake/non-prompt leptons are described by the shapes from the data-driven non-prompt lepton background estimate, while $t\bar{t}V$ are described by the Monte-Carlo samples. Two MVA trainings against the reducible background are done independently in ee + OF channel (OF - opposite flavour light leptons) and $\mu\mu$ channel due to the different fake leptons background fraction in the total background (channels involving electron are dominated by fake leptons). All MVAs are based on Gradient Boosted Decision Trees (BDTG), since they are less sensitive to statistical fluctuations. The signal and background samples are split in two subsets according to a unique event number ID to form "odd" and "even" samples. The training is done on the odd sample and applied to the even sample and vice-versa – later called cross-training. In the analysis all events are used.

The modeling of the input variables used to build the two BDT discriminants against $t\bar{t}V$ and the reducible background is discussed (section 5.2.4.1). These two discriminants are then presented (section 5.2.4.2) and combined into a final discriminant (section 5.2.4.3).

5.2.4.1 Modeling of MVA Input variables

To reject further the events with fake/non-prompt leptons as well as $t\bar{t}W$ +$t\bar{t}Z$, BDT scores, latter called $BDTG\_ttbar$ and $BDTG\_ttV$, are computed. Eight input variables are used when training MVA against fake/non-prompt lepton background in $ee + OF$ channel as well as against $t\bar{t}V$ background:

— Number of jets with $p_{\mathrm{T}} > 25$ GeV, N_{jets} merging the high jet multiplicity in N_{jets}=7 bin;
— Number of b-jets with $p_{\mathrm{T}} > 25$ GeV, $N_{b\text{-jets}}$
— leptonic flavor, ee, $e\mu$ μe and $\mu\mu$ where the first lepton corresponds to the one with the highest p_{T}, $2\times\mathrm{N}_{\mu_0}+\mathrm{N}_{\mu_1}$
— Distance between leading lepton and its closest jet, $\Delta R(\ell_0, \mathrm{jet})$;
— Distance between sub-leading lepton and its closest jet, $\Delta R(\ell_1, \mathrm{jet})$;
— Maximum between lepton $|\eta_{\ell_0}|$ and $|\eta_{\ell_1}|$, Max($|\eta_{\ell}|$);
— Sub-leading lepton p_{T}, $p_{\mathrm{T}}(\ell_1)$;
— E_T^{miss}

In total, three BDT trainings are performed:

— $t\bar{t}H$ *vs* $t\bar{t}V$:

1. inclusive in flavor, eight input variables used (including lepton flavor)

— $t\bar{t}H$ *vs* fake leptons:

2. ee+OF: eight input variables used (including lepton flavor)
3. $\mu\mu$: seven input variables used (lepton flavor is constant)

The first two rows of Figure 5.11 show the pre-fit distributions of these 8 input variables in a flavor inclusive channel, for data and signal plus background prediction in the pre-MVA region. A fair data modeling of the input variables is observed within the errors which include statistical and systematical uncertainties. For the $ee + OF$ channel and $\mu\mu$ channel, the pre-fit distributions of input variables can be found in Figure 5.12- 5.13.

5.2.4.2 BDT discriminant performance

The separation between signal and background is illustrated in Figure 5.14 where the BDT response distributions are shown for signal and background. A better agreement between the training sample and the test sample is observed with $BDTG\_ttV$ (left) than with $BDTG\_ttbar$ (middle and right), which is due to the much more abundant statistics in training. As expected, a much better signal-to-background separation is obtained for $BDTG\_ttbar$ compared to

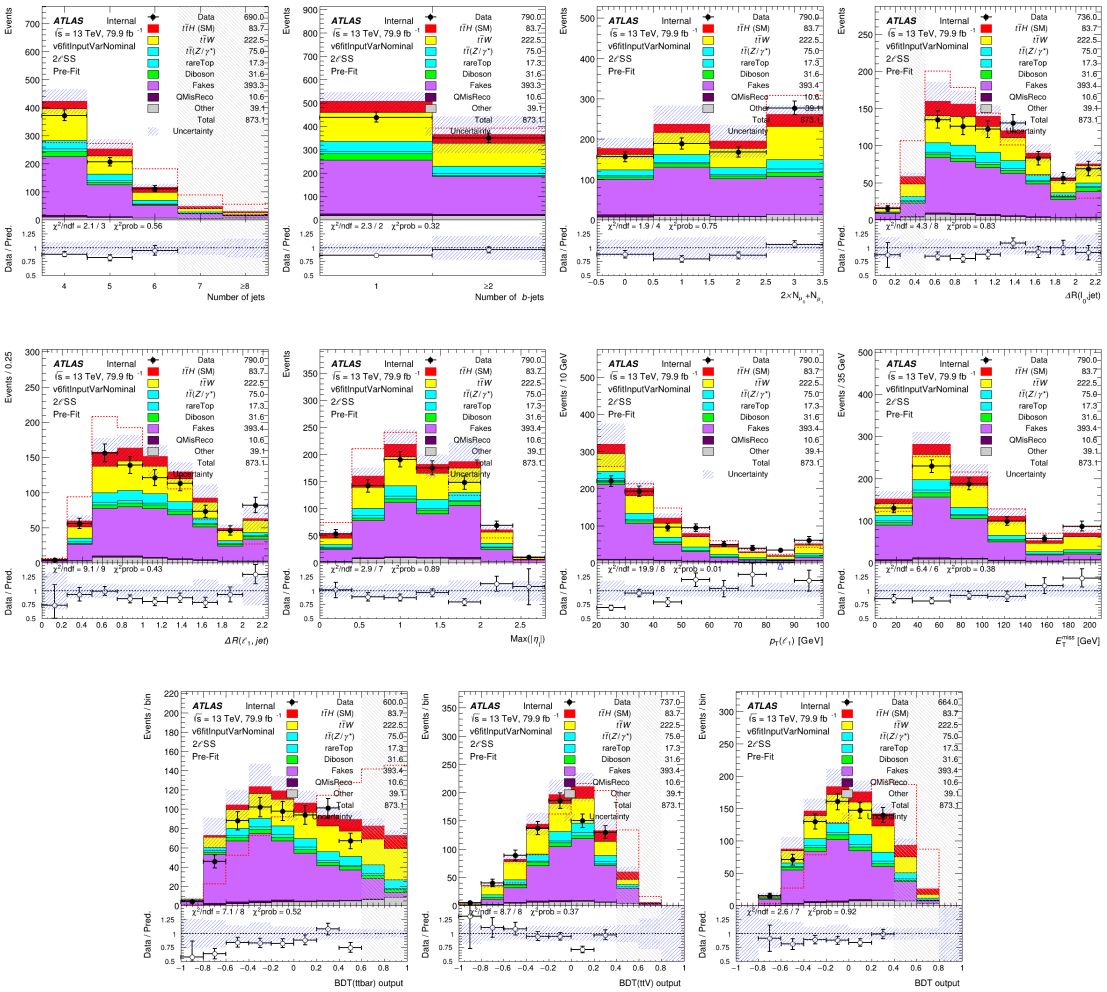

Figure 5.11 – Pre-fit distributions of the 8 input [2 first rows] and output [last row] MVA variable distributions in the pre-MVA region for data and signal plus background prediction in inclusive channel. Events with fake/non-prompt leptons and charge-flip electrons are estimated using data-driven methods and the irreducible background using MC samples. Errors include statistic and all systematic uncertainties. The blinding policy $S/B > 0.15$ per bin is applied. The first and last bins includes the underflows and overflows.

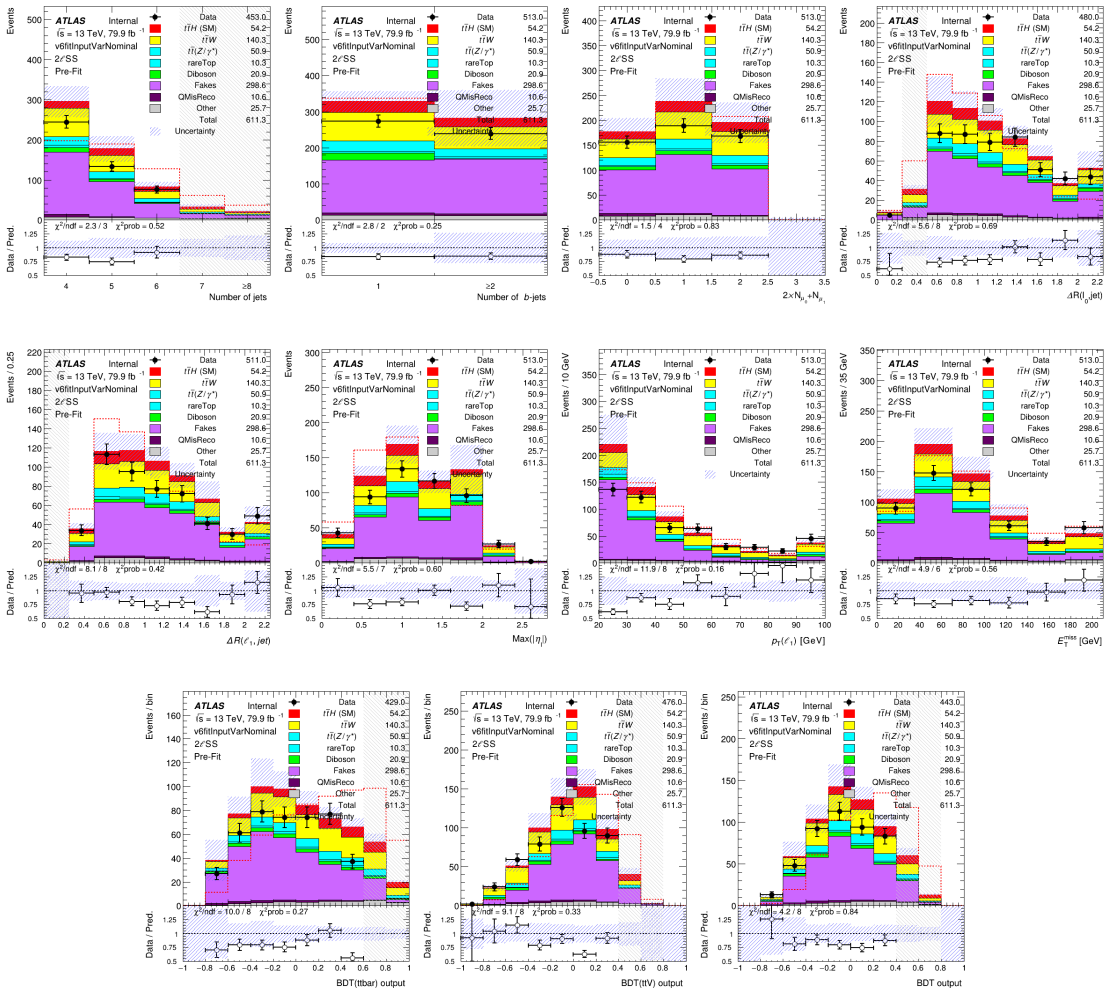

Figure 5.12 – Pre-fit distributions of the 8 input [2 first rows] and output [last row] MVA variable distributions in the pre-MVA region for data and signal plus background prediction with $ee+OF$ final states. Events with fake/non-prompt leptons and charge-flip electrons are estimated using data-driven methods and the irreducible background using MC samples. Errors include statistic and all systematic uncertainties. The blinding policy $S/B > 0.15$ per bin is applied. The first and last bins includes the underflows and overflows.

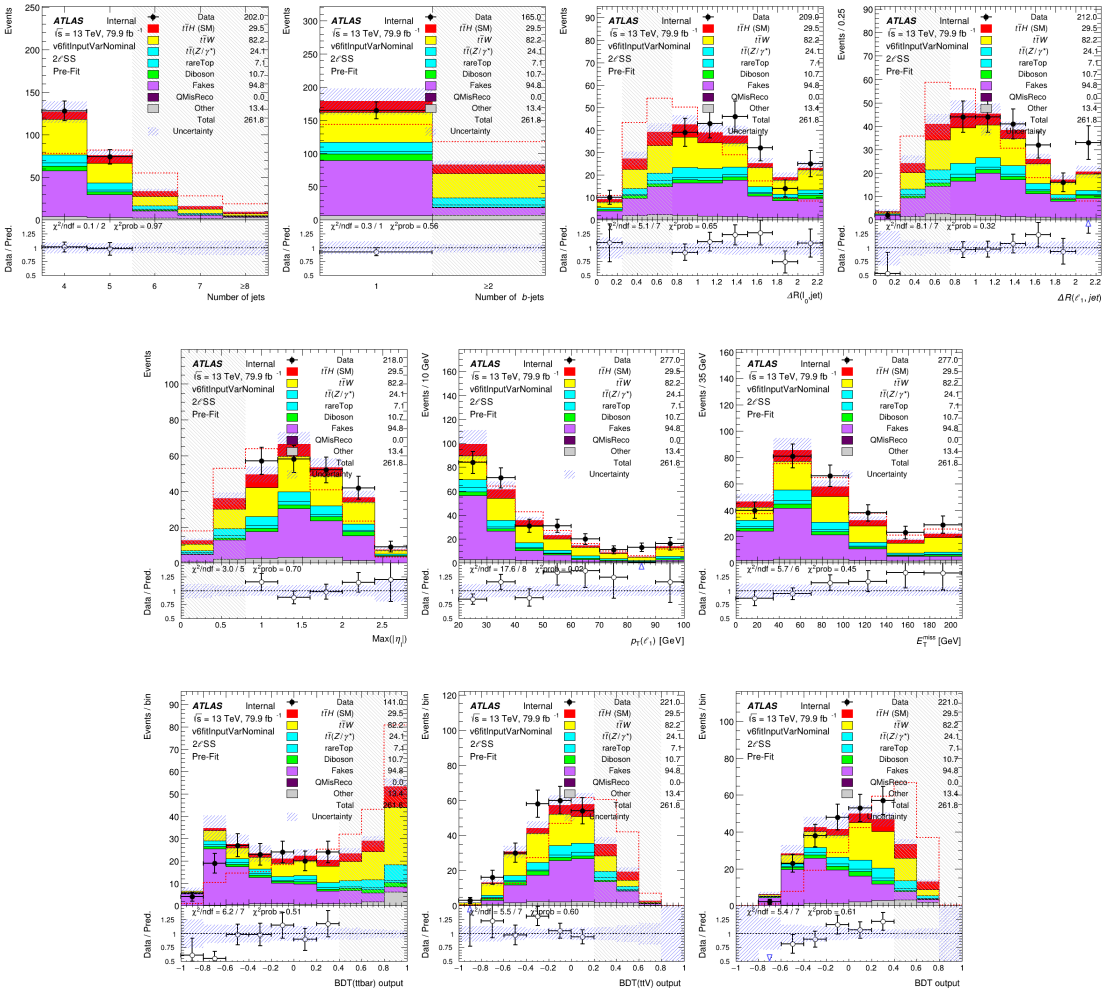

Figure 5.13 – Pre-fit distributions of the 7 input [2 first rows] and output [last row] MVA variable distributions in the pre-MVA region for data and signal plus background prediction with $\mu\mu$ final stat. Events with fake/non-prompt leptons and charge-flip electrons are estimated using data-driven methods and the irreducible background using MC samples. Errors include statistic and all systematic uncertainties. The blinding policy $S/B > 0.15$ per bin is applied. The first and last bins include the underflows and overflows.

$BDTG\_ttV$. The input variables that have the highest separation power are N_{jets}, $\Delta R(\ell_0, \text{jet})$, $\Delta R(\ell_1, \text{jet})$ and Max($|\eta_\ell|$) for $BDTG\_ttV$, Max($|\eta_\ell|$), N_{jets}, $\Delta R(\ell_0, \text{jet})$ and E_T^{miss} for $BDTG\_ttbar$ in $ee + OF$ channel and $N_{b\text{-jets}}$, $p_{\text{T}}(\ell_1)$, N_{jets} and $\Delta R(\ell_1, \text{jet})$ for $BDTG\_ttbar$ in $\mu\mu$ channel. The correlation matrix between input variables has been checked for signal and background in both BDTs (Figure 5.15). As expected, no strong correlations is observed, all being below 30% level. Finally, Figure 5.16 shows the background rejection versus signal efficiency (Receiver Operating Characteristic curve, later called ROC curve) obtained with odd and even events. Similar odd/even performance are obtained for both BDTs demonstrating that there is no overtraining.

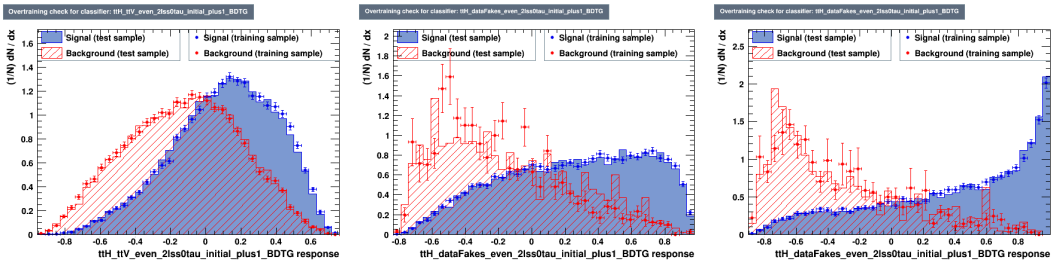

Figure 5.14 – Distribution of the BDT_ttV response in inclusive channel (left) and the BDT_ttbar response with $ee + OF$ (middle) and $\mu\mu$ (right).

Figure 5.11-5.13 bottom shows the pre-fit distributions of the two output BDTs ($BDTG\_ttbar$, $BDTG\_ttV$) and their averaged sum ($BDTG$), for data and signal+background prediction in different channels. A fair data modeling of the background is observed in the unblinded bins (S/B<0.15).

5.2.4.3 Final BDT Discriminant

To maximize the signal sensitivity, the full shape of the BDTs must be considered. Both BDTs are therefore combined into a final discriminant, later called $BDTG$, which is defined as :

$$BDTG = (BDTG\_ttbar + a \times BDTG\_ttV)/(1 + a) \tag{5.1}$$

where a is defined as the slope in the $BDTG\_ttbar$-$BDTG\_ttV$ plane. The discriminant $BDTG$ is then split in an optimized number of bins to separate signal and background using the TransfoD function (see section 4.6.3).

An extensive study was performed in the previous round of the analysis with 2015-2016 data to optimize the sensitivity in terms of number of bins and amount of signal and background in each bin. The optimal configuration was found to be a=1, z_b=6 and $z_s = 0$. This corresponds to a situation where the signal is constant in each bins of the BDTG discriminant. As a result the lowest bins are

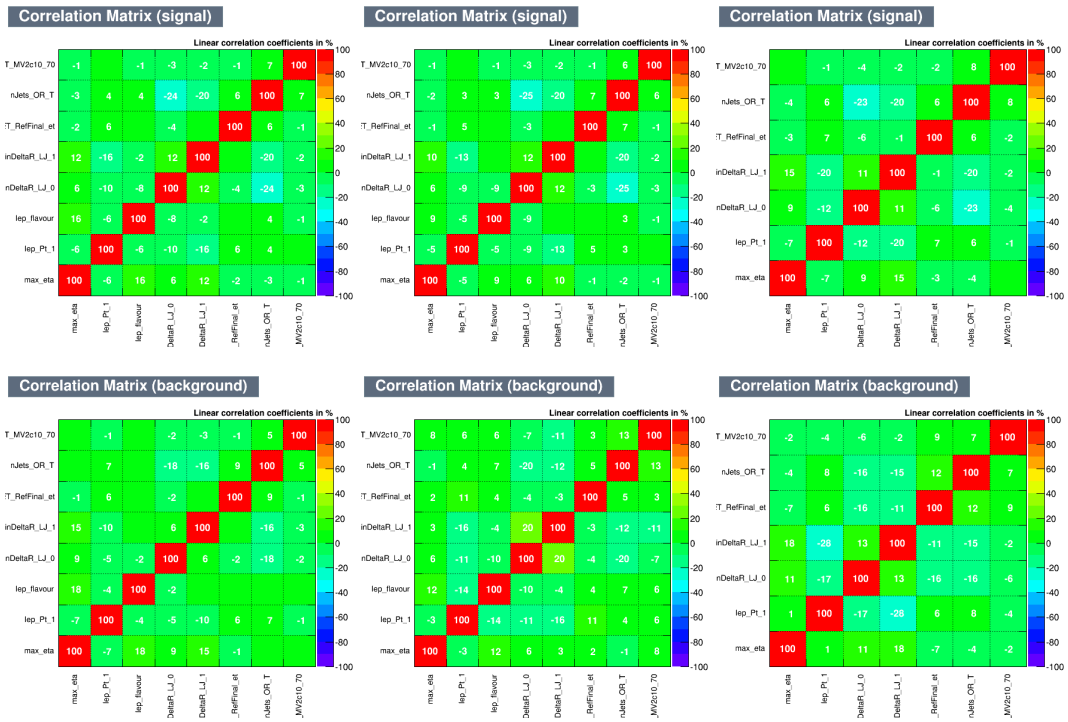

Figure 5.15 – Correlation matrices are shown between the input variables for the signal (up) and for the background in BDT_ttV (down left) and BDT_ttbar (down middle and right). Inclusive, $ee + OF$ and $\mu\mu$ channel from left to right.

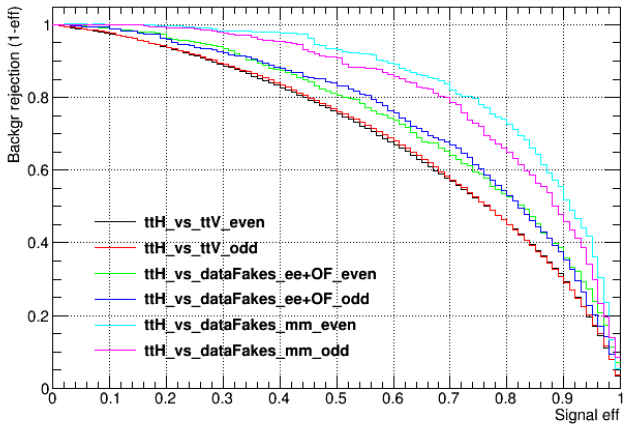

Figure 5.16 – Background rejection versus signal efficiency for all BDTs is shown when the training is done on odd and even events.

more populated in $t\bar{t}$, the central bins more populated in $t\bar{t}V$ and the highest bins more pure in $t\bar{t}H$. The final discriminant is therefore defined as :

$$BDTG = (BDTG\_ttbar + BDTG\_ttV)/2 \text{ with TransfoD(6,0)} \quad (5.2)$$

Because in the current analysis we split the 2ℓSS channel by flavor into four sub-channels the number of events is lower in the individual channels. A quick check was performed to estimate the expected significance if a smaller number of bins is used in the ee, $e\mu$ and μe channels (these channels are affected by smaller statistics). As can be seen in Table 5.5 keeping the same number of bins, i.e 6 bins, gives the best result (this is true for individual channel fit and combined fit). For the $\mu\mu$ channel the number of bins was also kept constant, 6 bins.

Number of bins	4	5	6
Expected significance, σ	2.17	2.14	2.21

Table 5.5 – Expected signal significance in the combined fit for different number of bins in the final discriminant for ee, $e\mu$ and μe channels.

5.2.5 Expected fit results

The fit configuration used as baseline for this analysis is described in details in Section 5.2.5.1. The Asimov fit results are given in Section 5.2.5.2, including a comparison with the results of the previous round of analysis (2015+2016 data).

5.2.5.1 Fit configuration

In the final fit configuration, the signal strength (μ_{ttH}) is the only free parameter and is extracted from a shape fit on $BDTG$ with 6 bins, see Eq.(5.2). The full list of nuisance parameters included in the fit is shown in Table 5.6. Physics object NPs follow the recommendation from each of the performance group. The scenario for the data-driven fake/non-prompt lepton and charge-flip electron event estimations corresponds to the description given in section 5.2.2. These are the most significant NPs which take care of the number of events in the fake lepton Control Region, the background subtraction when computing the fake rate in these CR, as well as the non-closure with $t\bar{t}$ MC events in ee, $e\mu$, $\mu\mu$ channels and the photon conversion fraction in ee and $e\mu$ channels. The two last NPs relates to the uncertainties on the real lepton efficiency and the charge-flip rate measurements. Overall, a total of 279 NPs is considered, around 15% are normalization-only NPs, the others being used for shape and/or normalization.

Systematic uncertainty	Value (%)	Type	Comp
Luminosity	2.0	N	1
Pile-Up reweighting		SN	1
Physics Objects			
Electron		SN	5+1
Muon		SN	15
taus		SN	3+6
Jet vertex fraction		SN	1
Jet		SN	29
E_T^{miss}		SN	3
b-tagging		SN	126
TOTAL (Experimental)	–	–	191
Fake Lepton			
& Charge Flip electron			
Lepton Loose real CR Stat		SN	1
Lepton bkgd sub. in real CR			
Lepton Loose fake CR Stat		SN	5 (μ) + 3 (e)
Lepton bkgd sub. in fake CR		SN	3 ($t\bar{t}W$, VV, rest)*
Lepton Loose CR Stat in BDT bins		SN	6*4
Non Closure (ee, $e\mu$, $\mu\mu$)	13.3, 9.0, 12.1	N	3
γ-conversion fraction (ee, $e\mu$,μe)		SN	4+3+4
Electron Charge Flip rate		SN	1
TOTAL (reducible bkg)	–	–	51
TOTAL (MC modeling)	–	–	37
TOTAL (Overall)	–	–	279

Table 5.6 – List of systematic uncertainties considered for the final fit configuration. An "N" means that the uncertainty is taken as normalization-only for all processes and channels affected, whereas an "S" denotes systematics that are considered shape-only in all processes and * means that parameters are 100% correlated. MC modeling is not described here since it is the same as in Table 4.13 (except the FCNC process).

5.2.5.2 Fit results

Figure 5.17 shows the pre-fit distributions entering in the fit for all sub-channels (ee, $e\mu$ (up right), μe (down left) and $\mu\mu$).

Figure 5.18 left shows that no pull but significant constraints on the fake lepton related NPs are observed, especially the ones linked to the photon conversions treatment (named AlphaSys). Figure 5.18 right shows the correlation matrix between the NPs. Some correlations (but not above 40%) are observed between the fake lepton NPs. These results indicate tension in the modeling of the fake lepton background, especially the one related to photon conversion.

Figure 5.19 left shows the ranking of all NPs for the combined fit. The first

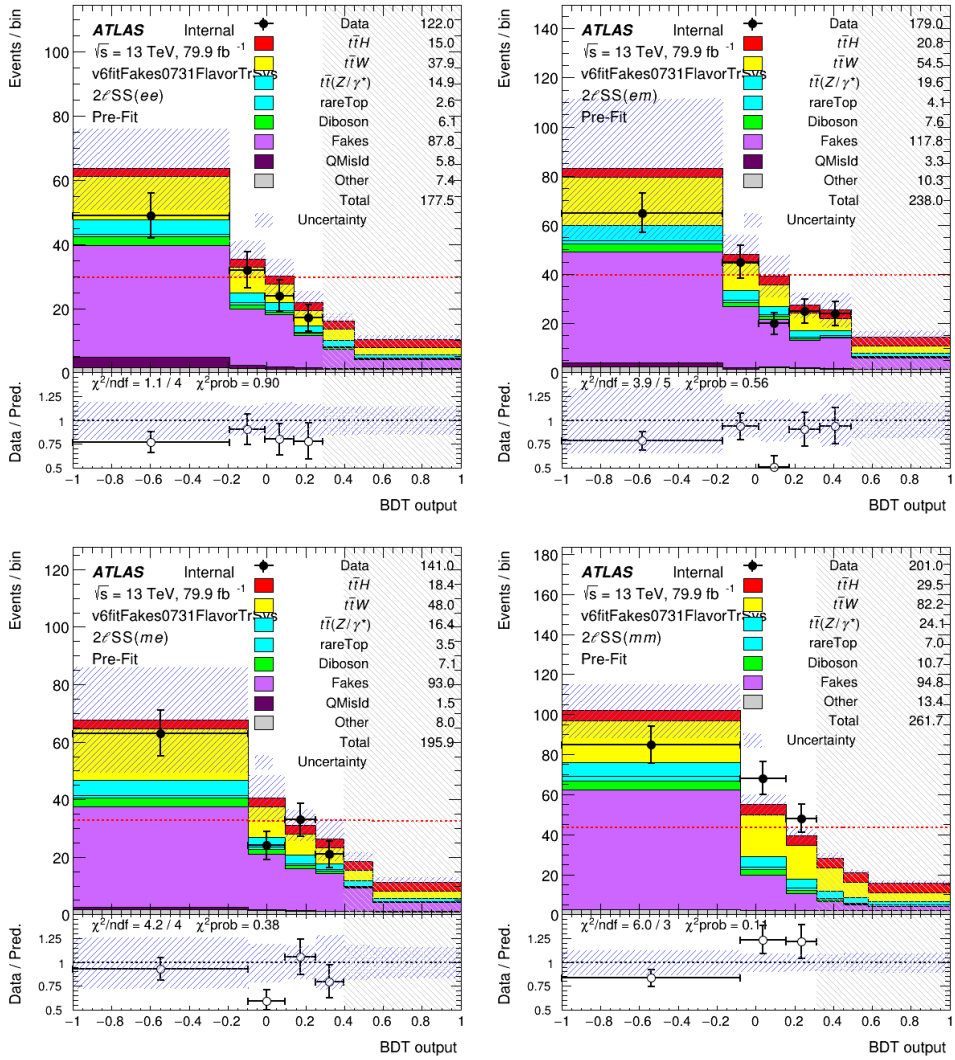

Figure 5.17 – Pre-fit $BDTG$ distribution summing signal and background for ee(up left), $e\mu$ (up right), μe (down left) and $\mu\mu$ (down right) channels. The errors include statistical and all systematic uncertainties described in Table 5.6. The red dash line shows the signal shape normalized to the total background.

ranked NP (Fakes_Mu_Stat_913) corresponds to statistical uncertainty in the $27 < p_{\mathrm{T}} < 200$ GeV bin at low $\Delta R(\mu_0, \mathrm{jet})$ of the muon fake rate CR, as shown in figure 5.8 (right). In the 2015+2016 analysis the same nuisance parameters have high impact (Fakes_Mu_Stat_17 and Fakes_Mu_Stat_13 corresponding to the muon fake rate at $50 < p_{\mathrm{T}} < 200$ and $20 < p_{\mathrm{T}} < 50$, at low $\Delta R(\mu_0, \mathrm{jet})$). Nuisance parameters used for $t\bar{t}H$ and $t\bar{t}W$ cross section (QCD scale) are still highly ranked in current analysis. All sub-channels are dominated by the fakes NPs in the individual fit.

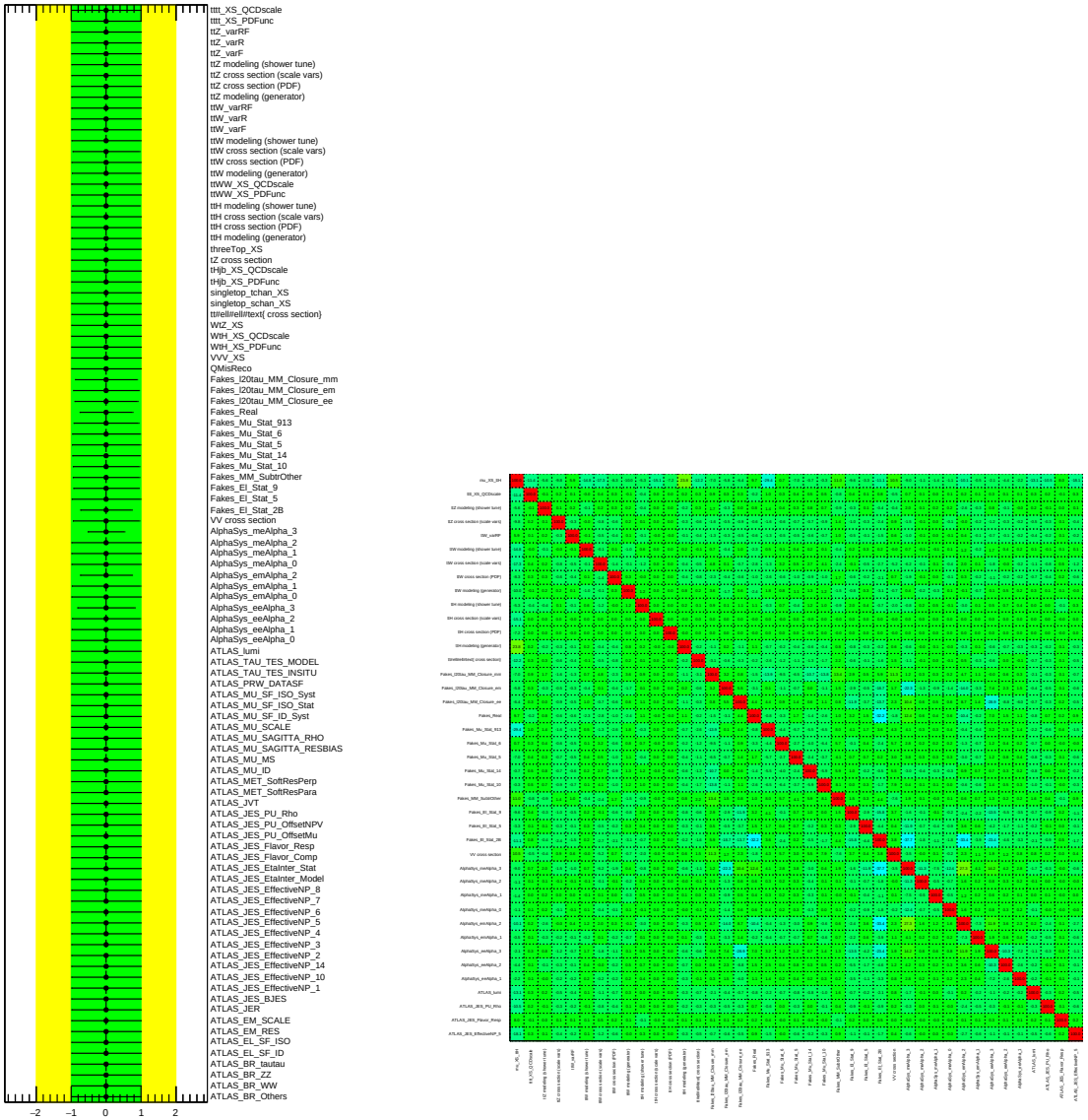

Figure 5.18 – Pull plot of nuisance parameters entering the fit (left) and their correlations plot(right).

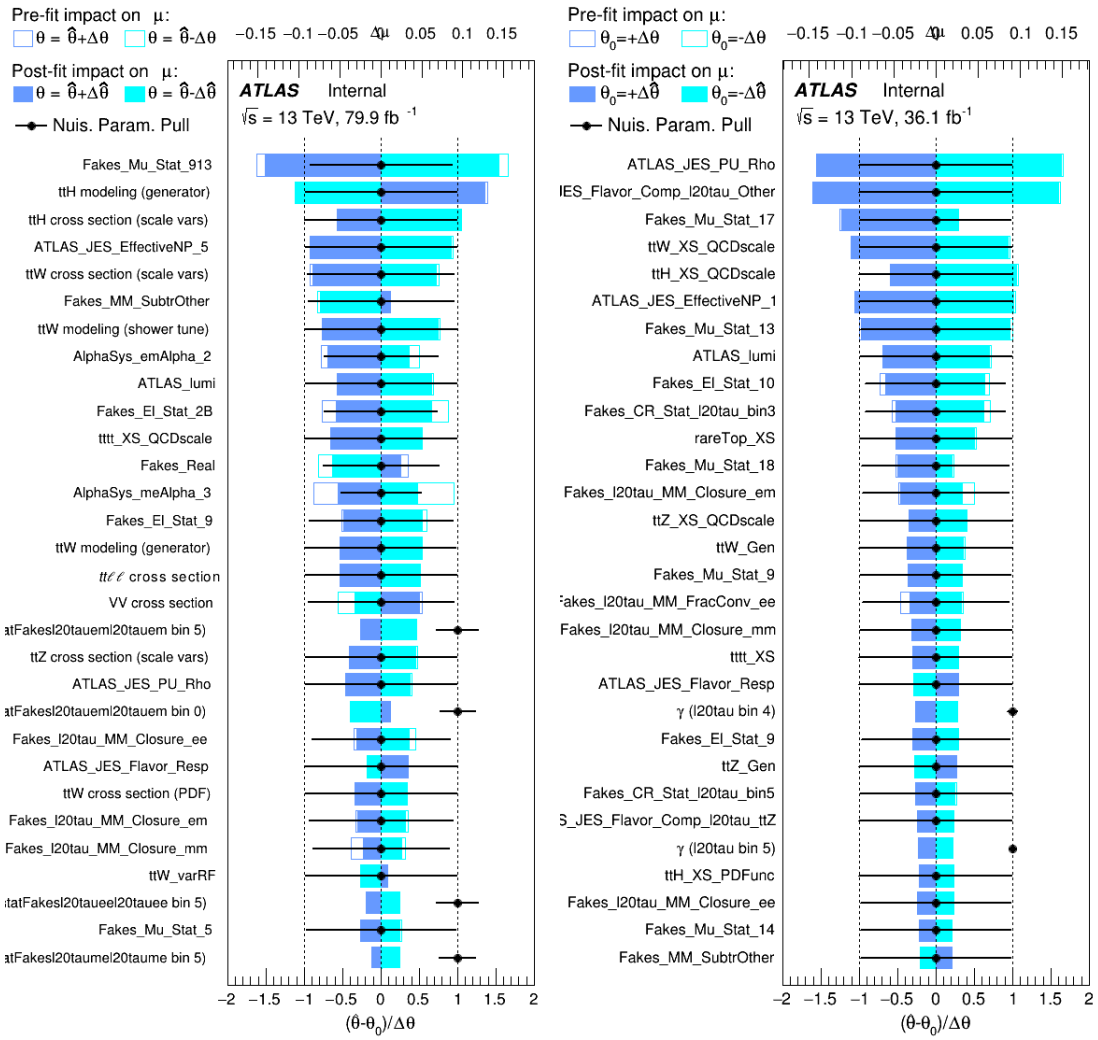

Figure 5.19 – The ranking of nuisance parameters from Table 5.6 by impact on the fitted POI in the combined Asimov fit (left). Ranking from previous analysis round is shown for comparison (right).

The signal strength of the combined fit is $\mu_{ttH} = 1.00^{+0.53}_{-0.48} = 1.00 \pm 0.50$. In more details, $\mu_{ttH} = 1.00^{+0.30}_{-0.29}(stat)^{+0.44}_{-0.38}(syst)$. The systematic uncertainties dominate the results. The expected significance is 2.21 σ (3.42 σ for stat only). The detailed results of the fit are given in Figure 5.20. For comparison, the result of the fit for the paper (2015+2016 dataset) is $\mu_{ttH} = 1.00^{+0.62}_{-0.56} = 1.00 \pm 0.59$. In more details, $\mu_{ttH} = 1.00^{+0.40}_{-0.38}(stat)^{+0.47}_{-0.41}(syst)$. For this previous result, the statistical uncertainties and systematic uncertainties are at a comparable level and the related significance is 1.8 σ (2.7 σ for stat only).

Overall, an improvement of 16 (27)% in the stat.+syst.(stat. only) significance is obtained, which is lower than what one would naively expect (the available statistics doubled).

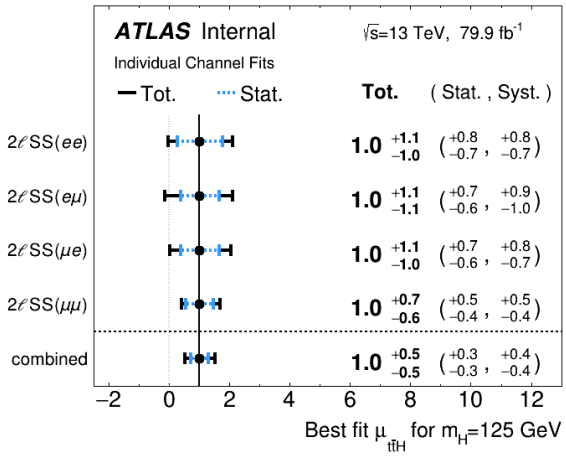

Figure 5.20 – Best fit for μ_{ttH} for individual channels split by flavor and combined fit result.

A combined fit was performed using the setup described earlier in this section but only using the 2015+2016 data sets, with the aim to have a fair comparison with the results from the previous analysis round (2015+2016). The expected significance obtained is 1.7σ. Comparing this result with the 1.9σ (stat.+syst.) obtained in the previous round of analysis shows that the current analysis is still suboptimal (worse results using the same dataset).

5.3 Current status of 80 fb^{-1} analysis

The fact that the fake lepton background composition presents large differences in loose and tight region leads to a limitation in the Matrix Method because a similar composition is expected in the loose and tight regions when the loose-to-tight extrapolation is performed. Additionally, the fake lepton rate, input of the Matrix Method, are obtained for the heavy flavor and not for conversions.

Even if more nuisance parameters were included to cope with this issue, they get constrained and the poor fit performance indicates that a proper procedure to estimates the background coming from photon conversion is necessary.

A new method based on fitting background templates has been proposed. In this method the shapes of the fake lepton backgrounds (heavy flavor, conversions) are treated separately. Their shape is estimated based on MC simulation (with proper systematics) while the normalization is determined from a fit to data (in a given CR). A new discriminating variable has been defined as the invariant mass of the track associated to the electron and the closest opposite-sign track to the electron energy cluster in the electromagnetic calorimeter to identify and reduce photon conversions. Additionally, there is the option to split the conversion in material conversion (originating from the interaction with the detector material) and inner conversion (originating from the primary vertex) and treat them separately for a better control. All these new ideas look promising and are under intense development and testing at the time of writing this thesis.

Conclusion

The success story of the Standard Model (SM) culminated with the discovery of the Higgs boson by the ATLAS and CMS experiments in 2012, as this was the last predicted particle to be discovered. The next step is to test the Higgs boson properties to the best scrutiny and explore uncharted corners of the phase space where new physics could be found.

In order to achieve the necessary sensitivity for the measurements a good understanding of the performance of the detector is required. Chapter 3 describes the electron reconstruction efficiency measurement with a Tag-and-Probe method in $Z \to ee$ events using up to 80 fb^{-1} of proton-proton collision data at $\sqrt{s} = 13$ TeV. The electron reconstruction efficiencies have values of 96-99 % with an uncertainty below 2%. The data to simulation ratios, known as scale factors (SFs), are between 0.99-1.03 at low E_{T} (15-20 GeV) with an uncertainty around 1%. At higher E_{T} the SF are very close to 1 (within 1 %) with an uncertainty below 1 %.

Non-prompt lepton tagger provides an efficient tool at reducing the leptons coming from heavy flavor decays which is a dominant background in analyses with multilepton final states like top FCNC and ttH addressed in this thesis (chapter 4 and 5). The non-prompt electron tagger SFs are generally between 0.92-0.99 (increasing from low E_{T} to higher E_{T}) and have an uncertainty of around 2% at low E_{T} and going below 1% at higher E_{T}. An additional systematic uncertainty was added to take into account pileup effects.

The flavor-changing neutral currents (FCNC) are forbidden in SM at tree level and strongly suppressed at higher orders. Beyond SM scenarios allow for significant enhancement in this processes. The top decay to a Higgs boson and an up-type quark ($t \to Hq$, $q = u, c$) is investigated in multilepton final states (2ℓSS and 3ℓ) using 36 fb^{-1} at $\sqrt{s} = 13$ TeV. The non-prompt lepton tagger is used to reduce the dominant non-prompt leptons component of the background and a MVA is further used to improve the signal-background separation. No excess over the SM values is observed and 95% confidence level upper limits are set on BR($t \to Hu$) and BR($t \to Hc$). The observed (expected) limits are BR($t \to Hu$)<0.19 (0.15)% and BR($t \to Hu$)<0.16 (0.15)%. These were the best limits on these processes in individual measurements and the results are published in $Phys.Rev.D$ journal [66].

The Higgs boson coupling to top quarks can be accessed directly in the Higgs boson associated production with a pair of top-antitop quarks (ttH). An analysis targeting $H \to WW, ZZ, \tau\tau$ is performed in seven multileptonic channels using

36.1 fb^{-1} and a combined observed (expected)significance of 4.1σ (2.8σ) is obtained. The combined measurement of $H \to WW, ZZ, \tau\tau$ (36.1 fb^{-1}), $H \to bb$ (36.1 fb^{-1}), $H \to \gamma\gamma$ (79.8 fb^{-1}) and $H \to ZZ \to 4l$ (79.8 fb^{-1}) gives an observed (expected) significance of 5.8σ (4.9σ), which passes the 5σ necessary to claim a discovery.

An analysis is performed targeting $H \to WW, ZZ, \tau\tau$ (79.8 fb^{-1}) to two lepton same-sign channel (2ℓSS) following the same strategy as the analysis $H \to WW, ZZ, \tau\tau$ (36.1 fb^{-1}). Better rejection of the non-prompt leptons increase the fraction of electrons from photon conversion limiting the applicability of the matrix method for estimating non-prompt lepton background. Proper methods for estimating separately the photon conversion are necessary and efforts are ongoing.

The LHC physics program has delivered so far only around 180 fb^{-1} and is expected to produce around 3000 fb^{-1} of data by the end of the program in 2037. The current long shutdown (LS2) 2019-2021 will allow to upgrade the accelerator to reach the designed energy of $\sqrt{s} = 14$ TeV for the Run 3. After Run 3, the luminosity will increase (high-luminosity LHC) and the pileup will eventually reach $<\mu>$=200. Important technical challenges remain ahead related to these harsh conditions. At the same time it is a unique opportunity to test the SM with unprecedented precision which could unveil deviations from SM or could lead to discoveries of new particles.

Bibliography

[1] Sheldon L. Glashow. "Partial-symmetries of weak interactions". In: *Nuclear Physics* 22.4 (1961), pp. 579–588. ISSN: 0029-5582. URL: http://www.sciencedirect.com/science/article/pii/0029558261904692 (cit. on pp. 11, 15).

[2] Abdus Salam. "Weak and Electromagnetic Interactions". In: *Elementary particle theory. Relativistic groups and analyticity.* Proceedings of the Eighth Nobel Symposium (Aspenäsgarden, Lerum, May 19–25, 1968). Ed. by Nils Svartholm. Stockholm: Almquist & Wiksell, 1968, pp. 367–377 (cit. on pp. 11, 15).

[3] Steven Weinberg. "A Model of Leptons". In: *Phys. Rev. Lett.* 19 (21 Nov. 1967), pp. 1264–1266. URL: https://link.aps.org/doi/10.1103/PhysRevLett.19.1264 (cit. on pp. 11, 15).

[4] ATLAS Collaboration. "Observation of a new particle in the search for the Standard Model Higgs boson with the ATLAS detector at the LHC". In: *Phys. Lett.* B716 (2012), pp. 1–29. arXiv: 1207.7214 [hep-ex] (cit. on pp. 11, 21, 22, 25).

[5] CMS Collaboration. "Observation of a new boson at a mass of 125 GeV with the CMS experiment at the LHC". In: *Phys. Lett.* B716 (2012), pp. 30–61. arXiv: 1207.7235 [hep-ex] (cit. on pp. 11, 21, 25).

[6] M. C. Gonzalez-Garcia and Michele Maltoni. "Phenomenology with Massive Neutrinos". In: *Phys. Rept.* 460 (2008), pp. 1–129. arXiv: 0704.1800 [hep-ph] (cit. on p. 12).

[7] F. Englert and R. Brout. "Broken Symmetry and the Mass of Gauge Vector Mesons". In: *Phys. Rev. Lett.* 13 (9 Aug. 1964), pp. 321–323. URL: https://link.aps.org/doi/10.1103/PhysRevLett.13.321 (cit. on p. 16).

[8] P.W. Higgs. "Broken symmetries, massless particles and gauge fields". In: *Physics Letters* 12.2 (1964), pp. 132–133. ISSN: 0031-9163. URL: http://www.sciencedirect.com/science/article/pii/0031916364911369 (cit. on p. 16).

[9] Peter W. Higgs. "Broken Symmetries and the Masses of Gauge Bosons". In: *Phys. Rev. Lett.* 13 (16 Oct. 1964), pp. 508–509. URL: https://link.aps.org/doi/10.1103/PhysRevLett.13.508 (cit. on p. 16).

[10] G. S. Guralnik, C. R. Hagen, and T. W. B. Kibble. "Global Conservation Laws and Massless Particles". In: *Phys. Rev. Lett.* 13 (20 Nov. 1964), pp. 585–587. URL: https://link.aps.org/doi/10.1103/PhysRevLett.13.585 (cit. on p. 16).

[11] John Ellis. "Higgs Physics". In: KCL-PH-TH-2013-49. KCL-PH-TH-2013-49. LCTS-2013-36. CERN-PH-TH-2013-315 (Dec. 2013), 117–168. 52 p. URL: https://cds.cern.ch/record/1638469 (cit. on p. 17).

[12] Gordon L. Kane and Mikhail A. Shifman. "Introduction to 'the supersymmetric world: The Beginnings of the theory'". In: (2001). arXiv: hep-ph/0102298 [hep-ph] (cit. on p. 19).

[13] Rudolf Haag, Jan T. Lopuszanski, and Martin Sohnius. "All Possible Generators of Supersymmetries of the s Matrix". In: *Nucl. Phys.* B88 (1975). [,257(1974)], p. 257 (cit. on p. 19).

[14] Hans Peter Nilles. "Supersymmetry, Supergravity and Particle Physics". In: *Phys. Rept.* 110 (1984), pp. 1–162. DOI: 10.1016/0370-1573(84)90008-5 (cit. on p. 19).

[15] Oliver Witzel. "Review on Composite Higgs Models". In: *PoS* LATTICE2018 (2019), p. 006. arXiv: 1901.08216 [hep-lat] (cit. on p. 19).

[16] Nima Arkani-Hamed, Savas Dimopoulos, and G. R. Dvali. "The Hierarchy problem and new dimensions at a millimeter". In: *Phys. Lett.* B429 (1998), pp. 263–272. arXiv: hep-ph/9803315 [hep-ph] (cit. on p. 19).

[17] Lisa Randall and Raman Sundrum. "A Large mass hierarchy from a small extra dimension". In: *Phys. Rev. Lett.* 83 (1999), pp. 3370–3373. arXiv: hep-ph/9905221 [hep-ph] (cit. on p. 19).

[18] D. de Florian et al. "Handbook of LHC Higgs Cross Sections: 4. Deciphering the Nature of the Higgs Sector". In: (2016). arXiv: 1610.07922 [hep-ph] (cit. on pp. 19, 103).

[19] ATLAS Collaboration. *Higgs production cros sections*. URL: https://twiki.cern.ch/twiki/bin/view/LHCPhysics/LHCHXSWGCrossSectionsFigures (cit. on p. 20).

[20] Morad Aaboud et al. "Observation of $H \to b\bar{b}$ decays and VH production with the ATLAS detector". In: *Phys. Lett.* B786 (2018), pp. 59–86. arXiv: 1808.08238 [hep-ex] (cit. on p. 21).

[21] A. M. Sirunyan et al. "Observation of Higgs boson decay to bottom quarks". In: *Phys. Rev. Lett.* 121.12 (2018), p. 121801. arXiv: 1808.08242 [hep-ex] (cit. on p. 21).

[22] ATLAS Collaboration. "Measurement of the Higgs boson mass in the $H \to ZZ* \to 4l$ and $H \to \gamma\gamma$ channels with $\sqrt{s} = 13$ TeV pp collisions using the ATLAS detector". In: *Physics Letters B* 784 (2018), pp. 345–366 (cit. on p. 22).

[23] ATLAS Collaboration. "Evidence for the spin-0 nature of the Higgs boson using ATLAS data". In: *Phys. Lett.* B726 (2013), pp. 120–144. arXiv: 1307.1432 [hep-ex] (cit. on p. 23).

[24] ATLAS Collaboration. "Study of the spin and parity of the Higgs boson in diboson decays with the ATLAS detector". In: *Eur. Phys. J.* C75.10 (2015). [Erratum: Eur. Phys. J.C76,no.3,152(2016)], p. 476. arXiv: 1506.05669 [hep-ex] (cit. on p. 23).

[25] A. David, A. Denner, M. Duehrssen, et al. "LHC HXSWG interim recommendations to explore the coupling structure of a Higgs-like particle". In: (2012). arXiv: 1209.0040 [hep-ph] (cit. on p. 23).

[26] ATLAS Collaboration. *Combined measurements of Higgs boson production and decay using up to 80 fb^{-1} of proton–proton collision data at $\sqrt{s}$ = 13 TeV collected with the ATLAS experiment*. Tech. rep. ATLAS-CONF-2018-031. Geneva: CERN, 2018. URL: http://cds.cern.ch/record/2629412 (cit. on p. 24).

[27] L. Evans and P. Bryant. "LHC Machine". In: *Journal of Instrumentation* 3.08 (2008), S08001–S08001 (cit. on pp. 25, 27).

[28] S. Myers and E. Picasso. "The design, construction and commissioning of the CERN large Electron–Positron collider". In: *Contemporary Physics* 31.6 (1990), pp. 387–403. eprint: https://doi.org/10.1080/00107519008213789 (cit. on p. 25).

[29] E. Mobs. "The CERN accelerator complex. Complexe des accélérateurs du CERN". In: (2016). General Photo. URL: https://cds.cern.ch/record/2197559 (cit. on p. 26).

[30] ATLAS Collaboration. *ALTAS Experiment – Luminosity Public Results Run 2*. Tech. rep. 2019. URL: https://twiki.cern.ch/twiki/bin/view/AtlasPublic/LuminosityPublicResultsRun2 (cit. on p. 28).

[31] ATLAS Collaboration. "The ATLAS Experiment at the CERN Large Hadron Collider". In: *Journal of Instrumentation* 3.08 (2008), S08003–S08003 (cit. on pp. 29, 31, 34, 35, 37, 40).

[32] K. Potamianos. "The upgraded Pixel detector and the commissioning of the Inner Detector tracking of the ATLAS experiment for Run-2 at the Large Hadron Collider". In: *PoS* EPS-HEP2015 (2015), p. 261. arXiv: 1608.07850 [physics.ins-det] (cit. on p. 31).

[33] M Capeans, G Darbo, K Einsweiller, et al. *ATLAS Insertable B-Layer Technical Design Report*. Tech. rep. CERN-LHCC-2010-013. ATLAS-TDR-19. Sept. 2010. URL: https://cds.cern.ch/record/1291633 (cit. on p. 31).

[34] B. Abbott et al. “Production and Integration of the ATLAS Insertable B-Layer”. In: *JINST* 13.05 (2018), T05008. arXiv: 1803.00844 [physics.ins-det] (cit. on p. 32).

[35] ATLAS Collaboration. “Electron and photon energy calibration with the ATLAS detector using LHC Run 1 data”. In: *Eur. Phys. J.* C74.10 (2014), p. 3071. arXiv: 1407.5063 [hep-ex] (cit. on p. 35).

[36] ATLAS Collaboration. “Monitoring and data quality assessment of the ATLAS liquid argon calorimeter”. In: *JINST* 9 (2014), P07024. arXiv: 1405.3768 [hep-ex] (cit. on p. 36).

[37] ATLAS Collaboration. *LAr data quality inefficiency in Run 2*. URL: https://twiki.cern.ch/twiki/bin/view/AtlasPublic/LArCaloPublicResults2015 (cit. on p. 36).

[38] T G Cornelissen, N Van Eldik, M Elsing, et al. *Updates of the ATLAS Tracking Event Data Model (Release 13)*. Tech. rep. ATL-SOFT-PUB-2007-003. ATL-COM-SOFT-2007-008. Geneva: CERN, 2007. URL: https://cds.cern.ch/record/1038095 (cit. on p. 42).

[39] ATLAS Collaboration. “Performance of the ATLAS Track Reconstruction Algorithms in Dense Environments in LHC Run 2”. In: *Eur. Phys. J.* C77.10 (2017), p. 673. arXiv: 1704.07983 [hep-ex] (cit. on p. 41).

[40] ATLAS Collaboration. “A neural network clustering algorithm for the ATLAS silicon pixel detector”. In: *JINST* 9 (2014), P09009. arXiv: 1406.7690 [hep-ex] (cit. on p. 41).

[41] T G Cornelissen, M Elsing, I Gavrilenko, et al. “The global $\chi 2$ track fitter in ATLAS”. In: *Journal of Physics: Conference Series* 119.3 (2008), p. 032013 (cit. on p. 41).

[42] R. Frühwirth. “Application of Kalman filtering to track and vertex fitting”. In: *Nuclear Instruments and Methods in Physics Research Section A: Accelerators, Spectrometers, Detectors and Associated Equipment* 262.2 (1987), pp. 444–450. ISSN: 0168-9002 (cit. on p. 41).

[43] ATLAS Collaboration. “Electron reconstruction and identification in the ATLAS experiment using the 2015 and 2016 LHC proton-proton collision data at $\sqrt{s} = 13$ TeV”. In: *Submitted to: Eur. Phys. J.* (2019). arXiv: 1902.04655 [physics.ins-det] (cit. on pp. 43, 45–47, 68, 76, 77, 93).

[44] W Lampl, S Laplace, D Lelas, et al. *Calorimeter Clustering Algorithms: Description and Performance*. Tech. rep. ATL-LARG-PUB-2008-002. ATL-COM-LARG-2008-003. Geneva: CERN, Apr. 2008. URL: https://cds.cern.ch/record/1099735 (cit. on p. 43).

[45] ATLAS Collaboration. *Improved electron reconstruction in ATLAS using the Gaussian Sum Filter-based model for bremsstrahlung*. Tech. rep. ATLAS-CONF-2012-047. Geneva: CERN, 2012. URL: https://cds.cern.ch/record/1449796 (cit. on p. 44).

[46] ATLAS Collaboration. "Electron and photon energy calibration with the ATLAS detector using 2015–2016 LHC proton-proton collision data". In: *Journal of Instrumentation* 14.03 (2019), P03017–P03017 (cit. on p. 44).

[47] ATLAS Collaboration. "Measurement of the photon identification efficiencies with the ATLAS detector using LHC Run 2 data collected in 2015 and 2016". In: *Eur. Phys. J.* C79.3 (2019), p. 205. arXiv: 1810.05087 [hep-ex] (cit. on p. 47).

[48] ATLAS Collaboration. "Muon reconstruction performance of the ATLAS detector in proton–proton collision data at $\sqrt{s} = 13$ TeV". In: *The European Physical Journal C* 76.5 (2016), p. 292. URL: https://doi.org/10.1140/epjc/s10052-016-4120-y (cit. on p. 49).

[49] ATLAS Collaboration. *Reconstruction, Energy Calibration, and Identification of Hadronically Decaying Tau Leptons in the ATLAS Experiment for Run-2 of the LHC*. Tech. rep. ATL-PHYS-PUB-2015-045. Geneva: CERN, 2015. URL: https://cds.cern.ch/record/2064383 (cit. on p. 50).

[50] ATLAS Collaboration. *Measurement of the tau lepton reconstruction and identification performance in the ATLAS experiment using pp collisions at* $\sqrt{s} = 13$ TeV. Tech. rep. ATLAS-CONF-2017-029. Geneva: CERN, 2017. URL: http://cds.cern.ch/record/2261772 (cit. on p. 50).

[51] M. Cacciari, G P Salam, and G. Soyez. "The anti-ktjet clustering algorithm". In: *Journal of High Energy Physics* 2008.04 (2008), pp. 063–063 (cit. on p. 50).

[52] ATLAS Collaboration. "Topological cell clustering in the ATLAS calorimeters and its performance in LHC Run 1". In: *Eur. Phys. J.* C77 (2017), p. 490. arXiv: 1603.02934 [hep-ex] (cit. on p. 50).

[53] ATLAS Collaboration. "Jet energy scale measurements and their systematic uncertainties in proton-proton collisions at $\sqrt{s} = 13$ TeV with the ATLAS detector". In: *Phys. Rev. D* 96 (7 2017), p. 072002. URL: https://link.aps.org/doi/10.1103/PhysRevD.96.072002 (cit. on pp. 50, 51).

[54] ATLAS Collaboration. "Measurements of b-jet tagging efficiency with the ATLAS detector using $t\bar{t}$ events at $\sqrt{s} = 13$ TeV". In: *Journal of High Energy Physics* 2018.8 (2018), p. 89. ISSN: 1029-8479. URL: https://doi.org/10.1007/JHEP08(2018)089 (cit. on p. 52).

[55] ATLAS Collaboration. *E_T^{miss} performance in the ATLAS detector using 2015-2016 LHC p-p collisions*. Tech. rep. ATLAS-CONF-2018-023. Geneva: CERN, 2018. URL: http://cds.cern.ch/record/2625233 (cit. on p. 53).

[56] ATLAS Collaboration. "Precision measurement and interpretation of inclusive W^+ , W^- and Z/γ^* production cross sections with the ATLAS detector". In: *Eur. Phys. J.* C77.6 (2017), p. 367. arXiv: 1612.03016 [hep-ex] (cit. on pp. 54, 55).

[57] ATLAS Collaboration. "Measurement of the W-boson mass in pp collisions at $\sqrt{s} = 7$ TeV with the ATLAS detector". In: *Eur. Phys. J.* C78.2 (2018). [Erratum: Eur. Phys. J.C78,no.11,898(2018)], p. 110. arXiv: 1701.07240 [hep-ex] (cit. on p. 54).

[58] K.A. Olive. "Review of Particle Physics". In: *Chinese Physics C* 38.9 (Aug. 2014), p. 090001. URL: https://doi.org/10.1088%2F1674-1137%2F38%2F9%2F090001 (cit. on p. 57).

[59] S. Frixione, G. Ridolfi, and P. Nason. "A positive-weight next-to-leading-order Monte Carlo for heavy flavour hadroproduction". In: *JHEP* 09 (2007), p. 126. arXiv: 0707.3088 [hep-ph] (cit. on pp. 59, 172).

[60] Torbjorn Sjöstrand, Stephen Mrenna, and Peter Z. Skands. "A brief introduction to PYTHIA 8.1". In: *Comput. Phys. Commun.* 178 (2008), pp. 852–867. arXiv: 0710.3820 [hep-ph] (cit. on pp. 59, 172).

[61] S. Agostinelli, J. Allison, K. Amako, et al. "Geant4—a simulation toolkit". In: *Nuclear Instruments and Methods in Physics Research Section A: Accelerators, Spectrometers, Detectors and Associated Equipment* 506.3 (2003), pp. 250–303. ISSN: 0168-9002. URL: http://www.sciencedirect.com/science/article/pii/S0168900203013688 (cit. on p. 59).

[62] ATLAS Collaboration. "The ATLAS Simulation Infrastructure". In: *The European Physical Journal C* 70.3 (2010), pp. 823–874. ISSN: 1434-6052. URL: https://doi.org/10.1140/epjc/s10052-010-1429-9 (cit. on p. 59).

[63] ATLAS Collaboration. "Electron efficiency measurements with the ATLAS detector using 2012 LHC proton–proton collision data". In: *The European Physical Journal C* 77.3 (2017), p. 195. URL: https://doi.org/10.1140/epjc/s10052-017-4756-2 (cit. on p. 59).

[64] R. T. Roberts. "Evidence for the associated production of the Higgs boson and a top quark pair with the ATLAS detector". Presented 03 Sep 2018. 2018. URL: https://cds.cern.ch/record/2652942 (cit. on pp. 72, 75, 76).

[65] ATLAS Collaboration. "Evidence for the associated production of the Higgs boson and a top quark pair with the ATLAS detector". In: *Phys. Rev. D* 97 (7 2018), p. 072003. URL: https://link.aps.org/doi/10.1103/PhysRevD.97.072003 (cit. on pp. 82, 93, 100, 102, 103, 136–138).

[66] ATLAS Collaboration. "Search for flavor-changing neutral currents in top quark decays $t \to Hc$ and $t \to Hu$ in multilepton final states in proton-proton collisions at $\sqrt{s} = 13$ TeV with the ATLAS detector". In: *Phys. Rev. D* 98 (3 2018), p. 032002. URL: https://link.aps.org/doi/10.1103/PhysRevD.98.032002 (cit. on pp. 93, 132, 160).

[67] ATLAS Collaboration. "Observation of Higgs boson production in association with a top quark pair at the LHC with the ATLAS detector". In: *Physics Letters B* 784 (2018), pp. 173–191. URL: http://www.sciencedirect.com/science/article/pii/S0370269318305732 (cit. on pp. 93, 103, 138–140).

[68] S. L. Glashow, J. Iliopoulos, and L. Maiani. "Weak Interactions with Lepton-Hadron Symmetry". In: *Phys. Rev. D* 2 (7 1970), pp. 1285–1292. URL: https://link.aps.org/doi/10.1103/PhysRevD.2.1285 (cit. on p. 94).

[69] K. Agashe et al. "Working Group Report: Top Quark". In: *Proceedings, 2013 Community Summer Study on the Future of U.S. Particle Physics: Snowmass on the Mississippi (CSS2013): Minneapolis, MN, USA, July 29-August 6, 2013*. 2013. arXiv: 1311.2028 [hep-ph] (cit. on pp. 94, 95).

[70] T. P. Cheng and M. Sher. "Mass-matrix ansatz and flavor nonconservation in models with multiple Higgs doublets". In: *Phys. Rev. D* 35 (11 1987), pp. 3484–3491. URL: https://link.aps.org/doi/10.1103/PhysRevD.35.3484 (cit. on p. 94).

[71] J R Andersen et al. "Handbook of LHC Higgs Cross Sections: 3. Higgs Properties". In: (2013). Ed. by S Heinemeyer, C Mariotti, G Passarino, et al. arXiv: 1307.1347 [hep-ph] (cit. on p. 96).

[72] ATLAS Collaboration. "Search for top quark decays t $\to$ qH with H $\to \gamma\gamma$ using the ATLAS detector". In: *Journal of High Energy Physics* 2014.6 (2014), p. 8. ISSN: 1029-8479. URL: https://doi.org/10.1007/JHEP06(2014)008 (cit. on p. 97).

[73] LHC Physics Top working group. "LHCTopWG Summary Plots". In: (2018). URL: https://twiki.cern.ch/twiki/bin/view/LHCPhysics/LHCTopWGSummaryPlots (cit. on p. 97).

[74] ATLAS Collaboration. "Search for top quark decays t $\to$ qH, with H $\to \gamma\gamma$, in $\sqrt{s}$ =13 TeV pp collisions using the ATLAS detector". In: *Journal of High Energy Physics* 2017.10 (2017), p. 129. ISSN: 1029-8479. URL: https://doi.org/10.1007/JHEP10(2017)129 (cit. on pp. 97, 98, 130).

[75] CMS Collaboration. "Search for the flavor-changing neutral current interactions of the top quark and the Higgs boson which decays into a pair of b quarks at $\sqrt{s} = 13$ TeV". In: (2017). arXiv: 1712.02399 [hep-ex] (cit. on pp. 97, 98).

[76] ATLAS Collaboration. "Search for flavour-changing neutral current top quark decays $t \to Hq$ in pp collisions at $\sqrt{s} = 8$ TeV with the ATLAS detector". In: *JHEP* 12 (2015), p. 061. arXiv: 1509.06047 [hep-ex] (cit. on p. 98).

[77] CMS Collaboration. "Search for top quark decays via Higgs-boson-mediated flavor-changing neutral currents in pp collisions at $\sqrt{s} = 8$ TeV". In: *JHEP* 02 (2017), p. 079. arXiv: 1610.04857 [hep-ex] (cit. on p. 98).

[78] CMS Collaboration. "Observation of $t\bar{t}H$ Production". In: *Phys. Rev. Lett.* 120 (23 2018), p. 231801. URL: https://link.aps.org/doi/10.1103/PhysRevLett.120.231801 (cit. on pp. 103, 140).

[79] J. Alwall, R. Frederix, S. Frixione, et al. "The automated computation of tree-level and next-to-leading order differential cross sections, and their matching to parton shower simulations". In: *Journal of High Energy Physics* 2014.7 (2014), p. 79. ISSN: 1029-8479. URL: https://doi.org/10.1007/JHEP07(2014)079 (cit. on p. 103).

[80] P. Artoisenet, R. Frederix, O. Mattelaer, et al. "Automatic spin-entangled decays of heavy resonances in Monte Carlo simulations". In: *Journal of High Energy Physics* 2013.3 (2013), p. 15. ISSN: 1029-8479. URL: https://doi.org/10.1007/JHEP03(2013)015 (cit. on p. 103).

[81] T. Sjöstrand, S. Mrenna, and P. Skands. "A brief introduction to PYTHIA 8.1". In: *Comput. Phys. Commun.* 178 (2008), p. 852. arXiv: 0710.3820 [hep-ph] (cit. on p. 103).

[82] M. Czakon and A. Mitov. "Top++: A program for the calculation of the top-pair cross-section at hadron colliders". In: *Computer Physics Communications* 185.11 (2014), pp. 2930–2938. ISSN: 0010-4655. URL: http://www.sciencedirect.com/science/article/pii/S0010465514002264 (cit. on p. 103).

[83] ATLAS Collaboration. *Estimation of non-prompt and fake lepton backgrounds in final states with top quarks produced in proton-proton collisions at $\sqrt{s}$ =8 TeV with the ATLAS detector*. Tech. rep. ATLAS-CONF-2014-058. Geneva: CERN, 2014. URL: https://cds.cern.ch/record/1951336 (cit. on p. 107).

[84] A. Hoecker, P. Speckmayer, J. Stelzer, et al. "TMVA - Toolkit for Multivariate Data Analysis". In: *arXiv e-prints*, physics/0703039 (2007), physics/0703039. arXiv: physics/0703039 [physics.data-an] (cit. on p. 111).

[85] R. Barlow and C. Beeston. "Fitting using finite Monte Carlo samples". In: *Computer Physics Communications* 77.2 (1993), pp. 219–228. ISSN: 0010-4655. URL: http://www.sciencedirect.com/science/article/pii/001046559390005W (cit. on p. 125).

[86] A L Read. "Presentation of search results: theCLstechnique". In: *Journal of Physics G: Nuclear and Particle Physics* 28.10 (Sept. 2002), pp. 2693–2704. URL: https://doi.org/10.1088%2F0954-3899%2F28%2F10%2F313 (cit. on p. 125).

[87] G. Cowan, K. Cranmer, E. Gross, et al. "Asymptotic formulae for likelihood-based tests of new physics". In: *The European Physical Journal C* 71.2 (2011), p. 1554. ISSN: 1434-6052. URL: https://doi.org/10.1140/epjc/s10052-011-1554-0 (cit. on p. 125).

[88] ATLAS Collaboration. "Search for top-quark decays $t \to Hq$ with 36 fb^{-1} of pp collision data at $\sqrt{s} = 13$ TeV with the ATLAS detector". In: *Submitted to: JHEP* (2018). arXiv: 1812.11568 [hep-ex] (cit. on pp. 130, 131).

[89] V. Barger, K. Hagiwara, and Y.-J. Zheng. "Probing the Higgs Yukawa coupling to the top quark at the LHC via single top + Higgs production". In: *Phys. Rev. D* 99 (3 2019), p. 031701. URL: https://link.aps.org/doi/10.1103/PhysRevD.99.031701 (cit. on p. 133).

[90] ATLAS Collaboration. "Search for the standard model Higgs boson produced in association with top quarks and decaying into a $b\bar{b}$ pair in pp collisions at $\sqrt{s} = 13$ TeV with the ATLAS detector". In: *Phys. Rev. D* 97 (7 2018), p. 072016. URL: https://link.aps.org/doi/10.1103/PhysRevD.97.072016 (cit. on p. 139).

[91] R. D. Ball et al. "Parton distributions for the LHC Run II". In: *JHEP* 04 (2015), p. 040. arXiv: 1410.8849 [hep-ph] (cit. on p. 172).

[92] H.-L. Lai et al. "New parton distributions for collider physics". In: *Phys. Rev. D* 82 (2010), p. 074024. arXiv: 1007.2241 [hep-ph] (cit. on p. 172).

[93] E. Re. "Single-top Wt-channel production matched with parton showers using the POWHEG method". In: *Eur. Phys. J. C* 71 (2011), p. 1547. arXiv: 1009.2450 [hep-ph] (cit. on p. 172).

[94] S. Alioli, P. Nason, C. Oleari, et al. "NLO single-top production matched with shower in POWHEG: $s-$ and $t-$channel contributions". In: *JHEP* 09 (2009), p. 111. arXiv: 0907.4076 [hep-ph] (cit. on p. 172).

[95] R. Frederix, E. Re, and P. Torrielli. "Single-top t-channel hadroproduction in the four-flavour scheme with POWHEG and aMC@NLO". In: *JHEP* 09 (2012), p. 130. arXiv: 1207.5391 [hep-ph] (cit. on p. 172).

[96] R. D. Ball et al. "Parton distributions with LHC data". In: *Nucl. Phys. B* 867 (2013), p. 244. arXiv: 1207.1303 [hep-ph] (cit. on p. 172).

[97] ATLAS Collaboration. *ATLAS Run 1 Pythia8 tunes*. ATL-PHYS-PUB-2014-021. 2014. URL: http://cds.cern.ch/record/1966419 (cit. on p. 172).

[98] J. Pumplin, D. R. Stump, J. Huston, et al. “New Generation of Parton Distributions with Uncertainties from Global QCD Analysis”. In: *JHEP* 07 (2002), p. 012. arXiv: hep-ph/0201195 [hep-ph] (cit. on p. 172).

[99] P. M. Nadolsky et al. “Implications of CTEQ global analysis for collider observables”. In: *Phys. Rev. D* 78 (2008), p. 013004. arXiv: 0802.0007 [hep-ph] (cit. on p. 172).

[100] M. H. Seymour and A. Siodmok. “Constraining MPI models using σ_{eff} and recent Tevatron and LHC Underlying Event data”. In: *JHEP* 10 (2013), p. 113. arXiv: 1307.5015 [hep-ph] (cit. on p. 172).

[101] P. Skands. “Tuning Monte Carlo Generators: The Perugia Tunes”. In: *Phys. Rev. D* 82 (2010), p. 074018. arXiv: 1005.3457 [hep-ph] (cit. on p. 172).

[102] J. Alwall et al. “The automated computation of tree-level and next-to-leading order differential cross sections, and their matching to parton shower simulations”. In: *JHEP* 07 (2014), p. 079. arXiv: 1405.0301 [hep-ph] (cit. on p. 172).

[103] T. Sjöstrand et al. “High-energy-physics event generation with Pythia 6.1”. In: *Comput. Phys. Commun.* 135 (2001), p. 238. arXiv: hep-ph/0010017 [hep-ph] (cit. on p. 172).

[104] M. Bahr et al. “Herwig++ Physics and Manual”. In: *Eur. Phys. J. C* 58 (2008), p. 639. arXiv: 0803.0883 [hep-ph] (cit. on p. 172).

[105] T. Gleisberg et al. “Event generation with SHERPA 1.1”. In: *JHEP* 02 (2009), p. 007. arXiv: 0811.4622 [hep-ph] (cit. on p. 172).

[106] F. Cascioli, P. Maierhofer, and S. Pozzorini. “Scattering Amplitudes with Open Loops”. In: *Phys. Rev. Lett.* 108 (2012), p. 111601. arXiv: 1111.5206 [hep-ph] (cit. on p. 172).

[107] T. Gleisberg and S. Hoeche. “Comix, a new matrix element generator”. In: *JHEP* 12 (2008), p. 039. arXiv: 0808.3674 [hep-ph] (cit. on p. 172).

[108] S. Schumann and F. Krauss. “A Parton shower algorithm based on Catani-Seymour dipole factorisation”. In: *JHEP* 03 (2008), p. 038. arXiv: 0709.1027 [hep-ph] (cit. on p. 172).

[109] S. Hoeche, F. Krauss, M. Schonherr, et al. “QCD matrix elements + parton showers: The NLO case”. In: *JHEP* 04 (2013), p. 027. arXiv: 1207.5030 [hep-ph] (cit. on p. 172).

[110] D. J. Lange. “The EvtGen particle decay simulation package”. In: *Nucl. Instrum. Meth. Phys. Res. A* 462 (2001), p. 152 (cit. on p. 172).

[111] P. Golonka and Z. Was. “PHOTOS Monte Carlo: A Precision tool for QED corrections in Z and W decays”. In: *Eur. Phys. J.* C45 (2006), pp. 97–107. arXiv: hep-ph/0506026 [hep-ph] (cit. on p. 172).

Appendix

A.1 Monte Carlo samples

A variety of MC samples was used in the ttHML and top FCNC analysis presented in this thesis. The configurations used for the event generation are summarized in table A.1.

Process	Generator	ME order	Parton Shower	PDF	Tune
$t\bar{t}W$	MG5_aMC	NLO	Pythia 8	NNPDF 3.0 NLO	A14
	(Sherpa 2.1.1)	(LO multileg)	(Sherpa)	(NNPDF 3.0 NLO)	(Sherpa default)
$t\bar{t}(Z/\gamma^* \to \ell\ell)$	MG5_aMC	NLO	Pythia 8	NNPDF 3.0 NLO	A14
	(Sherpa 2.1.1)	(LO multileg)	(Sherpa)	(NNPDF 3.0 NLO)	(Sherpa default)
$t\bar{t}H$	MG5_aMC	NLO	Pythia 8	NNPDF 3.0 NLO [91]	A14
	(MG5_aMC)	(NLO)	(Herwig++)	(CT10 [92])	(UE-EE-5)
$t\bar{t}t$, $t\bar{t}t\bar{t}$	MG5_aMC	LO	Pythia 8	NNPDF 2.3 LO	A14
$t\bar{t}W^+W^-$	MG5_aMC	LO	Pythia 8	NNPDF 2.3 LO	A14
$tHqb$	MG5_aMC	LO	Pythia 8	CT10	A14
tHW	MG5_aMC	NLO	Herwig++	CT10	UE-EE-5
tZ	MG5_aMC	LO	Pythia 6	CTEQ6L1	Perugia2012
tWZ	MG5_aMC	NLO	Pythia 8	NNPDF 2.3 LO	A14
s-, t-channel, Wt single top	Powheg-BOX v1 [93, 94, 95]	NLO	Pythia 6	CT10	Perugia2012
$t\bar{t}$	Powheg-BOX v2 [59]	NLO	Pythia 8	NNPDF 3.0 NLO	A14
	(Powheg-BOX v2)	(NLO)	(Herwig 7)	(NNPDF 3.0 NLO)	(H7-UE-MMHT)
	(Sherpa 2.1.1)	(NLO)	(Sherpa)	(NNPDF 3.0 NLO)	(Sherpa default)
	(MG5_aMC)	(NLO)	(Pythia 8)	(NNPDF 2.3 NLO)	(A14)
$t\bar{t}$, $t \to Hq$	MG5_aMC	NLO	Pythia 8	NNPDF 3.0 NLO	A14
$t\bar{t}\gamma$	MG5_aMC	LO	Pythia 8	NNPDF 2.3 LO	A14
$VV(\to \ell\ell XX)$, $qqVV$, VVV	Sherpa 2.1.1	MEPS NLO	Sherpa	CT10	Sherpa default
$Z \to \ell^+\ell^-$	Sherpa 2.2	MEPS NLO	Sherpa	NNPDF 3.0 NLO	Sherpa default

Table A.1 – The configurations used for event generation of signal and background processes. The samples used to estimate the systematic uncertainties are indicated in brackets. "V" refers to production of an electroweak boson (W or Z/γ^*). "Tune" refers to the underlying-event tuned parameters of the parton shower (PS) generator. The parton distribution function (PDF) shown in the table is the one used for the matrix element (ME). The PDF used for the parton shower is either NNPDF 2.3 LO [96] for samples using the A14 [97] tune or CTEQ6L1 [98, 99] for samples using either the UE-EE-5 [100] or the Perugia2012 [101] tune. "MG5_aMC" refers to MadGraph5_aMC@NLO with several versions from 2.1.0 to 2.3.3 [102]; "Pythia 6" refers to version 6.427 [103]; "Pythia 8" refers to version 8.2 [60]; "Herwig++" refers to version 2.7 [104]; "MEPS" refers to the method used in Sherpa [105, 106, 107, 108, 109] to match the matrix-element to the parton shower. Samples using Pythia 6 or Pythia 8 have heavy-flavor hadron decays modeled by EvtGen 1.2.0 [110]. All samples include leading-logarithm photon emission, either modeled by the parton shower generator or by PHOTOS [111].

A.2 Electron reconstruction efficiency

Below are shown invariant mass distribution for a low (high) E_{T} bin $15 < E_{\mathrm{T}} < 20$ ($40 < E_{\mathrm{T}} < 45$) GeV for denominator A.1 (A.4), for numerator A.2 (A.5) and for the electrons that fail the track quality requirement A.3 (A.6).

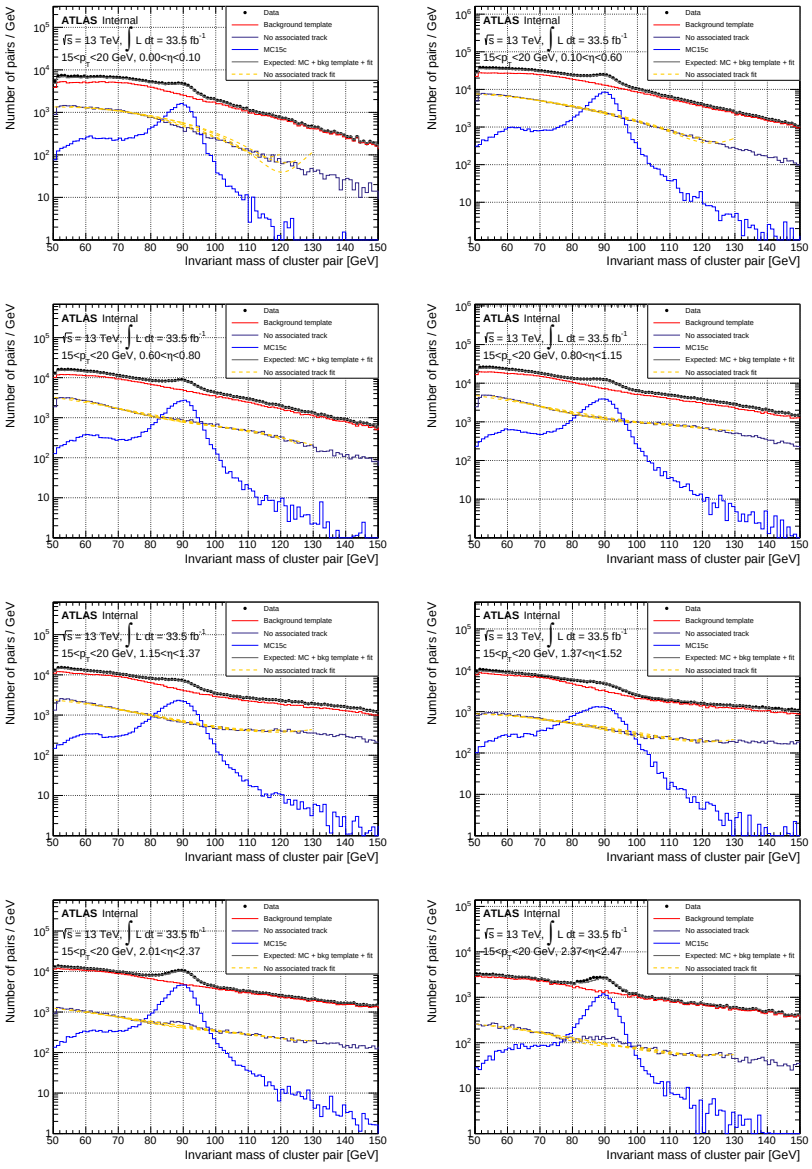

Figure A.1 – Invariant mass distributions at the denominator at $15 < E_{\mathrm{T}} < 20$ GeV displayed for $\eta > 0$ for 2016 data: all reconstructed electrons and photons are displayed. Photon background estimation is shown for the different fit ranges used as systematics.

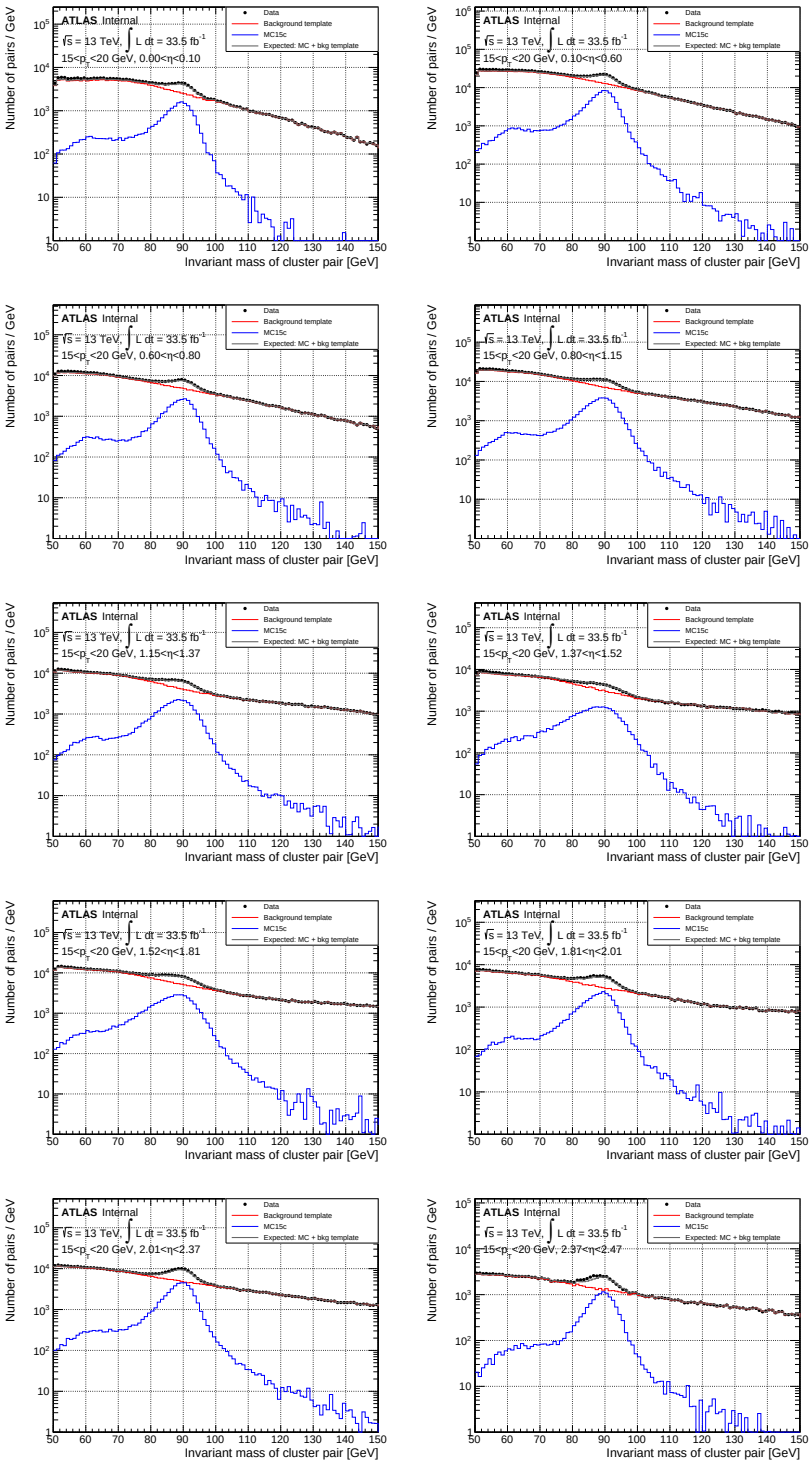

Figure A.2 – Invariant mass distributions at the numerator level in the bin $15 < E_{\mathrm{T}} < 20$ GeV displayed for $\eta > 0$ (similar plots, results for $\eta < 0$) for 2016 data: all electrons passing the track quality requirement and the corresponding background estimation are shown.

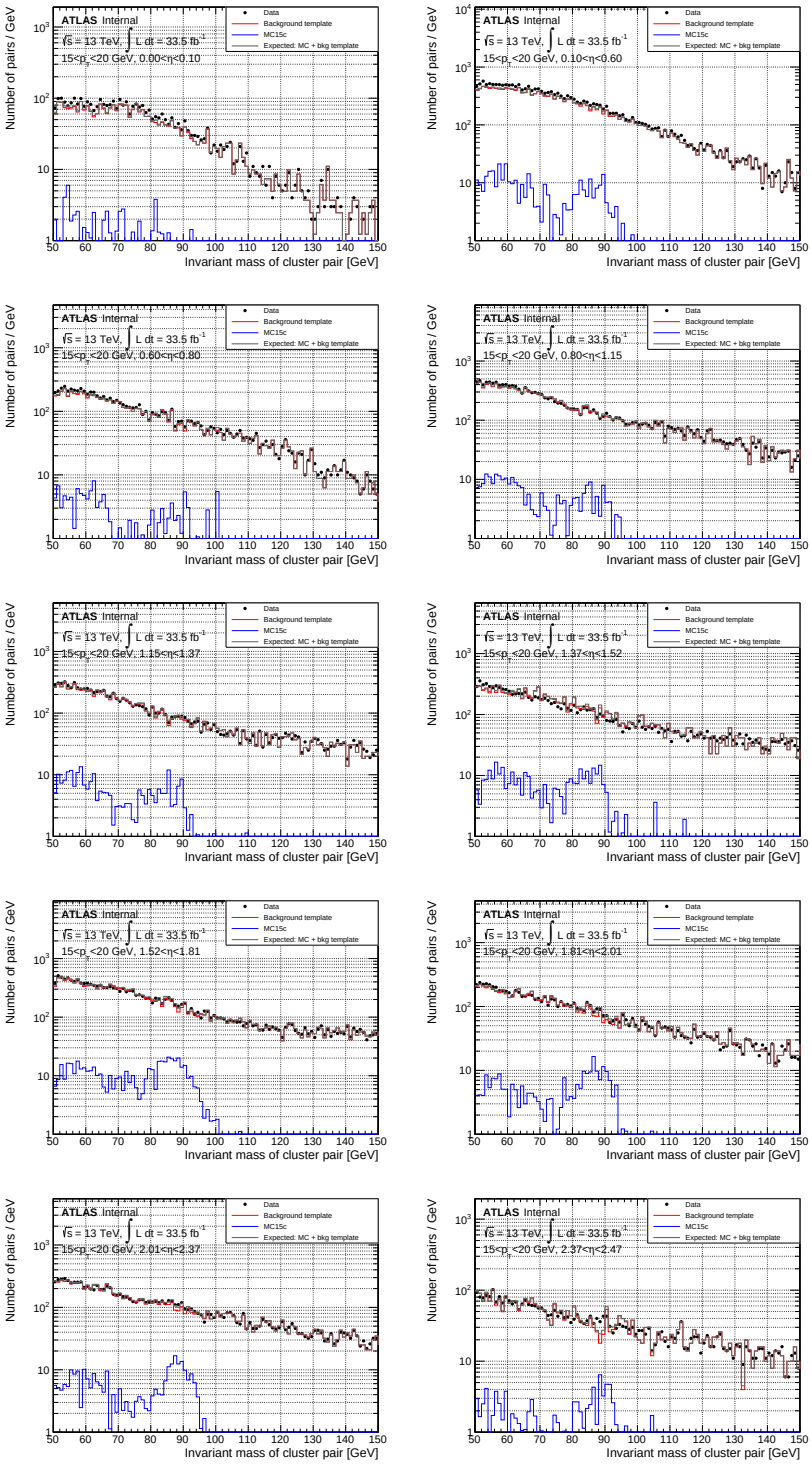

Figure A.3 – Invariant mass distributions at the numerator level in the bin $15 < E_{\mathrm{T}} < 20$ GeV displayed for $\eta > 0$ (similar plots, results for $\eta < 0$) for 2016 data: all electrons failing the track quality requirement and the corresponding background estimation are shown.

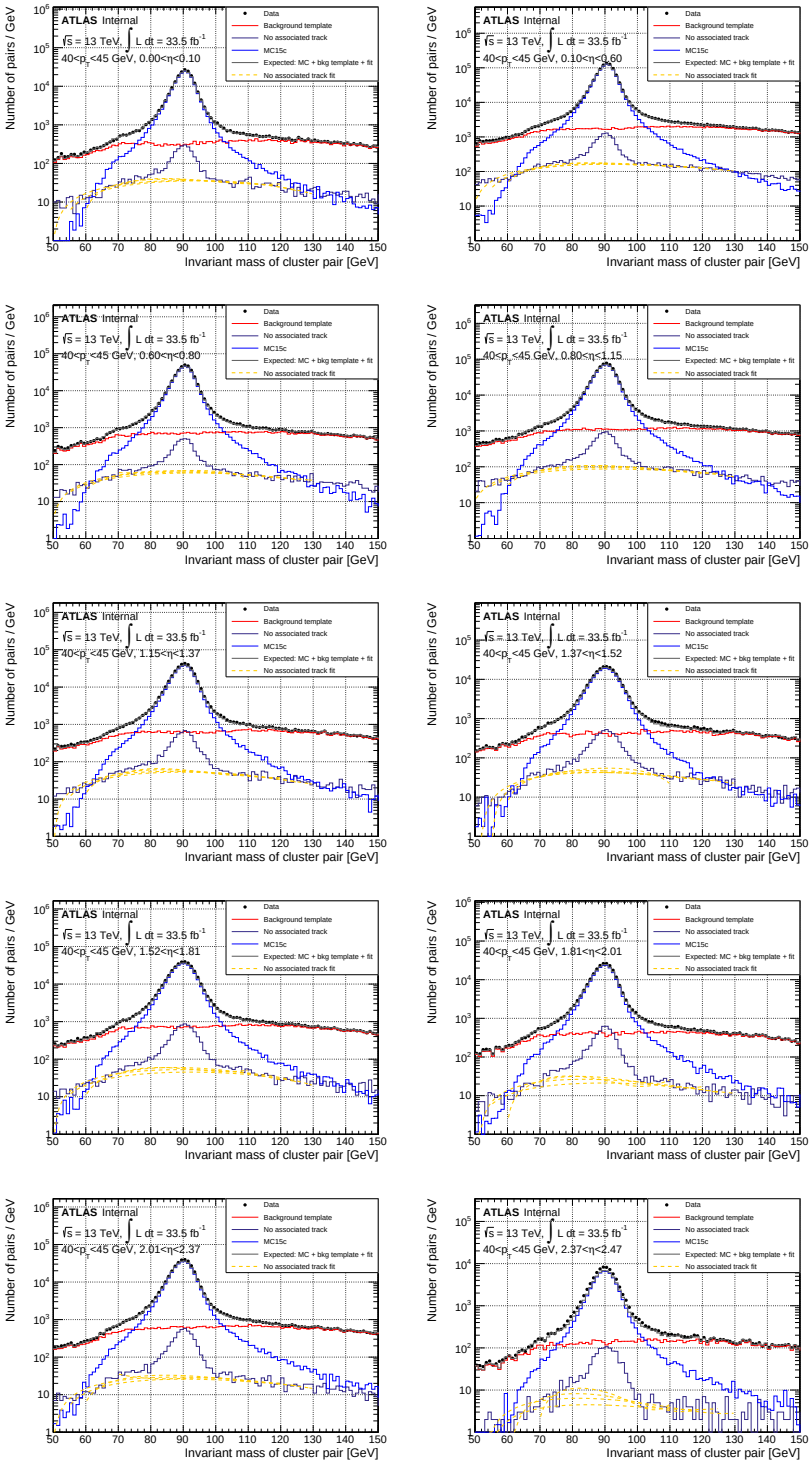

Figure A.4 – Invariant mass distributions at the denominator level in the bin $40 < E_{\mathrm{T}} < 45$ GeV displayed for $\eta > 0$ (similar plots, results for $\eta < 0$) for 2016 data: all reconstructed electrons and photons are displayed. Photon background estimation is shown for the different fit ranges used as systematics.

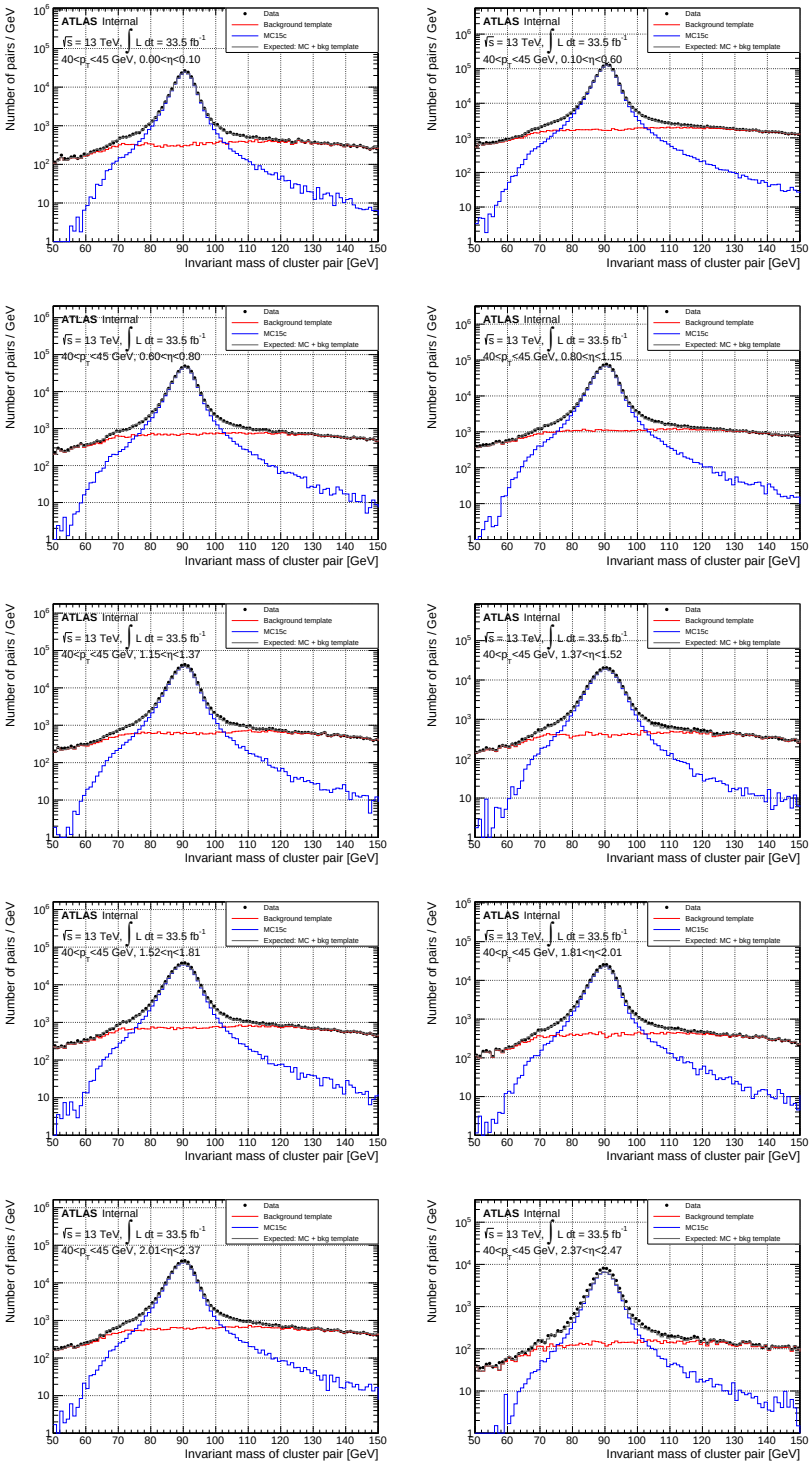

Figure A.5 – Invariant mass distributions at the numerator level in the bin $40 < E_{\mathrm{T}} < 45$ GeV displayed for $\eta > 0$ (similar plots, results for $\eta < 0$) for 2016 data: all electrons passing the track quality requirement and the corresponding background estimation are shown.

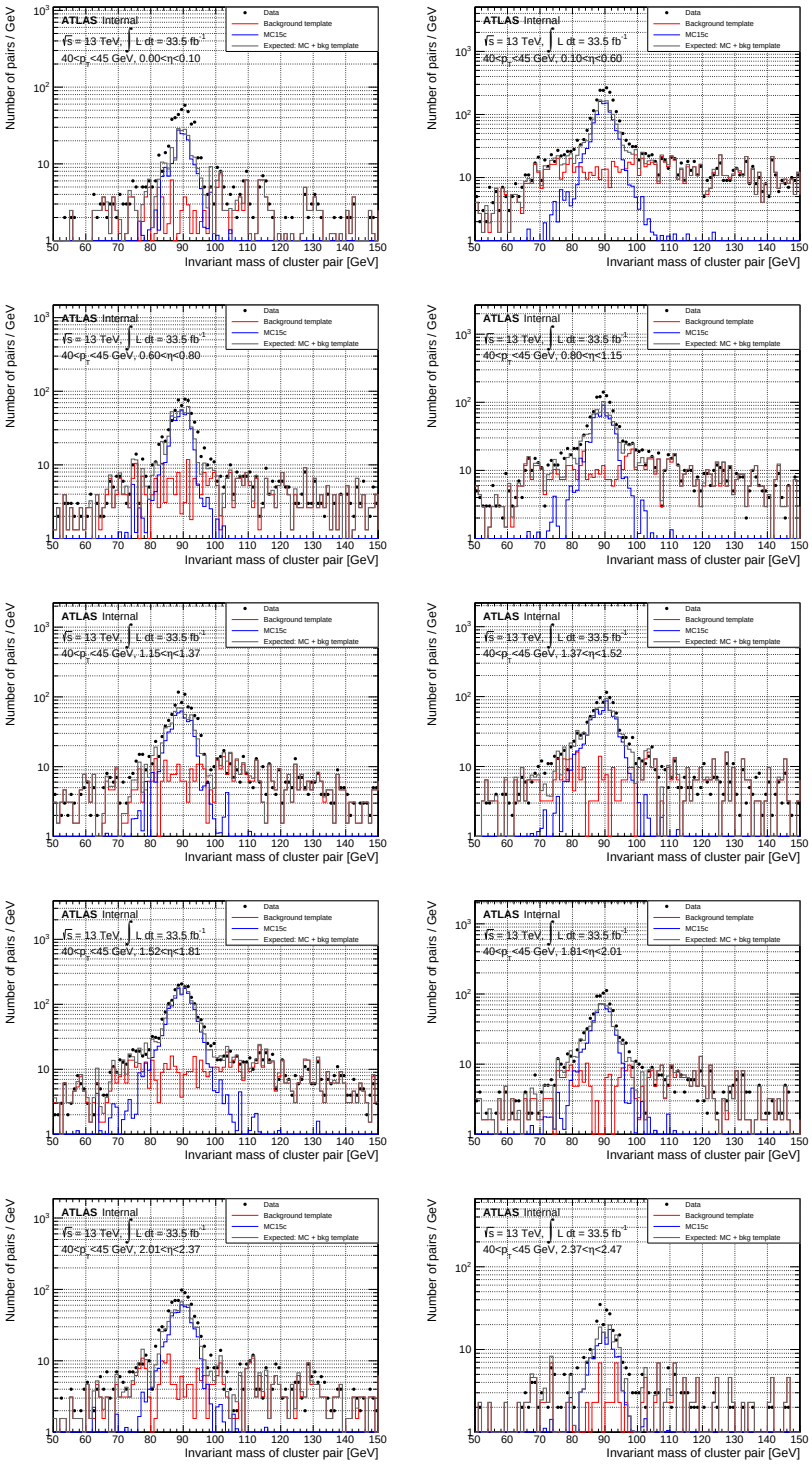

Figure A.6 – Invariant mass distributions at the numerator level in the bin $40 < E_{\mathrm{T}} < 45$ GeV displayed for $\eta > 0$ (similar plots, results for $\eta < 0$) for 2016 data: all electrons failing the track quality requirement and the corresponding background estimation are shown.

A.3 Electron non-prompt tagger (PLV) efficiency

A.3.1 Efficiency dependence on pileup

A dependence on the number of primary vertices was observed for the efficiency and SF for WP3 (see Chapter 3 for definition). Figure A.7 shows this dependence for the 2015 and 2017 dataset (2016 shown in main body). Corresponding to the SF variation, a systematic uncertainty is derived (RMS of SF distribution) which is shown in figure A.8.

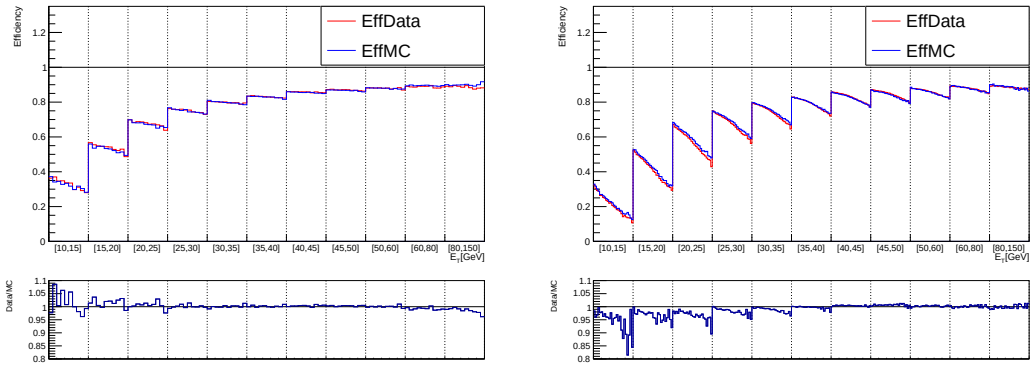

Figure A.7 – Efficiency and SF dependency on number of primary vertices (Nvtx) in bins of ET for 2015 (left) and 2017 (right).

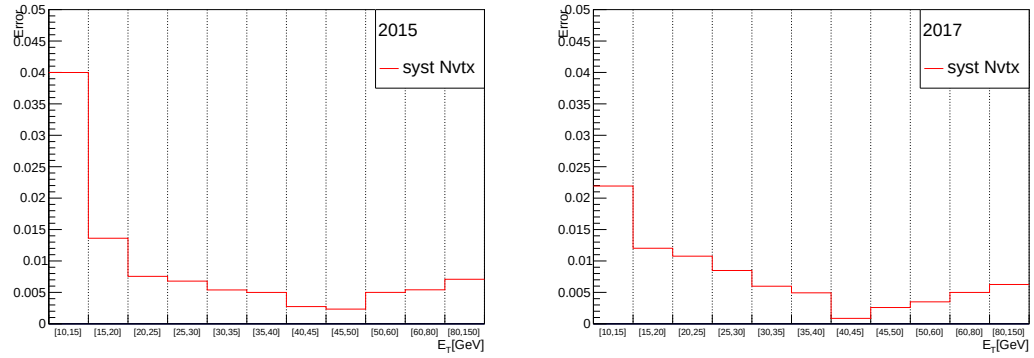

Figure A.8 – Additional systematic uncertainty derived from SFs dependency on Nvtx in bins of ET for 2015 (left) and 2017 (right).

A.3.2 Charge asymmetry dependence

A variation of the efficiency and SF is observed when performing the measurement with the electrons split in two categories based on their charge. The effect is clearly visible in figure A.9 in the inclusive distribution in η (left) and E_{T} (right).

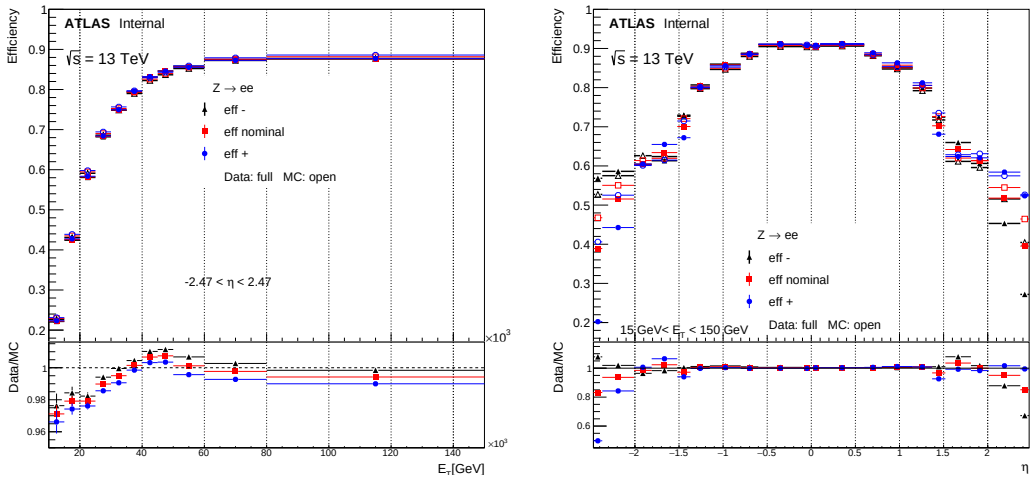

Figure A.9 – Efficiency and SF dependency on E_{T} inclusive in η (left) and on η inclusive in E_{T} (right) for nominal WP3 (red) and WP3 split by charge for 2017 data.

A.3.3 Electron Trigger Scale Factors

According to formula 3.2 the last component of the electron efficiency is the trigger efficiency that is computed on top of PromptLeptonVeto working point ($\epsilon_{\mathrm{trigger}} = Pass(WP3 + Trigger)/Pass(WP3)$). In figure A.2 are show the triggers for which electron trigger efficiency have been derived using the same Tag-and-Probe method described at the beginning of this section.

Three sets of Scale Factors were obtained by trigger category. For single electron triggers the logical OR is used to combine several triggers as shown in table A.2. The trigger efficiencies and Scale Factors for single electron triggers are given in figure A.10 (top) and also Scale Factors uncertainty (bottom). Similarly, trigger efficiency, scale factors and scale factors uncertainty are given for di-electron triggers in figure A.11 and for multi-lepton triggers (e-μ trigger, using electron leg only for efficiency measurement) in figure A.12. Overall the trigger Scale Factors are close to 1 (>0.97), particularly in central regions of η, with an uncertainty (statistically dominated) generally below 1%. Some fluctuations in Scale Factors are observed at low E_T (in the first bin after the turn-on value

	Single lepton (SL)	Di-electron(DL)*	Multi-lepton (ML)*
2015	HLT_e24_lhmedium_L1EM20VH || HLT_e60_lhmedium || HLT_e120_lhloose	HLT_2e12_lhloose_L12EM10VH	HLT_e17_lhloose_mu14
2016	HLT_e26_lhtight_nod0_ivarloose || HLT_e60_lhmedium_nod0 || HLT_e140_lhloose_nod0	HLT_2e17_lhvloose_nod0	HLT_e17_lhloose_nod0_mu14
2017	HLT_e26_lhtight_nod0_ivarloose || HLT_e60_lhmedium_nod0 || HLT_e140_lhloose_nod0	HLT_2e24_lhvloose_nod0**	HLT_e17_lhloose_nod0_mu14

Table A.2 – List of triggers used for calibration by year. **Only single electron leg* ***L12EM20VH seeded*

of the trigger) with high values (up to 1.3) in the "crack" region and low drops (down to 0.5) in the extreme η bins. The extreme η bins and the "crack" η bin suffer from lower available statistics as can be seen in the uncertainty plots where spikes in the statistic uncertainty can be observed.

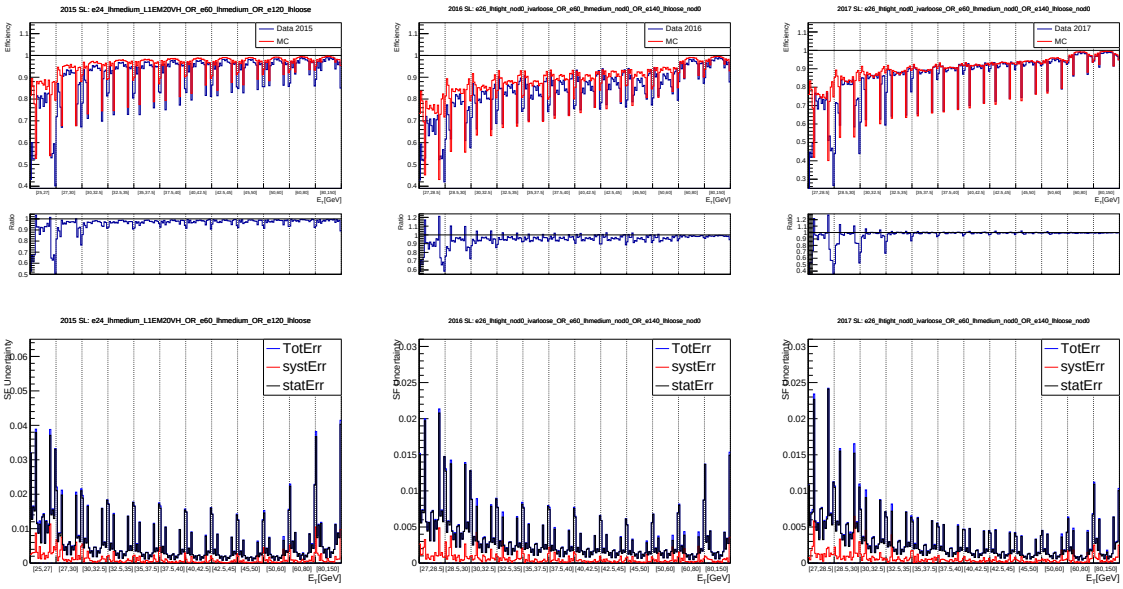

Figure A.10 – Single electron trigger efficiency and Scale Factors (top) by year 2015 (left), 2016 (center) and 2017 (right). Corresponding Scale Factor uncertainty (bottom) by year 2015 (left), 2016 (center) and 2017 (right). Each E_T bin contains 20 η bins [-2.47,2.47].

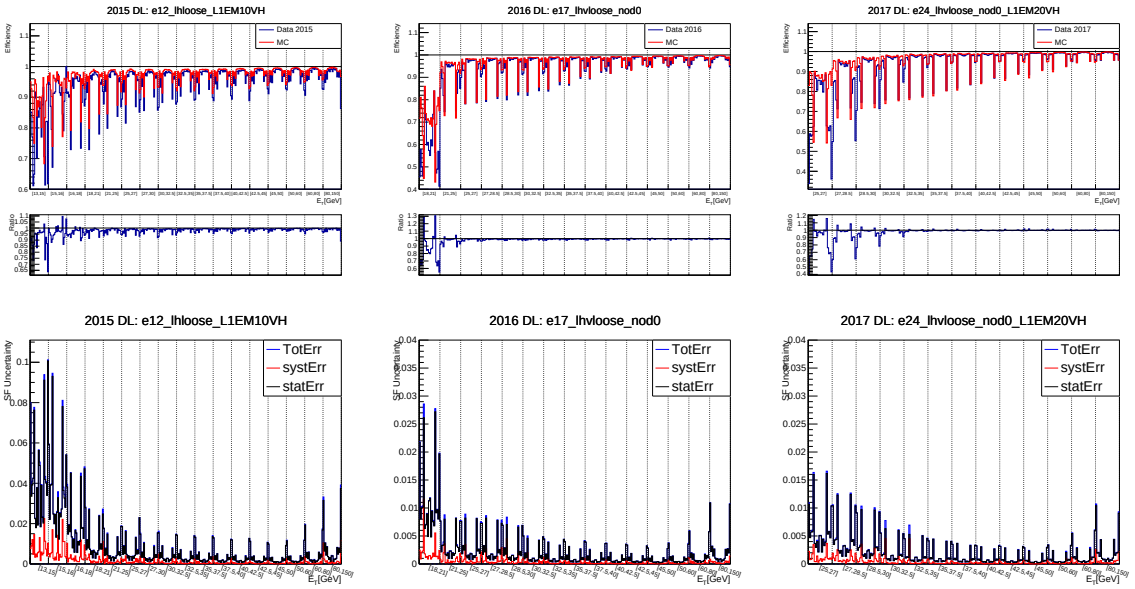

Figure A.11 – Di-electron trigger efficiency and Scale Factors (top) by year 2015 (left), 2016 (center) and 2017 (right). Corresponding Scale Factor uncertainty (bottom) by year 2015 (left), 2016 (center) and 2017 (right). Each E_T bin contains 20 η bins [-2.47,2.47].

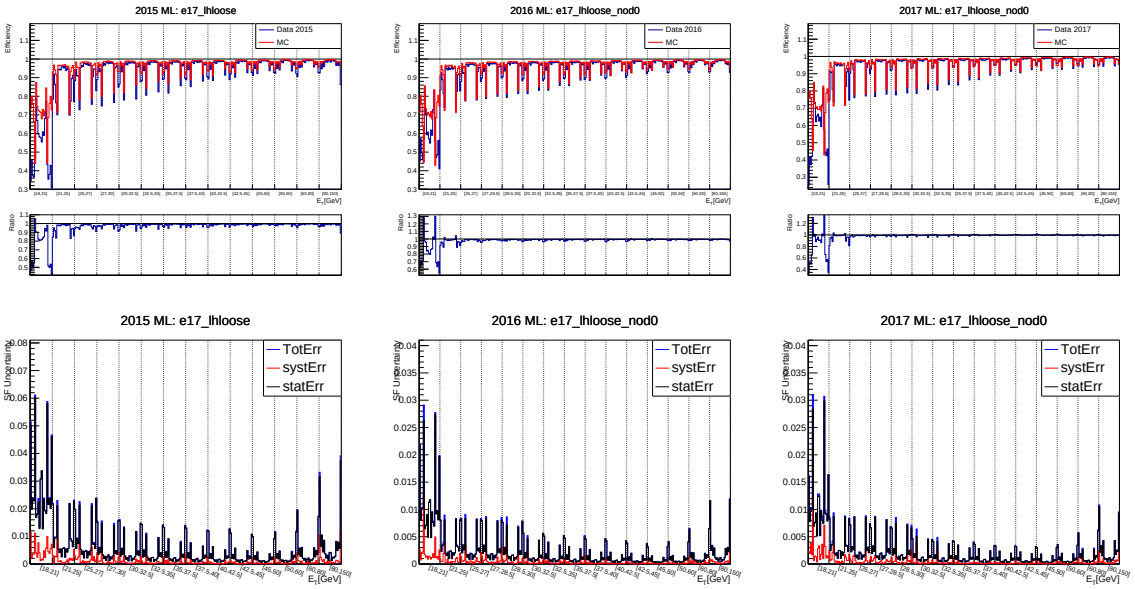

Figure A.12 – Multi-lepton trigger efficiency and Scale Factors (top) by year 2015 (left), 2016 (center) and 2017 (right). Corresponding Scale Factor uncertainty (bottom) by year 2015 (left), 2016 (center) and 2017 (right). Each E_T bin contains 20 η bins [-2.47,2.47].

A.3.3.1 Impact of M(tr+,tr-) cut on electron Scale Factors

To further reduce and to have a better handle on the conversions a new variable, M(tr+,tr-), is introduced (see section 5.3 for definition). Measurement of SFs is performed on two WPs involving M(tr+,tr-):

1. WP3 selections + M(tr+,tr-) > 100 MeV
2. WP3 selections + M(tr+,tr-) > 200 MeV

The fraction of electrons that do not pass this additional selection is 0.5% for the first bin (0-100 MeV) and 2% for the first and second bin (0-200 MeV). The large overflow (23% of entries) represents the electrons that do not have close by track with opposite charge.

The efficiencies and SFs for the two M(tr+,tr-) cuts (+WP3) and for the WP3 alone (for reference) are given in figure A.13 (parameterized in E_{T} and η). As expected, because of the small fraction of electrons that do not pass the additional M(tr+,tr-) selection, the efficiencies and SFs are minimally affected. The decrease in efficiency is observed to be at most few percent for M(tr+,tr-)>200 MeV and below percent for M(tr+,tr-)>100 MeV. The overall SFs change is insignificant (per-mile level) with only a few E_{T} x η bins having differences of percent level in the low η region (10-20 GeV) for M(tr+,tr-)>200 MeV WP.

Figure A.14 shows the efficiency and SFs inclusive in η or E_{T}.

Due to very small overall differences in SFs (and time constraints), no (re)derivation of the SFs is necessary at this stage. Figure A.15 shows the dependence of the efficiency and SFs on the M(tr+,tr-) variable. The SFs are stable and very close to 1 with no dependence on M(tr+,tr-) except the low M(tr+,tr-) region (M(tr+,tr-)<500 MeV) where an effect of up to 7-10% up deviation is observed.

The effect of derivation of the SFs in the whole range of $|\eta| < 2.47$ versus application on electrons only in restricted range of $|\eta| < 2.0$ was studied as a function of the M(tr+,tr-) variable. Individual efficiencies in data and MC were derived for all three years and comparison of SFs was performed. The residual effect is at worst 1% and hence negligible in this analysis as visible in Figure A.16

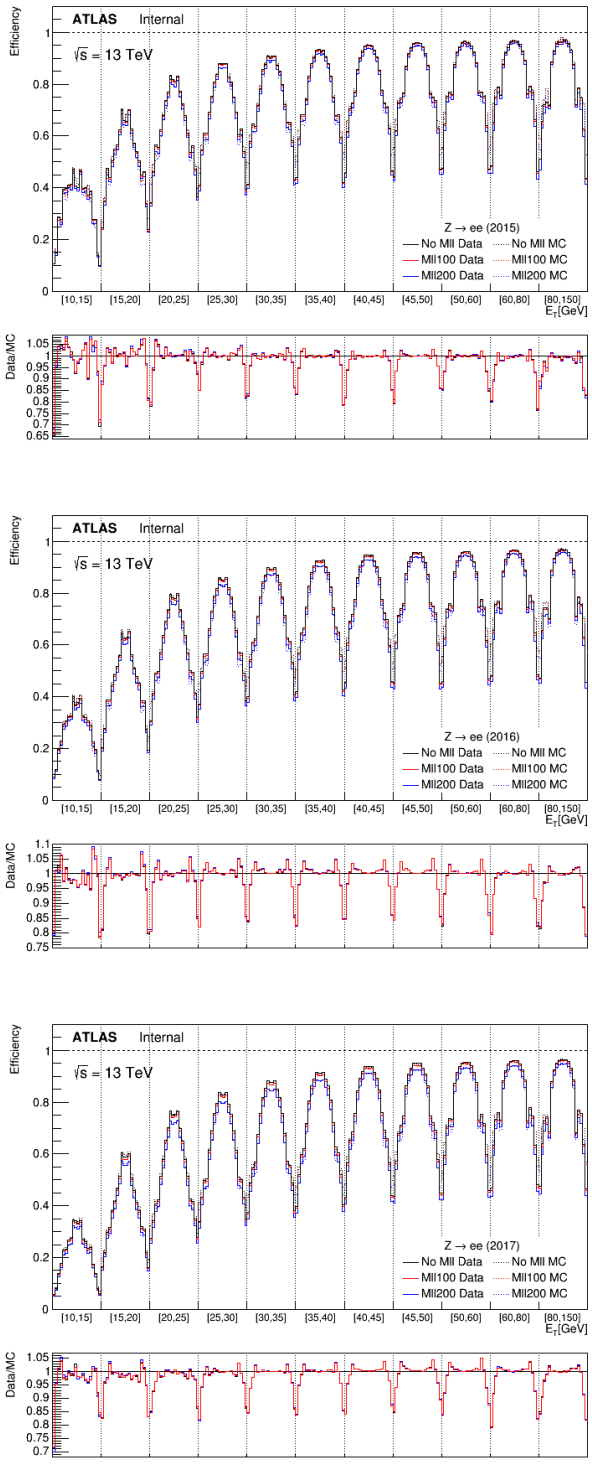

Figure A.13 – Efficiency and SF (ratio) for WP3, WP3 + M(tr+,tr-)>100 MeV and WP3 + M(tr+,tr-)>200 MeV in bins of E_{T} (each E_{T} bin contains 20 η bins). The plots correspond to 2015 (top), 2016 (middle) and 2017 (bottom) data.

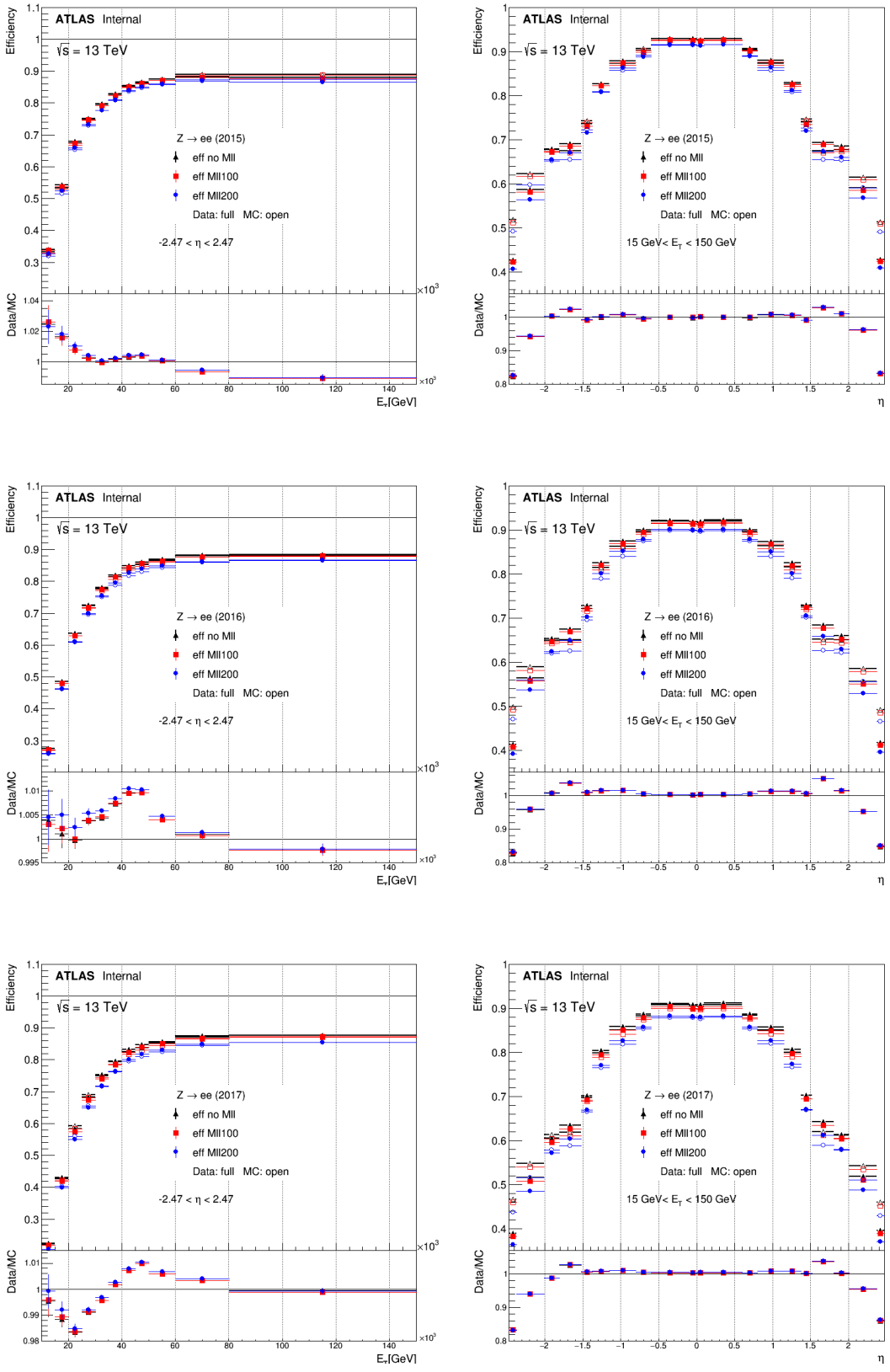

Figure A.14 – Efficiency and SF (ratio) for WP3, WP3 + M(tr+,tr-)>100 MeV and WP3 + M(tr+,tr-)>200 MeV in bins of E_{T} but inclusive in η (left) and in bins of η but inclusive in E_{T} (right) for 2015 (top), 2016 (middle) and 2017 (bottom) data.

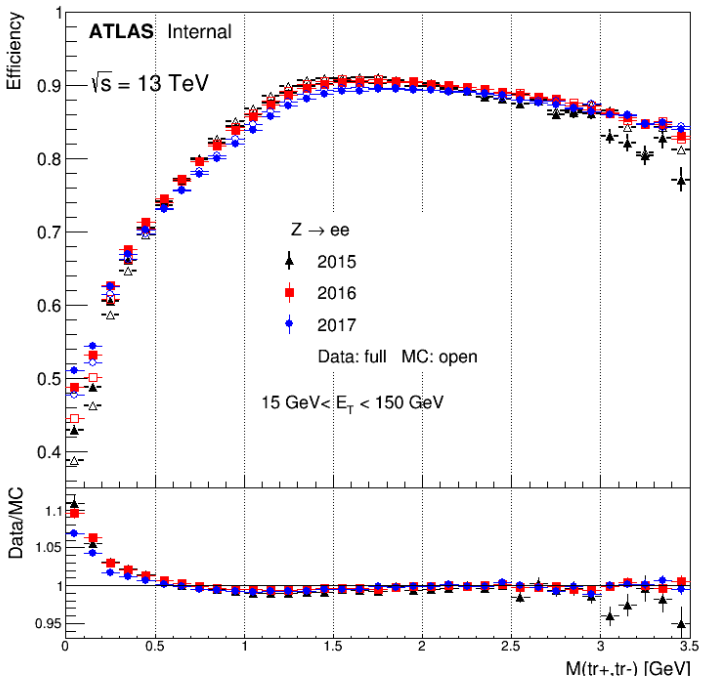

Figure A.15 – Efficiency and SF dependence on M(tr+,tr-) for WP3 selections.

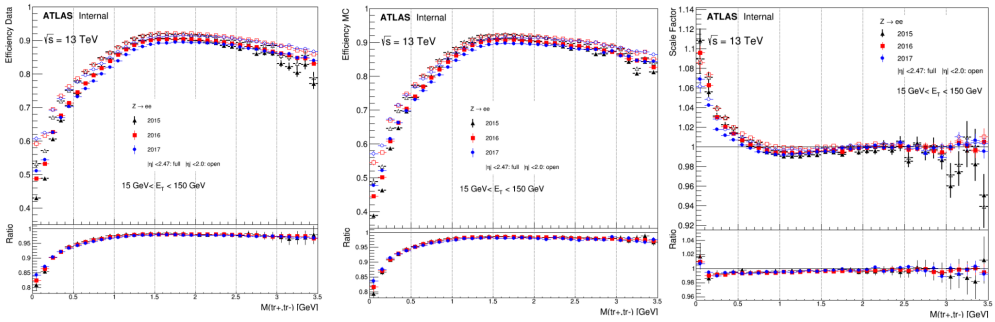

Figure A.16 – Data (left) and MC (middle) efficiencies as a function of the M(tr+,tr-) variable comparing efficiencies in the whole η range (full markers) and range restricted to the analysis phase space of $\eta < 2.0$ (open markers). The SF comparison is on the right with the bottom ratio presenting the negligible residual difference in the SFs.

Abstract

The Large Hadron Collider (LHC) is the largest particle collider in the world. It has a total length of about 27 km and is located at around 100 m under the French-Swiss border at the European Organization for Nuclear Research (CERN) near Geneva. Proton beams are accelerated in two counter-rotating beams that collide inside four main detectors. Investigating the outcome from the collisions allows studying the most fundamental laws of physics. In this thesis are analyzed proton-proton collisions at a center of mass energy of 13 TeV recorded during 2015-2017 with the ATLAS detector.

The first part of the thesis concerns the performance of the ATLAS detector, in particular electron efficiency measurements. A *Tag-and-Probe* method is used in $Z \to ee$ events to measure the electron reconstruction efficiency, which accounts for how well are the tracks reconstructed and matched to an energy cluster in the calorimeter. The measured electron reconstruction efficiency varies between 97% (15<E_T<25 GeV) up to 99% at higher transverse energies with an uncertainty level of around 1% and per-mile level, respectively. A similar method is employed to measure the electron efficiency of a new algorithm (PLI and PLV) designed to reduce the electrons originating from heavy flavor decays. The PLI efficiency is 60-70% at low E_T (E_T<20 GeV) increasing up to 95% at higher E_T. The efficiencies are measured both in data and in Monte Carlo simulation, and their ratios are used in physics analyses as scale factors for the simulations to match the data efficiency.

The second part of the thesis covers two physics topics involving the top quark and the Higgs boson.

A search for flavor-changing neutral currents (FCNC) in top decays to an up-type quark (u or c) and a Higgs boson ($t \to Hu$ or $t \to Hc$) is performed using the 2015-2016 data. These processes are strongly suppressed in the Standard Model (SM), however larger enhancements are predicted in new physics models. This analysis targets final states including exactly two light leptons, electron or muon, of the same sign (2ℓSS) or three light leptons (3ℓ) with multiple jets. Multivariate analyses (MVA) are used to improve signal-background separation. The measured branching ratio for the $t \to Hu$ ($t \to Hc$) process is found to be compatible with zero and a 95% confidence level upper limit is set at 0.19% (0.16%) with an expected limit of 0.15% (0.15%), the best limit in a single channel to date.

The Higgs boson production in association with a top quark pair (ttH) allows direct access to the top Yukawa coupling. The last part of the thesis describes

the ttH search in the 2ℓSS channel with 2015-2017 data. For the first time, the ttH production mode was observed by the ATLAS and CMS experiments, independently, by combining several decay channels. Further efforts and challenges to measure ttH in the 2ℓSS channel using the 2015-2017 data are discussed.

Résumé

Le Large Hadron Collider (LHC) est le plus grand collisionneur du monde avec une longueur totale de 27 km. Il est situé à l'Organisation pour la recherche Nucléaire (CERN), 100 mètres sous terre, sous la frontière franco-suisse. Les faisceaux de protons sont accélérés en sens inverse et se rencontrent dans quatre détecteurs. L'analyse des collisions permet d'étudier les lois les plus fondamentales de la physique. Cette thèse présente l'analyse des données enregistrées avec une énergie dans le centre de masse de 13 TeV, en 2015-2017, par le détecteur ATLAS.

La première partie de la thèse concerne la performance du détecteur ATLAS dans la reconstruction des électrons. Une méthode *Tag-and-Probe* est utilisée avec des évènements $Z \to ee$, pour mesurer la probabilité que des électrons soient reconstruits comme des traces et associés à un amas d'énergie dans le calorimètre électromagnétique. L'efficacité de reconstruction des électrons est mesurée entre 97% ($15 < E_{\mathrm{T}} < 25$ GeV) et 99% pour les énergies transverses plus grandes, avec une précision autour de 1% et de l'ordre du pour mille, respectivement. Une méthode similaire est employée pour mesurer l'efficacité des électrons après l'application d'un nouvel algorithme utilisé pour réduire la contribution des électrons venant des décroissances de quark de saveur lourdes (PLI et PLV). L'efficacité est mesurée à 60-70% à bas E_{T} ($E_{\mathrm{T}} < 20$ GeV) s'accroissant jusqu'à 95% à haut E_{T}. Dans les deux cas, les efficacités sont mesurées sur les données et sur la simulation Monte Carlo. Leurs rapports sont utilisés, dans les analyses de physique, comme facteur d'échelle sur la simulation pour reproduire les efficacités mesurées sur les données.

La seconde partie de la thèse couvre deux sujets de physique comprenant le quark top et le boson de Higgs.

Tout d'abord, une recherche de courants neutres changeant la saveur (FCNC) dans la décroissance du quark top en quark u ou c et un boson de Higgs est effectuée sur les données de 2015 et 2016. Ces processus sont très fortement supprimés dans le Modèle Standard, même si des rapports d'embranchements bien supérieurs sont prédits dans certains modèles de nouvelle physique. Cette analyse vise plus particulièrement des états finals avec exactement deux leptons de même signe (2ℓSS) et trois leptons (3ℓ) avec plusieurs jets. Des analyses multivariées (MVA) sont utilisées pour améliorer la séparation entre le signal et le bruit de fond. Les rapports d'embranchements mesurés dans les données pour les processus $t \to Hu$ ($t \to Hc$) sont compatibles avec zéro et des limites supérieures valant 0.19% (0.16%) sont obtenues à 95% de niveau de confiance. Ces

résultats sont les meilleurs pour un canal donné aujourd'hui.

La production du boson de Higgs avec une paire de quark top (ttH) permet un accès direct au couplage de Yukawa du quark top. La dernière partie de la thèse décrit la recherche de ce mode de production dans le canal multilepton. Ce mode de production a été observé indépendamment pour la première fois par les expériences ATLAS et CMS, en combinant plusieurs canaux de désintégration. Les défis et les efforts nécessaires pour mesurer la section efficace dans le canal 2ℓSS avec les données de 2015 à 2017 sont discutés.